

ISOMERIC CROSS SECTION RATIOS AND EXCITATION
FUNCTIONS OF SOME NUCLEAR REACTIONS INDUCED IN
STRONTIUM-88 BY PROTONS OF ENERGY 7-85 MeV

by

DESH RAJ SACHDEV, M.Sc. (Physics, Lucknow)
M.Sc. (Chemistry, Lucknow)

A thesis submitted to the Faculty of
Graduate Studies and Research in partial
fulfilment of the requirements for the
degree of Doctor of Philosophy

Radiochemistry Laboratory,
Department of Chemistry,
McGill University,
Montreal, Canada.

August 1966

NUCLEAR REACTIONS INDUCED IN STRONTIUM-88
BY PROTONS OF ENERGY 7-85 MeV

by

DESH RAJ SACHDEV



ACKNOWLEDGEMENTS

The author is pleased to take this opportunity of expressing his sincere appreciation to Dr. L. Yaffe for his encouragement and guidance throughout the course of this work.

Thanks are also due to:

Dr. N.T. Porile for direction during the absence of Dr. L. Yaffe from McGill University (1963-1965).

Dr. T.T. Sugihara for an evening of pleasant and valuable discussion.

Dr. B. Margolis for some helpful discussions and for providing the optical model proton transmission coefficients (computed by ABACUS-2) which were useful in comparing the results computed by the program used in this work.

Dr. R.E. Bell, Director of the Foster Radiation Laboratory, for permission to use the Cyclotron and Mr. R.H. Mills, the cyclotron operator, for assistance and cooperation in carrying out the bombardments.

Members of the Radiochemistry Laboratory for help in various ways.

The staff of the Computing Centre at McGill University for their cooperation in writing the programs and in carrying out the calculations.

The Chemistry Department of McGill University for Demonstratorships during the Academic Sessions 1960-1965.

The National Research Council for financial assistance in the form of grants during the summers of 1960-1965 and the Academic Sessions 1964-1966.

Mrs. C. Macfarlane for her superb typing and Dr. V.P. Gupta for proof-reading this thesis.

Finally, my wife, Pramila, for her patience and encouragement.

TABLE OF CONTENTS

	<u>Page</u>
I. <u>INTRODUCTION</u>	1
I-1. General	1
I-2. Compound Nucleus Mechanism and Statistical Model	3
I-3. Experimental Verification of Compound Nucleus Mechanism	10
I-4. Direct Interaction Mechanism and Cascade Evaporation Model	14
I-5. Monte Carlo Calculations	18
I-6. Optical Model and Nuclear Reactions ..	21
I-7. Isomer Ratios	27
I-7.1. Nuclear Isomers	27
I-7.2. Angular Momentum and Isomer Ratios	30
I-8. Present Work	36
II. <u>EXPERIMENTAL PROCEDURES</u>	38
II-1. Target Material and Irradiation Procedure	38
II-2. Chemical Procedures	40
II-2.1. Dissolution of Target and Separation into Elemental Fractions ..	42
II-2.2. Purification of Individual Elemental Fractions	44
II-3. Chemical Yields	49
II-4. Radiation Detection and Measurement Procedures	50
II-4.1. 4π - β Counting	52
II-4.2. Gamma-Ray Measurements	56
II-4.3. Positron Measurements	67

	<u>Page</u>
III. <u>TREATMENT OF DATA</u>	74
III-1. Absolute Disintegration Rates	74
III-1.1. 4π - β Counting Data	74
III-1.2. Gamma-Ray Measurement Data ..	75
III-1.3. Positron Measurement Data ..	76
III-2. Decay Curve Analysis	77
III-3. Corrections for the Disintegration Rates of Unshielded Species	78
III-3.1. Calculation for the Disintegration Rate of the Ground State of an Isomeric Nuclide	78
III-4. Calculation of Cross Section	80
III-5. Monitor Cross Sections	82
IV. <u>EXPERIMENTAL RESULTS</u>	84
IV-1. Individual Nuclides	84
IV-1.1. 105 day- ⁸⁸ Y	84
IV-1.2. 13.5 hr.- ^{87m} Y and 80 hr.- ^{87g} Y ..	87
IV-1.3. 48.5 min.- ^{86m} Y and 14.6 hr.- ^{86g} Y ..	89
IV-1.4. 2.68 hr.- ^{85m} Y and 5.0 hr.- ^{85g} Y ..	92
IV-1.5. 40 min.- ⁸⁴ Y	92
IV-1.6. 70 min.- ^{85m} Sr and 65 d.- ^{85g} Sr ..	94
IV-1.7. 18.7 d.- ⁸⁶ Rb	94
IV-1.8. 33 d.- ⁸⁴ Rb	96
IV-1.9. 83 d.- ⁸³ Rb	96
IV-1.10. 12.8 hr.- ⁶⁴ Cu and 38.3 min.- ⁶³ Zn ..	96
IV-2. Errors	97

	<u>Page</u>
V. <u>CALCULATIONS AND DISCUSSION</u>	132
V-1. Qualitative Considerations (Isomer Ratios)	132
V-2. Isomer Ratio Calculation for $^{88}\text{Sr}(p,2n)^{87\text{m,g}}\text{Y}$ Reaction	137
V-3. Parameters Necessary for the Calculation	138
V-3.1. The Spin Cutoff Parameter,	138
V-3.2. Average Kinetic Energies of Evaporated Neutrons	143
V-3.3. Multipolarity and Number of Gamma Rays Emitted	151
V-3.4. Transmission Coefficients	153
V-3.5. Level Density Parameter	154
V-4. Spin Distributions at Different Stages of De-excitation and Determination of Isomer Ratios	155
V-5. Comparison of Experimental Results with Calculations	157
V-6. Effect of Transmission Coefficients on Isomer Ratios	165
V-7. Excitation Functions	166
V-7.1. (p,xn) Reactions	167
V-7.2. (p,p3n) Reaction	170
V-7.3. (p,2pxn) Reactions	171
VI. <u>SUMMARY</u>	175
 <u>APPENDIX</u>	 177
App.-1. Calculations for the Disintegration Rates of the Ground and Metastable States of ^{85}Sr	177
App.-2. Optical Model and Transmission Coefficients	182
App.-3. Square-Well Model Transmission Coefficients	189
App.-4. Parameters Used for the Calculation of Transmission Coefficients (Optical Model)	191
 <u>REFERENCES</u>	 194

I. INTRODUCTION

I-1. GENERAL

An interaction between nucleons and/or nuclei is commonly termed a nuclear reaction. This includes a variety of processes such as elastic or inelastic scattering, spallation, fragmentation, fission, etc. In the present work strontium, enriched to greater than 99.8% in mass 88, was bombarded with protons in the energy range 7 to 85 MeV. Elastic or inelastic scattering studies, although important, have not been undertaken in this work. The process of fission involves the division of target nucleus into two or more roughly equal masses; while in fragmentation, chunks of nuclear matter are split off from the struck nucleus. The chance of occurrence of the latter two processes, in the range of energy and for the target nucleus under investigation, is very small. We will therefore concern ourselves with spallation reactions in which nucleons or small clusters of nucleons are ejected from the bombarded nucleus.

When a projectile (nucleon or a light complex nucleus) approaches a target nucleus, it finds itself under the influence of internucleonic forces. The incomplete understanding of nuclear structure, however, forbids one to construct an exact Hamiltonian for the energy of the system. One is therefore forced to replace the exact Hamiltonian with a simple one, the

solutions of which could be worked out. In other words, one constructs a model, usually analogous to a certain physical concept, and applies it to the limited task of explaining only a certain aspect of the problem. Thus, in nuclear reactions, even for the same projectile-target system, different models are used to explain different features of nuclear reactions depending on bombarding energy, mass of the target nucleus, etc.

Nuclear reactions are commonly interpreted with the aid of two mechanisms, depending on the excitation energy imparted to the nucleus by the incoming projectile. At low energies the compound nucleus mechanism⁽¹⁾, a two-step process, is employed. This involves a slow intermediate stage. At high energies, the direct interaction, a one-step process, is commonly invoked. For reactions proceeding by a compound nucleus mechanism, therefore, the products should not show any memory of the way of their formation which further leads to predictions of 'symmetry about 90° ' in the centre-of-mass system, and Maxwellian shape of the energy spectra of emitted particles. In the case of a direct interaction, however, the reaction products are expected to show a strong memory of their formation, and the ejected particles exhibit strong preference for emission in the forward direction and be energetic.

Both of these mechanisms are discussed in the following sections.

I-2. COMPOUND NUCLEUS MECHANISM AND
STATISTICAL MODEL

When Bohr⁽¹⁾ proposed his compound nucleus model, Bethe⁽²⁾ had already put forward a potential-well model (Section I-6) for neutron reactions, which unfortunately was unable to predict the narrow resonances found experimentally. Bohr realized that these narrow resonances are essentially a many-particle effect as the excited states of such a system would have many different configurations differing in small amounts of energy. Accordingly, he assumed the nucleus as a system of particles having strong interactions of short range between them. The process of a nuclear reaction could thus be visualized as follows. The impinging particle amalgamates with the nucleus as soon as it enters the boundary of nuclear forces. The excitation energy (kinetic + binding energies) and momentum splits between the particles at each collision and is quickly shared because of strong interaction (or short mean free path) attaining a quasi-equilibrium state. The excitation energy is shared nearly equally between the nucleons, most of the time, and the excited states are quasi-stationary. After a long time (long compared to the time the projectile takes in crossing the target nucleus), by fluctuation, when enough energy (greater than separation energy) gets concentrated on a nucleon or a group of nucleons, particle emission becomes possible. Alternatively, if the life-time of a compound state is comparable to the life

time for gamma emission, decay of the compound nucleus by gamma emission also becomes feasible. The nuclear reaction is thus divided into two independent stages,

1. formation of the compound nucleus, and
2. disintegration of the compound nucleus into reaction products.

The compound nucleus thus forgets the way or the channel in which it was formed, before the process of decay sets in, and the decay of this intermediate state is characterized only by the constants of motion (energy, angular momentum and parity), its size and shape. Experiments designed to test the validity of this hypothesis are described in the following section (I-3).

Widths and interspacings of resonance lines observed in the (n, γ) reactions of many elements show clearly that excited states at lower energies are quite sharp and relatively widely spaced. The mean life-time of the compound nucleus could be calculated by using the width of the resonance line in Heisenberg's uncertainty principle, i.e.

$$\tau = \frac{\hbar}{\Gamma} \quad (1)$$

These life-times are found to be about 10^{-14} - 10^{-15} seconds compared to 10^{-18} seconds required for a thermal neutron to cross a medium weight nucleus. The partial width for decay into a particular channel J is denoted by Γ_J and is related to

the total width by the relation

$$\Gamma = \sum_J \Gamma_J \quad (2)$$

When the excitation energy of the compound nucleus is increased, the chance of localizing enough energy on a nucleon, or a group of nucleons, increases. Further, some of the channels which were prohibited due to barriers (centrifugal and/or potential) also become accessible. All this results in a decrease of the mean life-time of the compound nucleus, and therefore an increase in the width (broadening) of the corresponding level. In addition, the spacing between the energy levels should be expected to decrease as the energy of the excited nucleus increases. Both these effects contribute towards the overlapping of levels and to a condition under which it should be impossible to excite a nucleus to a single level even under ideal energy resolution conditions. This is known as the Continuum Region.

Many states of the compound nucleus which enter into the reaction should, therefore, be expected to interfere. This will result in asymmetry of angular distribution of emitted particles about 90° in the centre-of-mass system, contrary to the result when the decay takes place from a single quantum state. It is assumed that 'the internal motion of the compound nucleus is completely randomized except for the exact quantum numbers, energy, angular momentum, etc.'⁽⁴⁾ Under this assumption there are no phase relations between the various

contributing states. If one further assumes that the width of the incident energy beam is larger than Γ , interference effects should cancel out and the symmetry in angular distribution is restored. Another problem arises if the overlapping states have different partial widths for a particular exit channel, affecting the independence hypothesis. This is, however, annulled by assuming that the overlapping states have the same relative partial widths for the various possible decay channels. These assumptions form the basis for the statistical model and allow the applicability of the Bohr assumptions to a region of overlapping states.

With these assumptions it becomes a simple matter to calculate the cross sections for individual reactions by comparing the excited nucleus to a heated liquid drop or radiation from a black body and by the use of the principle of detailed balance.^(3,4) According to this principle, the transition probability from a state 'a' to a state 'b', P_{ab} is related to the transition probability from a state 'b' to the state 'a' by the relation

$$\omega_a P_{ab} = \omega_b P_{ba}^* \quad (3)$$

where ω_a and ω_b denote the density of states for the state 'a' and 'b' respectively, and the asterisk on P_{ba} indicates the time-reversed transition, i.e. transitions in which all velocities and angular momenta have changed signs. The phase space considerations then lead to the desired results; and the

probability $P_{\nu}(\mathcal{E}, E_c)$ per unit time for the emission of a particle ν with channel energy between \mathcal{E} and $\mathcal{E} + d\mathcal{E}$ from a compound nucleus with excitation energy E_c is given by

$$P_{\nu}(\mathcal{E}, E_c) d\mathcal{E} = \frac{(2s_{\nu} + 1)}{\pi^2 \hbar^3} \cdot \mathcal{E} \cdot \mu \cdot \sigma_{\nu}(\mathcal{E}, E_f) \cdot \frac{\omega(E_f)}{\omega(E_c)} \cdot d\mathcal{E} \quad (4)$$

where μ = reduced mass of the emitted particle and residual nucleus system,

\mathcal{E} = channel energy or kinetic energy of the relative motion of the emitted particle and residual nucleus in the centre-of-mass system,

s_{ν} = spin of particle ν [($2s_{\nu} + 1$) is the statistical weight factor],

E_f = excitation energy of the residual nucleus,

$\sigma_{\nu}(\mathcal{E}, E_f)$ = inverse cross section for the capture of particle ν with relative kinetic energy \mathcal{E} by the residual nucleus at excitation energy E_f , and

$\omega(E_f)$ and $\omega(E_c)$ = density of states for residual and compound nuclei at appropriate excitation energies.

The total probability per unit time for emitting particle ν , is obtained by integrating (4) over its energy spectrum, i.e.

$$\frac{\Gamma_{\nu}}{\hbar} = \int_{\mathcal{E}} P_{\nu}(\mathcal{E}, E_f) d\mathcal{E} \quad (5)$$

and the total probability per unit time for the decay by all particles is obtained from (5) by summing over all particles and their corresponding energy spectra. The cross section for the

emission of particle ' ν ' is then obtained by finding the relative probability for the emission of this particle to all others, and multiplying 'it' with $\sigma_c(\epsilon_a)$, the cross section for the formation of a compound nucleus with projectile 'a' and with channel energy ϵ_a ; and is given by

$$\sigma(a, \nu) = \sigma_c(\epsilon_a) \cdot \frac{\Gamma_\nu}{\sum_i \Gamma_i} \quad (6)$$

Necessary limits for integration of equation (5) and similar equations, due to all other particles, are determined by potential barriers, separation energies and energy spectra of these particles. It may be noted that equation (6) has been derived for the evaporation of a single particle and the calculations will have to be repeated for the second particle when the residual nuclei, which are formed over a spectrum of energies, will be considered as the compound nuclei. It may also be pointed out that, in this derivation, effects due to angular momentum are ignored. To take these into account, equation (4) is modified to give rate of emission of particle ν from a particular angular momentum state J_c of the compound nucleus of excitation energy E_c to the residual nucleus of a particular angular momentum state J_f and excitation energy E_f as (5,6)

$$R(E_c, J_c, \epsilon, J_f) d\epsilon = \frac{(2s_\nu + 1)}{\pi^2 \hbar^3} \cdot \epsilon \cdot \mu \cdot \sigma(\epsilon, J_c, J_f) \cdot \frac{\omega(E_f, J_f)}{\omega(E_c, J_c)} \cdot d\epsilon \quad (7)$$

where the density of states in this case corresponds to a particular angular momentum J_c or J_f at appropriate excitation energies; and the inverse cross section also refers to particular angular momentum states besides other specifications mentioned above. Again, the probability per unit time for emission of particle ν , corresponding to equation (5), is obtained for the decay of a compound nucleus with particular spin J_c and excitation energy E_c as

$$\frac{\Gamma_{\nu}(E_c, J_c)}{\hbar} = \frac{(2s_{\nu} + 1)}{\pi^2 \hbar^3} \mu \int_{\epsilon} \sum_{J_f} \sigma_{\nu}(\epsilon, J_c, J_f) \frac{\omega(E_f, J_f)}{\omega(E_c, J_c)} d\epsilon \quad (8)$$

The summation over J_f is performed in order to take into account the probability of decay from a given state J_c to any state J_f . The cross section for the emission of particle ν from a particular spin state J_c is obtained by multiplying the relative probability for the emission of particle ν as compared to all other particles (as in the previous case) and the cross section for the formation of a compound nucleus with spin J_c at excitation energy E_c . This is therefore given by

$$\sigma_{J_c}(a, \nu) = \sigma_c(\epsilon_a, J_c) \frac{\Gamma_{\nu}(E_c, J_c)}{\sum_i \Gamma_i(E_c, J_c)} \quad (9a)$$

and the total cross section for the emission of particle ν from all compound states is given by

$$\sigma(a, \nu) = \sum_{J_c} \sigma_c(\epsilon_a, J_c) \frac{\Gamma_{\nu}(E_c, J_c)}{\sum_i \Gamma_i(E_c, J_c)} \quad (9b)$$

It may be remarked that, although inverse cross sections are for the excited state, it is possible only to calculate them for the ground state. Equation (9) has been used by Esterlund and Pate⁽⁷⁾ for analysing the excitation function (defined below) data for reactions involving the emission of a single nucleon.

The physical picture as emerging from the previous discussion is that an excited nucleus with excitation energy greater than particle emission threshold will evaporate particles (e.g. neutrons) and, when the excitation energy is not enough for particle emission, the excited nucleus approaches the ground state by emitting a cascade of gamma rays. As the emitted particles will have a spectrum of energies, residual nuclei will correspondingly be formed with a variety of excitation energies. Various conservation laws will apply at each de-excitation stage. Equation (4) could be further simplified (with suitable assumptions) to show that the energy spectra of emitted particles has a Maxwellian shape. The formation of peaks in the graphs, representing cross section versus energy (of the projectile) for a particular reaction product, is easily understood according to the afore-mentioned assumptions. These graphs are called 'Excitation Functions' and form a major part of this work.

I-3. EXPERIMENTAL VERIFICATION OF COMPOUND NUCLEUS MECHANISM

Bohr's theory is based on the assumption that particle emission occurs after a relatively long time has elapsed from the time the incident particle was captured. Probably the best verification would be the determination of these life-times from resonance widths of single levels. This has been done for slow

neutron reactions and typical life-times, as ascertained from resonance widths, are found to be 10^{-15} to 10^{-16} seconds.

Ericson⁽⁸⁾ has inferred approximate life-times of the excited states in a region between isolated neutron resonances and strongly overlapping levels, by utilizing fluctuations in total reaction cross sections. These fluctuations, which arise as a result of a few exit channels available at such excitation energies, occur with a period of $T = \frac{h}{\Gamma}$. By analysing Cranberg's⁽⁹⁾ data for total cross sections for 2.5 MeV neutrons (with 2 keV resolution) incident on Fe, he found the half-width about 5 keV corresponding to an approximate life-time of 10^{-19} seconds.

With the increase of excitation energy appreciably above the neutron binding energy, it however becomes impossible to determine the life-times from an individual level. It therefore becomes necessary to look towards more indirect ways such as those described below.

One of the classical experiments to test the validity of the Independence hypothesis is due to S.N. Ghoshal.⁽¹⁰⁾ Ghoshal studied the excitation functions of different nuclear reactions by forming the same compound nucleus (^{64}Zn) in two different ways, $^{63}\text{Cu} + p$, and $^{60}\text{Ni} + \alpha$. His results showed that, within experimental error, the relative cross sections of different products, for proton as well as for alpha particle bombardments, were the same at the same excitation energy (e.g. $\frac{\sigma(p, pn)}{\sigma(p, 2n)} = \frac{\sigma(\alpha, pn)}{\sigma(\alpha, 2n)}$). There is a point to note, however.

When a compound nucleus is formed with two different projectiles at the same excitation energy, the distributions in angular momenta must be different. The compound nuclei produced by two 'ways' are therefore not truly identical. The main point is that, for a particular spin (I), there is a corresponding particular energy (E) below which, on the average, no states of spin I or greater exist. When a compound nucleus possesses excitation which is slightly above the threshold for nuclear emission, neutrons will be emitted with very low energy and consequently with little or no angular momentum ($l = 0$). If the compound nucleus possesses high angular momentum while the residual nucleus is being formed with a slight excitation energy, transitions will be hindered. In such cases de-excitation by gamma emission will effectively compete with neutron emission. This is also sometimes stated by saying that rotational energy associated with spin is not available for particle emission. The threshold for particle emission will be raised and the excitation function shifted. Tests similar to those of Ghoshal have also been performed by workers like John⁽¹¹⁾, Rayudu⁽¹²⁾, and Porile⁽¹³⁾. Recently Grover and Nagle⁽¹⁴⁾ measured the excitation functions for (p,n) , $(p,2n)$, (α,n) and $(\alpha,2n)$ reactions by forming the same compound nucleus (^{210}Po). They found their results consistent with the compound nucleus mechanism, provided they took into account the competition between gamma and neutron emission, as well as the different distributions in angular momentum for the compound nucleus

formed by proton and alpha particle bombardments.

A relatively more reliable test would be to compare the shapes of the energy spectra of the particles emitted by the same compound nucleus formed in different ways. The method also compares the probability of direct interaction to compound nuclear processes. The energy spectra observed by Sherr and Brady⁽¹⁵⁾ and Lassen et al.⁽¹⁶⁾ for the alpha particles emitted by the compound nucleus ^{60}Ni formed by the reactions ($^{59}\text{Co} + p$) and ($^{56}\text{Fe} + \alpha$) respectively and at approximately the same excitation energy have very similar shapes, thus supporting Bohr's Independence hypothesis. It may also be remembered that these spectra do contain a direct interaction component although not a dominant one.

The Statistical Model predicts the angular distribution of emitted particles to be symmetrical about 90° to the direction of the incident beam. The first test of this symmetry was performed by Wolfenstein.⁽¹⁷⁾ Since then many workers have performed angular distribution studies using incident particles in the low and intermediate energy range (of the order of 10 MeV per nucleon). The results are consistent with the view that the total reaction cross section involves mostly compound nuclear processes, although there is a sizeable fraction (10 - 20%) which should be attributable to direct interaction.⁽¹⁸⁾ Recently Bodansky et al.⁽¹⁹⁾ studied the evaporation of coincident protons from the $^{58}\text{Ni}(\alpha, 2p)$ reaction. ^{58}Ni is a proton-rich target and at 32 MeV the cross section for compound

nuclear processes was found to be 560 ± 50 mb, which is over one-third of the total reaction cross section. Good agreement was observed between the predictions of the statistical theory and the experimental yield, energy and angular distribution. The author attributes over 90% of the observed (2p) events to compound nuclear processes with alpha particles of 32 MeV incident energy.

I-4. DIRECT INTERACTION MECHANISM AND
CASCADE EVAPORATION MODEL

The compound nucleus mechanism is quite successful in explaining most of the aspects of low- and medium-energy nuclear reactions. However, the same reasoning cannot be applied to high-energy reactions. For example, as noted by Serber⁽²⁰⁾, for high-energy bombardments (e.g. with 100-MeV nucleons) products close in mass to the target nucleus are produced in high yield as well as the lighter products. Also, the excitation function curves for simple nuclear reactions do not fall rapidly after crossing the peak as at lower energies but instead vary slowly. Both these observations are contrary to the predictions of the statistical model. Serber also noticed the decrease in the total cross section for the results of Cook et al.⁽²¹⁾ (particularly for light nuclei) when several nuclei were bombarded with 90-MeV neutrons; an effect which he ascribed to 'transparency' of the nuclear matter. To this could also be added the preferential forward emission of relatively high energy particles (close to the incident beam

energy) as observed in energy and angular distribution studies.

Serber⁽²⁰⁾ argued that the mean free path of a nucleon traversing nuclear matter increases with its energy, and for a 100-MeV nucleon it will be about 4×10^{-13} cm, which is comparable to nuclear radii. Therefore a nucleon might traverse the nucleus and emerge without a single collision (Transparency). He described the initial stage of a nuclear reaction in terms of a succession of two-body collisions between the incident nucleon and the individual nucleons in a nucleus, with the struck nucleon and the others, and so on. If the energy of the incident particle and the struck nucleon is high enough so that their wave-length would be small compared to the internucleon distance, the presence of other nucleons could be ignored (Impulse approximation), except for the application of the Pauli exclusion principle. The emergence of either or both particles after the collision will be determined by the geometrical position of the collision in the nucleus and the direction of the particle after the collision, as well as by their energy. The inter-collisions continue until the affected nucleons either leave the nucleus or their energy is reduced to an extent that they are unable to leave the nucleus. In this manner an internuclear cascade is generated. The stochastic nature of the problem is obvious as the outcome depends on the collisions between the nucleons, made in a random way.

As the emitted particle carries a large fraction of incident energy, the number of particles knocked out will be few

and the residual nuclei will usually be left behind with relatively small excitation energy at the end of this stage. Nevertheless there will be a broad distribution of energies in the residual nuclei, ranging from zero to maximum excitation (incident + binding) energy. The residual nuclei will share this energy amongst their constituents and a quasi-equilibrium state, exactly similar to compound nucleus, is formed. The evaporation of particles from this state should be in accordance with the Statistical Model. These two stages of cascade and evaporation are sometimes referred to as the Cascade-Evaporation Model.

Thus the Serber mechanism explains, at least qualitatively, why products close to the target mass are formed in such a high yield as well as the large range of mass numbers that could have been expected from the Statistical Model. The model also easily explains the 'tails' observed in the excitation functions of simple nuclear reactions such as (p, xn) and (p, pxn) etc., as well as the reason why the emitted particles are strongly peaked forward in the high energy nuclear reactions.

Asymmetry in angular distribution results at medium energies, as observed by many workers^(22,23,24), is also ascribed to Direct Interaction. Although several mechanisms have been proposed, the view of Austern et al.⁽²⁵⁾ regarding two-body interactions in the diffuse surface of the nucleus seems to be favoured.^(23,26-28) Incidentally, reactions such as 'stripping' or 'pick-up' are also included in this category because they too

proceed with the same mechanism and time scale.

Nuclear reactions could also be divided into two classes on the basis of 'time-scale'. A fast reaction (or direct interaction) takes place in a time which is of the order of the transit time of a nucleon across the nucleus ($\sim 10^{-22}$ seconds) while a slow reaction takes a very much longer time. When the incident particle strikes the target, the wave-length of the particle is usually short and the first collision should thus be considered as a two-body collision (except at low energy). If this collision should happen to be at an appropriate site, particle ejection should be possible and the ejected particle will take up an essential part of the momentum and energy of the incident particle, leading to an asymmetry in the angular distribution results. The 'appropriate' site for the medium-energy particle should be considered as the diffuse surface of the nucleus. The incident and/or struck particle could very well stay in the nucleus. There will be further collisions between the nucleons and each successive collision will result in the distribution of energy and momentum, while particle emission is possible at each step. A particle emitted as a result of a second collision will also manifest the 'memory' of the incident particle and will still show preference for forward peaking, although less pronounced. When the energy is finally distributed amongst all particles and about equally, a compound nucleus is formed. As explained before in the section on compound nucleus, the emission is now likely to be after a

long time, and in a statistical way.

We have seen how Bohr's theory could be coupled to the Direct Interaction theory to explain the mechanism of nuclear reactions. The following section outlines, very briefly, the application of the Monte Carlo method to cascade-evaporation calculations. As we proceed to the Optical Model in the succeeding section, it is important to mention another prediction of the compound nucleus model, as this has a strong bearing on the development of the optical model. Accordingly, the total cross section averaged over an energy interval which contains a large number of individual resonances decreases monotonically as the incident energy increases; and at a fixed energy increases with mass number. To this may also be added, as a reminder, that the differential cross section at a particular energy should be symmetrical around $\theta = \pi/2$.

I-5. MONTE CARLO CALCULATIONS

The random nature of both cascade and evaporation processes has attracted several workers to compare experimental results with the cascade and/or evaporation calculations, using Monte Carlo techniques.⁽²⁹⁻⁴¹⁾ A brief summary is given below.

Cascade Phase

Goldberger⁽³²⁾ first applied the Monte Carlo technique to the intra-nuclear cascade using the assumptions outlined for the Serber mechanism. Essentially the same procedure was followed by many later workers.^(30,31,33-37) They all assumed the nucleus as a degenerate Fermi gas of non-interacting nucleons

in a square potential well of radius $r_0 A^{1/3}$, with uniform density distribution. The radius parameter (r_0), depth of the well and cut-off energy (energy below which cascade particles were assumed to be captured) were, however different. Recently, Bertini⁽³¹⁾ attempted to approximate the Fermi-type charge distribution by dividing the nucleus into three concentric spheres of different densities. The most comprehensive calculations, however, for this phase (except for model) are due to Metropolis et al.⁽³⁰⁾ because they used a three-dimensional relativistic treatment, included meson production and its further participation in the cascade, followed many more cascades (1000) for each set of initial conditions to improve statistical accuracy and covered many targets and incident (nucleon) energies, up to about 1.8 BeV. According to this program, parameters like point-of-entry and collision partner are chosen at random. The distance of travel of a nucleon was determined from its mean free path which in turn was computed from the total collision cross sections with other nucleons and nuclear density. The collision cross sections were calculated from empirical relations which in turn had been verified from experimental data. The position of collision was examined to know whether it was in, or outside, the nucleus. If outside, the particle was supposed to have escaped. If within the nucleus, the collision partner was chosen and the collision mechanics worked out. The forbiddenness of collision was next examined on the basis of the Pauli exclusion principle. A forbidden collision was re-started from the position of the

forbidden collision while in the case of an allowed collision both the partners were followed in turn. The process is followed for the incident as well as for all the struck nucleons till they either leave the nucleus or their energy is reduced below the cut-off energy value. The program does not consider the presence of any aggregate of nucleons in the nucleus and therefore cannot predict the cascade emission of any complex unit such as deuterons or tritons, etc. The output consists of type, number, energy and angular distribution of the emitted particle, A, Z, and excitation energy of the residual nuclei.

Evaporation Phase

Calculations for the evaporation of particles from the excited nuclei remaining after the intra-nuclear cascade have been performed^(38-41,33,29) by using Weisskopf's formalism (equation 4), which gives the probability of emitting a particle 'i' (chosen at random) with kinetic energy ϵ_i . Studies in the first four references used analytic procedures for the calculation of emission probabilities, while Rudstam⁽³³⁾ and Dostrovsky et al.⁽²⁹⁾ used the Monte Carlo method. The calculation of Dostrovsky et al.⁽²⁹⁾ is most complete since usage of high speed computers allowed them to follow many cascades (500 in this case) thus improving the statistical accuracy besides considering the emission of many particles (neutron, proton, deuteron, triton, α -particle and ${}^3\text{He}$). The inverse cross section is calculated for the ground state and by empirical formulas, and the constants giving the best fit to the continuum

theory cross sections are obtained.^(42,43) The simple level-density formula is modified to take into account the pairing effect, while shell effects are not considered. Output of the program includes type, number, energy and angular distribution of the emitted particles besides A and Z of the final residual nuclei.

I-6. OPTICAL MODEL AND NUCLEAR REACTIONS

Bethe⁽²⁾ (1935) was the first to put forward a potential-well model to explain results of low energy neutron reactions. In this model, the nucleus was approximated as a potential well of constant depth which abruptly became zero at the surface of the nucleus. The model predicted elastic scattering predominantly; broad maxima with spacings of several MeV for the cross section as a function of energy; and at higher energies, the differential cross section to show strong forward peaking at almost all energies. The model, however, met an instant failure as the neutron resonances pertained to capture rather than scattering and were sharp and narrowly spaced.

As explained in the preceding sections, Bohr's compound nucleus model explained neutron resonances very well, but also predicted that the neutron cross sections, averaged over an energy interval of many resonances, increased monotonically as a function of A and monotonically decreased as a function of energy. The decisive experimental results of Barschall and coworkers^(44,45), however, showed that the average

total cross section for low-energy neutrons, as a function of energy, exhibited broadly spaced maxima⁽⁴⁶⁾ (sometimes referred to as giant resonance) as predicted by Bethe's model. The cross section as a function of A varied gradually but significantly over a range which was attributed to a slowly varying nuclear radius.⁽⁴⁶⁾ Both these results were incompatible with the predictions of Bohr's model. Further, the work of Gugelot⁽⁴⁷⁾ and others indicated that the average differential cross section is in many cases forwardly peaked, contrary to the predictions of the Bohr model.

By this time, the 'Shell Model' had also established its reputation in the interpretation of nuclear spectra and many other experimental results. The compound nucleus had also been very successful in explaining low-energy neutron resonances, and evidence, such as long life-times of resonance states, etc., had also appeared in support of the Independence hypothesis. Further, whereas the compound nucleus corresponded to a completely absorbing nucleus, the real potential well had no absorption. At this stage, Feshbach, Porter, and Weisskopf⁽⁴⁶⁾ proposed a complex potential well ($V = V_0 + iW$) model to explain the results of low-energy neutron reactions.^(44,45) While the real part (V_0) of the complex potential could account for elastic scattering (shape - see below), the imaginary part (W) would represent any process which involved energy exchanges between projectiles and the target nucleus. The latter part is also sometimes referred to as 'Absorption' and includes all

non-elastic scattering events like inelastic scattering, compound nucleus, direct interaction, etc. There is, however, a finite probability that after absorption the incident particle may re-emerge in the entrance channel and form part of the elastic scattering. This part of elastic scattering is termed 'compound elastic scattering' and together with shape elastic scattering (scattering due to real potential) represents the total elastic scattering. It may be remarked that the real potential (V_0) is very similar to the shell model potential except that a neutron with several MeV may not be expected to face exactly the same potential which acts upon the nucleus in its ground state.

Although Feshbach et al.⁽⁴⁶⁾ successfully interpreted Barschall's data, they noted the necessity of 'rounding-off' the corners of the discontinuous potential, as this gave too much scattering and not enough absorption. Many more refined potentials with surface thickness and spin-orbit coupling terms have been introduced since then. These will be discussed in the Appendix in connection with calculations of cross sections and transmission coefficients on the basis of the optical model. It may, however, be noted that, whereas the real part of the potential V_0 decreases with energy, the imaginary part increases with energy.

This model, which is more commonly referred to as the 'Optical Model' because of its analogy to the passage of light through a partly-absorbing medium, has been extremely successful

in describing elastic scattering as well as 'Absorption' (in the sense described above) at low and at high energies. It is, however, silent after that. In order to know more, Weisskopf⁽⁴⁸⁻⁵⁰⁾ has suggested a three-step description of the course of a nuclear reaction.

In the first stage, the incident particle approaches the target nucleus, feels the influence of the nucleus as a whole, which is represented by a complex potential $[V(r)]$ and gets deviated or absorbed. If deviated, distinct identities of the target nucleus as well as the incident particle are retained and the event is considered as elastic scattering. Absorption of the particle, on the other hand, leads to the second stage of the nuclear reaction. This is called an 'independent particle stage' and can be represented by the optical model as the incident beam is scattered or absorbed by the complex potential well.

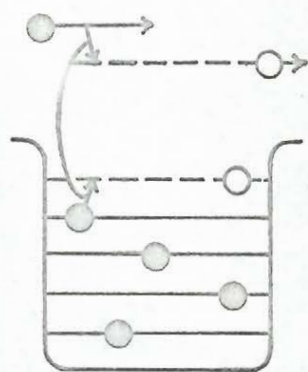
The second stage is called a 'Compound System' by Weisskopf⁽⁴⁸⁾ and represents all systems after the particle has been removed from the entrance channel. Fig. 1⁽⁴⁷⁾ illustrates graphically what happens when a particle enters the nucleus and collides with its constituents.

The nucleus is replaced by a potential well and the nucleons move independently, except that Pauli's principle prohibits the occupancy of the same quantum state by two identical particles. The description of the various graphs is as follows.

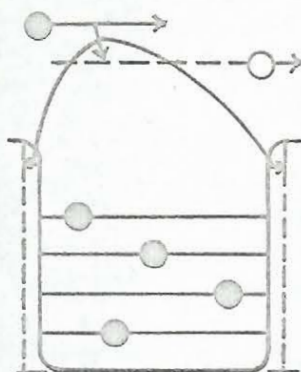
Figure 1

GRAPHIC REPRESENTATION OF WHAT HAPPENS
WHEN A PARTICLE ENTERS A NUCLEUS

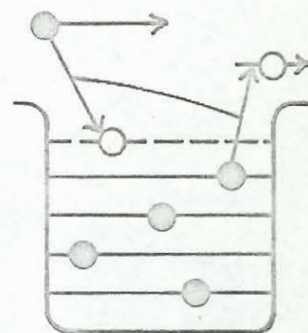
(Reproduced from 'Physics Today'
Vol. 14, No. 7, July 1961)



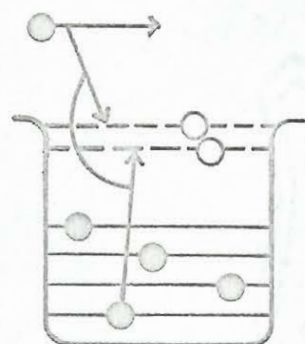
a. DIRECT
INELASTIC
SCATTERING



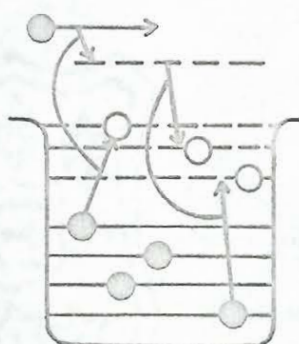
b. DIRECT
INELASTIC
SCATTERING
(COLLECTIVE)



c. DIRECT
REACTION



d. COMPOUND
NUCLEUS
FORMATION
(1 STEP)



e. COMPOUND
NUCLEUS
FORMATION
(2 STEPS)

(1) The incident particle loses part of its energy by lifting a nucleon to an excited state. It has been called 'direct inelastic scattering' because it involves only one collision.

(2) The incident particle could set up excitations of collective modes of a nucleus, e.g. surface vibration or rotation, etc.

(3) The third graph represents an 'exchange collision'. The incident particle transfers enough energy to the struck nucleon so that it could leave the nucleus while being trapped itself.

(4) According to this graph, the incident particle lifts a low-lying nucleon and loses so much of its energy that neither of them are able to escape the nucleus. Further collision with other nucleons would then distribute the kinetic energy of the incident particle to many nucleons and a state of long life-time is formed. The decay of this state should then be possible only after a number of collisions when, accidentally, enough energy gets concentrated on a particle. Such a decay should be governed by well-known statistical probability rules as described in conjunction with the strong interaction model.

(5) If, after a process as represented in (1) or (2), the incident nucleon makes another collision (before getting out of the nucleus completely), it may result in either nucleon not having enough energy to escape, then again compound nucleus formation would be possible.

If we separate the emitting part of a nuclear reaction from what happens within the nucleus in the stage described above, it is easy to notice that this (third) stage is in many ways similar to the independent particle stage in the time-reversed direction. The interaction between the residual nucleus and the emitted particle can again be represented by a complex potential.

Fig. 2 describes these stages in a schematic way.

It is thus seen that the weak interaction model indicates that the direct interaction process is a feature of nuclear reactions at all energies. At the same time, it also shows that in many cases the entire or part of the energy of the incident particle is transferred to all the constituents of the target nucleus, forming a state of long life time, even longer than expected from strong interaction model.⁽⁴⁹⁾ As is evident, the properties of the various events very much depend on the collision site in the nucleus. This is particularly so for charged particles because the potential barriers are much lower in the surface region.

I-7. ISOMER RATIOS

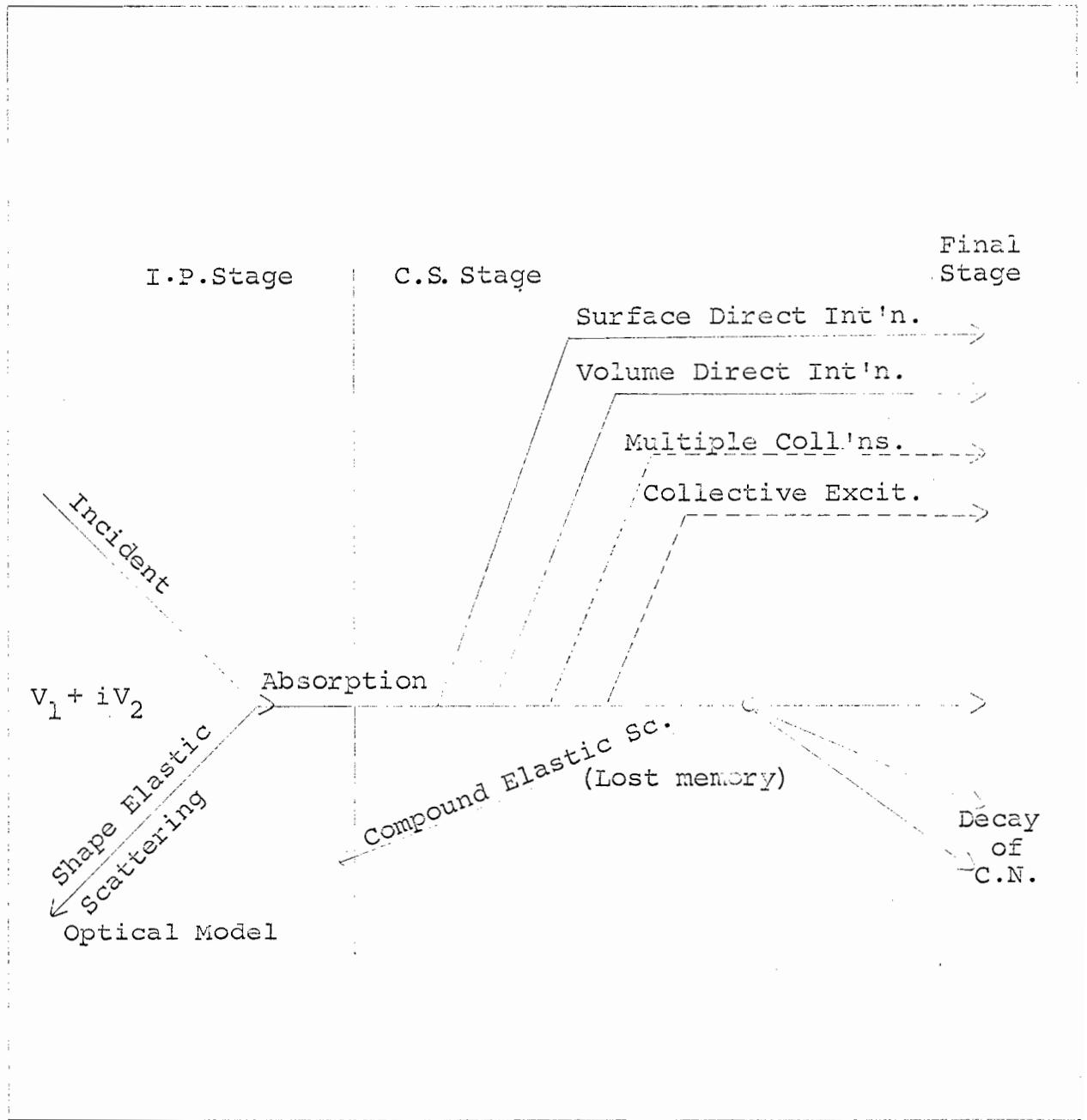
I-7.1. Nuclear Isomers

After the completion of the particle emission stage in a nuclear reaction, residual nuclei are left behind in a large number of excited states. The excited nucleus gives up its excitation by successive transitions, from a higher state to a lower, until the ground state is reached. Generally, these

Figure 2

SCHEMATIC REPRESENTATION OF DIFFERENT
STAGES IN A NUCLEAR REACTION

(Reproduced from 'Physica'
Vol. 22, 952, 1956)



gamma transitions take place in less than 3×10^{-11} seconds.⁽⁵¹⁾ This limit is imposed by the present state of electronic detection equipment, although indirect measurements indicate that mean life-times of such transitions range from 10^{-13} - 10^{-16} seconds. Occasionally, however, some nuclides having an excited state (close to the ground state) with a measurable half-life are also observed. Such an excited state, which decays with this characteristic 'delayed' transition, is termed an isomeric state (or level), the transition itself being an isomeric transition. It may be noted that, as the half-life of the metastable state is long, this state could decay by any other radioactive decay mode as well, such as β -transition, electron capture, etc. More than 250 isomers with half-lives ranging from 10^{-11} seconds* to many years have been observed. Existence of more than two isomeric states in the same nucleus has also been observed in a few cases.

An explanation of isomerism was first proposed by von Weizsäcker⁽⁵²⁾ in 1936. He suggested that a metastable state could be the first excited state above the ground state with an angular momentum quite different from that of the ground state. By assigning a spin difference ($\Delta I = \ell$) of few units (~ 5) and energy difference (ΔE) of a few keV, he showed that

*The lower limit of life-times, particularly if the results of indirect measurements are also included, eliminates the distinction between a normal and an isomeric level. The definition of an isomeric state in terms of 'measurable half-life' is in this context somewhat vague.

calculated half-lives of metastable states could be compared with those observed. Expressions for gamma transition probabilities, using the independent particle model, were derived by Blatt and Weisskopf.⁽⁵³⁾ In the shell model, this condition is usually met by odd A nuclides, where the number of neutrons or protons, whichever is odd, lies close to a 'magic' number.

I-7.2. Angular Momentum and Isomer Ratios

Normally, both the ground and metastable state of a nucleus should be expected to be formed in a nuclear reaction. If one denotes the cross section for the formation of a high spin isomer by σ_H and that of a low spin by σ_L , the ratio of formation cross section σ_H/σ_L , usually called an isomer ratio, represents the relative probability of formation of these two states of the same nuclide. Formation cross sections are also referred to in terms of metastable (σ_m) and ground state (σ_g).

Angular momentum like energy, parity, etc., must be conserved in a nuclear reaction. It has been a conclusion of discussions in the preceding sections that the compound nucleus in conjunction with the statistical model is a fairly good approximation for protons of energy of at least up to about 30 MeV. Accordingly, the total angular momentum of an intermediate compound nucleus system is given by the vectorial addition of target spin, intrinsic spin of the projectile and the orbital angular momentum carried in by the projectile. The presence of the centrifugal barrier, however, restricts the

amount of angular momentum of the particle entering (or leaving) the target. The compound nuclei are therefore formed in a variety of spin states. The decay mode of an excited compound nucleus will be determined by the amount of excitation energy. If the excitation energy is greater than the separation energy of the last neutron (or proton), it is quite reasonable to assume that a neutron will be emitted. (Gamma competition is discussed in Section I-3.)

Emission of a neutron will result in the new spin distribution for the levels of the residual nucleus. If the excitation energy is not sufficient for the evaporation of a neutron, a cascade of photons will be emitted. The amount of angular momentum carried away by each photon is determined by the multipolarity of the gamma transition. Thus each transition will again result in a new spin distribution. The last gamma ray is assumed to populate either low or high spin states of the isomers, the well-known preference being for one requiring the smallest change in the spin.

A point which leads to an important conclusion was deliberately omitted from the previous paragraph. When an excited nucleus decays either by particle or photon emission, the probability of decay from an excited state of a certain angular momentum J_c to an excited state of angular momentum J_f is proportional to the density of levels of angular momentum J_f . This level density is given by the expression⁽⁵⁴⁻⁵⁶⁾

$$\rho(J_f, E_f) = \rho(0, E_f) (2J_f + 1) e^{-J_f(J_f + 1)/2 S^2} \quad (10)$$

where $\rho(0, E_f)$ = density of levels of zero angular momentum, and

E_f = excitation energy for the residual nucleus.

The quantity S is called the spin density parameter or spin cut-off parameter.* As this parameter characterizes the spin distribution, it is important to determine its value and variation with energy. One achieves this task from isomer ratio measurements by fitting the calculated values of isomer ratios (based on the afore-mentioned principles) to those determined experimentally.

Parameter S is also related to the nuclear moment of inertia 'I' by the relation^(54,55)

$$S^2 = It/\hbar^2 \quad (11)$$

where 't' is termed as thermodynamic temperature (Lang and LeCouteur, 1954⁽⁵⁶⁾). According to the Fermi gas model

$$I = I_r = \frac{2}{5} M_n R^2 A \quad (12)$$

where I_r = 'rigid' body moment of inertia,

M_n = mass of a nucleon,

R = nuclear radius, and

A = mass number.

*Symbol ' σ ' is commonly used for spin cut-off parameter.

However, as the same symbol also represents cross section, adoption of a different symbol was preferred in order to avoid confusion.

A number of workers have determined the values of effective nuclear moment of inertia through spin cut-off parameter and equation (11). Invariably, the values of moment of inertia thus determined correspond only to a fraction of the rigid body moment of inertia. ($\sim 0.3 - 0.8$)⁽⁵⁷⁻⁶²⁾ This reduction of moment of inertia has usually been attributed to a pairing interaction. According to this, particles (protons and neutrons) in the nucleus tend to couple to form states of zero angular momentum; and these pairs must be broken before they can re-couple to form states of higher angular momentum.

The simple Fermi gas model should thus be modified to take pairing interaction into account. Hurwitz and Bethe⁽⁶⁵⁾ suggested that excitation energy should be measured from a fictitious ground state corresponding to a surface with no pairing or shell effects. Such a surface has usually been taken as the odd-odd mass surface. Corrections for pairing are then applied by subtracting pairing energies for even-even and odd mass nuclides.

Two new approaches to the problem of pairing interaction have recently been proposed by Lang and Lecouteur⁽⁶⁶⁾ and Lang.⁽⁶⁷⁾ According to the first, which is referred to as the independent pairing model, Lang and Lecouteur derive expressions for 'level density', spin cut-off parameter, effective excitation energy, etc., by assuming the nucleus as a 'Fermi gas with pairs of degenerate single particle states'. It is termed an independent pairing model because pairing interactions

for a particular pair are assumed to be independent of all other pairs. Although the equations are derived for deformed nuclei with an axis of symmetry, Lang and Lecouteur suggest that the treatment is roughly valid for spherical nuclei. One of the attractive features of the model is that the resulting formulae are exactly the same when the pairing energy ' 2Δ ' is made zero.

The second model (Lang⁽⁶⁷⁾ 1963) utilizes the Bardeen, Cooper, and Schrieffer⁽⁶⁸⁾ (BCS) theory of the superconducting state of a metal in the case of the nucleus. The interactions between electrons of equal and opposite momentum in a metal are replaced by nucleons, similar except for the projection of their angular momenta on the symmetry axis. Expressions for condensation energy, critical energy and temperature, spin cut-off parameter, etc., are derived by Lang for energies similar to those employed in this work. Vonach, Vandenbosch, and Huizenga⁽⁶⁹⁾ applied it to the calculation of isomer ratio with slight modifications. In this thesis, the approach is that given by these authors. More details of these models, as those required for the calculation, are given in Chapter V.

We have seen that an isomer ratio represents a net result of changes in angular momentum at various stages of the path of a nuclear reaction. With the increase in energy of the projectile (say protons) the average angular momentum of the compound nucleus also increases. The emitted particles are usually of low energy and thus carry only a small amount of angular momentum. Dipole emission also constitutes a major

portion of gamma transitions (Section V-3.3). The angular momentum removed at various steps of the de-excitation process should therefore be relatively small. As the increase in average angular momentum should favour population of higher spin states, increase in the isomer ratio as a function of energy of the projectile should also be expected. The increase in angular momentum (and consequently isomer ratio) should be particularly steep if the projectile is a heavy ion, as these could bring a large amount of angular momentum into the system. A number of investigators⁽⁵⁷⁻⁶⁴⁾ have proved these arguments. If the proton energy is increased beyond 40 MeV, the proportion of events proceeding via the cascade-evaporation mechanism increases significantly. This leads to only partial transfer of angular momentum to the target-projectile system. Isomer ratios should therefore be expected either to level off or decrease with energy.

Experimental data for isomer ratios for various nuclear reactions have recently been compiled by Wing.⁽⁷⁰⁾ Numerous other publications have appeared since then, but only those of interest have been listed.⁽⁵⁷⁻⁶⁴⁾ Vandenbosch et al.⁽⁶²⁾ have measured isomer ratios for $^{87m,g}\text{Y}$ produced in various nuclear reactions. In two reactions, viz. $^{85}\text{Rb}(\alpha, 2n)$ and $^{87}\text{Sr}(d, 2n)$ they produced ^{89}Y as the compound nucleus. This compound nucleus is also produced in the nuclear reactions studied in this work. As the excitation energy region and measurement procedures are also the same, it should be of interest to compare the isomer ratios and the parameters required to fit calculated

values to the experimental ones for $^{87m,g}\text{Y}$ as produced by the $^{88}\text{Sr}(p,2n)$ reaction. Isomer ratios have also been measured for $^{88}\text{Sr}(p,3n)^{86m,g}\text{Y}$, $^{88}\text{Sr}(p,4n)^{85m,g}\text{Y}$ and $^{88}\text{Sr}(p,p3n)^{85m,g}\text{Sr}$ nuclear reactions.

I-8. PRESENT WORK

The present work is a radiochemical study of nuclear reactions induced in ^{88}Sr by protons in the energy range 7 - 85 MeV. Various reasons for choosing such a system are:

1. Commercially* available enriched ^{88}Sr ($> 99.8\%$) is essentially mono-isotopic.
2. $^{88}\text{Sr}(p,xn)$ reactions yield a number of neutron-deficient isotopes with reasonable half-lives. It is therefore of interest to measure and compare the excitation functions of these reactions over an energy range where the Compound Nucleus mechanism slowly gives way to the Direct Interaction mechanism.
3. Nuclear reactions of the type $(p,2pxn)$ are complicated because the products of these reactions could also be formed by $[p,\alpha(x-2)n]$ reactions. As the thresholds for the latter reactions are very much lower than for the former, excitation function curves with two peaks are expected. It should therefore be of interest to observe such excitation functions; and the long half-lives of ^{84}Rb and ^{83}Rb ($x = 3$ and 4 respectively) permit this to be conveniently realized. It is also of interest to compare excitation functions for the $(p,2pn)$ reaction with these afore-mentioned excitation functions.

* Obtained from Isotope Division, Oak Ridge National Laboratory.

4. Three pairs of isomers with $x = 2, 3$ and 4 are formed in (p, xn) reactions. Another pair is produced by the $(p, p3n)$ reaction. Current studies of isomer ratios in nuclear reactions are directed to the understanding of spin dependence in level density. Available calculation procedures demand that the nuclear reaction of interest should proceed by the compound nucleus mechanism. Isomer ratios for the $(p, 2n)$ reaction should therefore be useful for such a task for proton energies up to about 30 MeV. Isomer ratios for other nuclear reactions should also be of qualitative interest as they should reflect the effect of increasing percentage of direct interaction over compound nuclear reactions vis-a-vis the expected increase of isomer ratio due to increase in projectile energy.

II. EXPERIMENTAL PROCEDURES

II-1. TARGET MATERIAL AND IRRADIATION PROCEDURE

The target material was a mixture of 'spec-pure' copper oxide* (CuO) and strontium nitrate⁺ [Sr(NO₃)₂], enriched in ⁸⁸Sr (> 99.8%). The isotopic analysis of two strontium samples used in the present work, as provided by the supplier, are shown in Table I.

Table I
ISOTOPIC ANALYSIS OF ENRICHED STRONTIUM SAMPLES

Isotope	Sample No. 69(a)		Sample No. 1370(a)	
	Atomic %	Precision	Atomic %	Precision
84	< 0.01	-	< 0.01	-
86	0.05	±0.01	0.05	-
87	0.13	0.05	0.11	±0.02
88	99.82	0.05	99.84	0.02

The isotopic analysis of both samples are nearly the same and were considered mono-isotopic in mass '88' in this work. Spectrographic analysis of impurities was also made available. The impurities were very insignificant in amount and it was estimated that none would interfere in this work. The copper

* Obtained from Johnson, Matthey and Company.

⁺ Obtained from Isotope Division, Oak Ridge National Laboratory, Oak Ridge, Tennessee, U.S.A.

in the mixture served to monitor the beam with the aid of $^{63}\text{Cu}(p,n)^{63}\text{Zn}$ (up to 15 MeV) or $^{65}\text{Cu}(p,pn)^{64}\text{Cu}$ nuclear reactions.

The mixture was prepared by intimately mixing the accurately weighed amounts of these two compounds in a pestle and mortar, in an approximate atomic ratio of Sr:Cu :: 1:1. Small amounts of the resulting mixture were analysed for copper by EDTA titrations and the results indicated homogeneous mixing. The densities of CuO and $\text{Sr}(\text{NO}_3)_2$ are 6.4 and 2.986 gm per cm^3 respectively, and care was taken in loading the mixture into aluminum tubes (see below) so that no desegregation occurred.

Aluminum tubing with an outside diameter of 0.0625" and wall thickness of 0.0015", supplied by Precision Tube Company, Philadelphia, Pa., served as a container for the target. The mixture (10-20 mg) was loaded into tared tubes (pinched shut at one end) and the weight of the sample was determined by weighing in a micro-balance. After the mixture was loaded, the other end of the tube was also closed and both ends bent diagonally. The aluminum tube was then rolled flat with the help of a glass rod in order to make a thin and uniform target. The energy degradation of the beam was checked by use of the range-energy relations of Sternheimer.⁽⁷¹⁾ For a target of superficial density of about 70 mg per cm^2 (as in the present work), the energy of the beam was degraded by about 1.5 MeV for protons of 7 MeV energy, about 1 MeV at 12 MeV (mean correction) and correspondingly less at higher energies. This was within the energy spread (± 2 MeV) of the proton beam as reported in

this work.

The targets, prepared in this way, were fastened to an aluminum target holder (Fig. 3) which was in turn screwed to the cyclotron probe. The targets were then inserted in the cyclotron 'dee' at a fixed distance corresponding to the desired bombardment energy. A recent calibration curve (Jan. 15, 1964) of radial distance versus energy of the proton beam, as provided by the Radiation Laboratory, was used for the purpose. The durations of bombardments varied with the half-life of the desired activity as well as the intensity of the proton beam, and ranged from 10 - 70 minutes.

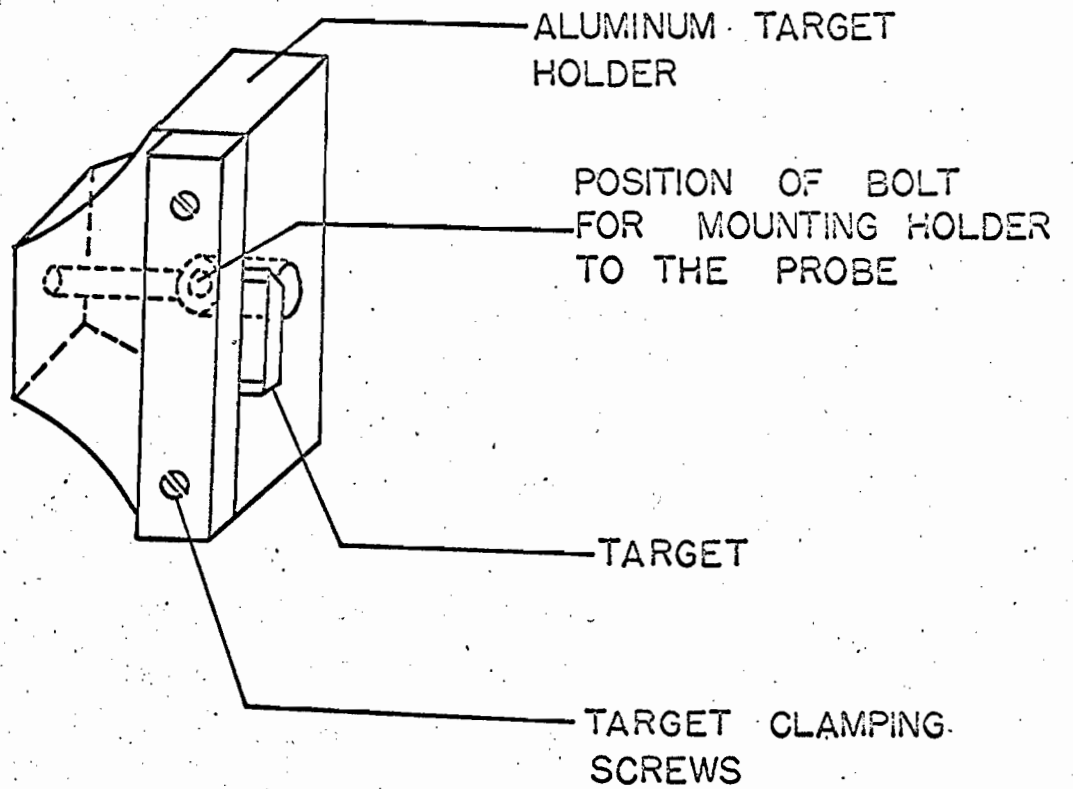
II-2. CHEMICAL PROCEDURES

If the target is exposed to 85 MeV protons, one should expect the isotopes of the following elements to be present: yttrium, strontium, rubidium, krypton, bromine and probably selenium as spallation products of strontium; zinc, copper, nickel, cobalt, iron and probably manganese from copper; silicon and almost all the elements below silicon in atomic number due to aluminum, oxygen and nitrogen. Separation procedures for the elements of interest, i.e. yttrium, strontium, rubidium, copper and zinc (for bombardments up to 15 MeV) described in the following pages, were designed after taking into account the presence of these elements and also their half-lives.

Ion-exchange steps, where used, were based on the work of Kraus and Nelson.⁽⁷²⁾ Solvent extraction, used for yttrium,

Figure 3

ASSEMBLY OF TARGET AND TARGET HOLDER



was an extension to a macro-scale level of Dyrssen and Ekberg's⁽⁷³⁾ work for carrier-free separation of yttrium from strontium. Precipitation steps of rubidium tetraphenylborate and rubidium chlorostannate (Rb_2SnCl_6) were taken from Handley and Burros⁽⁷⁴⁾ and Goeking et al.⁽⁷⁵⁾ respectively.

In all cases, carriers (and consequently activities) were recovered in the form of solutions (water or dilute acids), so that 2 ml of these could be taken in a screw-cap glass vial (15.5 mm O.D. x 50 mm) for gamma-ray and positron activity measurements. The same were also useful for making sources for negatron measurements using a $4\pi\text{-}\beta$ proportional assembly. (Section II-4, Radiation Detection and Measurement Procedures.)

II-2.1. Dissolution of Target and Separation into Elemental Fractions

After irradiation, the target was detached from the target holder and transferred to a 40 ml centrifuge tube containing known amounts of standard carriers in the form of chlorides of elements of interest [yttrium \sim 10 mg, strontium \sim 10 mg (in addition to the known weight in the target, as this was only 3 - 5 mg), rubidium \sim 20 mg, zinc \sim 10 mg]. The target was dissolved by adding a small amount of HCl and a drop of hydrogen peroxide. The solution was evaporated to dryness and the residue taken up in a small amount of 9N HCl (less than 1 ml). The solution was next transferred to the anion-exchange*

* Baker analysed reagent, Dowex-1 x-8, Mesh 100-200, Ionic form --- $\bar{\text{Cl}}$, was the only anion-exchange resin used throughout this work, and in all cases, an anion-exchange column, pre-equilibrated with the same solution in which the ions to be separated were taken up, was used.

column which had been pre-equilibrated with 9N HCl. The dimensions of the column were about 16 cm long and 8 mm I.D. for irradiations with protons of energies less than 27 MeV. At higher energies the size of the column was, however, reduced to 8 cm in length with the same I.D., as short half-lives were involved. The centrifuge tube was rinsed twice with 0.5 ml portions of 9N HCl and the washings added to the column. Thereafter, the elution of the column was continued with 9N HCl and the eluates collected (after rejecting an amount corresponding to the free volume of the column) in about 7 ml. The eluate at this stage contained yttrium, aluminum, strontium, rubidium, sodium, nickel and beryllium as elements of importance while copper and zinc, besides a host of other unwanted impurities, remained adsorbed on the column. The column was kept for a later recovery of copper and separation of other activities proceeded. If, however, ^{63}Zn was to be used as a monitor, zinc was eluted at this stage. Further details regarding the separation of copper and zinc are given below.

The eluate containing yttrium, etc., was evaporated to near-dryness to expel excess acid. The residue was dissolved in about 10 ml of 'boiled out' demineralized water and yttrium hydroxide precipitated by adding an excess of CO_2 -free sodium hydroxide. The time of separation of strontium and rubidium activities from yttrium was noted at this stage. After being centrifuged, the supernate was decanted into another centrifuge tube and the precipitate of yttrium hydroxide left for

purification at a later stage. The supernate was quickly scavenged twice with ferric hydroxide to reduce contamination due to yttrium. Strontium carbonate was precipitated from the supernate by adding a few drops of saturated sodium carbonate solution, stirring, warming and cooling. The time of separation of rubidium from strontium was also noted at this stage. After centrifugation, strontium carbonate was left for later treatment while the supernate was scavenged by a combined precipitation of yttrium and strontium carbonates. The supernate was next neutralized with dilute HCl to a phenolphthalein end-point and the precipitate of aluminum hydroxide removed again by centrifugation. The supernate of the last stage was preserved for a later recovery of rubidium (after about two weeks) as only relatively long-lived isotopes of rubidium were concerned.

II-2.2. Purification of Individual Elemental Fractions

Yttrium: The precipitate of yttrium hydroxide was washed with demineralized water containing enough sodium hydroxide to prevent precipitation of aluminum; dissolved in a small amount of dilute HNO_3 and evaporated to dryness. The residue was transferred to a separatory funnel with 20 ml of 0.1N HNO_3 and shaken with 20 ml of alcohol-free chloroform containing 1 ml of dibutyl phosphate* for three minutes. The organic phase was transferred to a second separatory funnel and

* Eastman Organic Chemicals. Technical: 55% dibutyl phosphate
and 45% monobutyl phosphate.

washed with another 20 ml of 0.1N HNO₃ by shaking for one minute. The organic phase was again transferred to a third separatory funnel, 1 ml of methyl isobutyl carbinol (4-methyl-2-pentanol) added and yttrium back-extracted into the aqueous phase by shaking with 20 ml of 1N HNO₃ for three minutes. The aqueous phase was again shaken for one minute with another 20 ml of alcohol-free chloroform containing 1 ml of methyl isobutyl carbinol to minimize any trace of organic phosphates in the aqueous phase. The aqueous phase was then boiled to expel volatile organic material.

The metastable states of ⁸⁷Y and ⁸⁶Y nuclides have γ -rays very similar in energy to those of ^{87m}Sr and ^{85m}Sr respectively. The growth of the strontium activities from the parent yttrium activities therefore interfered in the measurements of afore-mentioned yttrium nuclides. This difficulty was avoided by separating the daughter strontium activities from the yttrium sample, by a 'milking' experiment, and performing γ -ray measurements (on the yttrium fraction) as quickly as possible. The milking experiment was performed as follows:-

After the solution of yttrium was boiled to expel the organic matter about 5 mg of strontium hold-back carrier was added and yttrium hydroxide precipitated with 1:1 ammonia. The solution was centrifuged, decanted and washed with 10 ml of demineralized water. Yttrium hydroxide was dissolved in a small amount of dilute HNO₃, the solution diluted and 2 ml of this solution was taken for activity measurements. The entire

procedure till activity measurements required 6 - 9 minutes. This procedure was repeated, at least four times at appropriate intervals, to get points for decay curve analysis of the nuclide of interest at each bombarding energy. Chemical yields were determined for all individual samples.

Strontium: Strontium carbonate, obtained during the general separation, was washed with 2 ml of water (containing a drop of sodium carbonate) and the supernate discarded after centrifugation. The precipitate was dissolved in a few drops of dilute HNO_3 , a few mg each of rubidium and yttrium hold-back carriers added and strontium nitrate precipitated by adding about 12 ml of cold fuming nitric acid. The mixture was allowed to stand for about 5 minutes in an ice bath, where-after it was centrifuged, decanted and the precipitate washed with 2 ml of cold fuming nitric acid. Strontium nitrate was dissolved in about 10 ml of demineralized water and the solution scavenged three times by precipitating a few mg of iron as ferric hydroxide. Strontium oxalate was next precipitated by adding a few drops of saturated oxalic acid and dilute ammonia. The precipitate was again dissolved in a few drops of dilute HNO_3 and strontium nitrate precipitated as before. Strontium nitrate was washed twice with 2 ml of cold fuming nitric acid in the last step.

Strontium nitrate was then dissolved in water, made up to volume and an aliquot transferred to the vial for activity measurements.

Rubidium: The supernate of rubidium, as obtained during the general separation procedure, was reduced to a small volume by evaporation and then to complete dryness after adding a small amount of concentrated HNO_3 to decompose any ammonium salts (produced by atmospheric ammonia - if any).

The residue was taken up in 10 ml of 1M HCl solution and cooled in an ice bath. Four ml of the refrigerated sodium tetraphenylborate reagent* were added, dropwise and with constant stirring. The mixture was allowed to stand in an ice bath for ten minutes with occasional stirring. The mixture was centrifuged, the supernate discarded, and the precipitate washed with 5 ml of cold water.

The precipitate of rubidium tetraphenylborate was dissolved in acetone (1-2 ml) and a similar amount of acetone added. About 10 ml of 50% (vol/vol) solution of concentrated HCl in ethanol was added to this solution and rubidium chlorostannate precipitated by adding 4 ml of saturated stannic chloride (SnCl_4) in 50% concentrated HCl in ethanol solution. The solution was well stirred to ensure the completion of

*The reagent was prepared and stored as described by Handley and Burros.⁽⁷⁴⁾ Four gm of the reagent and 1 gm of aluminum chloride hexahydrate were dissolved in 100 ml of demineralized water. The solution was made just alkaline with phenolphthalein indicator and dilute sodium hydroxide ($\sim 6\text{N}$), allowed to stand overnight and filtered. The filtrate was diluted to 200 ml and stored in a refrigerator. No decomposition was noted for a couple of months when the solution was used.

precipitate. The mixture was centrifuged, the supernate discarded and the precipitate washed twice with 3 ml (each) of 50% HCl-ethanol mixture.

The precipitate of rubidium chlorostannate was dissolved in warm 3N HCl solution and passed through a pre-equilibrated anion-exchange column (about 12 cm in length and 8 mm I.D.). Rubidium passed through the column and was collected in the eluate with 3N HCl, while tin remained adsorbed on the column.

The rubidium chloride solution was evaporated to dryness to expel the acid. The residue was dissolved in about 2.5 - 3 ml of demineralized water and sucked into a long capillary-mouthed polythene bottle (total capacity about 10 ml). Duplicate sources for 4π - β measurements were prepared from this solution by using a semi-micro balance. Two ml of the solution (also weighed) were taken for γ -ray measurements in a screw-cap vial. After the γ -ray measurements were completed, the contents of the vial were used for chemical yield determinations.

Zinc: As mentioned previously, zinc carrier was added for the low-energy bombardments (up to 15 MeV) when the $^{63}\text{Cu}(p,n)^{63}\text{Zn}$ reaction served to monitor the proton beam. The ion-exchange column, from the general separation scheme, was washed with 0.15N HCl. Most of the elements including copper are removed while zinc is still strongly adsorbed on the column. Zinc was then eluted with $< 0.01\text{N}$ HCl, made up to volume and 2 ml of the solution were taken in a vial for activity measurements.

Copper: Copper, adsorbed on the ion-exchange column, was washed with 4.5N HCl to elute cobalt till the copper band was slightly above the bottom of the column. For a long column (used for irradiations below 27 MeV) this required more than 20 ml of 4.5N HCl. The eluate was then changed to 1.5N HCl and the copper band collected in the smallest amount of eluate. The copper eluate was dried under an infra-red lamp and the residue dissolved in slightly more than 2 ml of water, of which 2 ml was pipetted into the counting vial.

If, however, a small ion-exchange column was used (for irradiations above 27 MeV), the dry residue (as obtained in the last stage) was taken up in 1 ml of 4.5 N HCl and transferred to a pre-equilibrated anion-exchange column. The centrifuge tube was rinsed twice with 0.5 ml of 4.5N HCl and the washings transferred to the column. Washings were continued with 4.5N HCl and the procedure repeated as in the previous paragraph.

It may be remarked that the activity of the copper samples was measured about 36 hours after the end of irradiation to allow for the decay of 3.3 hr ^{61}Cu formed by the $^{63}\text{Cu}(p,p2n)^{61}\text{Cu}$ or $^{65}\text{Cu}(p,p4n)^{61}\text{Cu}$ reactions.

II-3. CHEMICAL YIELDS

The chemical yields were determined by known standard analytical procedures and the following were adopted.

Yttrium: The chemical yield was determined by measuring the absorbance of a complex formed by yttrium and sodium alizarine sulphonate in an acetate-buffered solution as described by Sandell.⁽⁷⁶⁾ A Beckman spectrophotometer (Model DU)

and standard 1 cm cells were used. A standard absorbance curve is shown in Fig. 4.

Strontium: The chemical yield for this element was determined by direct titration with ethylene-diamine tetra-acetic acid (disodium salt) using phthalein-complexone as an indicator, as described by Welcher.⁽⁷⁷⁾

Rubidium: The well-known precipitation procedure using chloroplatinic acid reagent (10%) as given by Vogel⁽⁷⁸⁾ (for potassium) was used for the determination of the chemical yield of this element.

Copper: Direct titration with EDTA using murexide as an indicator, as given by Welcher⁽⁷⁹⁾, was adopted.

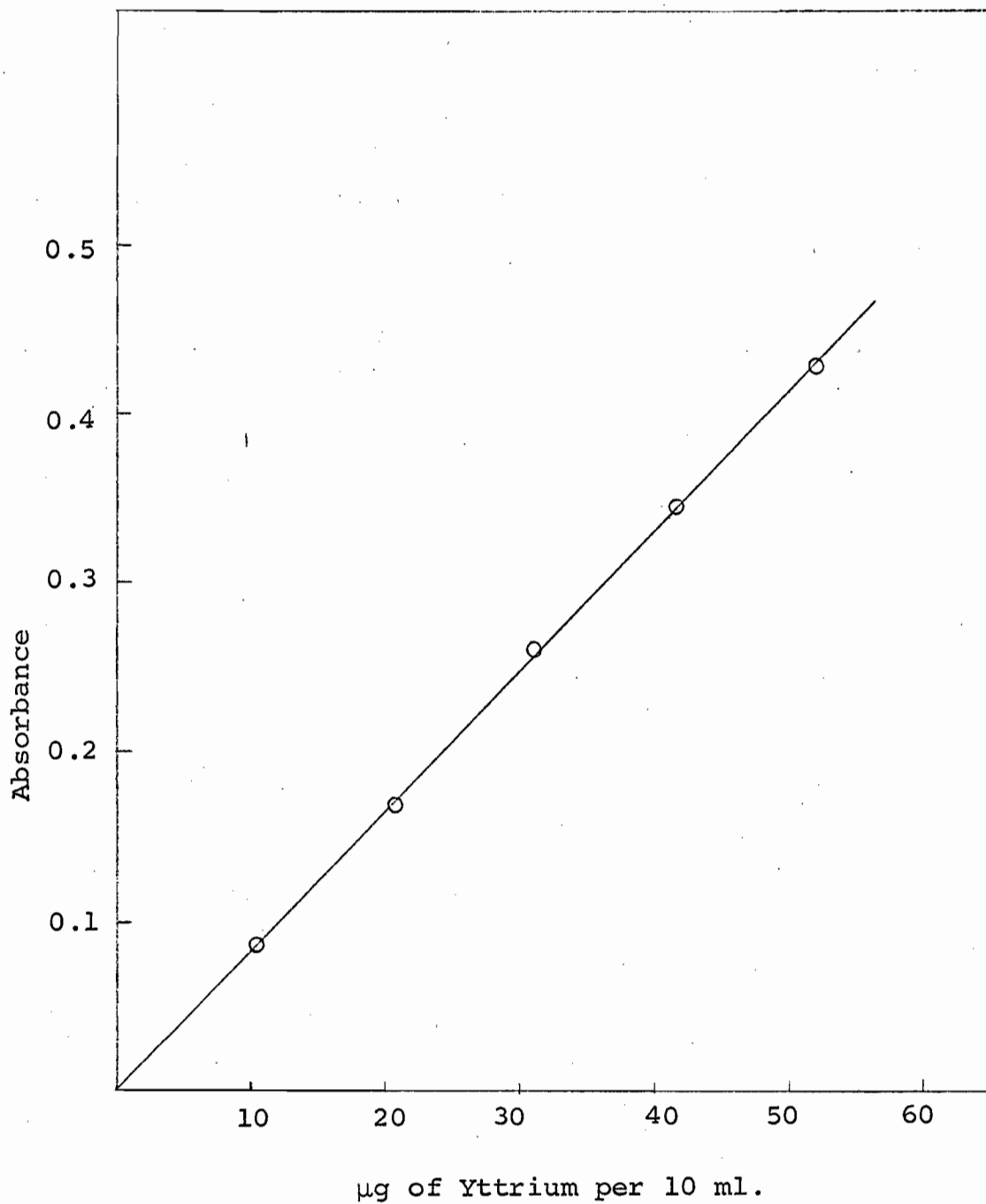
Zinc: Direct titration with EDTA using eriochrome Black T as an indicator, as described by Welcher⁽⁸⁰⁾, was used for this element.

II-4. RADIATION DETECTION AND MEASUREMENT PROCEDURES

The neutron-deficient nuclides concerned in this work decayed by positron emission and/or electron capture processes. For those nuclides decaying predominantly by electron capture process, it was convenient to follow the gamma rays of the excited states of the daughter products using scintillation detectors in conjunction with pulse height analysers. Some other nuclides had a reasonable percentage of positron branching ratio ($> 30\%$) and a coincident technique for the annihilation gamma rays of 0.511 MeV was preferred for them. A single

Figure 4

STANDARD ABSORBANCE CURVE FOR YTTRIUM-SODIUM
ALIZARINE SULPHONATE COMPLEX



nuclide, ^{86}Rb , produced as a result of the $^{88}\text{Sr}(p,2pn)$ reaction, decayed by negatron emission and was assayed with a $4\pi\text{-}\beta$ proportional counter.

II-4.1. $4\pi\text{-}\beta$ Counting

Pate and Yaffe⁽⁸¹⁻⁸⁵⁾ have systematically studied the various aspects of this technique for measuring β -activities. The method comes closest to the ideal of recording one event for each disintegration. The particle detection efficiencies for both Geiger as well as proportional counters are close to 100% and the problems connected with scattering do not exist in this set-up. The decay schemes are unimportant so long as events following particle emission (like gamma emission, internal conversion, etc.) take place within the resolving time of the counter. A knowledge of the decay scheme is, however, required for measuring internal conversion electrons due to isomeric transitions and for making corrections for self-absorption and source-mount absorption (see below) corresponding to the energy and branching ratios of various β -components. The following corrections are necessary.

- (i) Correction due to background.
- (ii) Correction due to resolution losses.
- (iii) Correction due to absorption in the source-mount.
- (iv) Correction due to absorption in the source-material itself.

Procedure: A flow-type proportional counter, using methane gas (C.P.) at atmospheric pressure, was used in this work. This

assembly was similar to that described by Pate and Yaffe.⁽⁸²⁾ The counter chamber and a block diagram of the entire counting assembly are shown in Figs. 5 and 6 respectively. The figures are self-explanatory and any further details may be obtained from the cited reference. The proportional counter has the advantage of having short resolving times ($\sim 1-2 \mu\text{sec}$), permitting high counting rates without resorting to corrections due to resolution losses.

Radioactive sources were mounted on VYNS (a copolymer of polyvinyl chloride and polyvinyl acetate) films, made according to the prescription of Pate and Yaffe.⁽⁸¹⁾ These films had a superficial density of about $10 - 15 \mu\text{gm per cm}^2$ and were rendered conducting by depositing a thin layer of gold ($5 - 10 \mu\text{gm per cm}^2$) in vacuum. Just before use, the central portion (about 1 cm in diameter) of the film was treated with a few drops of 0.1% insulin solution to make it hydrophilic. Most of the insulin was removed and the treated part was washed several times with distilled water. An aliquot of the solution of rubidium activities was then added to the film, and was dried slowly under the infra-red lamp. During the evaporation process the film was rotated by hand occasionally to keep the entire area wet till it was completely dry.

The source, thus prepared, was inserted in a groove, between the two halves of the counting chamber. The counter gas flushed the counter for several minutes before the count began and was adjusted to a slow flow. A suitable polarization

Figure 5

A SCHEMATIC DIAGRAM OF THE 4π -COUNTING CHAMBER

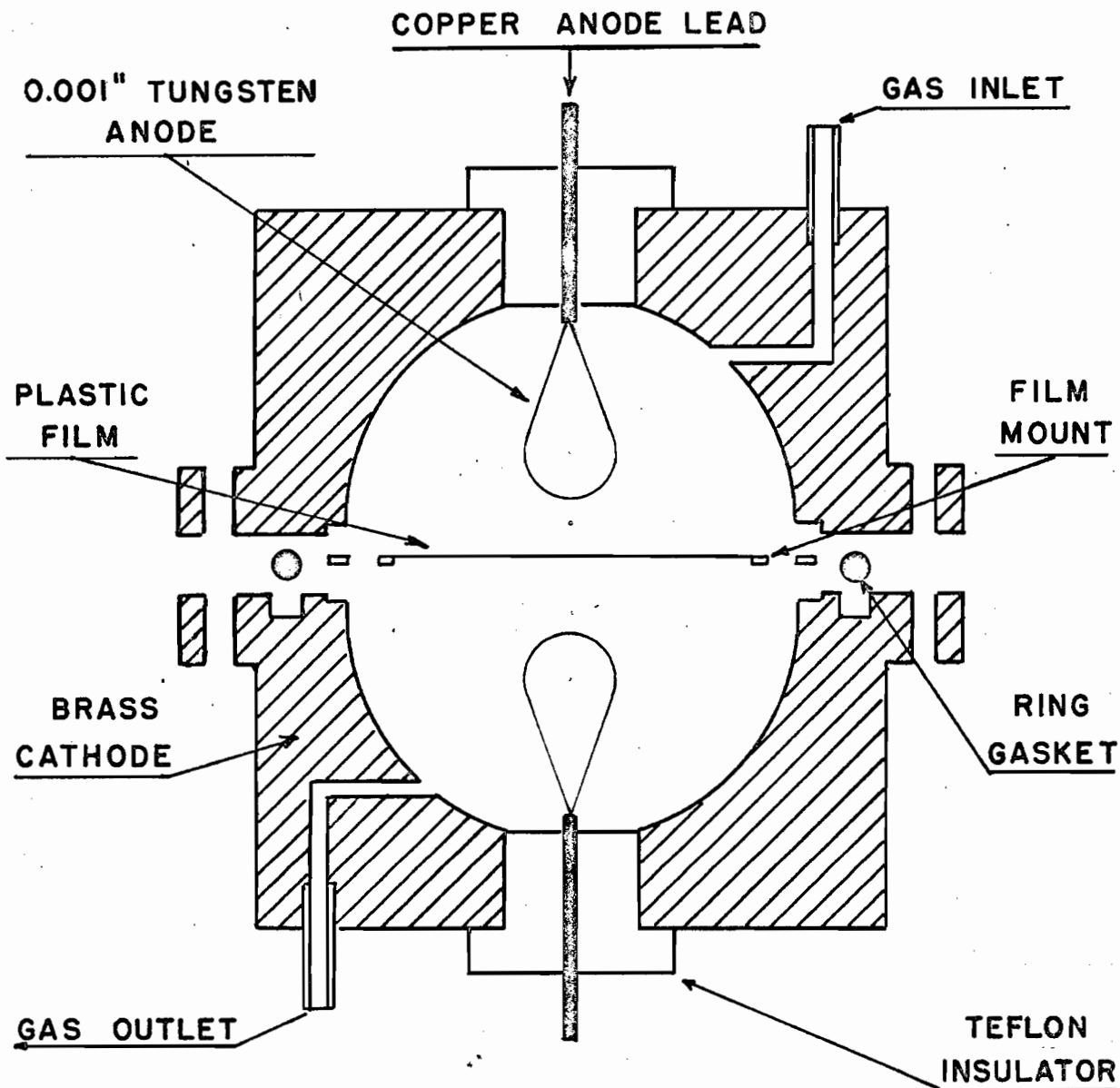
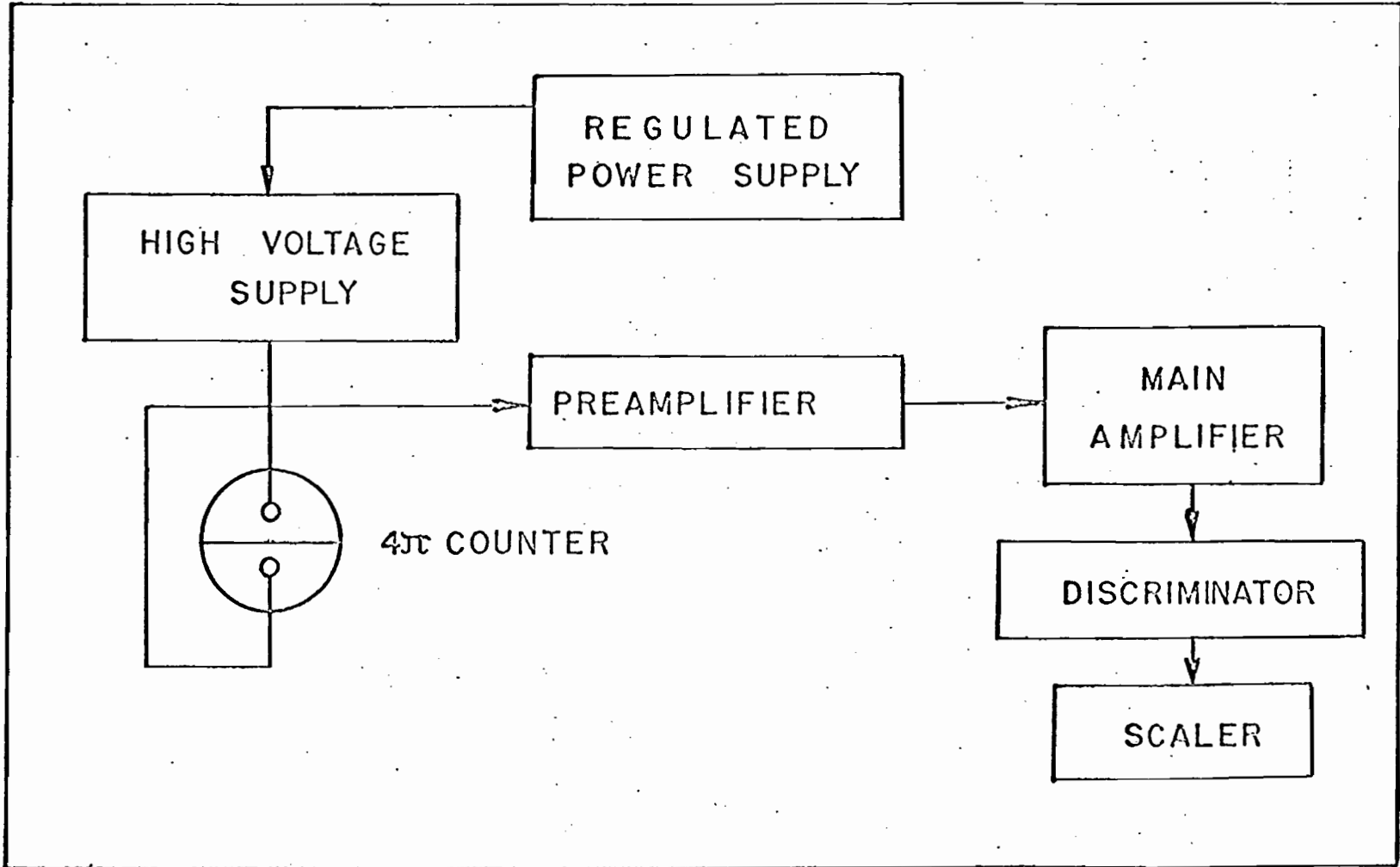


Figure 6

BLOCK DIAGRAM OF THE 4π -COUNTING ASSEMBLY



potential (2700 volts) and a discriminator bias (15 volts) were chosen from the plateau and bias curves. The counting time and aliquot size of the source were adjusted to record at least ten thousand counts to reduce statistical errors.

Source-mount and self-absorption corrections, as required for the nuclide concerned, are dealt with in the 'Treatment of Data'.

II-4.2. Gamma-Ray Measurements

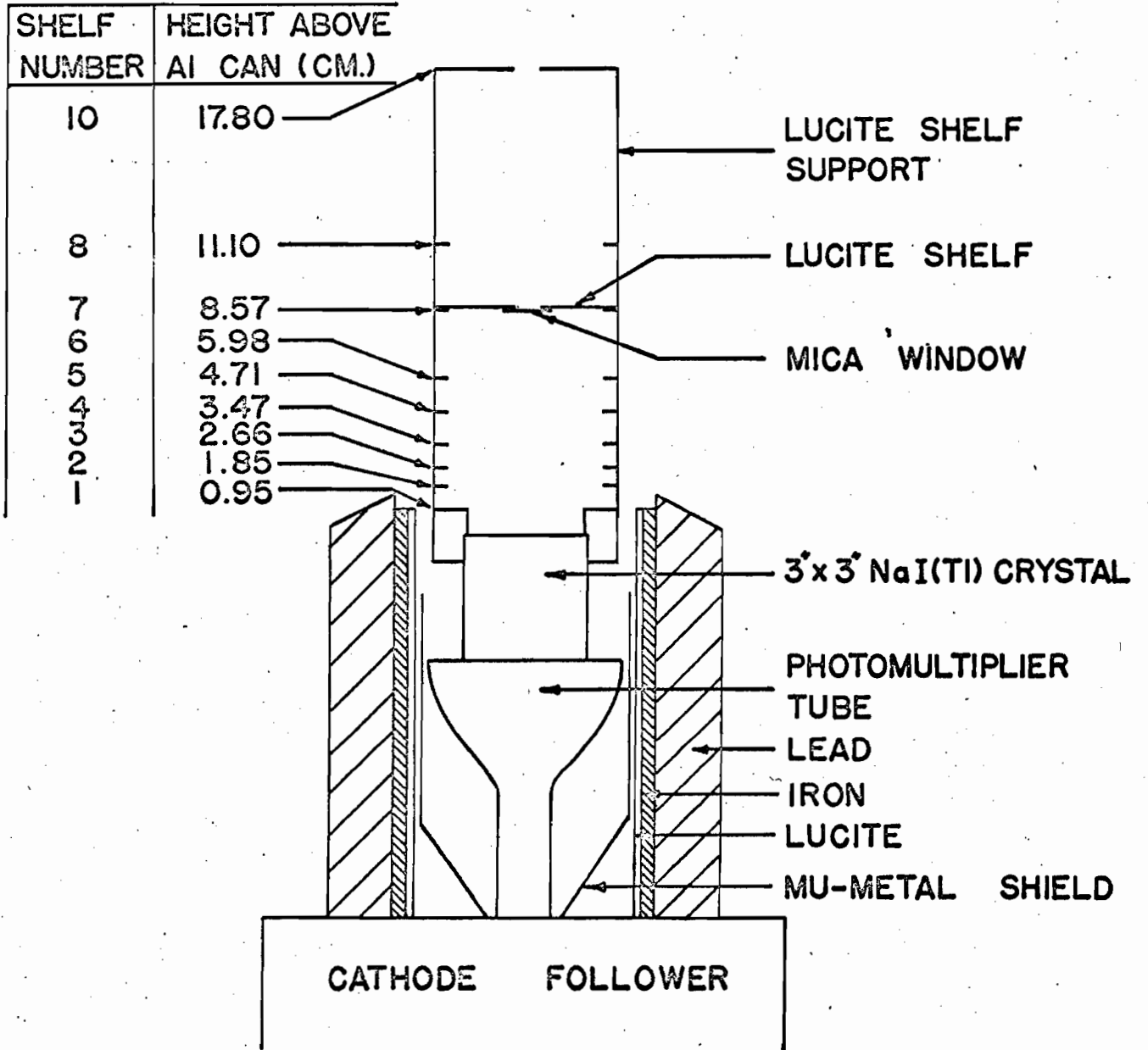
For gamma-ray measurements, scintillation spectrometry, using thallium activated-sodium iodide crystal [NaI(Tl)] as a detector, is most widely used. This was also employed in the present work.

Equipment: Part of the work was done with a commercially available (Harshaw Chemical Company) thallium activated-sodium iodide crystal (3" x 3"), hermetically sealed in an aluminum can and optically coupled to a Dumont '6364' photomultiplier. The latter was shielded from magnetic fields by a mu-metal shield, and the detection assembly was shielded by a 1.5" thick cylindrical lead housing. The lead shielding was lined with 0.25" iron and 0.125" lucite to attenuate fluorescent X-rays from lead. To facilitate different geometrical arrangements for the sample-detector system, a lucite sample positioning rack was attached to the crystal. The detector and shielding are shown in Fig. 7.

High voltage (1100 volts) necessary for the operation of the photomultiplier tube was obtained from a Baird-Atomic

Figure 7

NaI(Tl) DETECTOR, PHOTOMULTIPLIER TUBE, SHIELDING
AND SOURCE POSITIONING RACK



(Model 318) stabilized power supply. The output from the photomultiplier tube was fed to a pre-amplifier (Hamner Electronics Limited - Model N-351) which in turn fed a variable gain non-overloading linear amplifier (Baird-Atomic, Model 215). These amplified pulses were passed on to a 100-channel pulse height analyser (Computing Devices of Canada Limited, Model AEP-2230) through a cathode follower. The analyser had a magnetic core memory from which the data could be displayed on a cathode ray tube or recorded on a Westronic recorder (Model 2705) which accepted the analog signals. The analog signals could also be converted to decimal form by a decimal scaler (C.D.C. type 450) and the print-out taken on a Victor digit-matic printer (C.D.C. type 460).

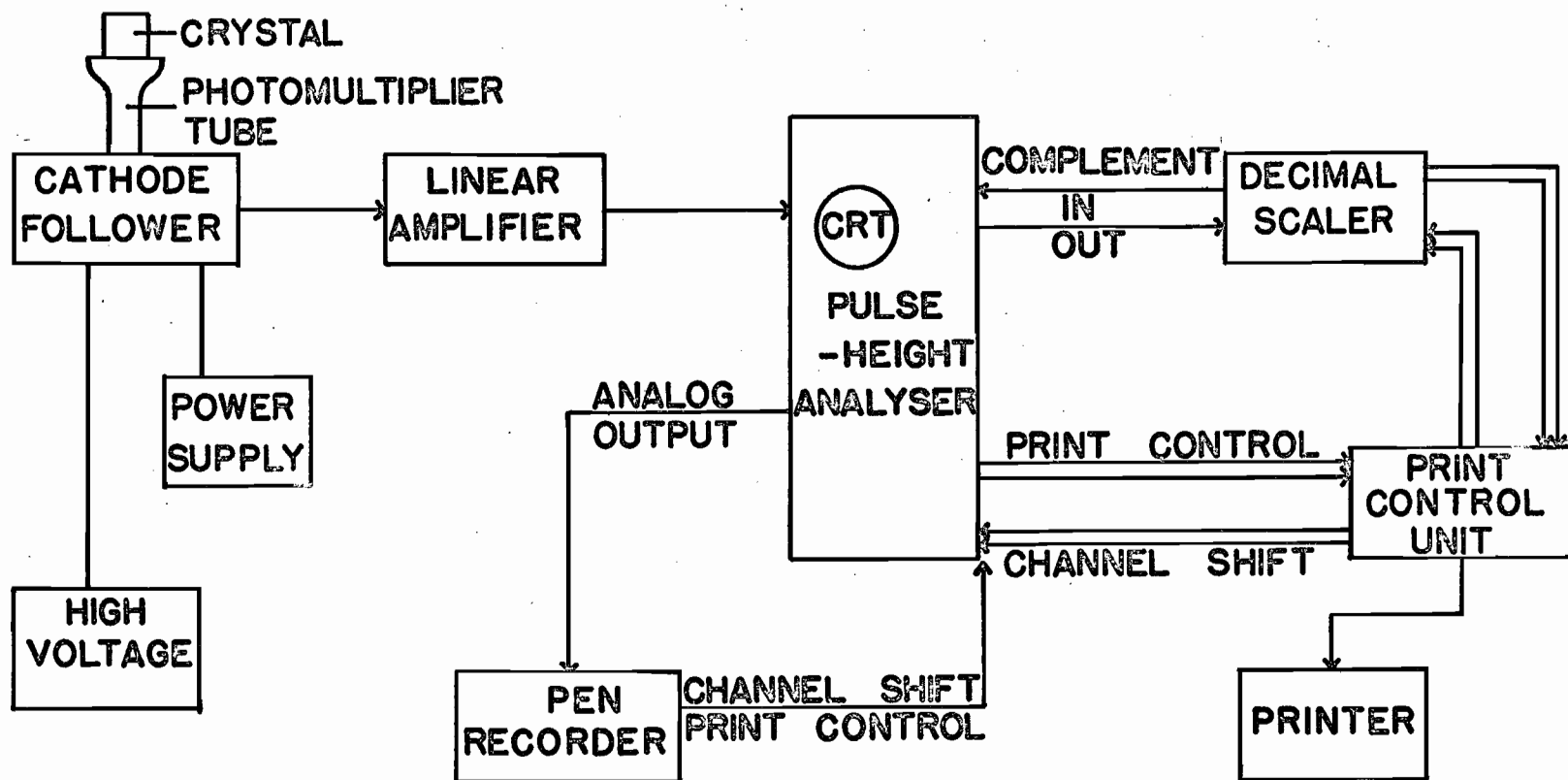
The dead time of the counter varied from 35 μ sec to 135 μ sec depending on the pulse height. These dead time losses did not distort the spectrum but only the over-all amplitude was reduced. The pulse height analyser was equipped with a calibrated micro-ammeter which indicated the percentage resolution losses directly. A block diagram of the entire assembly is shown in Fig. 8.

Analysis of gamma-ray spectra: Gamma-rays interact with matter in the following ways.

Photoelectric effect: In this process, a photon of energy ($E = h\nu$) ejects a bound electron (binding energy B) from an atom or a molecule with kinetic energy ($h\nu - B$). The phenomenon is most important at low energies and in heavy

Figure 8

**BLOCK DIAGRAM OF 100-CHANNEL PULSE-HEIGHT
ANALYSER ASSEMBLY**



elements. In the NaI(Tl) crystal, therefore, most of the events take place with iodine, producing photo-electrons and X-rays from residual nuclei. Absorption of both photo-electrons as well as X-rays within the crystal produces a pulse of maximum height.

Compton effect: In this process, only a part of the incident gamma-ray energy is transferred to the electron while the remainder is left as the energy of the scattered photon. Compton scattering also decreases with energy.

The scattered photons may either escape the crystal or further interact with the absorber. A series of Compton processes, followed by a photo-electric event with absorption of both X-ray and photo-electron is again recorded as a pulse of maximum height by the detector.

Pair production: A gamma ray, with energy greater than 1.02 MeV, could create a positron and an electron pair, the sum of kinetic energies of which equals $(E - 1.02 \text{ MeV})$. Annihilation of a positron, at the end of its path, again produces two gamma quanta of 0.511 MeV and at 180° to each other. Absorption of both these gamma quanta by photo-electric events or a combination of processes mentioned above will again result in the complete absorption of gamma-ray energy within the crystal and thus be recorded as a full energy event.

The atomic cross section for pair production increases with the energy of the gamma-ray.

Thus the result of either process is a transfer of

gamma-ray energy to the electrons, which in turn produce a proportional number of light photons. These light photons strike the photocathode of the photomultiplier tube, producing a corresponding number of photo-electrons. These photo-electrons are multiplied by the dynodes of the photomultiplier tube. Owing to the statistical uncertainty associated with the latter process, the output pulses corresponding to mono-energetic gamma-rays show statistical fluctuations. This results in the formation of peaks which are nearly Gaussian in distribution. These peaks are more commonly referred to as 'photopeaks', although any one process or any combination of the processes mentioned above could lead to complete absorption of gamma-ray energy within the crystal. The ability of a given detector system to resolve two peaks is described in terms of its 'resolution' which is defined as a ratio of 'full width at half maximum of a photopeak to the position of peak mid-point', expressed in percent. The photopeak corresponding to the 661 keV gamma-ray due to ^{137}Cs is usually referred to as a standard and the resolution, for the detector system described above, was found to be 12.8%. A number of spectra, obtained with the assembly described above, are shown in Figs. 9 - 11.

Photopeaks are normally used to identify and measure the gamma-rays. As implied in the above discussion, only a fraction of gamma-rays striking the crystal lose all of their energy in the NaI(Tl) crystal and thus contribute to photopeaks. This fraction is known as 'intrinsic photopeak efficiency'.

Figure 9

GAMMA-RAY SPECTRA OF ^{86m}Y AND ^{88}Y

- (a) Gamma-ray spectrum of separated yttrium sample taken 135 days after bombardment at 33 MeV, 0.9 MeV and 1.84 MeV gamma rays are due to 105-day ^{88}Y .
- (b) Gamma-ray spectrum of separated yttrium activities taken 89 minutes after bombardments at 54 MeV, 0.208 MeV peak is due to ^{86m}Y , 0.38 MeV 'edge' is due to ^{87m}Y and ^{87m}Sr , and the large peak at 0.51 MeV is due to ^{87g}Y and annihilation gamma rays of ^{86g}Y .

Estimated background is indicated by dotted lines.

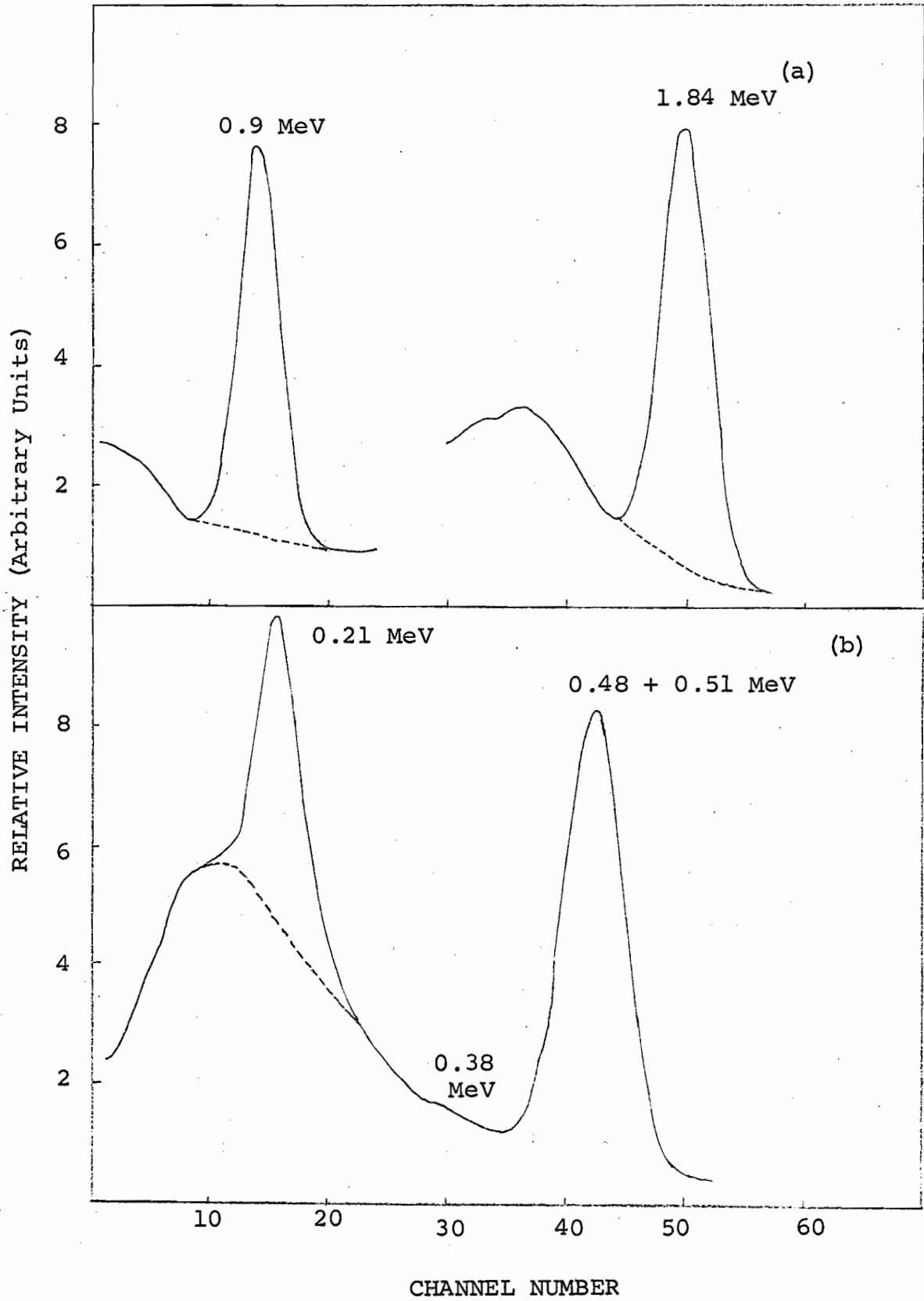


Figure 10

GAMMA-RAY SPECTRA OF ^{83}Rb , ^{84}Rb AND ^{86}Rb

- (a) Gamma-ray spectrum of separated rubidium activities taken 9.6 days after bombardment at 85 MeV, composite peak at 0.51 MeV is due to ^{83}Rb and annihilation gamma rays due to ^{84}Rb , 0.88 MeV peak is due to ^{84}Rb , while 1.08 MeV peak is due to ^{86}Rb .
- (b) 0.88 MeV and 1.08 MeV gamma rays of the same sample (a) shown on an increased scale.

Dotted lines indicate the estimated background.

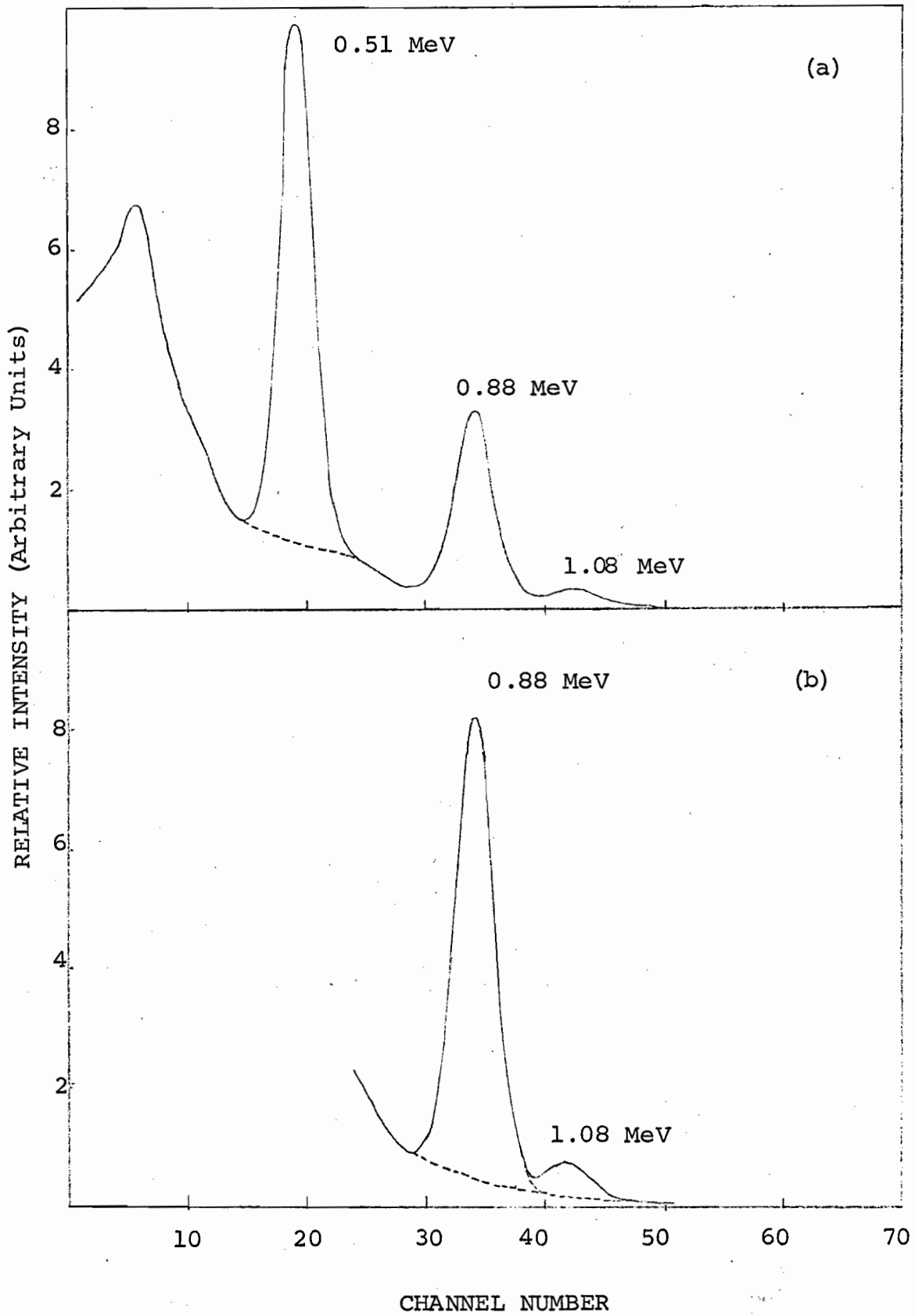


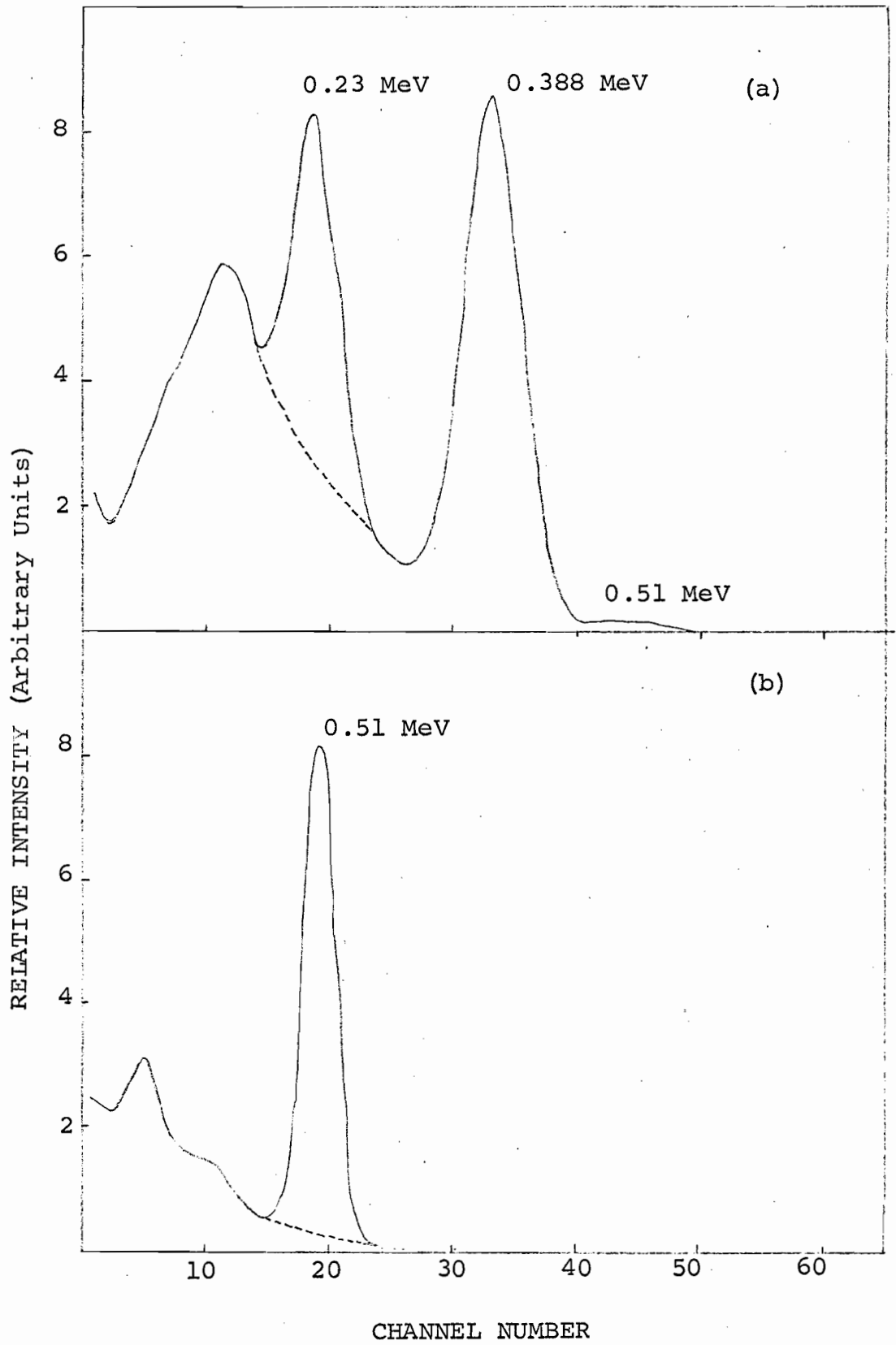
Figure 11

GAMMA-RAY SPECTRA OF ^{85m}Sr AND ^{85g}Sr

(a) Gamma-ray spectrum of separated strontium activities taken 197 minutes after bombardment at 48 MeV, 0.23 MeV peak is due to ^{85m}Sr , 0.388 MeV peak is due to ^{87m}Sr , and 0.51 MeV peak (small) is due to ^{85g}Sr .

(b) Same sample as in (a) recorded after 42 days for ^{85g}Sr .

Estimated background is indicated by dotted lines.



These intrinsic photopeak efficiencies have been determined by a number of workers.⁽⁸⁶⁻⁸⁸⁾ However, experimental over-all photopeak efficiencies determined by using a number of standard sources covering a useful range of gamma-ray energies (30 keV to 3 MeV) by a group of workers⁽⁸⁹⁾ in this Laboratory were used in the present work.

Gamma-ray spectra of various activities measured in this work, together with the procedure used in the estimation of the background under each photopeak and the conversion of the photopeak area to the disintegration rate, are described under 'Treatment of Data'.

It has been stated that the resolution of the above-described detector system was found to be 12.8%. The measurements of ⁸⁷Y were rendered difficult because of superposition of parts of the photopeaks due to the 0.39 MeV and 0.48 MeV gamma rays. It was therefore decided to use a different detector. An 'Integral Line' detector assembly (12S12; Serial No. 354, Harshaw Chemical Company) with a resolution of less than 8% guaranteed by the manufacturer and checked by the author as close to 7.5% for the 661 keV gamma ray due to ¹³⁷Cs was used. Typical spectra at two different times after the end of the bombardment time are shown in Fig. 12

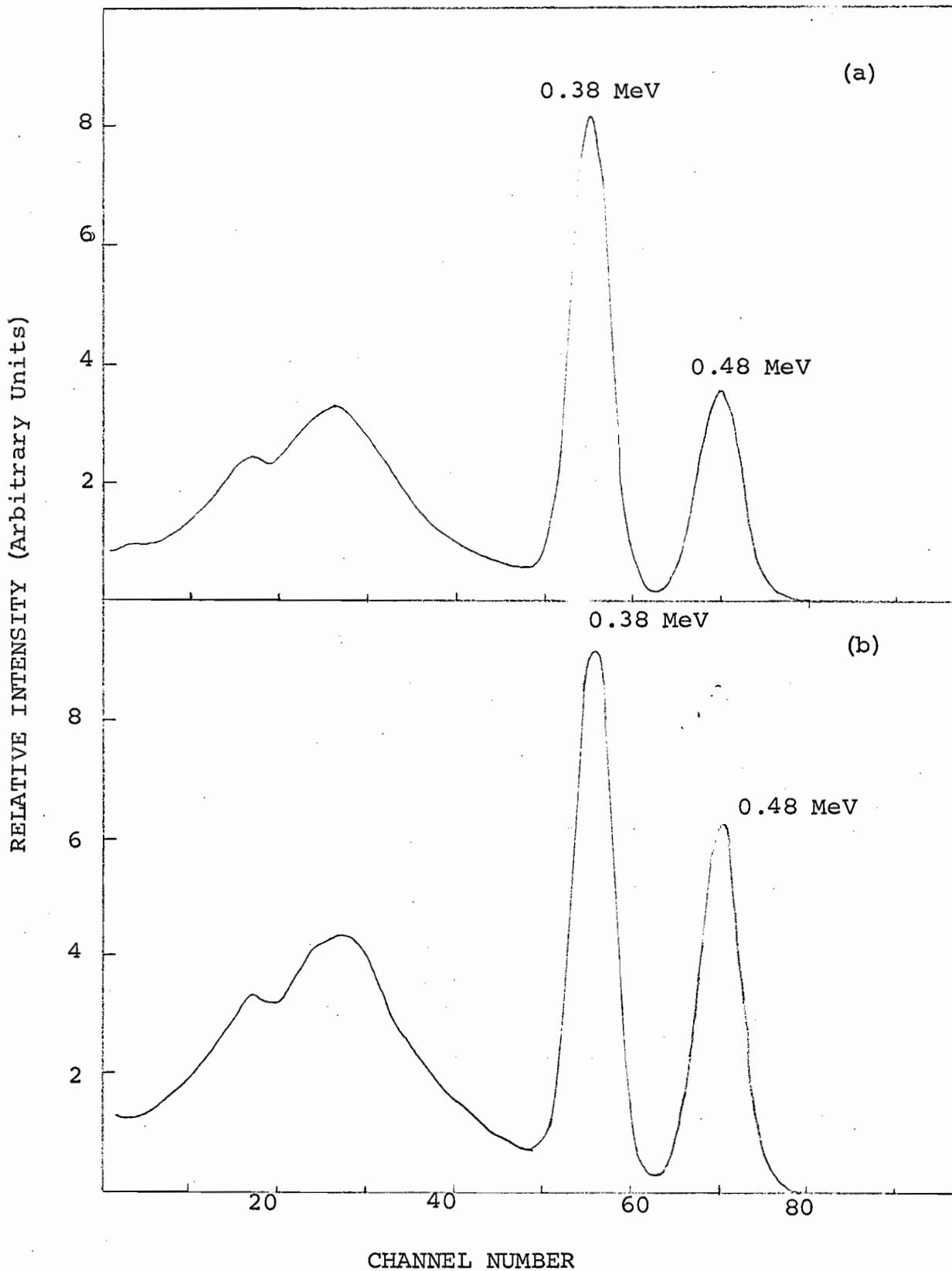
The output from the Integral Line detector was fed into a RIDL pre-amplifier (Model 31-15) which was passed on to an amplifier and 400-channel Pulse Height Analyser (RIDL Model 34-12B). High voltage (1020 volts) was also provided by a

Figure 12

GAMMA-RAY SPECTRA OF ^{87m}Y AND ^{87g}Y

Gamma-ray spectra of separated yttrium sample, taken
(a) 31.5 hours and (b) 62.5 hours respectively,
after bombardment at 21 MeV,
0.38 MeV peak is due to ^{87m}Y and ^{87m}Sr , and
0.48 MeV peak is due to ^{87g}Y .

Spectra taken using 'Integral Line' detector assembly
with 7.5% resolution.



stabilized power supply from the pulse height analyser unit. The data stored in the pulse height analyser were printed on a Digital Recorder (Model H 43562 A, Hewlett-Packard).

II-4.3. Positron Measurements

A positron, at the end of its path, combines with an electron, both of which annihilate by releasing two gamma quanta of 511 keV and at 180° to each other. If two detectors, such as NaI(Tl) scintillation phosphors, are placed in a line on each side of the source and their output gated to accept only 511-keV pulses in coincidence, then the positron emission rate can be determined. The main advantage of such a technique is that it discriminates, fairly well, against all other types of radiations. The rare accidental coincidences could be corrected by placing a third detector, under identical conditions but at 90° to them, and coupling it for coincidence to either of these detectors.

Equipment: Harshaw 'Integral Line' assemblies of 6S6 type, in which the NaI(Tl) crystal (1.5" x 1.5") and a matching photomultiplier tube are encapsulated in a single light-tight housing with an aluminum entrance window, constituted the detectors for the system. These units were plugged into cathode-follower preamplifiers designed by Mr. Heinstein of the Radiation Laboratory, McGill University. The output from each photomultiplier was fed into a linear amplifier (Cosmic* Model 901) which could operate at high counting rates without

* Cosmic Radiation Laboratories, Inc., Bellport, N.Y., U.S.A.

distortion and provide suitably shaped signals for operation with a multiple coincident unit (Cosmic Model 801). The latter contains fast-slow coincidence circuits with single channel analysers to impose amplitude restrictions in the slow circuits. The coincident outputs from the multiple coincident unit were recorded on Marconi Scalers (AEP-908). High voltages for the 180° detectors were obtained from a Victoreen regulated high voltage power supply (Model-683) while the detector placed at 90° was supplied by another high voltage power supply (Model 400 BDA, John Fluke and Co., Seattle, Washington). Power requirements for the preamplifiers were met by a Lambda regulated power supply (Model-25) while those for the multiple coincident unit were supplied by the unit itself. All other units were supplied by the line voltage-regulated power supply. Block diagrams 13 and 14 show the assembly and coincident conditions.

The sample (vial) holder was made by drilling a small hole (~ 1 mm in depth) in a lucite block which was mounted on another holder, itself fixed (firmly) on a smooth bench. The sample vial was closely surrounded by a copper tube, sufficiently thick to stop all positrons up to 3 MeV in energy. The detectors, required to be at 180° , were placed on either side of the sample on the bench and the detector at 90° was placed on a similar bench (cut from the same piece) at right angles to the other bench. All the three detectors were of the same shape as well as height and 'saw' the radioactive source identically. Resolution of all the crystals was approximately 10% for the

Figure 13

**BLOCK DIAGRAM FOR THE ANNIHILATION
COINCIDENCE ASSEMBLY**

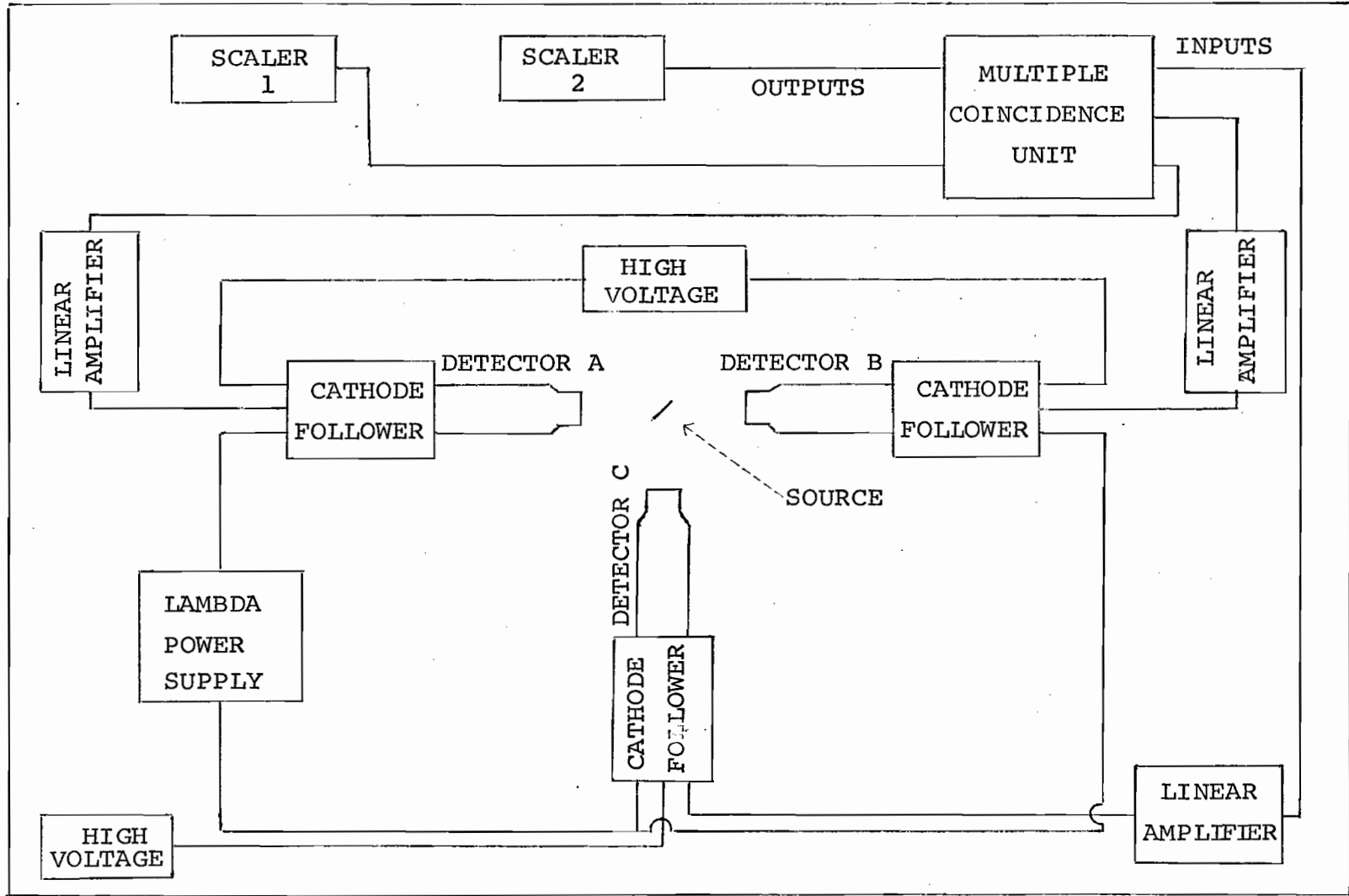
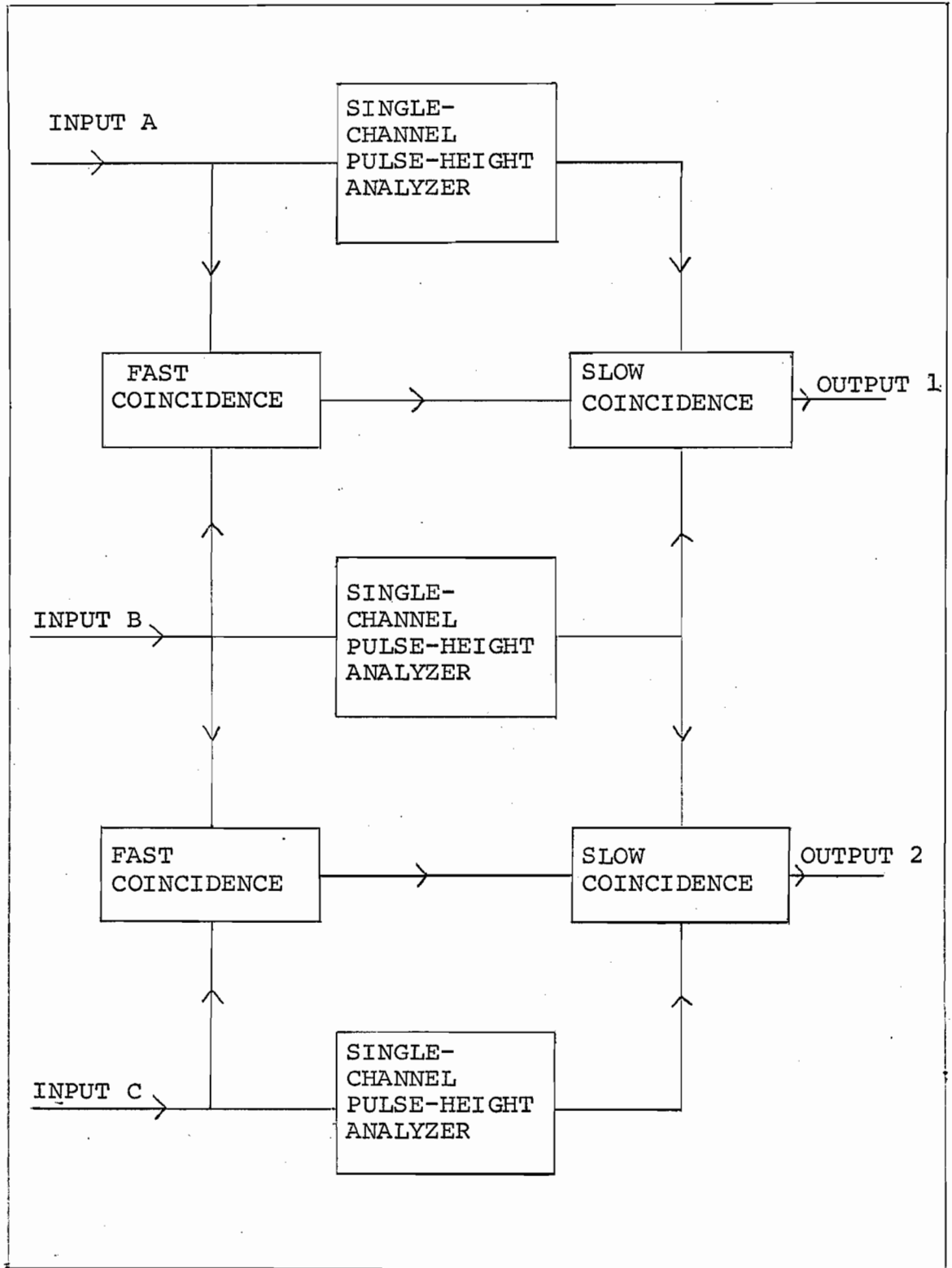


Figure 14

BLOCK DIAGRAM OF THE 'FAST-SLOW'
COINCIDENCE ARRANGEMENT (90)



661 keV gamma ray due to ^{137}Cs .

Calculation and Working Procedure: In order to measure absolute positron emission rates in the samples, a knowledge of the efficiency of the detection system is required. This was obtained as follows, using a ^{22}Na sample whose activity had been determined with the $4\pi\text{-}\beta$ counter.

The detectors were arranged at a fixed distance of 3'' (see below) from the centre of the source to avoid any confusion or delay in adjustments. High voltages between 1050 to 1075 volts were applied to the photomultiplier tubes. The window of each pulse height analyser was adjusted to admit pulses falling in the entire photopeak of the 511 keV gamma ray. The discriminator was next biased to a value slightly lower than the base line in order to cut down a large number of unwanted pulses corresponding to low-energy signals and noise in the coincidence circuit. Coincidence conditions were then imposed for the crystals at 180° to each other and either of the 180° crystals and a 90° crystal, as shown in the block diagrams (Figs. 13 and 14). Coincidence counts corresponding to the standard source of ^{22}Na were determined before measuring other samples. It may be noted that the standard and the samples were prepared in the same way.

The measurements of coincidence data in this way may, however, be affected by the following factors.

(1) There is a chance of recording coincident pulses between an annihilation gamma ray and a nuclear gamma ray, and between

nuclear gamma rays themselves. The probability of recording a coincidence between nuclear gamma rays is the same regardless if the crystals are at 180° or at 90° to each other. However, the probability of recording a coincidence between a nuclear gamma ray and an annihilation gamma ray is somewhat less for crystals at 180° than when the crystals are at 90° to each other (particularly so when our crystals are small in size). The background, recorded for crystals at 90° to each other, never exceeded more than 5% of the recorded coincident pulses for crystals at 180° in the worst cases in this work. No further correction to this background was therefore thought necessary and the background was subtracted from the coincident pulses (at 180°) in a straightforward manner.

(2) Another problem arises due to 'summing effects' which occur when two gamma rays strike the crystal within the resolving time of the detector. This is particularly serious when low-energy gamma rays, which are detected with high efficiency, are also involved. Addition of a nuclear gamma-ray pulse to an annihilation photopeak event will likely cause this pulse not to fall within the energy limits of the pulse height window and coincident records will be lower. Similarly summing of a low-energy gamma ray with Compton spectrum of 511 keV annihilation ray may cause this pulse to produce events which fall within the window for the 511 keV gamma ray and thus add to the coincident records. The summing effect could be reduced by increasing the source-detector distance and its optimum value (between detection

rates and summing effects) was determined from the experimental measurements of the activities of ^{86}Y , ^{22}Na , and ^{63}Zn for different source-detector distances. While ^{86}Y has many coincident gamma rays (Figs. 16 and 17), ^{22}Na has one (100%) gamma ray in coincidence with positrons and ^{63}Zn has even less coincident gamma-ray activity. It was found that for a source-detector distance of 3" and up, the ratio of the activities of $^{86}\text{Y}/^{22}\text{Na}$ and $^{22}\text{Na}/^{63}\text{Zn}$ was nearly constant. This indicated that the summing effect could be neglected after this source-detector distance, and a distance of 3" was selected in this work.

III. TREATMENT OF DATA

In this chapter, we will discuss the conversion of gross data obtained from various activity measurements into absolute disintegration rates, procedures employed for decay curve analysis, corrections for growth and finally a calculation for the cross section for the independent formation of nuclides.

III-1. ABSOLUTE DISINTEGRATION RATES

The corrections necessary to transform a counting rate into a disintegration rate are dependent on the assembly used for the measurement and are described accordingly.

III-1.1. 4 π - β Counting Data

The samples measured on this assembly contained relatively long-lived activities of ^{83}Rb , ^{84}Rb , and ^{86}Rb . Of these, 4 π -data were used to extract the results for ^{86}Rb only. Corrections for source-mount and self-absorption were therefore required, corresponding to energies for different β -components of this nuclide. Maximum energies for the β -spectra of the two components of $^{86}\text{Rb}^{(92)}$ are 1.78 MeV (91%) and 0.7 MeV (9%). The source-mount absorption for the films used (20 - 25 $\mu\text{g}/\text{cm}^2$) was found to be negligible for these end-point energies.⁽⁸³⁾ The sources were estimated to be about 200 μg per cm^2 in thickness and β -particles with $\mathcal{E}_{\text{max}} = 1.78$ MeV will have negligible absorption while the β -component with $\mathcal{E}_{\text{max}} = 0.7$ MeV will have a self-absorption⁽⁹³⁾ of about 0.94. The over-all

self-absorption factor (when branching ratios are also taken into account) corresponds to about 0.995 and a factor of 0.99 was used in this work.

Absolute disintegration rates (D) were then obtained by using the expression

$$D = \frac{C.R.}{0.99} \times \frac{100}{C.Y.} \times F \quad (13)$$

where C.R. = counting rate,
F = dilution factor, and
C.Y. = chemical yield in percent.

III-1.2. Gamma-Ray Measurement Data

Gamma-ray spectra of various activities measured in this work are shown in Figs. 9-12. The difficulty in estimating the background stems from the fact that photopeaks due to lower energy gamma rays are situated on the Compton distributions for the higher energy gamma rays. Lazar⁽⁹⁴⁾ and Heath⁽⁹⁵⁾ have suggested a method by which the known shape of the pulse height distribution of the highest energy gamma ray is subtracted from the entire spectrum. The process is repeated for the next highest gamma ray until all the components are analysed. The process, however, is very tedious when applied to a number of spectra.

The procedure followed by us was to draw the background by hand in a way which was similar to that adopted in determining the efficiencies. The estimated background, as shown in the

various spectra (Figs. 9-12), was then subtracted from the total area under each photopeak obtained as counts in all the channels comprising the photopeak. In some cases the photopeak was situated on a background with a steep slope (Figs. 9b and 11a) and the errors involved in estimating the background were consequently high.

After the areas under each photopeak were calculated, absolute disintegration rates for the corresponding measurements were determined by using the expression

$$D = \frac{A_p}{E_p} \times \frac{100}{(100 - \Delta R)} \times \frac{1}{\Delta t} \times F \times (1 + \alpha_T) \times \frac{100}{\text{B.R.}} \times \frac{100}{\text{C.Y.}} \quad (14)$$

where A_p = the area of the photopeak in terms of counts,

E_p = overall photopeak efficiency for a particular gamma-ray energy and source position,

ΔR = resolution loss in percent,

Δt = duration for the measurement, usually in minutes,

F = dilution factor,

α_T = total conversion coefficient,

B.R. = branching ratio for the observed decay mode in percent,

C.Y. = chemical yield in percent.

The branching ratios and conversion coefficients were taken from Nuclear Data Sheets⁽⁹²⁾ or from more recent literature.

III-1.3. Positron Measurement Data

As mentioned before, no corrections were applied to positron measurement data except for the normal subtraction of

the background. The disintegration rates were then obtained from the expression

$$D = C.R. \times F \times \frac{100}{C.Y.} \times \frac{100}{B.R.} \quad (15)$$

III-2. DECAY CURVE ANALYSIS

Generally, each separated element contained more than one isotope, depending upon the energy of bombardment. Data obtained by positron measurements or from 4π - β proportional counter measurements, therefore, usually represented a case of multi-component decay. In some cases, however, it was possible to measure gamma rays of a characteristic energy with a scintillation crystal in conjunction with a pulse height analyser (Figs. 9-12), which corresponded to the decay of a single radioactive species.

The multi-component disintegration rates, due to independently decaying species, were resolved into constituent components by a Least Squares Analysis Computer Program*. The same program was also utilized when growth and decay of the ground state of an isomeric nuclide (metastable state decaying completely to the ground state) was analysed by measuring a radiation due to the ground state. Disintegration rates were finally obtained for times at the end of bombardment (D^0) or at

* 'CLSQ, the Brookhaven Decay Curve Analysis Program' by J.B. Cumming (BNL-6470) was slightly modified for adoption to Fortran IV codes and a 7044 computer available at McGill University.

chemical separation (D^8).

III-3. CORRECTIONS FOR THE DISINTEGRATION RATES OF UNSHIELDED SPECIES

The unshielded species involved in this work are ground states of isomeric nuclides (when a metastable state decays to the ground state) or isomeric states of an unshielded nuclide of ^{85}Sr . The corrections for the latter are somewhat involved and are discussed in the Appendix, while the former are discussed below.

III-3.1. Calculation for the Disintegration Rate of the Ground State of an Isomeric Nuclide

The case is very similar to the radioactive chain $A \rightarrow B \rightarrow C$, when one is interested in the determination of the disintegration rate for the independent formation of B or of the ground state of an isomeric pair. If D_1^0 and D_{2c}^0 represent the disintegration rates of metastable and ground states respectively, at the end of bombardment time, the disintegration rate of the ground state at any time is given by

$$D_2 = \frac{\lambda_2}{\lambda_2 - \lambda_1} D_1^0 (e^{-\lambda_1 t} - e^{-\lambda_2 t}) + D_{2c}^0 e^{-\lambda_2 t} \quad (16)$$

Equation (16) could be used directly or after simplifications to get D_{2c}^0 . When the metastable state is short lived relative to the ground state (as is the case in the present work), measurements for D_2 could be made after a long time compared to the half-life of the metastable state and (16) becomes

$$\begin{aligned}
 D_2 &= \frac{-\lambda_2}{\lambda_2 - \lambda_1} D_1^o e^{-\lambda_2 t} + D_{2c}^o e^{-\lambda_2 t} \\
 &= \left(\frac{\lambda_2}{\lambda_2 - \lambda_1} D_1^o + D_{2c}^o \right) e^{-\lambda_2 t}
 \end{aligned}
 \tag{17}$$

A plot of $\log D_2$ versus time will be a straight line and extrapolation to zero-time will yield D_{2c}^o .

The disintegration rate is next corrected for the growth during bombardment. During bombardment, the rate equation for the ground state is given by

$$\frac{dN_2}{dt} = \lambda_1 N_1 + R_2 - \lambda_2 N_2
 \tag{18}$$

where R_2 is the rate for the formation of the ground state for a particular flux of protons. Again, since

$$\lambda_1 N_1 = R_1 (1 - e^{-\lambda_1 t})
 \tag{19}$$

equation (18) becomes

$$\frac{dN_2}{dt} + \lambda_2 N_2 = R_1 (1 - e^{-\lambda_1 t}) + R_2
 \tag{20}$$

which gives

$$N_2 = \frac{R_1 + R_2}{\lambda_2} (1 - e^{-\lambda_2 t}) + \frac{R_1}{\lambda_1 - \lambda_2} (e^{-\lambda_1 t} - e^{-\lambda_2 t})
 \tag{21}$$

or

$$D_2 = (R_1 + R_2)(1 - e^{-\lambda_2 t}) + \frac{R_1 \lambda_2}{\lambda_1 - \lambda_2} (e^{-\lambda_1 t} - e^{-\lambda_2 t})$$

Substituting for R_1 and R_2 from (19) and putting $t = t_b$ as the duration of bombardment, equation (21) becomes

$$D_{2c}^0 = D_2^0 + \frac{D_1^0}{(1 - e^{-\lambda_1 t_b})} \left[1 + \frac{\lambda_2 e^{-\lambda_1 t_b} - \lambda_1 e^{-\lambda_2 t_b}}{\lambda_1 - \lambda_2} \right] \quad (22)$$

from which D_2^0 , the disintegration rate for the independent formation of the ground state, can be calculated.

Equations (16) or (17) and (22) were used to calculate the disintegration rates for the ground states of isomeric nuclides when metastable states decayed by isomeric transition.

III-4. CALCULATION OF CROSS SECTION

After determining the disintegration rate at the end of bombardment time, the cross section for the formation of a particular nuclide 'A' can be calculated (using the thin target approximation) by the equation

$$D_A^0 = I n_T \sigma_A (1 - e^{-\lambda_A t_b}) \quad (23)$$

where D_A^0 = disintegration rate of 'A' at the end of bombardment,
 I = flux of protons as number per cm^2 per sec,
 n_T = number of target atoms exposed to the beam,
 σ_A = formation cross section of A,
 λ_A = decay constant for A,
 t_b = duration of bombardment.

The proton flux in the internal circulating beam was

determined by using the monitor reactions, $^{63}\text{Cu}(p,n)^{63}\text{Zn}$ or $^{65}\text{Cu}(p,pn)^{64}\text{Cu}$, the excitation functions of which are reliably known (next section). Since the copper oxide and strontium nitrate were intimately mixed, they were exposed to the proton beam under identical conditions. The formation cross sections for the monitor reaction is given by

$$D_M^o = I n_M \sigma_M (1 - e^{-\lambda_M t b}) \quad (24)$$

Eliminating 'I' between (23) and (24) and rearranging, we get

$$\sigma_A = \frac{n_M}{n_T} \times \frac{D_A^o}{D_M^o} \times \frac{(1 - e^{-\lambda_M t b})}{(1 - e^{-\lambda_A t b})} \times \sigma_M \quad (25)$$

Again, the number of atoms of a particular mass (involved in the nuclear reaction) in a known weight of the compound is given by

$$n = N.A. \times \frac{W}{G.M.W.} \times I.A. \times 6.02 \times 10^{23} \quad (26)$$

where N.A. = number of atoms of the element of interest in a molecule,

W = weight in gm of the compound,

G.M.W. = gram molecular weight of the compound,

I.A. = isotopic abundance of the nuclide undergoing nuclear reaction.

For copper oxide as well as strontium nitrate, the factor N.A. is unity and we have

$$n_T = \frac{W_T}{G.M.W._T} \times I.A._T \times 6.02 \times 10^{23} \quad (27)$$

and

$$n_M = \frac{W_M}{G.M.W._M} \times I.A._M \times 6.02 \times 10^{23} \quad (28)$$

Substituting (27) and (28) in (25), we get

$$\sigma_A = \frac{I.A._M}{I.A._T} \times \frac{W_M}{W_T} \times \frac{G.M.W._T}{G.M.W._M} \times \frac{D_A^0}{D_M^0} \times \frac{(1 - e^{-\lambda_M t_b})}{(1 - e^{-\lambda_A t_b})} \times \sigma_M \quad (29)$$

Equation (29) was used for the calculation of cross sections of all nuclides (as well as isomeric states) once the disintegration rates at the end of bombardment times were calculated for their independent formation during irradiation.

III-5. MONITOR CROSS SECTIONS

The monitor cross sections used in this work were taken from the excitation function curves due to S.N. Ghoshal⁽¹⁰⁾ for $^{63}\text{Cu}(p,n)^{63}\text{Zn}$ and S. Meghir and L. Yaffe⁽⁹⁶⁾ for $^{65}\text{Cu}(p,pn)^{64}\text{Cu}$ reaction. These values, together with corresponding bombarding energies of protons, are reproduced in Table II.

Table II

MONITOR CROSS SECTIONS USED IN THE PRESENT WORK

Bombardment Energy	Cross Section $^{63}\text{Cu}(p,n)^{63}\text{Zn}^{(10)}$ (mb)	Cross Section $^{65}\text{Cu}(p,pn)^{64}\text{Cu}^{(96)}$ (mb)
7*	250	-
9.5	435	-
12	515	-
15	460	-
18.5	-	144
21.5	-	380
24	-	482
24.7	-	488
25.5	-	486
26.5	-	480
28.7	-	422
30	-	388
33	-	334
36	-	298
40	-	265
42	-	252
44	-	240
45	-	235
48	-	220
54	-	198
60	-	180
66	-	167
72	-	156
78	-	148
85	-	140

*An accurate measurement of the cross section for $^{63}\text{Cu}(p,n)^{63}\text{Zn}$ reaction at 6.75 MeV of proton energy has been recently reported by Humes et al.⁽⁹¹⁾ The reported value of 239 ± 13 mb is in excellent agreement with the value taken from Ghoshal⁽¹⁰⁾ and used in this work for calculating the cross section at 7 MeV.

IV. EXPERIMENTAL RESULTS

The cross sections and other pertinent data obtained at different proton bombardment energies (up to 85 MeV), for various product nuclides of interest, are tabulated in this chapter. The corresponding excitation function curves and isomer ratios for the isomeric nuclides, as obtained from these cross-section values, are also presented. A brief account of the decay schemes of the individual nuclides as required in the calculations is also given and Table III summarizes the characteristics of the nuclides as well as activity measurement procedures used in the work.

IV-1. INDIVIDUAL NUCLIDES

IV-1.1. 105 day-⁸⁸Y

The decay scheme^(97,98) of this nuclide, formed by the (p,n) reaction, is shown in Fig. 13(a). The 0.3 msec metastable state decayed to the ground state by an isomeric transition and it was not possible for us to make measurements of such a short-lived species. The formation cross sections of the nuclide could, however, be determined by measuring the radiations connected with the decay of the ground state only, as the relatively very small half-life of the metastable state introduced insignificant errors in the disintegration rates determined for times at the end of bombardments. The ground state could be measured by either of the characteristic gamma rays of 0.9 and

Table III

PERTINENT DECAY SCHEME DATA AND DETECTION METHODS
USED FOR THE PRODUCT NUCLIDES OF INTEREST

Nuclide	Half-Life	Radiation Followed	Branch Abundance (%)	Conversion Coefficient	Detection Method	Ref.
^{88}Y	105 d.	γ - 1.84 MeV	99.4	0	G.M.*	97, 98
$^{87\text{m}}\text{Y}$	13.5 h.	γ - 0.483 } 0.381 } MeV	98.6	0.0035	G.M.	92
$^{87\text{g}}\text{Y}$	80 h.	γ - 0.483 MeV	98.6	0.0035	G.M.	92
$^{86\text{m}}\text{Y}$	48.5 m.	γ - 0.208 MeV	100	0.05	G.M.	101, 102
$^{86\text{g}}\text{Y}$	14.6 h.	β^+	30	-	P.M. ⁺	100, 103
$^{85\text{m}}\text{Y}$	2.68 h.	β^+	55	-	P.M.	105
$^{85\text{g}}\text{Y}$	5 h.	β^+	70	-	P.M.	105
^{84}Y	40 m.	β^+	86.5	-	P.M.	92
$^{85\text{m}}\text{Sr}$	70 m.	γ - 0.225 MeV	86.7	0.024	G.M.	92
$^{85\text{g}}\text{Sr}$	65 d.	γ - 0.514 MeV	100	0.007	G.M.	92
^{86}Rb	18.7 d.	β^-	100	-	4 π - β	92
^{84}Rb	33 d.	γ - 0.88 MeV	77	0	G.M.	92, 108
^{83}Rb	83 d.	γ - 0.525 MeV	93	0	G.M.	109
^{64}Cu	12.8 h.	β^+	19	-	P.M.	92
^{63}Zn	38.3 m.	β^+	93	-	P.M.	110

*G.M. - Gamma-ray measurements.

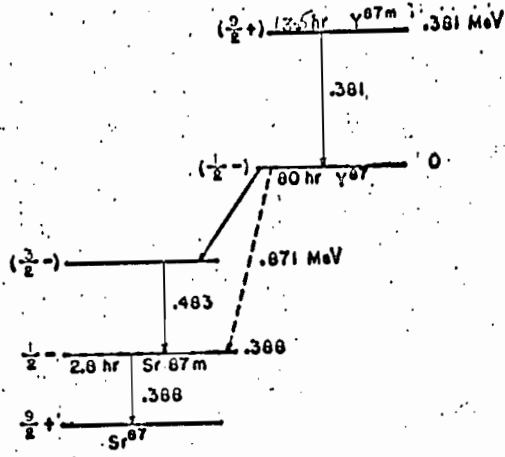
⁺P.M. - Positron measurements.

Figure 15

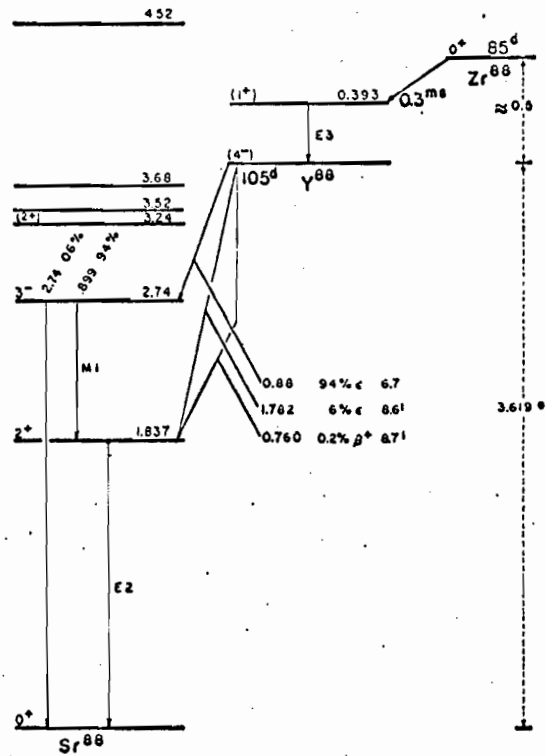
DECAY SCHEMES OF ^{88}Y AND ^{87}Y

(a) ^{88}Y (98)

(b) $^{87\text{m,g}}\text{Y}$ (92)



(b)



(a)

1.84 MeV energies and the results reported below are based on the activity measurements made with the 1.84 MeV gamma ray. In one case (at 33 MeV), the disintegration rates for times at the end of bombardment (D^0) were checked by measurements made with both gamma rays and were found to be the same. Branching ratios⁽⁹⁸⁾ of 94% and 99.4% were used for 0.9 and 1.84 MeV gamma rays respectively.

The calculated cross sections are presented in Table IV and the excitation function curve is shown in Fig. 20.

IV-1.2. 13.5 hr.-^{87m}Y and 80 hr.-^{87g}Y

The decay scheme of this isomeric nuclide is shown in Fig. 15(b). The reported half-lives for the metastable state are 14 hr.⁽⁹⁹⁾ and 13 ± 1 hr.⁽⁶²⁾ We have analysed our data according to 13.5 hr. and they seemed more consistent with this value. The half-life for the ground state was found to be in very good agreement with the reported⁽⁹⁹⁾ value.

Yamazaki et al.⁽¹⁰⁰⁾ suggested a positron branch of about 5%, associated with the decay of ^{87m}Y, in order to explain their experimental results while investigating the decay scheme for the 14.6 hr.-^{86g}Y. We have checked this possibility by making positron measurements and determining the ^{87m}Y activity (due to isomeric transition) by analysing the growth and decay of ^{87g}Y at a bombardment of 21 MeV. A positron branch of less than 1% (0.95%) was found, part of which was again attributable to ^{86g}Y, which was formed as a result of ⁸⁷Sr(p,2n)⁸⁶Y and ⁸⁶Sr(p,n)⁸⁶Y reactions, the ⁸⁷Sr ($\sim 0.2\%$) and ⁸⁶Sr ($\sim .05\%$)

isotopes being present in the target sample. (Table I, Experimental Procedures.) It was not possible for us to check for the decay of ^{87m}Y by electron capture which has been reported⁽⁹⁹⁾ to be less than 15%. We have therefore assumed that ^{87m}Y decays exclusively by isomeric transition.

Activity measurements for ^{87m}Y and ^{87g}Y were made by following the growth and decay of the 0.483 MeV gamma ray associated with the decay of ^{87g}Y , till bombarding energies of 26.5 MeV. A branching ratio of 98.6% (0.6% due to 0.3% β^+ branch) and a conversion coefficient⁽⁹²⁾ of 0.0035 were taken into account in the calculations. Activity measurements for bombardments at 30 and 33 MeV were made by a milking procedure and measurement of the 0.38 MeV gamma ray for ^{87m}Y as described before; and the 0.483 MeV gamma ray for ^{87g}Y after the decay of ^{86g}Y . This was necessary because ^{86g}Y , formed at higher energies, decayed with a similar half-life (14.6 hr.) to ^{87m}Y and had a large branching ratio for positron emission. After 33 MeV, the cross sections for the formation of ^{87m}Y decreased sharply while the positron-emitting activities increased, rendering it difficult to make measurements with the 0.38 MeV gamma ray for ^{87m}Y . The measurements for this nuclide were therefore discontinued for energies higher than 33 MeV.

The cross sections and isomer ratios are presented in Tables V - VII while curves for excitation functions and isomer ratios are shown in Figs. 21 and 22 respectively.

IV-1.3. 48.5 min. - ^{86m}Y and 14.6 hr. - ^{86g}Y

The metastable state was first reported by Haskin and Vandebosch⁽¹⁰¹⁾ and was subsequently confirmed by Kim et al.⁽¹⁰²⁾ The decay scheme for the ground state has been proposed by Yamazaki et al.⁽¹⁰⁰⁾ and Wapstra et al.⁽¹⁰³⁾ and is still incomplete. The decay scheme for the metastable state is shown in Fig. 16(a) while the ground state is presented in Figs. 16(b) and 17.

The reported half-lives for the metastable state are 49 ± 1.5 min. and 48 ± 1 min. Although our data could be analysed with either of these values, a mean value of 48.5 min. was used in this work. The activity measurements were made by following the 208-keV gamma ray with an internal conversion coefficient of 0.05 (a mean of 0.04 ± 0.01 ⁽¹⁰²⁾ and 0.06 ± 0.01 ⁽¹⁰¹⁾).

The ground state was measured by positron measurements. A branching ratio of 28.1% is obtained from the decay scheme of Yamazaki et al.⁽¹⁰⁰⁾ while, at the same time, a total of 113% results by adding percentage branching ratios for the positron and electron capture decay processes. Also, as mentioned in the preceding section, Yamazaki et al.⁽¹⁰⁰⁾ were forced to assign about 5% of the positrons to ^{87m}Y . A branching ratio of 31.5% is obtained from the decay scheme of Wapstra et al.⁽¹⁰³⁾ (Fig. 17). A value of 30% was therefore arbitrarily selected and used in our calculations.

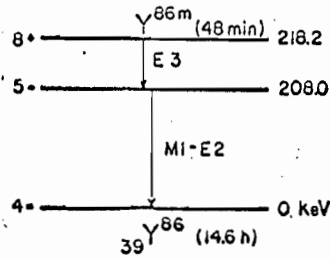
The cross sections and isomer ratios are given in

Figure 16

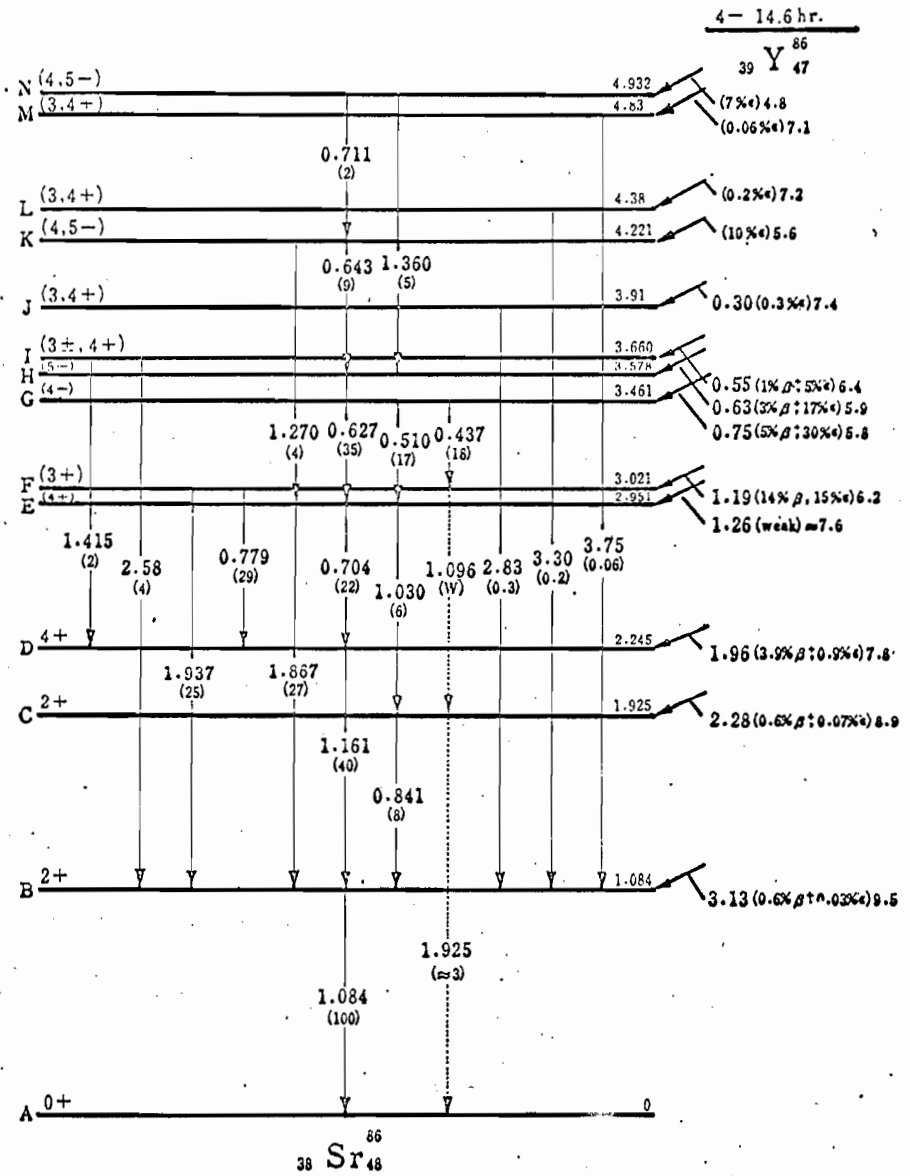
DECAY SCHEME OF ^{86}Y

(a) $^{86\text{m}}\text{Y}$ (102)

(b) $^{86\text{g}}\text{Y}$ (100)



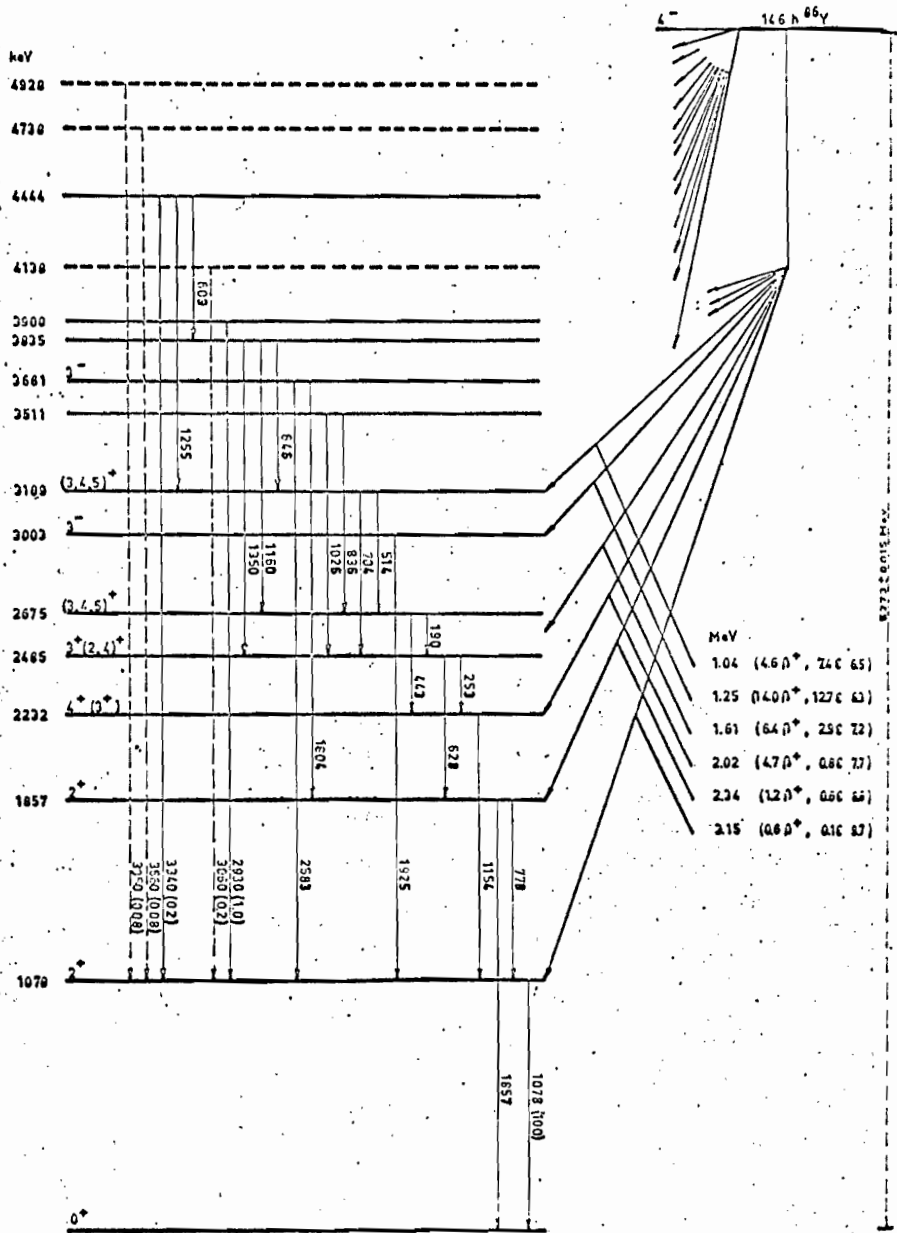
(a)



(b)

Figure 17

DECAY SCHEME OF $^{86}\text{g}_Y(103)$



Tables VIII - X and the excitation functions and isomer ratio curves in Figs. 23 and 24 respectively.

IV-1.4. 2.68 hr. - ^{85m}Y and 5.0 hr. - ^{85g}Y

The existence of this isomeric pair was first reported by Horen and Kelly.⁽¹⁰⁴⁾ A more thorough study of the decay scheme (Fig. 18) was reported by Dostrovsky et al.⁽¹⁰⁵⁾ and we have used their data in the calculations of our results. Recently, Nieckarz and Caretto⁽¹⁰⁶⁾ also reported the half-lives for the isomers, which are in good agreement with those of Dostrovsky et al.⁽¹⁰⁵⁾

Dostrovsky et al. could not observe any transition between the two isomeric states and set an upper limit of about 1% for the direct isomeric transitions. They obtained figures of 55% and 70% for the positron branching ratios for 2.68 hr. and 5.0 hr. isomers respectively. The results were calculated from the positron measurement data and these branching ratios were used for both the isomers. The calculated cross sections and isomer ratios are tabulated in Tables XI - XIII, and excitation functions and isomer ratio curves are given in Figs. 25 and 26 respectively.

IV-1.5. 40 min. - ^{84}Y

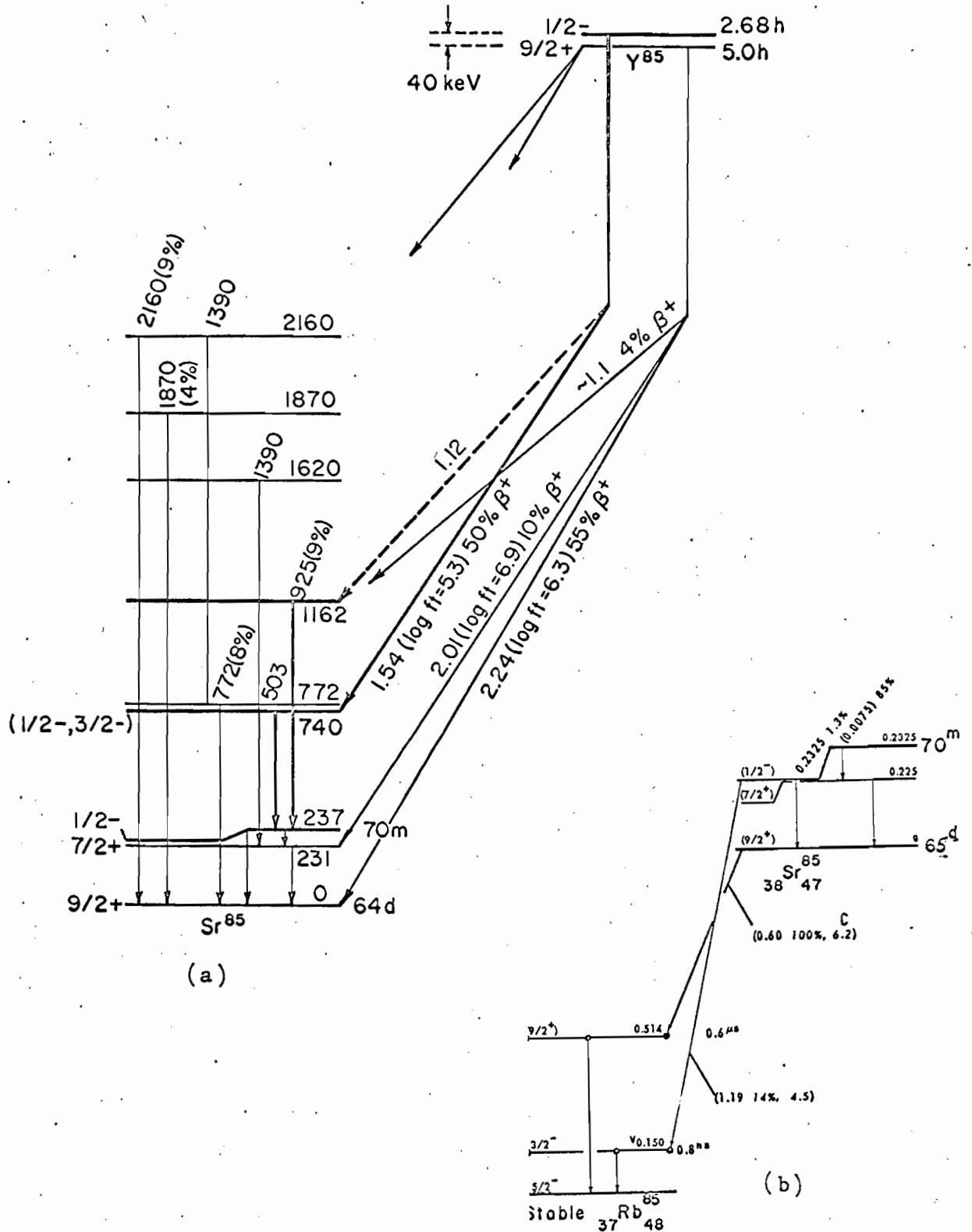
The activity measurements for this nuclide, formed by the (p,5n) reaction, were made by performing positron measurements. The reported half-lives for this nuclide are 39 ± 2 min.⁽¹⁰⁷⁾ and 42 and 43 minutes.⁽⁹²⁾ A value of 40 min. was adopted in this

Figure 18

DECAY SCHEMES OF ^{85}Y AND ^{85}Sr

(a) $^{85\text{m,g}}\text{Y}$ (105)

(b) $^{85\text{m,g}}\text{Sr}$ (92)



work, and the data analysed with this half-life was quite consistent. A branching ratio of 86.5%⁽⁹²⁾ was used in the calculation and the results for cross sections are given in Table XIV. The excitation function curve is presented in Fig. 27.

IV-1.6. 70 min. - ^{85m}Sr and 65 d. - ^{85g}Sr

The decay scheme⁽⁹²⁾ of this isomeric pair is presented in Fig. 18(b). The metastable state was measured by following the 0.23 MeV gamma ray with a branching ratio of 86.0% and a total conversion coefficient of 0.024.

The ground state was measured by its characteristic gamma ray of 0.514 MeV. A branching ratio of 100% and conversion coefficient of 0.007 were used in the calculations.

The calculated values of cross sections and associated data, and isomer ratios are given in Tables XV - XVIII, and excitation functions and isomer ratio curves are shown in Figs. 28 and 29 respectively.

IV-1.7. 18.7 d. - ⁸⁶Rb

The decay scheme⁽⁹²⁾ of this shielded nuclide is shown in Fig. 19(a), and is a case similar to that of ⁸⁸Y. The relatively short-lived (1.04 min.) metastable state decays to the ground state and was not measured in this work. The ground state decays by negatron emission and was measured by the 4 π - β proportional assembly. The calculated values of cross sections are given in Table XIX and the excitation function curve is shown in Fig. 30.

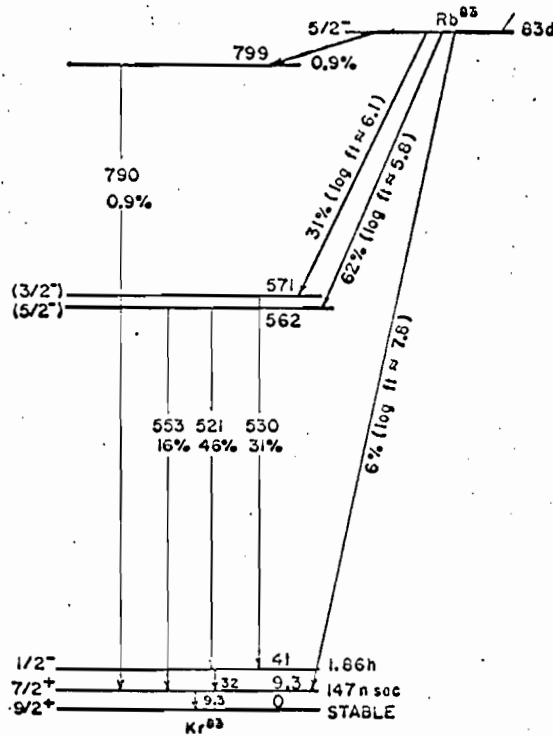
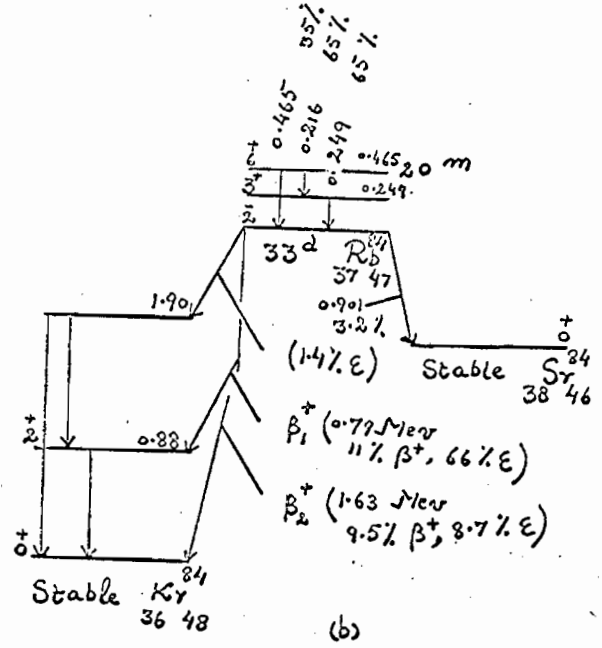
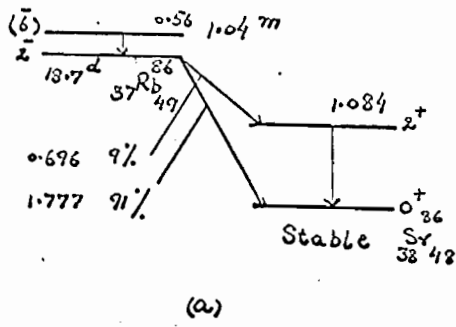
Figure 19

DECAY SCHEMES OF ^{83}Rb , ^{84}Rb , AND ^{86}Rb

(a) ^{86}Rb (92)

(b) ^{84}Rb (92, 108)

(c) ^{83}Rb (109)



IV-1.8. 33 d.-⁸⁴Rb

The decay scheme^(108,92) of this shielded isomeric nuclide is shown in Fig. 19(b). Again we did not measure the metastable state (20 min.) and the cross sections for the nuclide were obtained from activity measurements associated with the decay of the ground state. The characteristic gamma ray of 0.88 MeV was followed and a branching ratio⁽¹⁰⁸⁾ of 77% was used for the calculation of the cross sections (Table XX). The excitation function curve is shown in Fig. 31.

IV-1.9. 83 d.-⁸³Rb

The decay scheme [Fig. 19(c)] of this nuclide was recently studied by Dostrovsky et al.⁽¹⁰⁹⁾ and the nuclide was measured by the composite photopeak due to 521, 530, and 553 keV gamma rays. A branching ratio of 93%⁽¹⁰⁹⁾ was used in calculating the results.

After about 60 MeV, this nuclide is also expected to be formed from the decay of its precursor, i.e. ⁸³Sr. The 34 hr. half-life of this isotope is, however, sufficiently long so that any corrections (within experimental error) may be disregarded when the rubidium activities could be separated from its parents in about an hour from the end of bombardment.

The cross sections for this nuclide are given in Table XXI, and the excitation function curve is shown in Fig. 32.

IV-1.10. 12.8 hr.-⁶⁴Cu and 38.3 min.-⁶³Zn

These monitor activities were measured by performing positron measurements. Branching ratios of 19%⁽⁹²⁾ and 93%⁽¹¹⁰⁾

were used in the calculations of disintegration rates for ^{64}Cu and ^{63}Zn .

IV-2. ERRORS

Errors involved in the determination of cross sections are mainly of two types. The first class represents, what may be termed as 'constant' errors, and includes errors due to decay schemes (e.g. in branching ratios, conversion coefficients or half-lives, etc.), efficiencies for the detection systems, etc. On the other hand, errors such as those involved in the estimation of backgrounds of the gamma-ray spectra, decay curve analyses, chemical yields, dilutions, etc. are 'random' in nature.

Errors due to decay schemes are not definitely known and are therefore not included in the over-all estimation of errors. An error of $\pm 5\%$ had been quoted⁽⁸⁹⁾ for the efficiencies determined for the gamma-ray measurement assembly coupled to the 100-channel pulse-height analyser. A similar error was estimated for the efficiencies of the higher resolution gamma-ray and positron measurement assemblies.

The random errors were estimated as follows.

1. Errors in the determination of the photopeak vary with the complexity of the spectrum. An error of $\pm 5 - 15\%$ was estimated.
2. Chemical yields were determined by titrations, spectrophotometry as well as precipitation methods. An error of $\pm 2\%$ was estimated for chemical yields determined by titration

or the precipitation method, while a higher value of $\pm 5\%$ was allowed for spectrophotometric results.

3. An error of $\pm 3-5\%$ was estimated for the decay curve analysis.

4. An error of $\pm 1\%$ was estimated for pipetting, etc., and a similar allowance was made for weighing in the balance.

The over-all error was estimated by taking the square root of the sum of squares of all these individual errors considered above, for both the nuclide and the monitor. These errors ranged from $\pm 10\%$ to 20% for the nuclides studied in this work.

In estimating the errors for daughter nuclides (e.g. ground states of some isomeric nuclides), care was used to take into account the errors involved in the measurements of the parent nuclide as well as its percentage contribution to the disintegration rates of the daughter nuclide. Errors estimated for the isomer ratios varied from 8% to 22% .

The spread in the beam energy, as reported by the Foster Radiation Laboratory, was assumed to be ± 2 MeV. This is represented by horizontal bars in the excitation function curves while the estimated error, due to factors mentioned before, is shown by vertical bars.

Another 'constant' error (constant for a particular energy rather than for the nuclide), reference to which has not been made in the above discussion, is the error in the values of monitor cross sections. Errors in the monitor cross sections

are also reflected in the cross sections determined by using them, and are particularly troublesome in the region of steep slopes of the excitation function curves because of the energy spread in the proton beam (± 2 MeV).

For low-energy bombardments (till 15 MeV), monitor cross section values were taken from Ghoshal's⁽¹⁰⁾ results; errors for which could not be evaluated. Meghir and Yaffe⁽⁹⁶⁾ quote a figure of $\pm 14\%$ in their results for the $^{65}\text{Cu}(p,pn)^{64}\text{Cu}$ excitation function, but we have not taken into account either of these errors in monitor cross sections in our results.

Table IV

INDEPENDENT CROSS SECTIONS FOR THE FORMATION OF ^{88}Y FROM ^{88}Sr

Proton Energy (MeV)	Monitor σ (mb)	D_A^0 dis/min $\times 10^{-5}$	D_M^0 dis/min $\times 10^{-8}$	R	Ratio of Saturation Factors $\times 10^{-2}$	Nuclide σ (mb) $\pm 12\%$
7	250	8.69	19.3	0.992	23.2	260
9.5	435	19.5	28.7	0.992	21.6	630
12	515	20.7	30.4	0.992	27.0	940
15	460	57.8	66.5	0.992	24.1	960
18.5	144	48.4	1.02	0.444	1.92	580
21.5	380	22.4	2.41	0.444	1.92	300
24.7	488	12.9	2.99	0.444	1.92	180
28.7	422	7.53	3.93	0.444	1.92	69
33	434	6.75	3.26	0.444	1.92	59
36	298	4.56	2.22	0.444	1.92	52
40	265	3.74	2.04	0.444	1.92	41
42	252	1.66	2.55	1.27	1.92	40
48	220	2.28	1.30	0.444	1.92	33
54	198	2.10	1.33	0.444	1.92	27
60	180	1.47	0.90	0.444	1.92	25
66	167	0.753	1.26	1.27	1.92	24
72	156	0.650	1.48	1.27	1.92	17
78	148	0.139	0.311	1.27	1.92	16
85	140	1.35	2.84	1.27	1.91	16

Symbols denoting the tabulated quantities are defined in the following page.

D_A^0 = disintegration rate of the 'concerned' nuclide at the end of bombardment (Equation 23).

D_M^0 = disintegration rate of the monitor nuclide at the end of bombardment (Equation 24).

$R = \frac{n_M}{n_T}$ = ratio of number of monitor to target atoms
(Equations 27 and 28).

Ratio of saturation factor = $\frac{1 - e^{-\lambda_M t_b}}{1 - e^{-\lambda_A t_b}}$ (Equation 29).

Figure 20

EXPERIMENTAL EXCITATION FUNCTION FOR

$^{88}\text{Sr}(p,n)^{88}\text{Y}$ REACTION

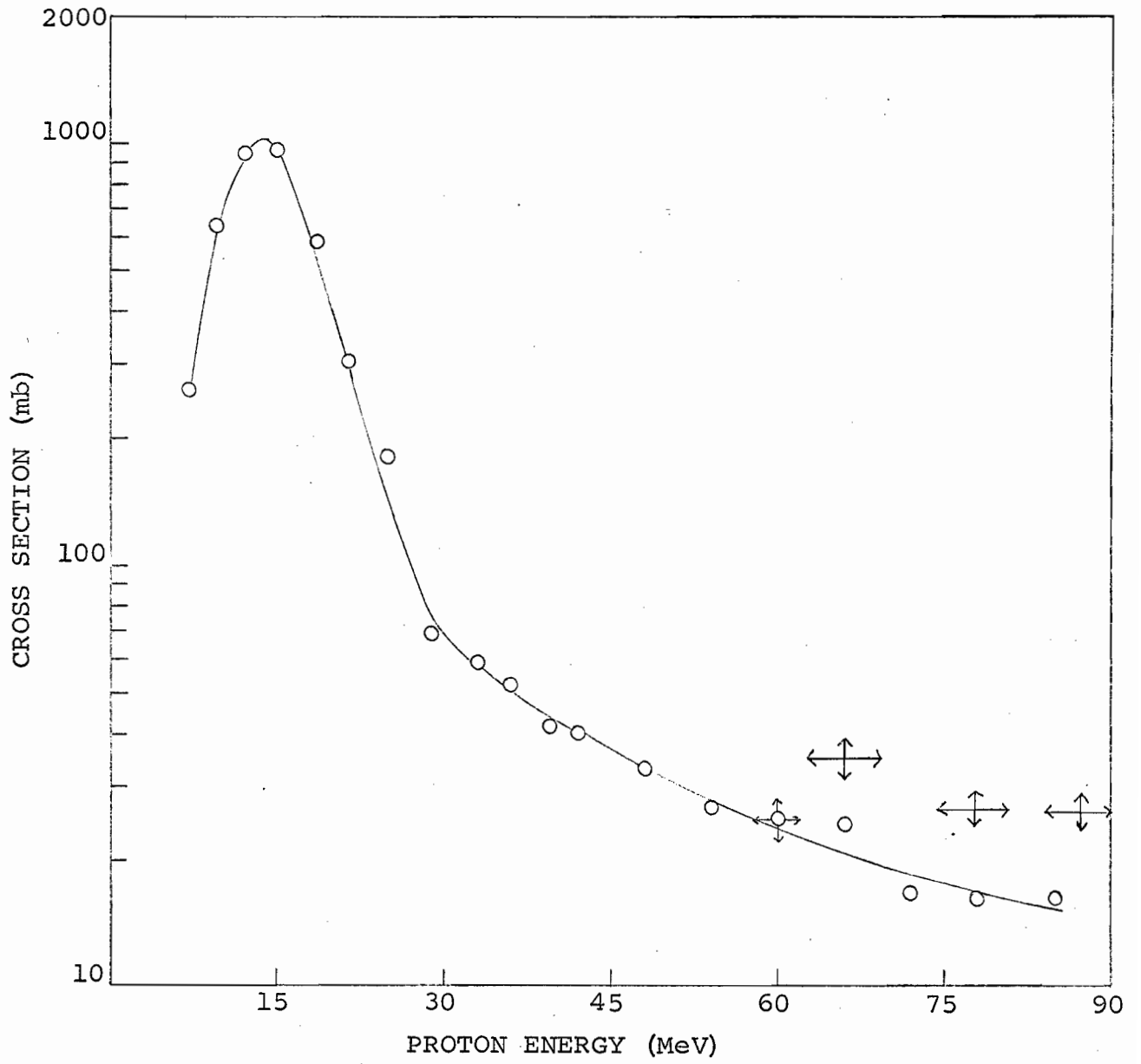


Table V

INDEPENDENT CROSS SECTIONS FOR THE FORMATION OF ^{87m}Y FROM ^{88}Sr

Proton Energy (MeV)	Monitor σ (mb)	D_A^0 dis/min $\times 10^{-7}$	D_M^0 dis/min $\times 10^{-8}$	R	Ratio of Saturation Factors	σ_m (mb) $\pm 11\%$
15	460	0.343	10.9	2.84	18.6	77
18.5	144	3.82	0.329	1.27	1.05	220
21.5	380	8.74	1.36	1.27	1.05	330
24	482	13.0	1.28	1.27	1.05	650
25.5	488	18.0	1.70	1.27	1.05	690
26.5	480	14.2	1.39	1.27	1.05	650
30	388	15.2	1.35	1.27	1.05	580*
33	334	12.2	1.69	1.27	1.05	320*

* Error $\pm 15\%$

Table VI

INDEPENDENT CROSS SECTIONS FOR THE FORMATION OF $^{87}\text{g}_\text{Y}$ FROM ^{88}Sr

Proton Energy (MeV)	Monitor σ (mb)	D_A^o dis/min $\times 10^{-6}$	D_M^o dis/min $\times 10^{-8}$	R	Ratio of Saturation Factors	σ_g (mb) $\pm 11\%$
15	460	0.983	10.9	2.84	110	130
18.5	144	7.30	0.329	1.27	6.21	250
21.5	380	12.2	1.36	1.27	6.18	270
24	482	17.1	1.28	1.27	6.22	510
25.5	488	23.0	1.70	1.27	6.21	520
26.5	480	15.5	1.39	1.27	6.21	420
30	388	14.4	1.35	1.27	6.21	330*
33	334	11.6	1.69	1.27	6.21	180*

*Error $\pm 15\%$

Table VII

INDEPENDENT CROSS SECTIONS AND ISOMER RATIOS FOR
THE FORMATION OF NUCLEAR ISOMERS OF ^{87}Y FROM ^{88}Sr

Proton Energy (MeV)	σ_m (mb) \pm 11%	σ_g (mb) \pm 11%	Nuclide $\sigma (= \sigma_m + \sigma_g)$ (mb)	Isomer Ratio $\frac{\sigma_m}{\sigma_g} (= \frac{\sigma_H}{\sigma_L}) \pm$ 8%
15	77	130	210	0.60
18.5	220	250	470	0.89
21.5	330	270	600	1.21
24	650	510	1160	1.28
25.5	690	520	1210	1.32
26.5	650	420	1070	1.55
30	580*	330*	910	1.79*
33	320*	180*	500	1.78*

*Error \pm 15%

Figure 21

EXPERIMENTAL EXCITATION FUNCTIONS FOR $^{88}\text{Sr}(p,2n)^{87m}\text{Y}$,
 $^{88}\text{Sr}(p,2n)^{87g}\text{Y}$ AND $^{88}\text{Sr}(p,2n)^{87m+g}\text{Y}$ REACTIONS

Δ ^{87m}Y - cross section

\square ^{87g}Y - cross section

\circ $^{87m+g}\text{Y}$ - cross section

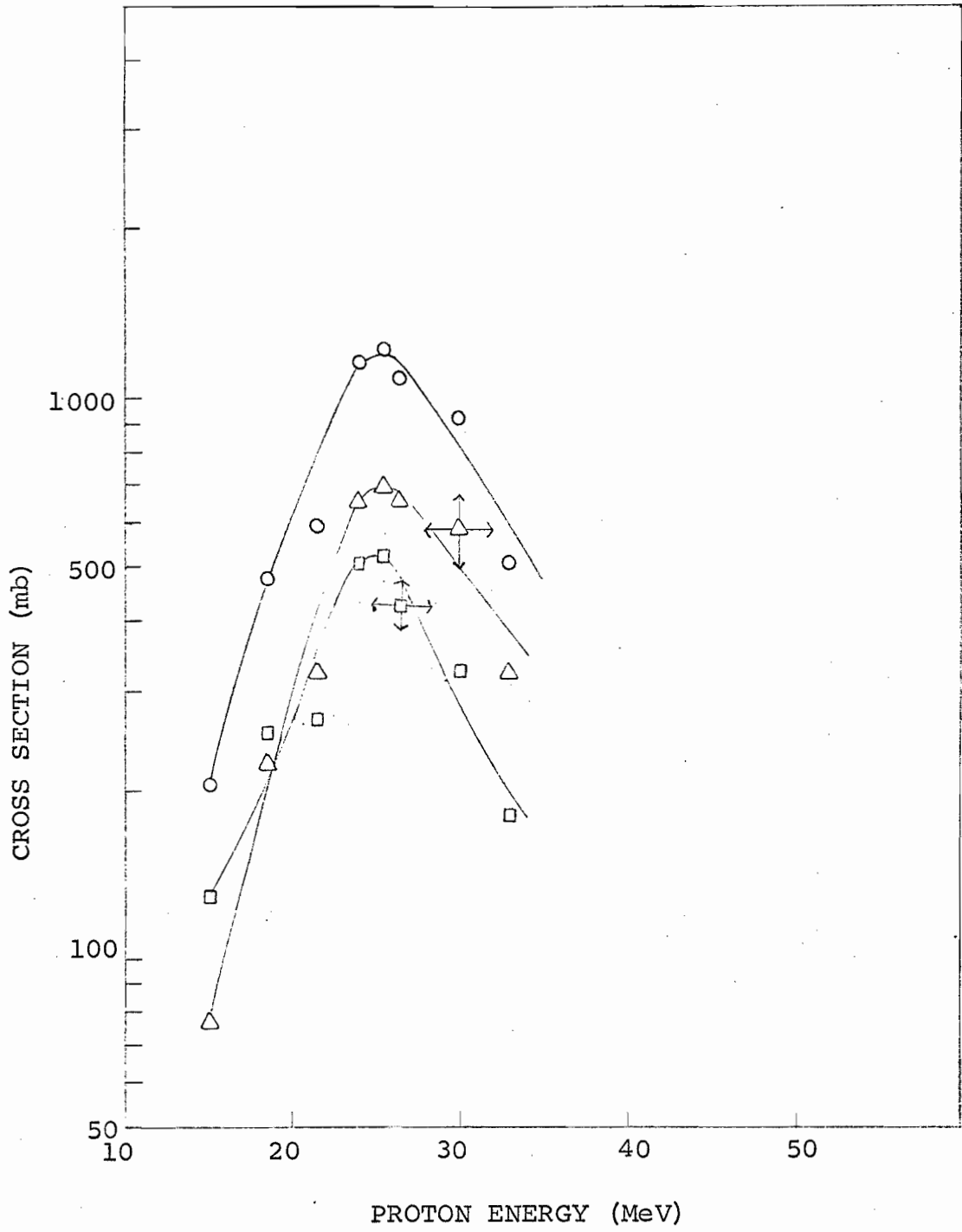


Figure 22

EXPERIMENTAL ISOMER RATIOS $\left(\frac{\sigma_H}{\sigma_L}\right)$ FOR

$^{88}\text{Sr}(p, 2n)^{87m, g}\text{Y}$ REACTION

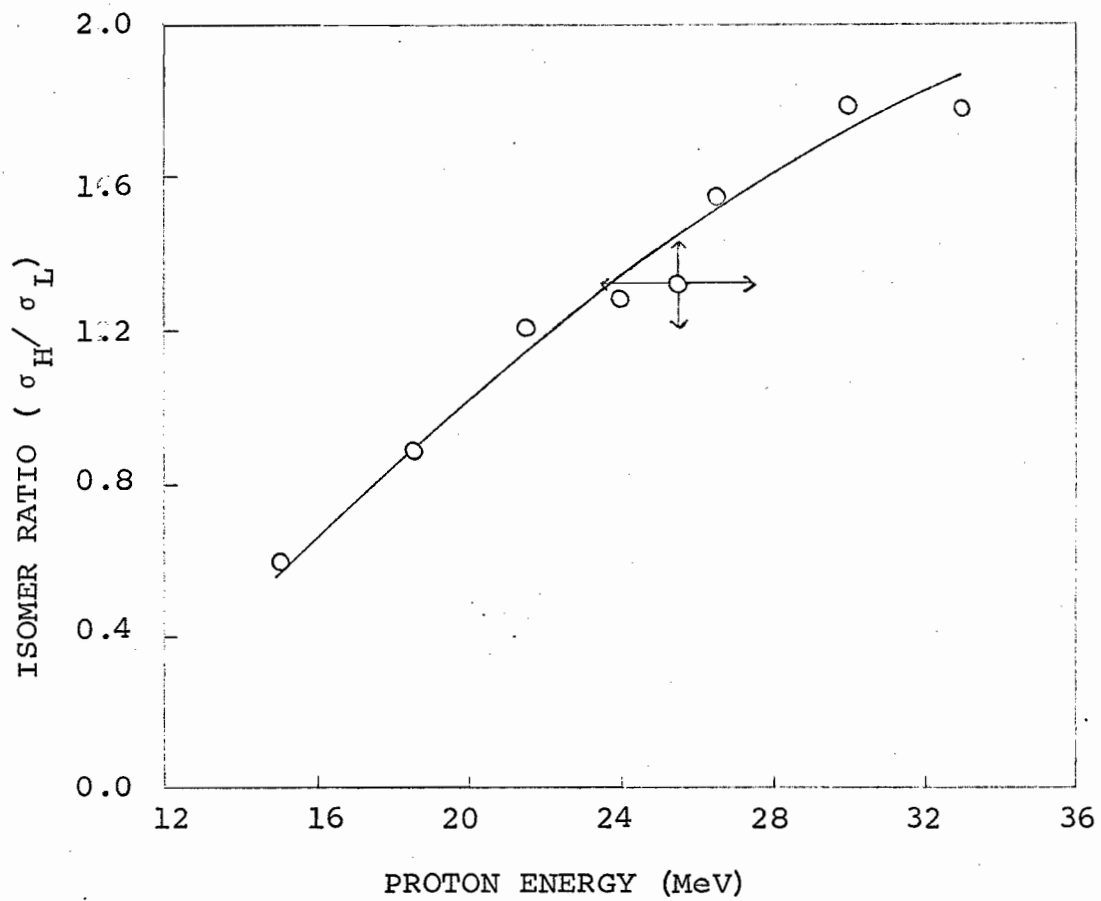


Table VIII

INDEPENDENT CROSS SECTIONS FOR THE FORMATION OF ^{86m}Y FROM ^{88}Sr

Proton Energy (MeV)	Monitor σ (mb)	D_A^0 dis/min $\times 10^{-8}$	D_M^0 dis/min $\times 10^{-7}$	R	Ratio of Saturation Factors $\times 10^2$	σ_m (mb) $\pm 18\%$
33	334	18.4	32.6	0.444	9.16	77
36	298	24.3	22.2	0.444	9.16	130
40	265	33.2	20.4	0.444	9.16	180
42	252	15.6	25.5	1.27	9.16	180
48	220	1.05	2.60	1.27	6.97	79
54	198	1.0	3.0	1.27	7.01	59
60	180	0.722	2.77	1.27	6.97	42
66	167	0.739	3.29	1.27	6.97	33
72	156	0.485	2.67	1.27	7.19	26
78	148	0.671	5.01	1.27	7.19	18
85	140	0.803	5.91	1.27	7.19	17

Table IX

INDEPENDENT CROSS SECTIONS FOR THE FORMATION OF $^{86}\text{g}_\text{Y}$ FROM ^{88}Sr

Proton Energy (MeV)	Monitor σ (mb)	D_A^0 dis/min $\times 10^{-7}$	D_M^0 dis/min $\times 10^{-7}$	R	Ratio of Saturation Factors	σ (mb) $\pm 20\%$
28.7	422	5.19	39.3	0.444	1.14	28
33	334	37.4	32.6	0.444	1.14	190
36	298	45.7	22.2	0.444	1.14	310
40	265	44.3	20.4	0.444	1.14	290
42	252	18.5	25.5	1.27	1.14	260
48	220	0.878	2.60	1.27	1.14	110
54	198	0.603	3.00	1.27	1.14	58
60	180	0.292	2.77	1.27	1.14	27
66	167	0.416	3.29	1.27	1.14	31
72	156	0.198	2.67	1.27	1.14	17
78	148	0.526	5.01	1.27	1.14	23
85	140	0.575	5.91	1.27	1.14	20

Table X

INDEPENDENT CROSS SECTIONS AND ISOMER RATIOS FOR
THE FORMATION OF NUCLEAR ISOMERS OF ^{86}Y FROM ^{88}Sr

Proton Energy (MeV)	Nuclide		$\sigma (= \sigma_m + \sigma_g)$ (mb)	Isomer Ratio $\frac{\sigma_m}{\sigma_g} (= \frac{\sigma_H}{\sigma_L}) \pm 20\%$
	σ_m (mb) $\pm 18\%$	σ_g (mb) $\pm 20\%$		
28.7	-	28	28	-
33	77	190	270	0.40
36	130	310	440	0.43
40	180	290	470	0.60
42	180	260	440	0.68
48	79	110	190	0.73
54	59	58	120	1.02
60	42	27	69	1.50
66	33	31	64	1.10
72	26	17	43	1.55
78	18	23	41	0.80
85	17	20	37	0.88

Figure 23

EXPERIMENTAL EXCITATION FUNCTIONS FOR $^{88}\text{Sr}(p,3n)^{86m}\text{Y}$,
 $^{88}\text{Sr}(p,3n)^{86g}\text{Y}$ AND $^{88}\text{Sr}(p,3n)^{86m+g}\text{Y}$ REACTIONS

Δ ^{86m}Y - cross section

\square ^{86g}Y - cross section

\circ $^{86m+g}\text{Y}$ - cross section

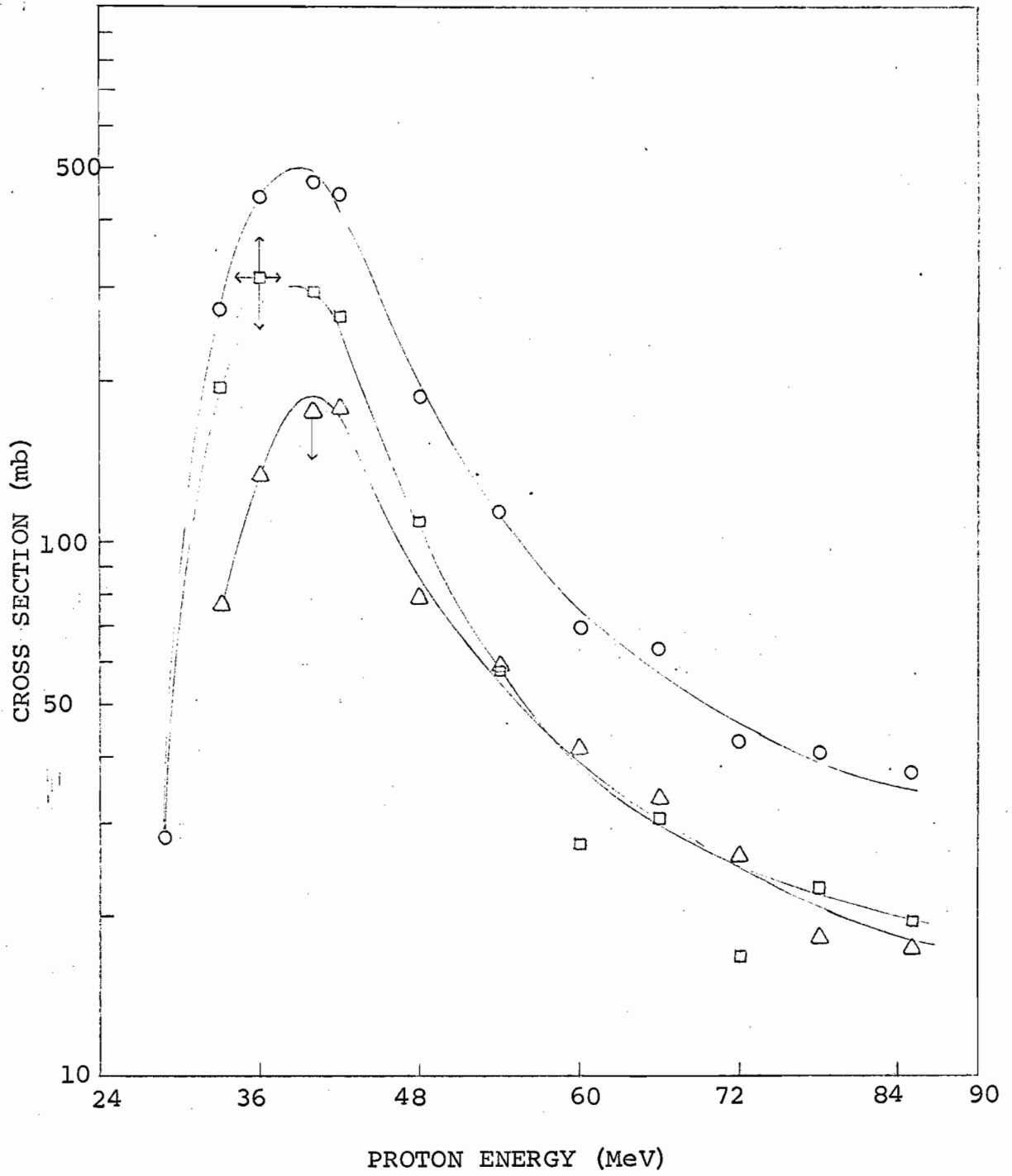


Figure 24

EXPERIMENTAL ISOMER RATIOS $\left(\frac{\sigma_H}{\sigma_L}\right)$ FOR

$^{88}\text{Sr}(p, 3n)^{86\text{m,g}}\text{Y}$ REACTION

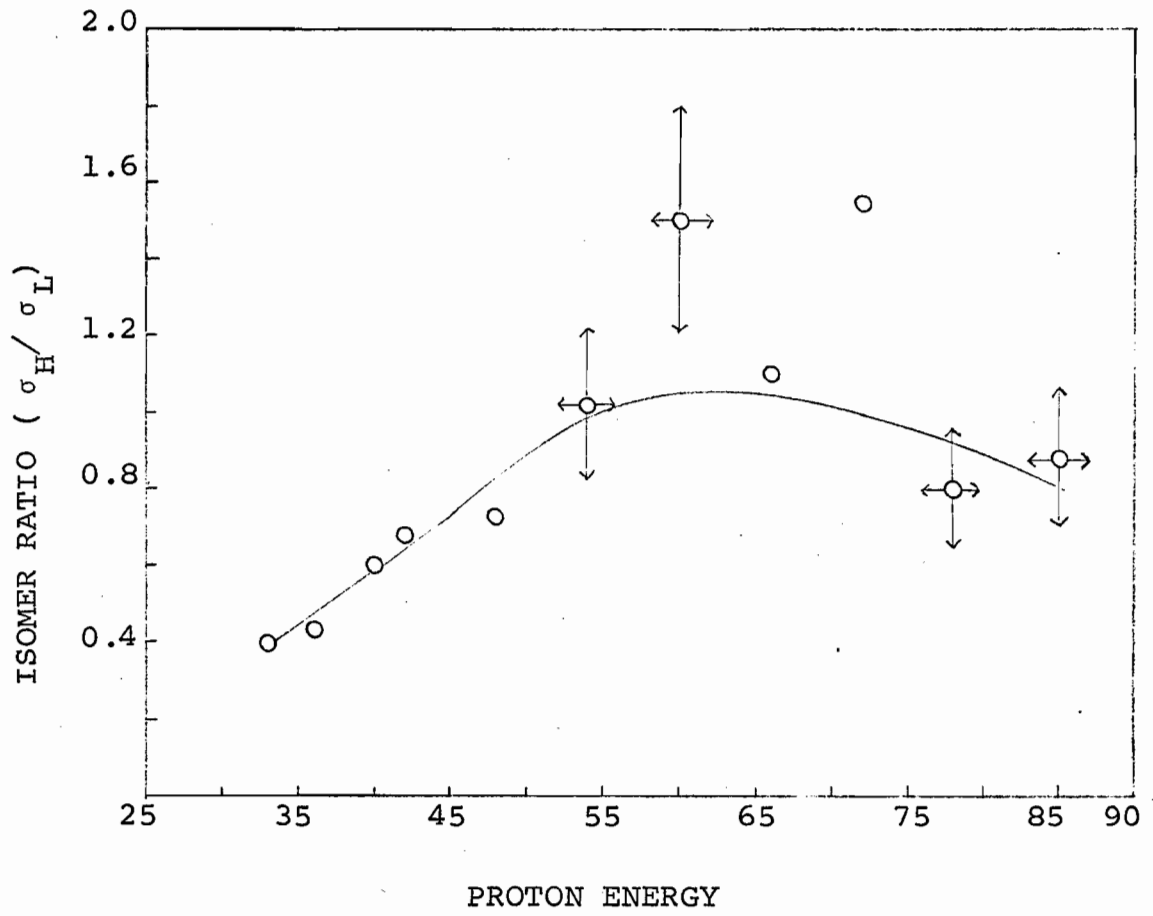


Table XI

INDEPENDENT CROSS SECTIONS FOR THE FORMATION OF ^{85m}Y FROM ^{88}Sr

Proton Energy (MeV)	Monitor σ (mb)	D_A^0 dis/min $\times 10^{-7}$	D_M^0 dis/min $\times 10^{-7}$	R	Ratio of Saturation Factors	σ_m (mb)	σ_m (Average) (mb) $\pm 10\%$
42	252	7.44	25.5	1.27	0.231	21.6	22
45	235	9.52	12.8	1.27	0.216	47.9	48
48 A	220	41.0	13.0	0.444	0.231	71.2	59
48 B	220	2.10	2.60	1.27	0.215	48.5	
54 A	198	60.2	13.3	0.444	0.231	91.9	94
54 B	198	5.36	3.00	1.27	0.215	96.6	
60 A	180	25.2	9.00	0.444	0.231	51.7	53
60 B	180	3.09	2.77	1.27	0.215	54.8	
66 A	167	11.5	12.6	1.27	0.229	44.3	46
66 B	167	3.48	3.29	1.27	0.215	48.2	
72 A	156	9.84	14.8	1.27	0.231	30.4	28
72 B	156	1.63	2.67	1.27	0.216	26.1	
78 A	148	1.70	3.11	1.27	0.231	23.7	23
78 B	148	2.68	5.01	1.27	0.216	21.7	
85 A	140	11.9	28.4	1.27	0.235	17.5	19
85 B	140	3.06	5.91	1.27	0.216	19.9	

Table XII

INDEPENDENT CROSS SECTIONS FOR THE FORMATION OF ^{85}gY FROM ^{88}Sr

Proton Energy (MeV)	Monitor σ (mb)	D_A^0 dis/min $\times 10^{-7}$	D_M^0 dis/min $\times 10^{-7}$	R	Ratio of Saturation Factors	σ_g (mb)	σ_g (Average) (mb) $\pm 10\%$
42	252	0.488	25.5	1.27	0.407	2.5	2.5
45	235	7.44	12.8	1.27	0.396	68.7	69
48 A	220	36.1	13.0	0.444	0.407	110.4	95
48 B	220	1.85	2.60	1.27	0.395	78.5	
54 A	198	51.6	13.3	0.444	0.407	139	140
54 B	198	4.23	3.00	1.27	0.395	140	
60 A	180	27.4	9.00	0.444	0.407	99	91
60 B	180	2.52	2.77	1.27	0.395	82.1	
66 A	167	9.44	12.6	1.27	0.406	64.5	59
66 B	167	2.07	3.29	1.27	0.395	52.7	
72 A	156	6.46	14.8	1.27	0.407	35.2	34
72 B	156	1.14	2.67	1.27	0.396	33.5	
78 A	148	1.10	3.11	1.27	0.407	27.1	27
78 B	148	1.79	5.01	1.27	0.396	26.6	
85 A	140	9.36	28.4	1.27	0.410	24.0	23
85 B	140	1.79	5.91	1.27	0.396	21.3	

Table XIII

INDEPENDENT CROSS SECTIONS AND ISOMER RATIOS FOR
THE FORMATION OF NUCLEAR ISOMERS OF ^{85}Y FROM ^{88}Sr

Proton Energy (MeV)	σ_m (mb) \pm 10%	σ_g (mb) \pm 10%	Nuclide $\sigma (= \sigma_m + \sigma_g)$ (mb)	Isomer Ratio $\frac{\sigma_g}{\sigma_m} (= \frac{\sigma_H}{\sigma_L}) \pm 8\%$
42	22	2.5	25	0.12
45	48	69	120	1.43
48	59	95	150	1.52
54	94	140	230	1.49
60	53	91	140	1.70
66	46	59	100	1.27
72	28	34	62	1.22
78	23	27	50	1.18
85	19	23	42	1.21

Figure 25

EXPERIMENTAL EXCITATION FUNCTIONS FOR $^{88}\text{Sr}(p,4n)^{85\text{m}}\text{Y}$,
 $^{88}\text{Sr}(p,4n)^{85\text{g}}\text{Y}$ AND $^{88}\text{Sr}(p,4n)^{85\text{m}+\text{g}}\text{Y}$ REACTIONS

- Δ $^{85\text{m}}\text{Y}$ - cross section
- \square $^{85\text{g}}\text{Y}$ - cross section
- \circ $^{85\text{m}+\text{g}}\text{Y}$ - cross section

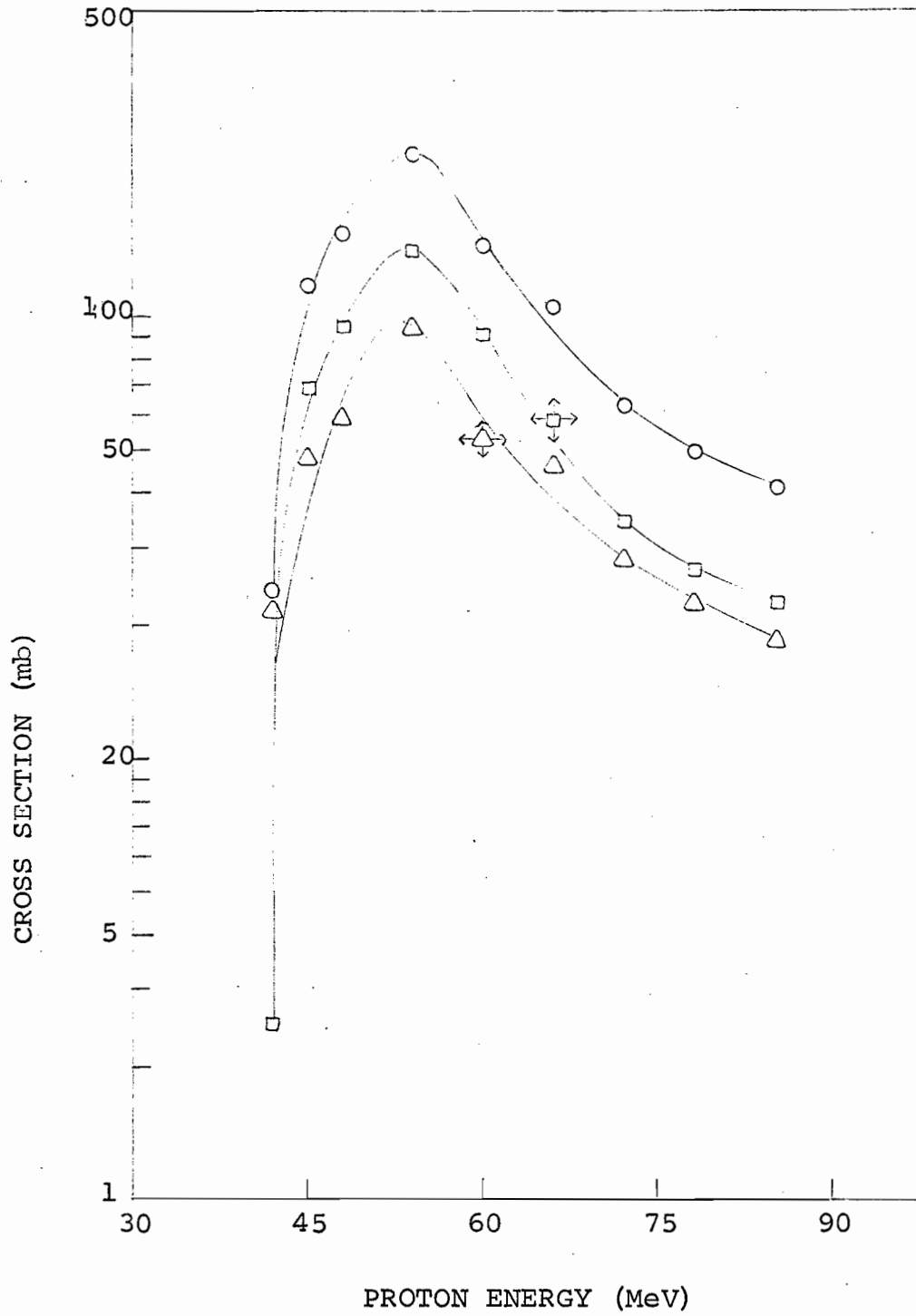


Figure 26

EXPERIMENTAL ISOMER RATIOS $\left(\frac{\sigma_H}{\sigma_L}\right)$ FOR

$^{88}\text{Sr}(p,4n)^{85m,8\gamma}$ REACTION

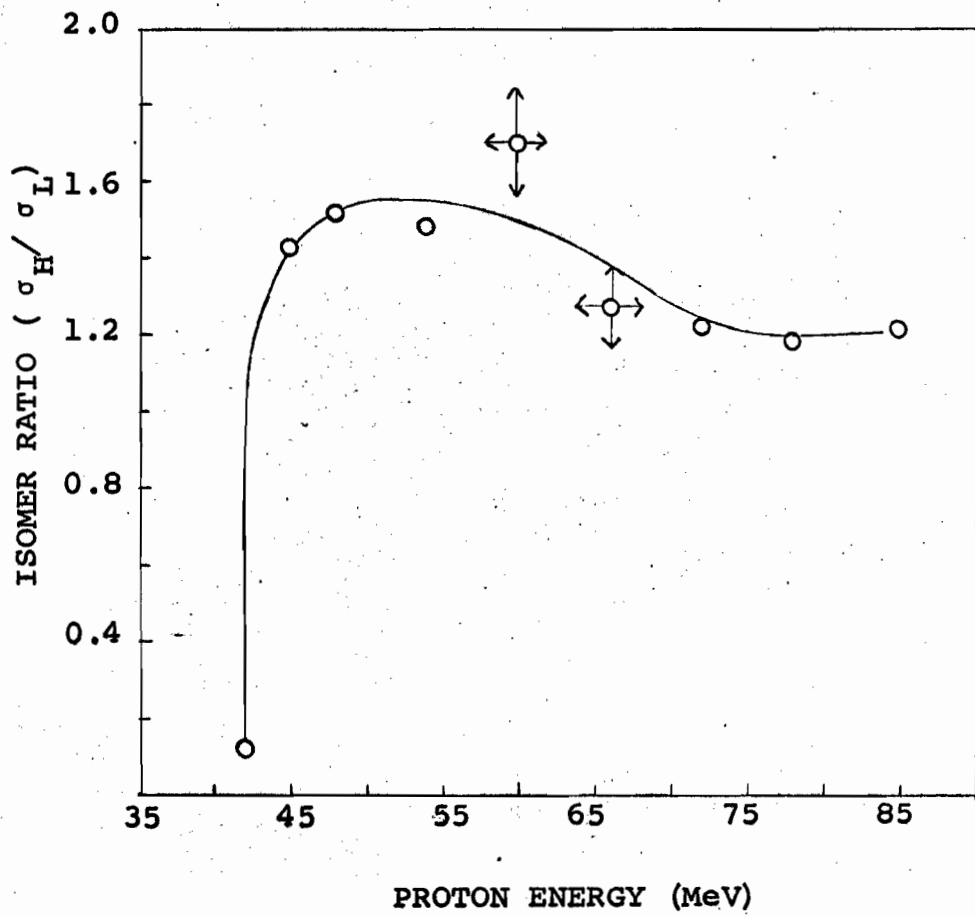


Table XIV

INDEPENDENT CROSS SECTIONS FOR THE FORMATION OF ^{84}Y FROM ^{88}Sr

Proton Energy (MeV)	Monitor σ (mb)	D_A^0 dis/min $\times 10^{-7}$	D_M^0 dis/min $\times 10^{-7}$	R	Ratio of Saturation Factors $\times 10^2$	Nuclide σ (mb) $\pm 18\%$
60	180	2.30	2.77	1.27	5.87	11
66	167	6.39	3.29	1.27	5.87	24
69	161	17.8	8.10	1.27	5.74	26
72	156	5.28	2.67	1.27	6.09	24
78	148	8.01	5.01	1.27	6.09	18
85	140	6.49	5.91	1.27	6.09	12

Figure 27

EXPERIMENTAL EXCITATION FUNCTION FOR

$^{88}\text{Sr}(p,5n)^{84}\text{Y}$ REACTION

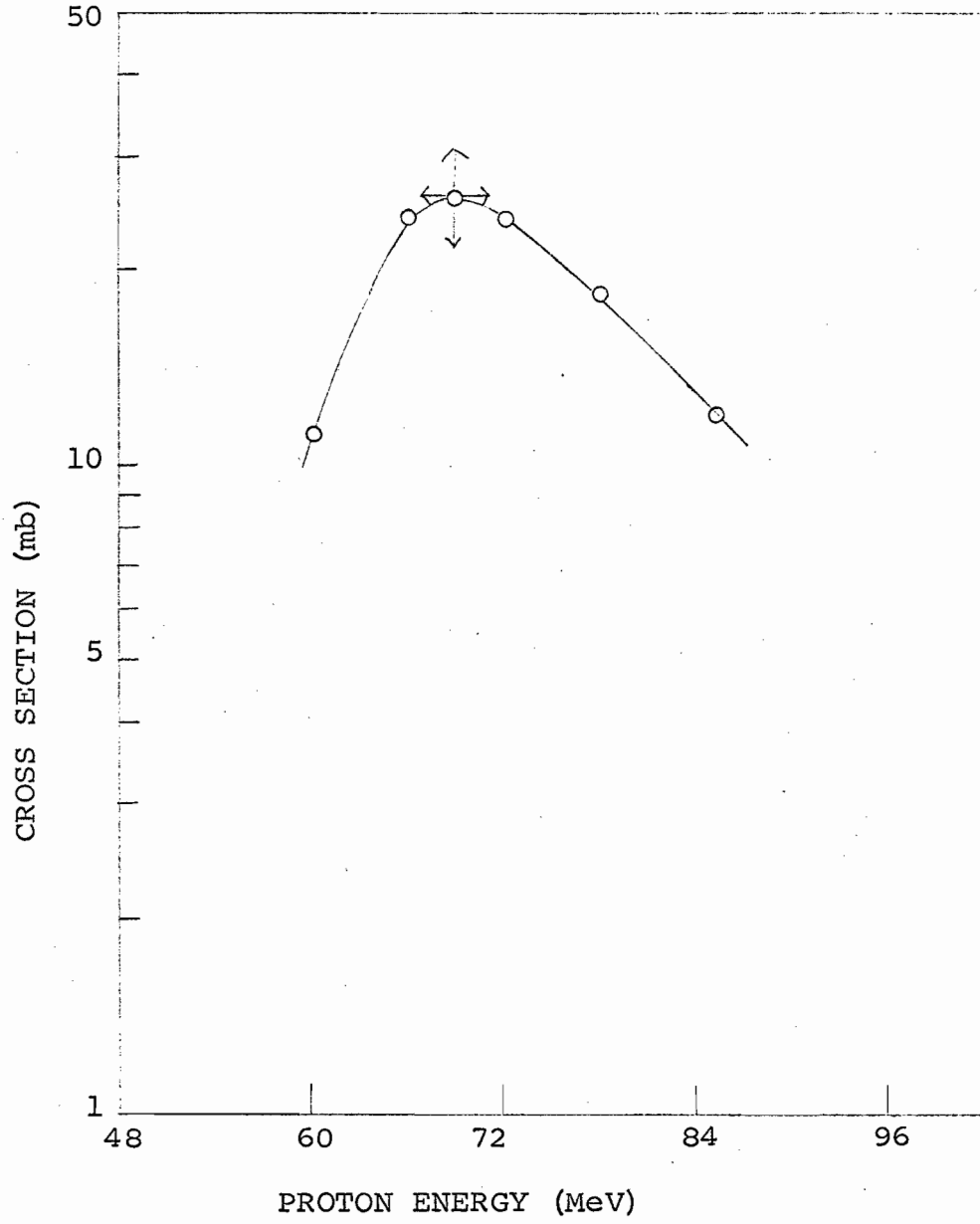


Table XV

DISINTEGRATION RATES OF INDEPENDENTLY PRODUCED ^{85m}Sr AND ^{85g}Sr

Proton Energy (MeV)	$t_s - t_o = t$ (min)	D_{85m}^s dis/min x 10^{-7}	D_{85m}^o dis/min x 10^{-7}	D_{85g}^s dis/min x 10^{-5}	D_{85g}^o dis/min x 10^{-5}
42	63	7.98	7.43	2.82	1.75
48	87	43.4	46.7	25.3	15.7
54	121	45.5	32.3	42.1	29.4
60	112	23.9	27.2	21.8	14.9
66	92	12.5	14.7	10.2	7.44
72	67	14.0	16.7	10.9	8.47
78	53	3.29	4.09	2.18	1.68
85	55	25.1	32.2	17.5	13.4

t_s = time at which the daughter activity was separated from the parent.

t_o = time at which the bombardment ended.

D_{85m}^s = disintegration rate of the metastable state at the time of separation, i.e. t_s .

D_{85g}^s = disintegration rate of the ground state at the time of separation.

D_{85m}^o = disintegration rate of the metastable state for the time at the end of bombardment (t_o) after making appropriate corrections. (Appendix)

D_{85g}^o = disintegration rate of the ground state for the time at the end of bombardment after making the appropriate corrections. (Appendix)

Table XVI

INDEPENDENT CROSS SECTIONS FOR THE FORMATION OF $^{85\text{m}}\text{Sr}$ FROM ^{88}Sr

Proton Energy (MeV)	Monitor σ (mb)	D_A^0 dis/min $\times 10^{-7}$	D_M^0 dis/min $\times 10^{-7}$	R	Ratio of Saturation Factors	σ_m (mb) $\pm 20\%$
42	252	7.43	25.5	1.27	0.118	11
48	220	46.7	13.0	0.444	0.118	41
54	198	32.3	13.3	0.444	0.118	25
60	180	27.2	9.00	0.444	0.118	28
66	167	14.7	12.6	1.27	0.115	28
72	156	16.7	14.8	1.27	0.118	26
78	148	4.09	3.11	1.27	0.118	29
85	140	32.2	28.4	1.27	0.122	25

Table XVII

INDEPENDENT CROSS SECTIONS FOR THE FORMATION OF ^{85}gSr FROM ^{88}Sr

Proton Energy (MeV)	Monitor σ (mb)	D_A^o dis/min $\times 10^{-5}$	D_M^o dis/min $\times 10^{-7}$	R	Ratio of Saturation Factors $\times 10^{-2}$	σ_g (mb) $\pm 12\%$
42	252	1.75	25.5	1.27	1.19	26
48	220	15.7	13.0	0.444	1.19	140
54	198	29.4	13.3	0.444	1.19	230
60	180	14.9	9.00	0.444	1.19	160
66	167	7.44	12.6	1.27	1.19	150
72	156	8.47	14.8	1.27	1.19	130
78	148	1.68	3.11	1.27	1.19	120
85	140	13.4	28.4	1.27	1.18	100

Table XVIII

INDEPENDENT CROSS SECTIONS AND ISOMER RATIOS FOR
THE FORMATION OF NUCLEAR ISOMERS OF ^{85}Sr FROM ^{88}Sr

Proton Energy (MeV)	σ_m (mb) \pm 20%	σ_g (mb) \pm 12%	Nuclide $\sigma (= \sigma_m + \sigma_g)$ (mb)	Isomer Ratio $\frac{\sigma_g}{\sigma_m} (= \frac{\sigma_H}{\sigma_L}) \pm$ 22%
42	11	26	37	2.4
48	41	140	180	3.4
54	25	230	260	9.1
60	28	160	190	5.6
66	28	150	180	5.2
72	26	130	160	5.1
78	29	120	150	4.2
85	25	100	130	4.0

Figure 28

EXPERIMENTAL EXCITATION FUNCTIONS FOR $^{88}\text{Sr}(p,p3n)^{85\text{m}}\text{Sr}$,
 $^{88}\text{Sr}(p,p3n)^{85\text{g}}\text{Sr}$ AND $^{88}\text{Sr}(p,p3n)^{85\text{m}+\text{g}}\text{Sr}$ REACTIONS

Δ $^{85\text{m}}\text{Sr}$ - cross section

\square $^{85\text{g}}\text{Sr}$ - cross section

\circ $^{85\text{m}+\text{g}}\text{Sr}$ - cross section

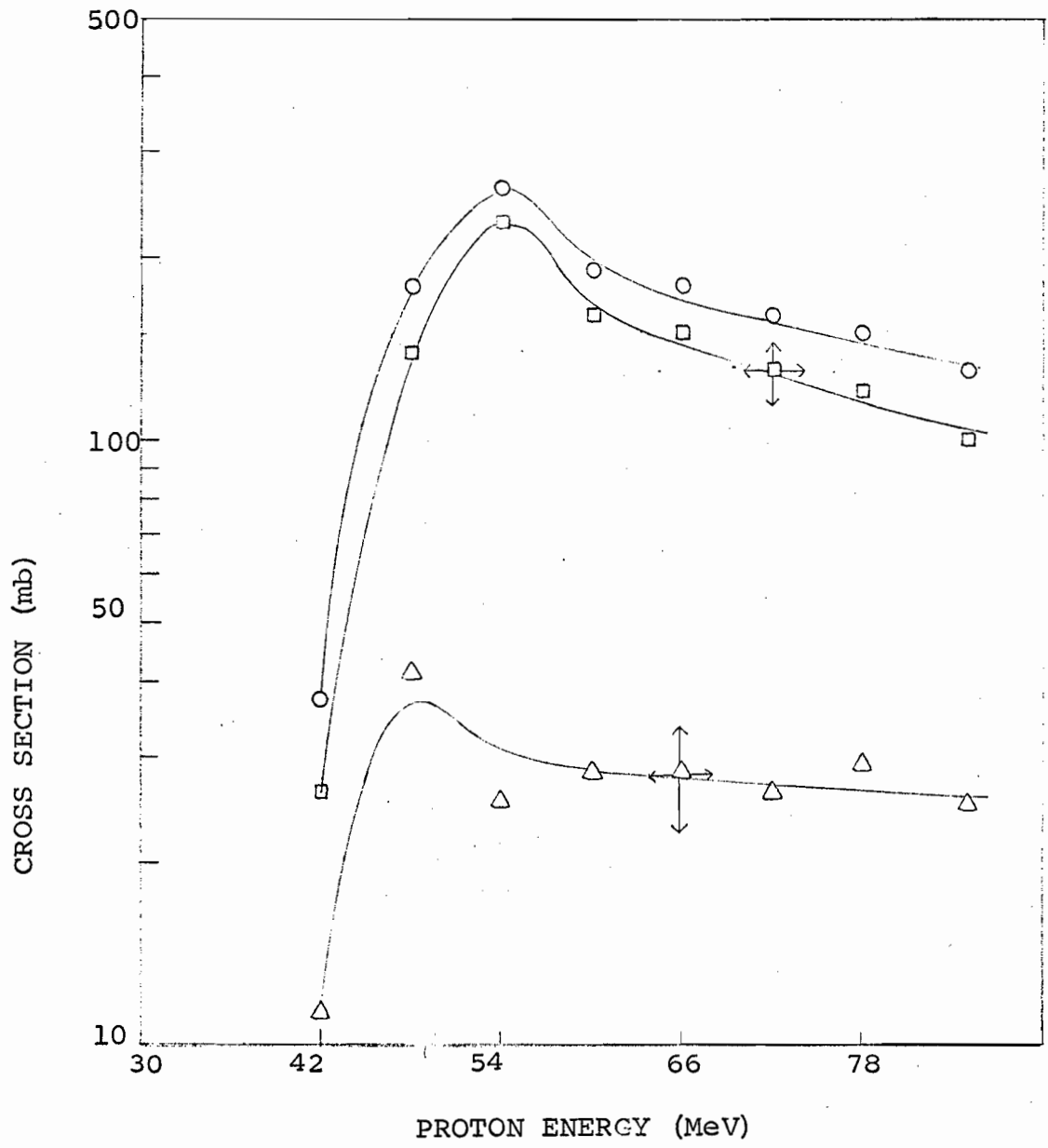


Figure 29

EXPERIMENTAL ISOMER RATIOS FOR

$^{88}\text{Sr}(p,p3n)^{85\text{m},g}\text{Sr}$ REACTION

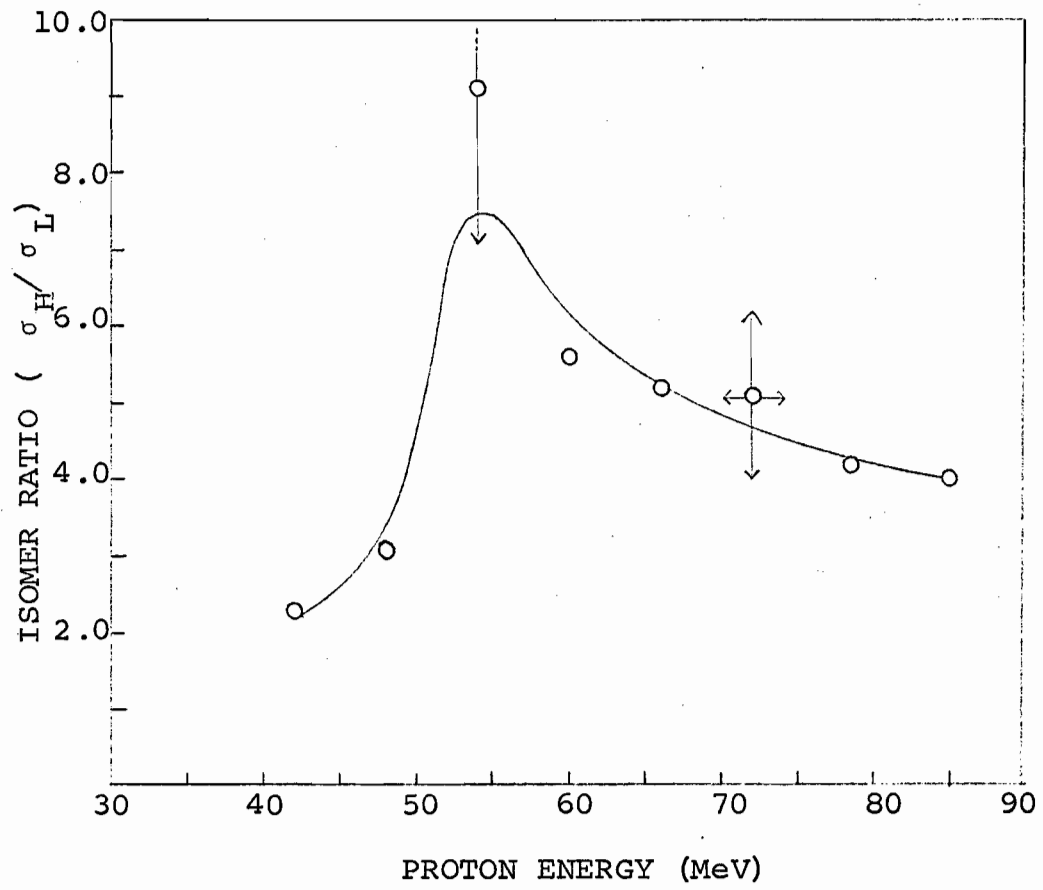


Table XIX

INDEPENDENT CROSS SECTIONS FOR THE FORMATION OF ^{86}Rb FROM ^{88}Sr

Proton Energy (MeV)	Monitor σ (mb)	D_A^o dis/min $\times 10^{-5}$	D_M^o dis/min $\times 10^{-7}$	R	Ratio of Saturation Factors	Nuclide σ (mb) $\pm 10\%$
33	334	0.716	32.6	0.444	34.1	1.1
36	298	1.14	22.2	0.444	34.1	2.3
40	265	2.75	20.4	0.444	34.1	5.4
42	252	2.06	25.5	1.27	34.1	8.8
48	220	5.62	13.0	0.444	34.1	14
54	198	7.14	13.3	0.444	34.1	16
60	180	9.79	9.00	0.444	34.1	30
66	167	5.56	12.6	1.27	34.2	32
72	156	6.50	14.8	1.27	34.1	30
78	148	1.20	3.11	1.27	34.1	25
85	140	10.2	28.4	1.27	34.0	22

Figure 30

EXPERIMENTAL EXCITATION FUNCTION FOR

$^{88}\text{Sr}(p, 2pn)^{86}\text{Rb}$ REACTION

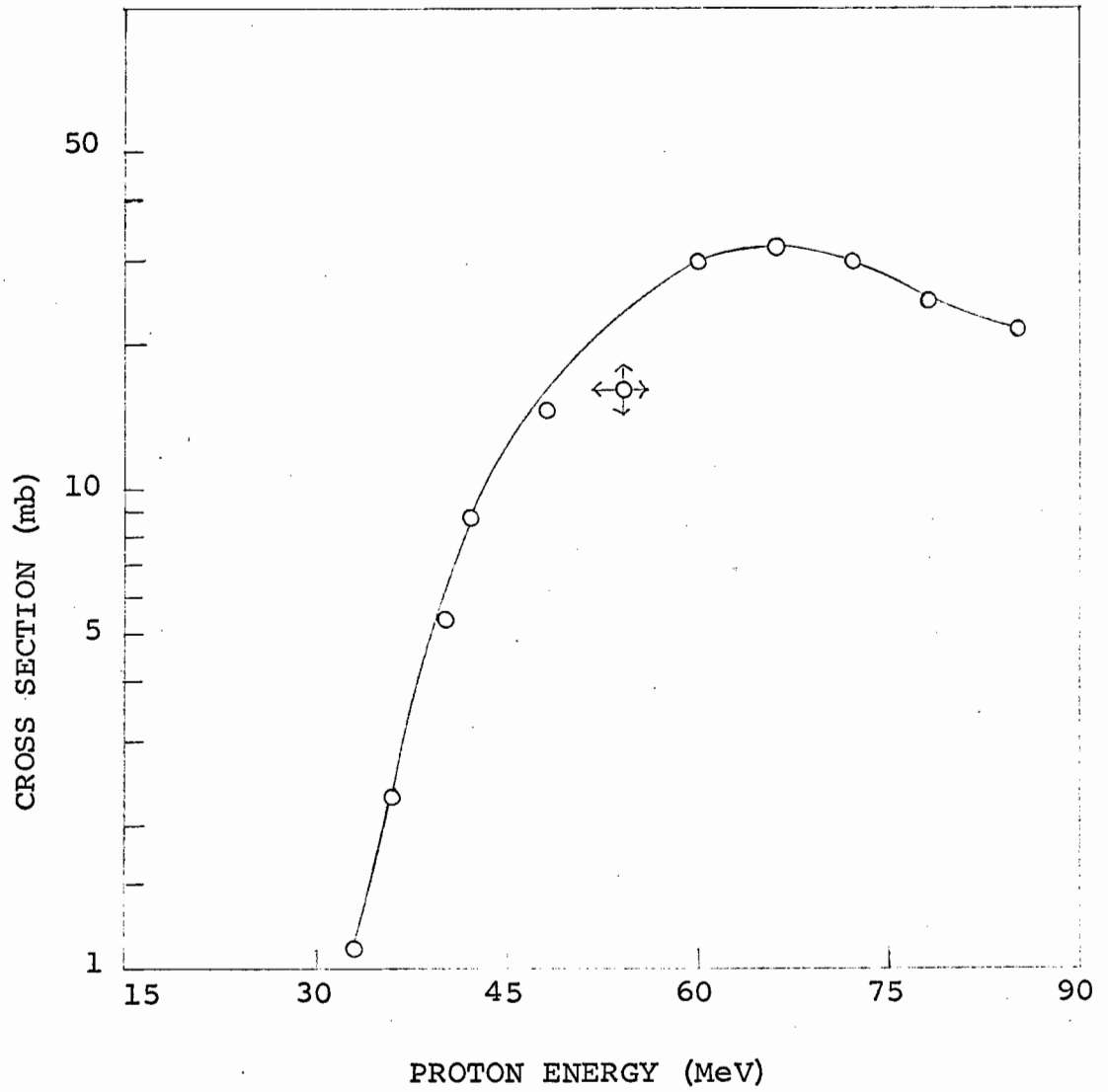


Table XX

INDEPENDENT CROSS SECTIONS FOR THE FORMATION OF ^{84}Rb FROM ^{88}Sr

Proton Energy (MeV)	Monitor σ (mb)	D_A^o dis/min $\times 10^{-5}$	D_M^o dis/min $\times 10^{-7}$	R	Ratio of Saturation Factors	Nuclide σ (mb) $\pm 11\%$
24.7	488	0.682	29.9	0.444	60.2	3
28.7	422	4.85	39.3	0.444	60.2	14
33	334	9.88	32.6	0.444	60.2	27
36	298	8.78	22.2	0.444	60.2	32
40	265	7.02	20.4	0.444	60.2	24
42	252	2.32	25.5	1.27	60.2	18
48	220	2.66	13.0	0.444	60.2	12
54	198	2.38	13.3	0.444	60.2	10
60	180	4.50	9.00	0.444	60.2	24
66	167	4.10	12.6	1.27	60.4	42
72	156	6.11	14.8	1.27	60.2	49
78	148	1.25	3.11	1.27	60.2	46
85	140	11.4	28.4	1.27	60.0	43

Figure 31

EXPERIMENTAL EXCITATION FUNCTION FOR

$^{88}\text{Sr}(p,\alpha n)^{84}\text{Rb} + ^{88}\text{Sr}(p,2p3n)^{84}\text{Rb}$ REACTIONS

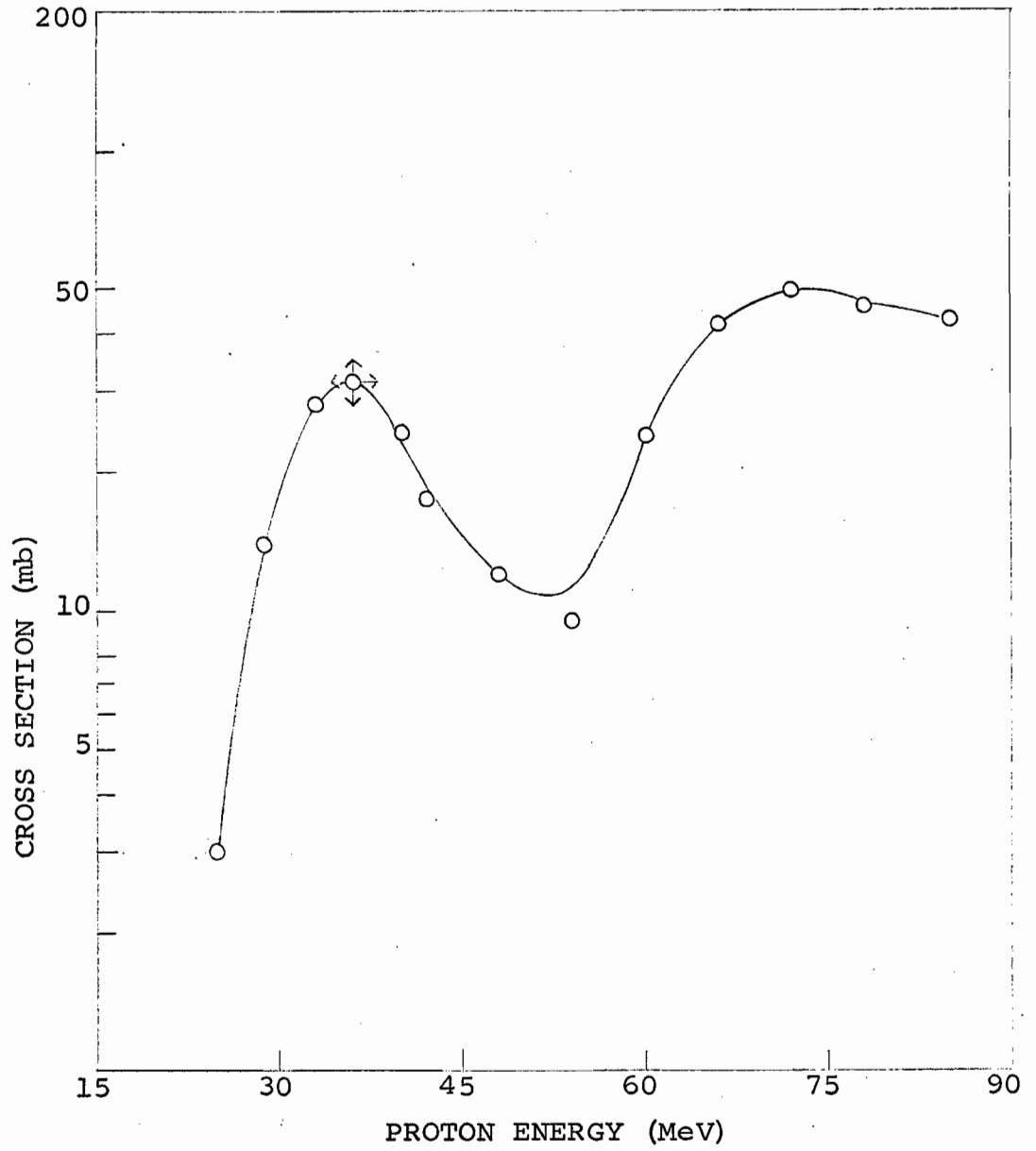


Table XXI

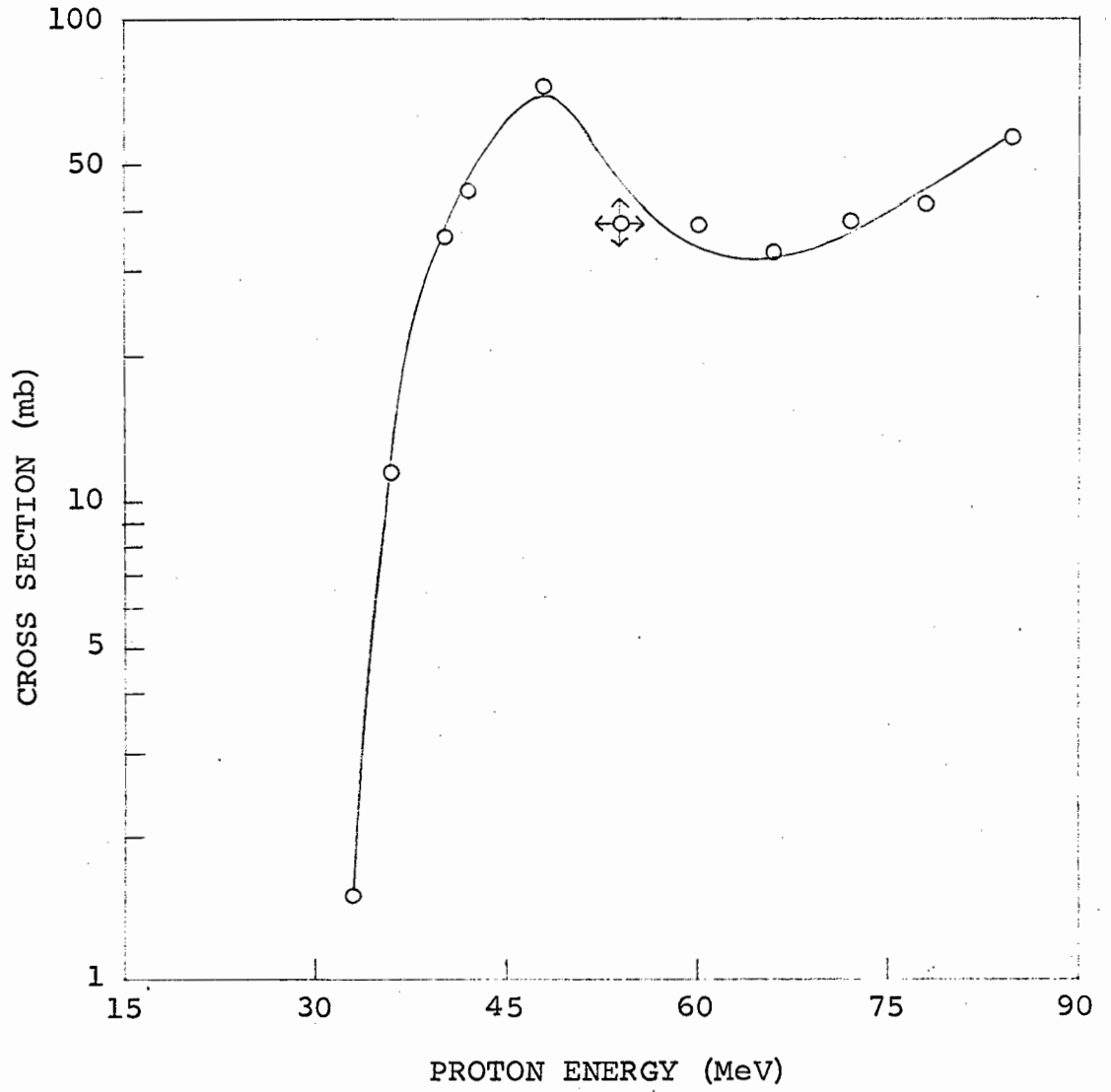
INDEPENDENT CROSS SECTIONS FOR THE FORMATION OF ^{83}Rb FROM ^{88}Sr

Proton Energy (MeV)	Monitor σ (mb)	D_A^o dis/min $\times 10^{-4}$	D_M^o dis/min $\times 10^{-7}$	R	Ratio of Saturation Factors $\times 10^{-2}$	Nuclide σ (mb) $\pm 11\%$
33	334	2.16	32.6	0.444	1.51	1.5
36	298	12.7	22.2	0.444	1.51	11
40	265	40.6	20.4	0.444	1.51	35
42	252	23.2	25.5	1.27	1.51	44
48	220	64.4	13.0	0.444	1.51	73
54	198	37.9	13.3	0.444	1.51	38
60	180	27.9	9.00	0.444	1.51	37
66	167	12.9	12.6	1.27	1.52	33
72	156	18.8	14.8	1.27	1.51	38
78	148	4.51	3.11	1.27	1.51	41
85	140	60.1	28.4	1.27	1.51	57

Figure 32

EXPERIMENTAL EXCITATION FUNCTION FOR

$^{88}\text{Sr}(p, \alpha 2n)^{83}\text{Rb} + ^{88}\text{Sr}(p, 2p4n)^{83}\text{Rb}$ REACTIONS



V. CALCULATIONS AND DISCUSSION

V-1. QUALITATIVE CONSIDERATIONS (ISOMER RATIOS)

The experimental isomer ratios of (p,2n), (p,3n), (p,4n) and (p,p3n) reactions, for the ranges of energies studied in this work, have been presented in Figs. 22, 24, 26 and 29 respectively. The decay schemes, shown in the preceding chapter, indicated the spins of the relevant states. In all cases, an isomer ratio referred to the ratio of cross sections of the higher spin to that of the lower spin isomeric state.

Figure 33 shows a plot of excitation energy versus isomer ratio for the nuclear isomers of ^{87}Y produced in different reactions. The isomer ratios for the reactions of $^{85}\text{Rb}(\alpha,2n)$ and $^{87}\text{Sr}(d,2n)$ [Fig. 33(a) and (b) respectively] were studied by Vandenbosch et al.⁽⁶²⁾ whereas those for $^{88}\text{Sr}(p,2n)$ reaction were obtained in this work. In all cases, the same compound nucleus, ^{89}Y , was produced and the reactions were studied in the same range of excitation energy. The excitation energy of the compound nucleus, E_c , was obtained from the relation

$$E_c = E_{cm} + Q \quad (30)$$

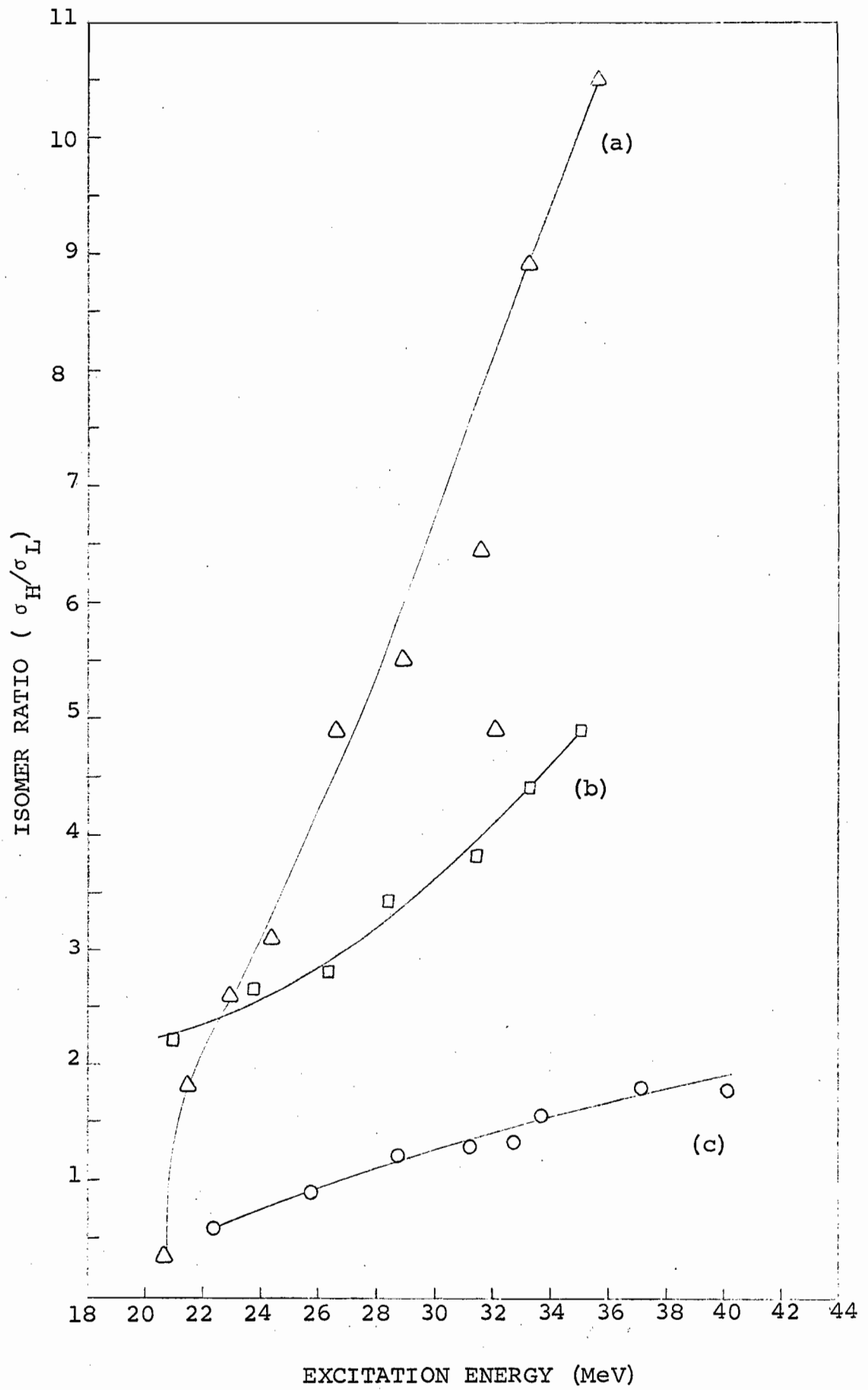
where E_{cm} is the kinetic energy of the projectile in the centre-of-mass system and Q is the 'Q' value for the formation of the compound nucleus. The latter were calculated from the mass tables of Wapstra et al.⁽¹¹²⁾

Figure 33

EXPERIMENTAL ISOMER RATIOS ($\frac{\sigma_H}{\sigma_L}$) AS A FUNCTION OF
EXCITATION ENERGY FOR THE REACTIONS

- (a) $^{85}\text{Rb}(\alpha, 2n)^{87m, g}\text{Y}$ }
(b) $^{87}\text{Sr}(d, 2n)^{87m, g}\text{Y}$ } Ref. 62
(c) $^{88}\text{Sr}(p, 2n)^{87m, g}\text{Y}$ -- Present work

The same compound nucleus (^{89}Y) was produced
in all the reactions



The effect of angular momentum on the formation cross sections of nuclear isomers is distinctly evident from the figure. The alpha particles can bring a larger amount of angular momentum into the compound nucleus system than deuterons which in turn could carry in a larger amount than protons at the same excitation energy. This is reflected in the progressively increasing slopes of the curves showing proton, deuteron, and alpha particle reactions. The higher isomer ratios for deuteron and alpha particle reactions to those of protons are also due to the fact that ^{88}Sr is an even-even nucleus and thus has a spin of zero for its ground state, while ^{87}Sr and ^{85}Rb have spins of $\frac{9}{2}$ and $\frac{5}{2}$ respectively for their ground states. A quantitative calculation for the theoretical estimation of isomer ratios for the $^{88}\text{Sr}(p,2n)$ reaction and its comparison with experimental results is presented in the next section.

The competition between neutron and gamma-ray emission near the threshold of a reaction was mentioned in Chapter I (Section I-3). While the first neutron may be emitted with a reasonable kinetic energy (because of higher excitation energy of the residual nucleus after the emission of the first neutron) the second neutron will be emitted with very low energy, even slightly above the threshold. The unavailability of high spin states at low excitation energies thus forces the competition between neutron and gamma rays, which will be reflected in isomer ratios in that the isomer ratios will be lower near the threshold of the concerned reaction while they will be higher

near the threshold of another reaction [e.g. (p,3n) reaction].

The finite energy difference between the ground and metastable states could also be important near the threshold of the reaction. The energies of certain emitted pairs of neutrons in a (p,2n) reaction may be such that it might be possible to populate only the ground state isomer. The isomer ratio in such a case then will also be low. The considerations of this and the preceding paragraph should therefore be important for the (p,2n) reaction at 15 MeV proton energy.

The isomer ratio for the $^{88}\text{Sr}(p,3n)^{86g,m}\text{Y}$ reaction (Fig. 24) increases with energy, becomes steady at about 50 MeV proton energy and then exhibits a decreasing trend with the increase of energy. The initial increase beyond the peak of the excitation function curve (~ 40 MeV) is probably explainable on the following grounds. The spins [Fig. 16(a)] of the metastable and ground states for this isomeric pair are 8 and 4 respectively while the relevant intermediate level (which is important for the final spin distribution) has a spin of 5. Thus at the end of the de-excitation stage, the states with angular momentum values of 6 or less should be expected to contribute to the formation of the ground state while states with angular momentum values of 7 or greater should decay to the metastable state. The spin distributions of the compound nuclei formed at 39 and 45 MeV have been computed using square-well transmission coefficients (Fig. 34) and the average angular momentum (root mean square values as computed by the program of Hofner et al.⁽¹¹⁴⁾).

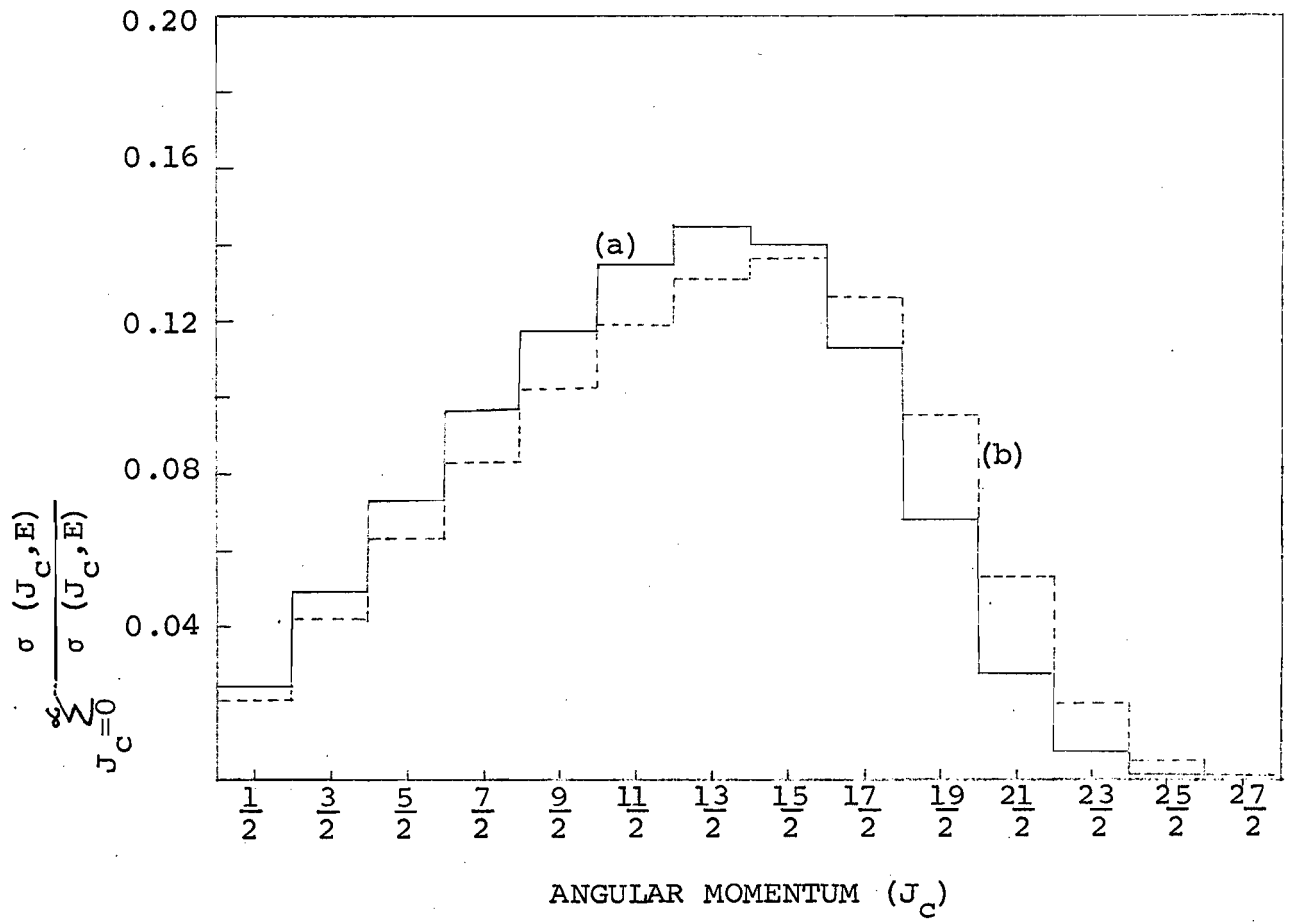
Figure 34

ANGULAR MOMENTUM DISTRIBUTION OF COMPOUND NUCLEI
PRODUCED BY PROTONS OF DIFFERENT ENERGY

(a) 39 MeV (full line)

(b) 45 MeV (dashed line)

Square-well transmission coefficients with $r_0 = 1.5 F$
were used in computing the spin distributions



at these energies corresponds to about 6.4 and 6.9 \hbar respectively. Following the emission of neutrons and the gamma-ray cascade, the spin distributions shift to lower values as is evident in Fig. 41. It thus seems not very improbable that the isomer ratio should be less than unity even at the peak of the excitation function curve and continue to increase further till direct interaction mechanism becomes a dominant feature.

The isomer ratios for the (p,4n) and (p,p3n) reactions increase with increasing energy and then show a decreasing trend at excitation energies higher than the peak values for the corresponding excitation function curves. The decrease at higher energies is usually attributed to the direct interaction according to which only a part of angular momentum and energy is transferred to the excited system, left behind after the initial knock-on phase of the nuclear reaction.

V-2. ISOMER RATIO CALCULATION FOR $^{88}\text{Sr}(p,2n)^{87\text{m}}\text{Sr}$ REACTION

The calculations were performed using a formalism due to Vandenbosch and Huizenga^(57,119) and based on the assumptions of the statistical model. They have also coded a computer program⁽¹¹⁴⁾ (Fortran IBM-704) which, with slight changes, was also used by the author.

In their formalism, Vandenbosch and Huizenga have neglected the effect of competition on spin distribution (and consequently isomer ratios) due to de-excitation modes other than those of interest. Dudey and Sugihara⁽¹¹⁵⁾ and Need⁽¹¹⁶⁾ have

investigated this problem. Following these investigations, Vandenbosch et al.⁽⁶²⁾ investigated the effect of competing channels in the particular case of the $^{87}\text{Sr}(d,2n)^{87\text{m}}\text{Sr}$ reaction. They found that the results were affected very insignificantly. This is of particular interest to us as the compound nucleus in this case and in our investigations is the same and should be expected to have a similar negligible effect.

The theory of the calculation procedure is described in the cited references^(57,113,114), and a description of the required parameters as used in the computations is described below.

V-3. PARAMETERS NECESSARY FOR THE CALCULATION

V-3.1. The Spin Cutoff Parameter, δ

The importance of this parameter has been well emphasized in Chapter I (I-7.2). In performing isomer ratio calculations, this parameter must be supplied at each stage of de-excitation of the excited nucleus. Various models, as used to determine its values, are described below.

V-3.1.(a) Fermi Gas Model: The equation of state for this model is given⁽⁶⁷⁾ by

$$U = at^2 - t \quad (31)$$

where $U = E =$ excitation energy as measured from the normal ground state,

and $t =$ thermodynamic temperature.

Also, the spin cutoff parameter ' δ ' is given by

$$S^2 = ct = \frac{It}{\hbar^2} \quad (32)$$

where 'c' is a parameter which could be interpreted in terms of moment of inertia 'I' as in equation (32) or be described by the relation⁽⁴⁾

$$c = \langle m^2 \rangle g \quad (33)$$

where 'm' is the magnetic quantum number and the quantity $\langle m^2 \rangle$ is the mean square value of 'm' for single particle states close to the Fermi level. The single particle level density 'g' is related to the level density parameter 'a' by the relation⁽⁶⁷⁾

$$a = \frac{\pi^2}{6} g \quad (34)$$

For nucleons moving independently in an infinite square-well potential, the moment of inertia^(4,55) becomes equal to the rigid body moment of inertia 'I_r' and is given by

$$I_r = \frac{2}{5} M_n R^2 A \quad (12)$$

where M_n = mass of the nucleon,
 R = radius of the nucleus, and
 A = mass number.

Combining equations (31), (32) and (12), one obtains

$$S^2 = \frac{2}{5} \frac{M_n R A^2}{\hbar^2} \cdot \frac{1 + \sqrt{1 + 4a U}}{2a} \quad (35)$$

in which only the positive root of 't' was selected, as negative temperatures are not permitted.

Equation (35) was used to construct a plot (Figs.35-38) of 'S' versus excitation energy (E) for a simple Fermi gas

model. The radius parameter value of 1.2×10^{-13} cm was used for evaluating the nuclear radius (R).

The moment of inertia which corresponds to a fraction of rigid body value is normally required to fit the calculated isomer ratios to those obtained experimentally. The spin cutoff parameter values corresponding to a fractional rigid-body moment of inertia were also obtained from the same graph.

It has been pointed out before (Section I-7.2) that this reduction of moment of inertia from its rigid body value is usually attributed to pairing interaction. For a Fermi gas model this is taken into account by measuring the excitation energy from the mass surface of an odd-odd nuclide. Pairing corrections for the odd-even and even-even nuclides are then applied as follows.

$$\begin{aligned} U &= E && \text{for odd-odd nucleus} \\ U &= E - \Delta && \text{for odd-even nucleus} \\ \text{and } U &= E - 2\Delta && \text{for even-even nucleus} \end{aligned} \tag{36}$$

where Δ is the pairing energy and is taken⁽¹¹⁷⁾ to be $\Delta = 1.35$ MeV for mass numbers 87 and 88.

Equation (35) was again used for constructing the plot of \mathcal{S} versus excitation energy except that U is taken from (36) for the nuclide concerned. Such a plot, however, leaves \mathcal{S} undefined for excitation energies of up to Δ MeV for odd mass nuclides (even-even nuclides were not involved). The value of $\mathcal{S}^2 = \langle m^2 \rangle$ was taken for this range as pointed out by Vandenbosch et al.⁽⁶²⁾ The constructed plots for this model

(called 'shifted' Fermi gas model after Vonach et al.⁽⁶⁹⁾) for various level density parameter values and mass numbers 87 and 88 are shown in Figs. 35 to 40.

V-3.1.(b) Independent Pairing Model: In this model, the effective excitation energy is measured from a fictitious reference surface which lies even below the even-even mass surface, and is obtained from the following expressions.^(62,66,67)

$$\begin{aligned}
 U' &= E + \frac{1}{3}g \Delta^2 && \text{for even-even nuclides} \\
 U' &= E + \frac{1}{3}g \Delta^2 + \Delta && \text{for odd-even nuclides} \\
 \text{and } U' &= E + \frac{1}{3}g \Delta^2 + 2\Delta && \text{for odd-odd nuclides}
 \end{aligned}
 \tag{37}$$

The spin cutoff parameter is obtained from

$$\mathcal{S}^2 = c't = ct e^{-0.874 \Delta/t}
 \tag{38}$$

while the thermodynamic temperature 't' is obtained from the equation of state

$$U' = at^2 - t
 \tag{39}$$

The plots of \mathcal{S} versus E, as obtained from equation (38), are shown in Figs. 35-40 for various level density parameter values and mass numbers 87 and 88. We have followed the suggestion of Vandenbosch et al.⁽⁶²⁾ in not adding $\langle m^2 \rangle$ or $\langle 2m^2 \rangle$ to the values of \mathcal{S}^2 as obtained from (38) to odd-mass or odd-odd nuclides respectively as suggested by Lang and LeCouteur⁽⁶⁶⁾ but have taken \mathcal{S}^2 to be equal to $\langle m^2 \rangle$ for excitation energies of less than Δ MeV in the case of odd mass nuclides.

V-3.1.(c) Super Conductor Model: The strength of pairing interaction in this model is reflected in a quantity called 'correlation parameter' (θ_0). Although Lang⁽⁶⁷⁾ assumed it to be approximately equal to the pairing energy Δ , Vonach et al.⁽⁶⁹⁾ suggest a better approximation of

$$\theta_0 = 1.3 \Delta \quad (40)$$

The calculations reported in this work are also based on this value. The ground state of the superconductor lies below the Fermi level by a condensation energy, C_0 , and is obtained from the equation

$$C_0 = 0.47 at_c^2 \quad (41)$$

where t_c is the critical temperature and is related to the correlation parameter by the expression

$$t_c = 0.57 \theta_0 \quad (42)$$

The critical energy above which the superconductor behaves like a simple Fermi gas whose ground state is shifted upwards by the condensation energy ' C_0 ' is given by

$$U_c = at_c^2 + C_0 = 1.47 at_c^2 \quad (43)$$

The spin cutoff parameter is given by the relation

$$S^2 = ct A(U) \quad (44)$$

where $A(U)$ is an integral arising out of saddle-point integration.

Vonach et al.⁽⁶⁹⁾ have tabulated its values as a function of the ratio of thermodynamic temperature to critical temperature.

The procedure followed in constructing the plot of spin cutoff parameter versus excitation energy as obtained from (44) was as follows. The critical temperature was evaluated from equation (42) making use of (40) and known pairing energy; and was used in determining U_c from (43). A table of $\frac{U}{2at_c^2}$ was made for assumed values of 'a' while the excitation energy, U, was varied at a step of 1 MeV. The corresponding values of 't' and A(U) were noted from the table of Vonach et al.⁽⁶⁹⁾ for each calculated value of $\frac{U}{2at_c^2}$. The spin cutoff factor was thus obtainable from these values of 't' and A(U), using $c = \frac{I}{h^2}$. As the formalism mentioned in the preceding paragraph is true for an even-even ground state, the effective excitation energies (U) were derived by adding Δ or 2Δ to E_c for the odd mass or odd-odd nuclides respectively. The constructed plots of \mathcal{S} versus E for this model, for various values of 'a' and mass numbers 87 and 88, are shown in Figs. 35 to 38.

V-3.2. Average Kinetic Energies of Evaporated Neutrons

The energy distribution of neutrons evaporated from an excited nucleus is expected to be of the form⁽¹²²⁾

$$N(\epsilon_n) \propto \epsilon_n \exp(-\epsilon_n/T) \quad (45)$$

where $N(\epsilon_n)$ is the relative number of neutrons of kinetic energy ϵ_n ; T is the nuclear temperature of the residual nucleus and is linked to the excitation energy of the residual nucleus by the relation⁽⁶⁷⁾

$$E = aT^2 - 4T \quad (46)$$

Figure 35

VARIATION OF SPIN CUTOFF PARAMETER WITH
EXCITATION ENERGY FOR VARIOUS MODELS,
A = 88 (ODD-ODD) AND $a = \frac{A}{8}$ (11 MeV⁻¹)

(The excitation energy was measured
from the normal ground state)

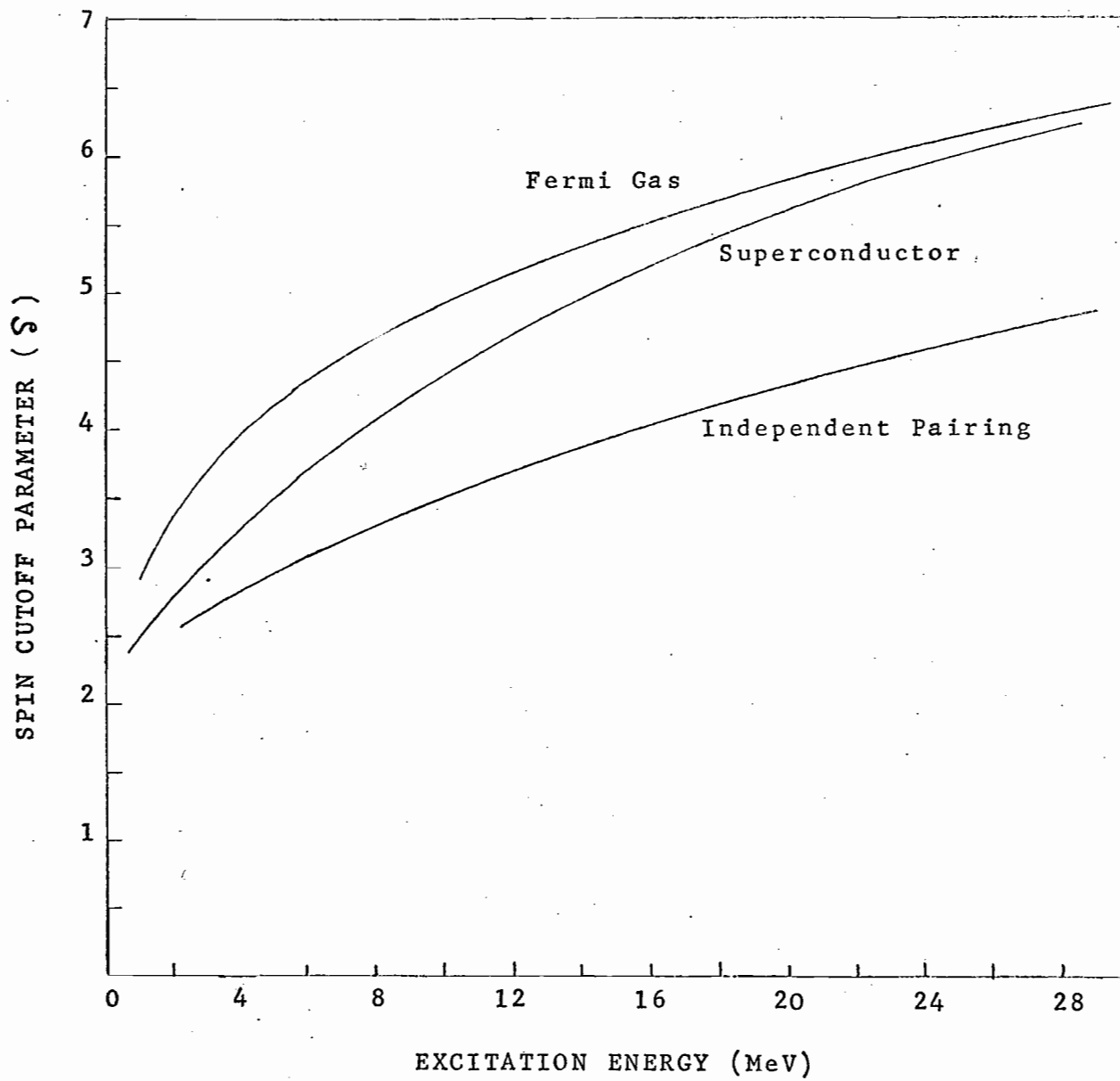


Figure 36

VARIATION OF SPIN CUTOFF PARAMETER WITH
EXCITATION ENERGY FOR VARIOUS MODELS,
 $A = 88$ (ODD-ODD) AND $a = \frac{A}{5.5}$ (16 MeV^{-1})

(The excitation energy was measured
from the normal ground state)

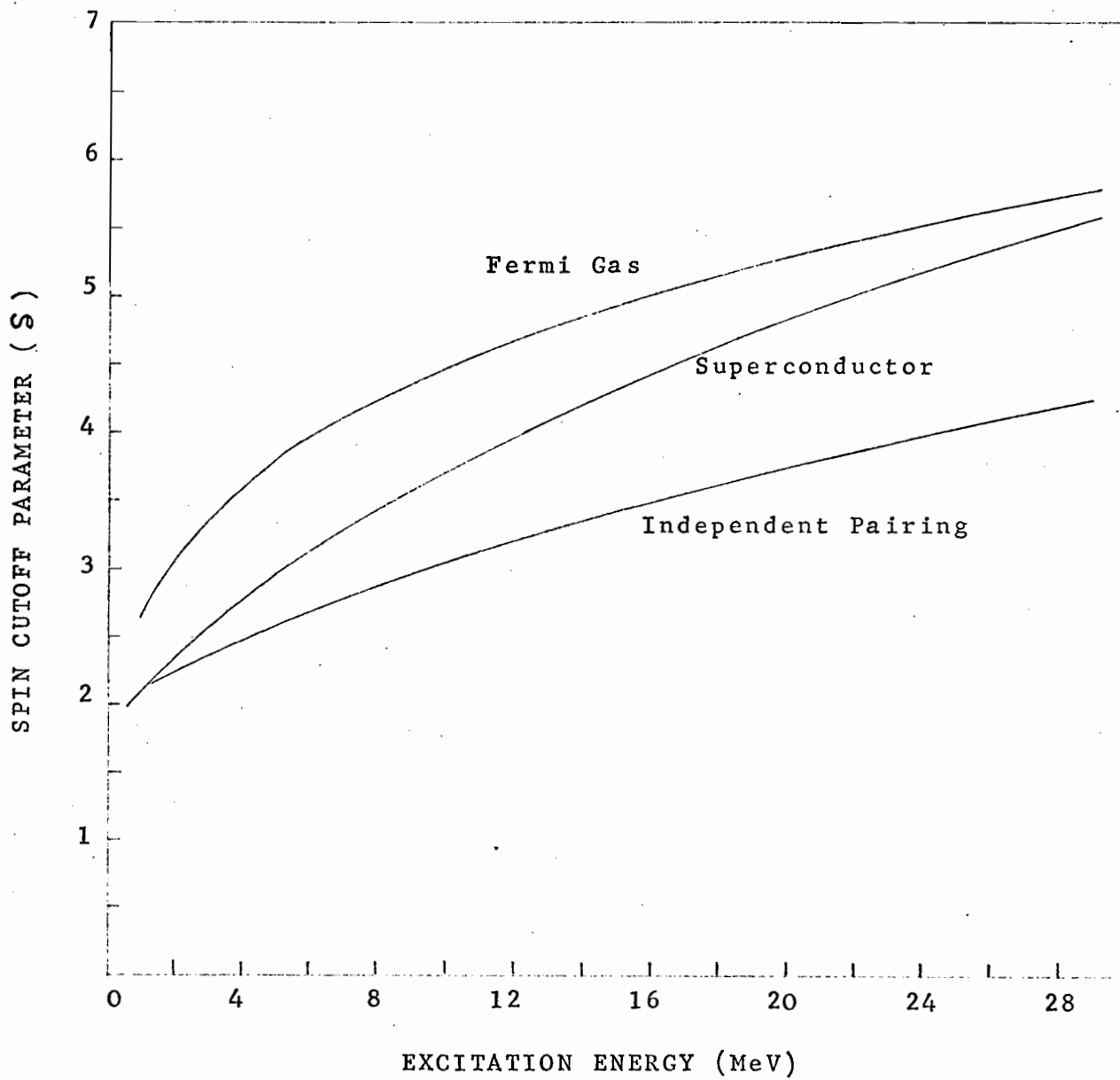


Figure 37

VARIATION OF SPIN CUTOFF PARAMETER WITH
EXCITATION ENERGY FOR VARIOUS MODELS,

$A = 88$ (ODD-ODD) AND $a = \frac{A}{4}$ (22 MeV^{-1})

(The excitation energy was measured
from the normal ground state)

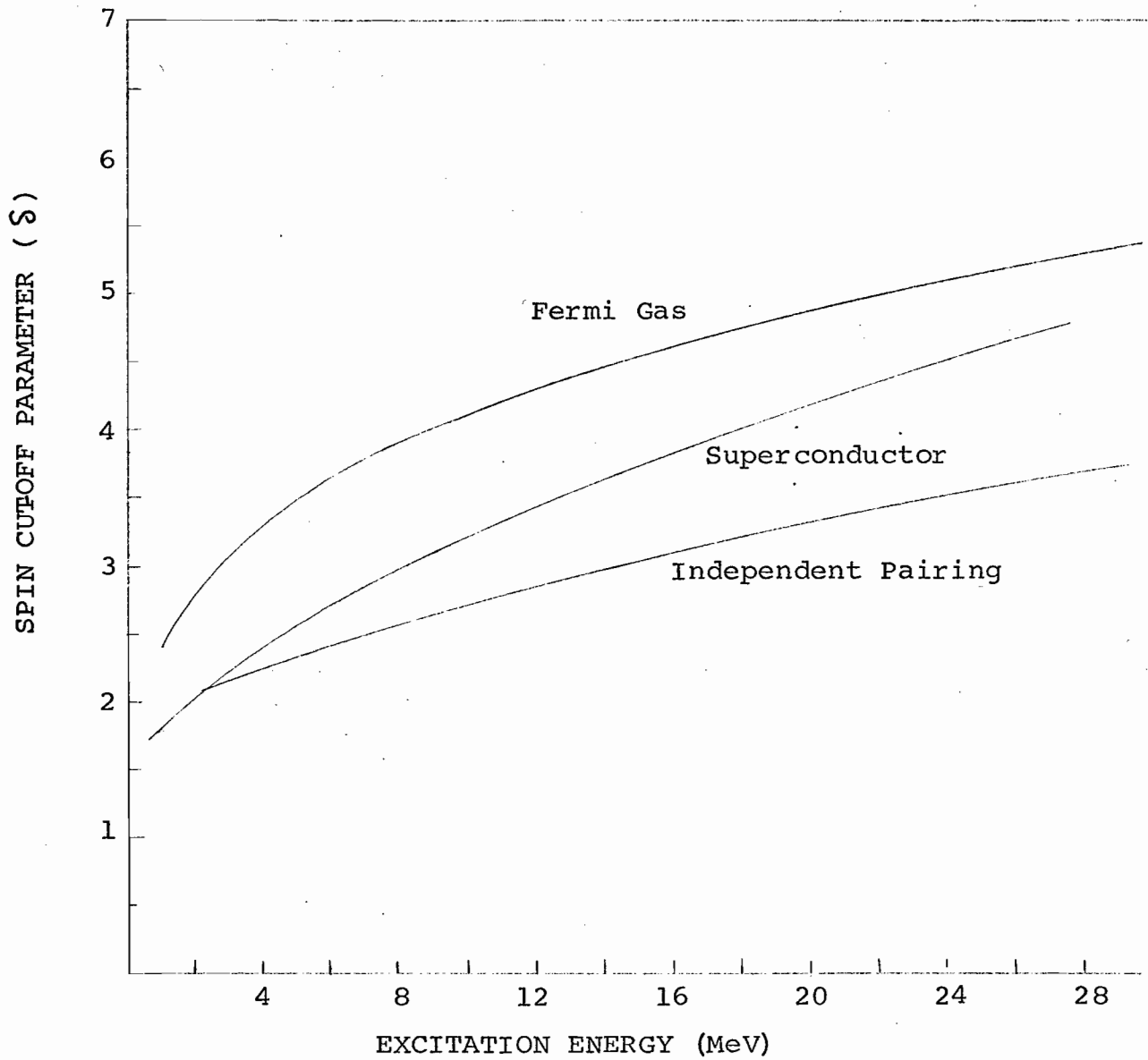


Figure 38

VARIATION OF SPIN CUTOFF PARAMETER WITH
EXCITATION ENERGY FOR VARIOUS MODELS,
A = 87 (ODD-EVEN) AND $a = \frac{A}{8}$ (11 MeV⁻¹)

(The excitation energy was measured
from the normal ground state)

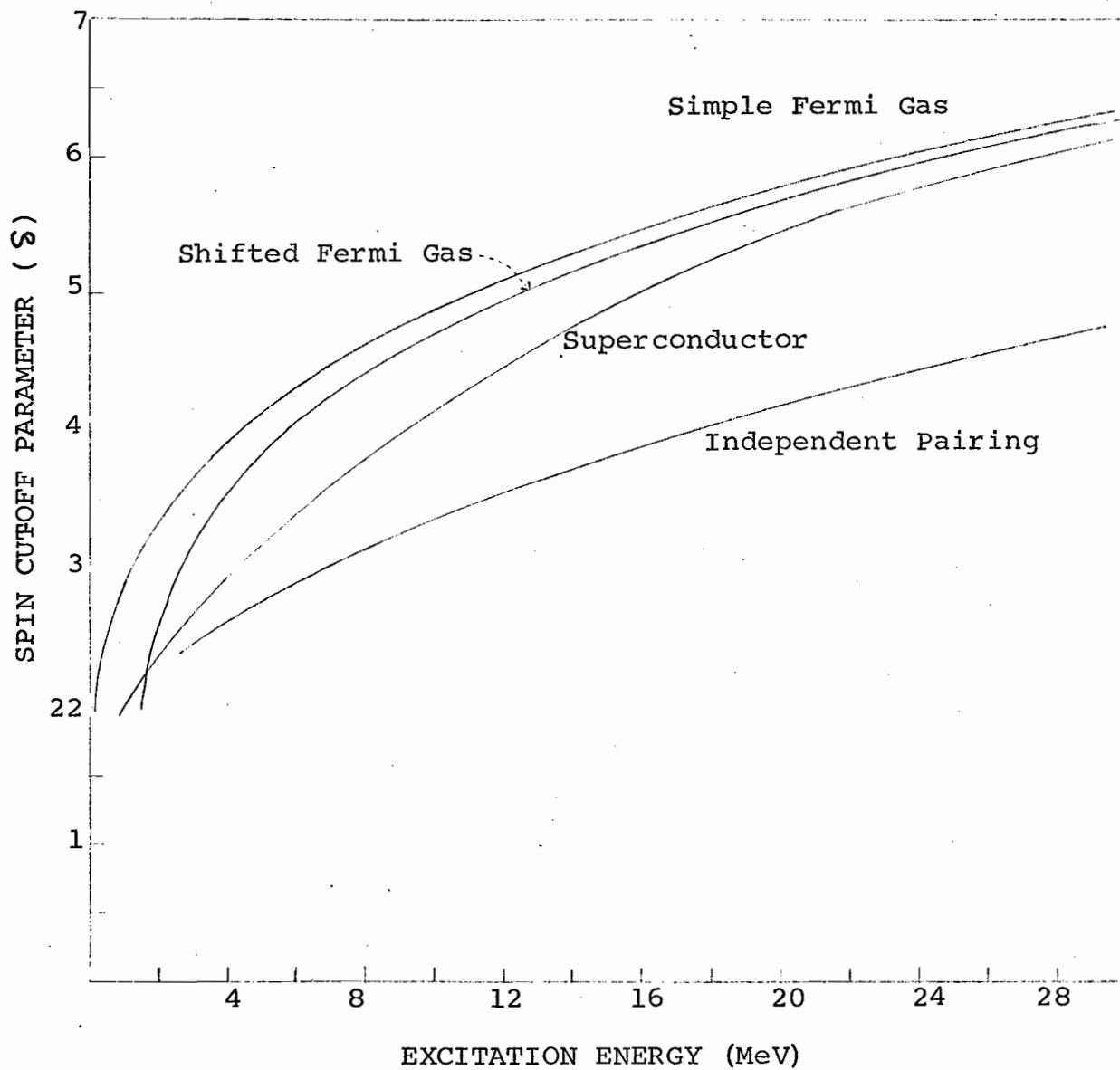


Figure 39

VARIATION OF SPIN CUTOFF PARAMETER WITH
EXCITATION ENERGY FOR VARIOUS MODELS,
A = 87 (ODD-EVEN) AND $a = \frac{A}{5.5}$ (16 MeV⁻¹)

(The excitation energy was measured
from the normal ground state)

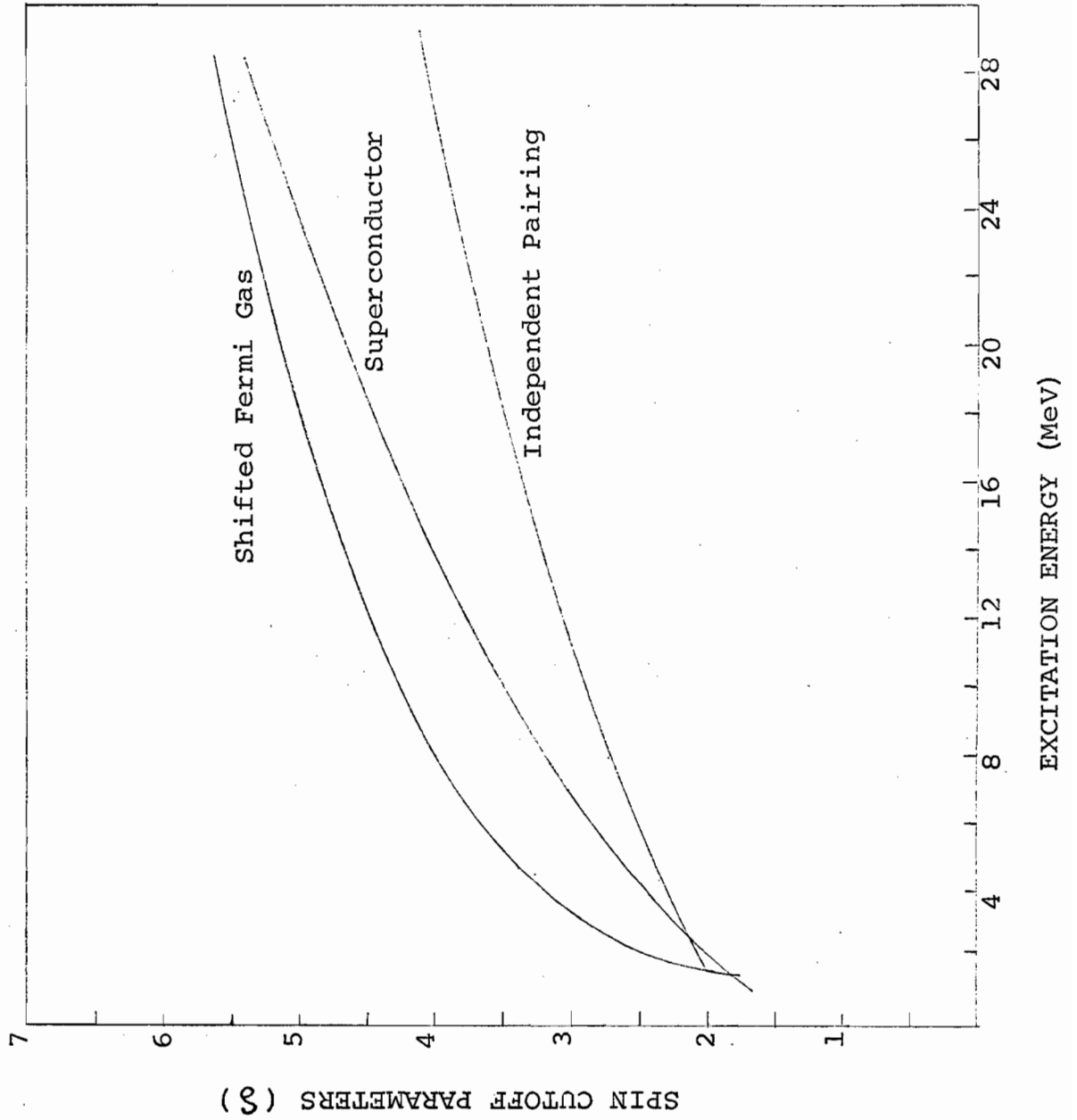
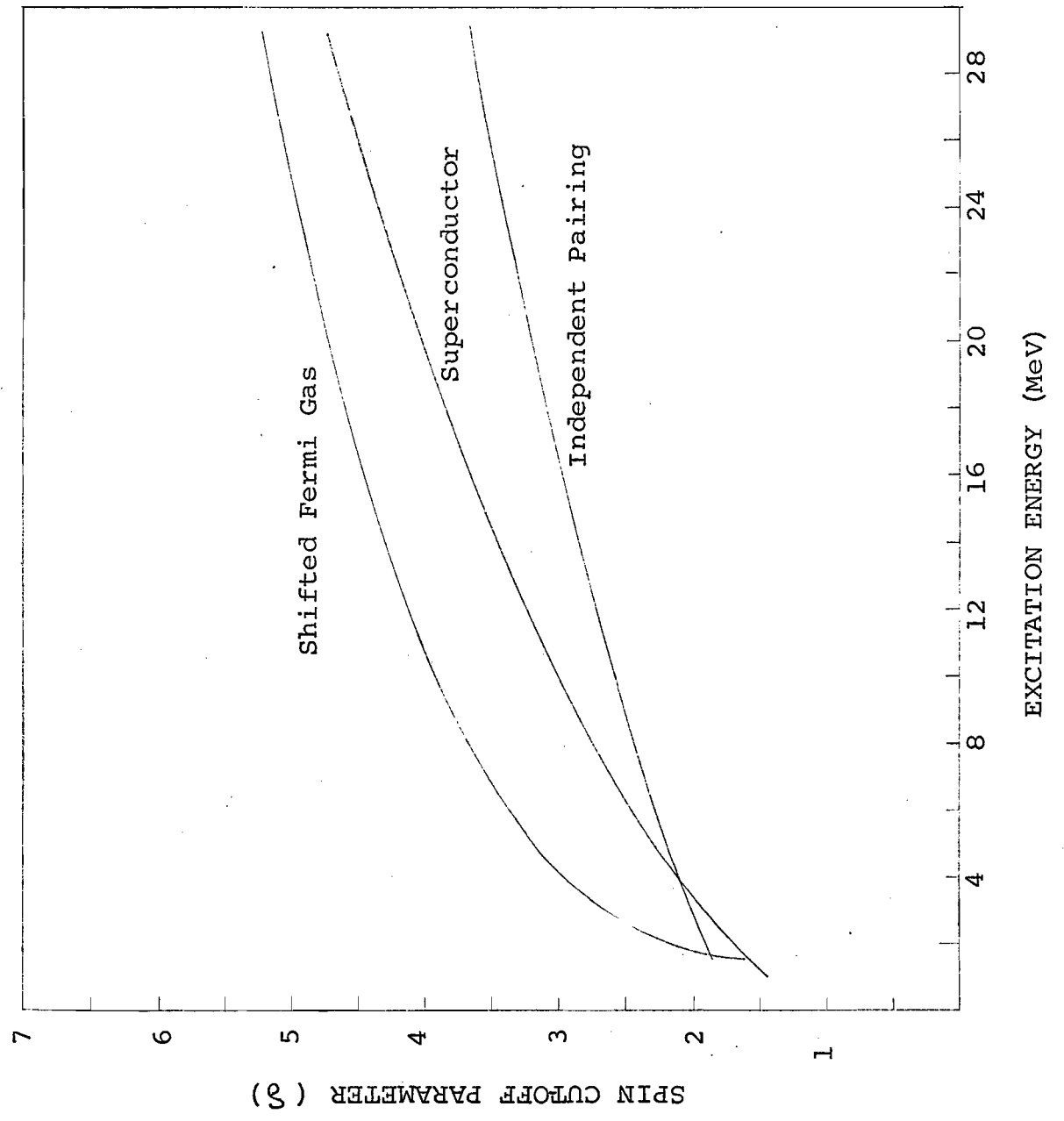


Figure 40

VARIATION OF SPIN CUTOFF PARAMETER WITH
EXCITATION ENERGY FOR VARIOUS MODELS,

$A = 87$ (ODD-EVEN) AND $a = \frac{A}{4}$ (22 MeV^{-1})

(The excitation energy was measured
from the normal ground state)



where 'a' is the familiar level density parameter.

Bishop^(60,119) has shown that the energy spectrum of neutrons represented by (45) could be approximated by assuming that the neutrons are emitted with an average energy of (2T); the temperature being obtained from the average excitation energy of the residual nucleus. His results also showed that the calculated isomer ratios are rather insensitive to small changes in the neutron energy.

The average energy of the neutrons was estimated as follows. The excitation energy of the compound nucleus, 'E_c', is given by equation (30), i.e.

$$E_c = E_{cm} + Q \quad (30)$$

The average excitation energy of the residual nucleus (E_r) is obtained by

$$E_r = E_c - B_n - 2T - \Delta_p \quad (47)$$

where B_n = binding energy of the 'outgoing' neutron,
 2T = average kinetic energy of the evaporated neutron, and
 Δ_p = pairing energy correction (as discussed in Fermi model sub-section of the last section).

For the calculations of average kinetic energies of neutrons, the pairing correction was applied only in the context of the Fermi gas model. Substituting (47) in (46), one gets

$$E_r = E_c - B_n - 2T - \Delta_p = aT^2 - 4T$$

or

$$aT^2 - 2T - (E_c - B_n - \Delta_p) = 0 \quad (48)$$

from which 'T' could be obtained as

$$T = \frac{1 + \sqrt{1 + (E_c - B_n - \Delta_p)a}}{a} \quad (49)$$

A positive root of T was again selected as negative temperatures are not allowed.

Nuclear temperatures calculated from equation (49) for various values of 'a' were compared with the temperatures obtained from inelastic neutron scattering data as plotted by Vonach et al. (69) (at appropriate excitation energies for the residual nuclei). A level density parameter, which gave good agreement with inelastic scattering data, was selected. The average kinetic energies of neutrons calculated with this value of 'a' were used in the calculations of isomer ratios by all models. It may be noted that the excitation energy

$$= E_c - B_n - 2T$$

was used in place of E_c to repeat the calculations for the evaporation of the second neutron.

V-3.3. Multipolarity and Number of Gamma Rays Emitted

The experimental evidence to decide multipolarity of gamma rays emitted in the final phase of the de-excitation stage is very meagre. Independent particle model calculations of Strutinski et al. (120) show that neutron capture gamma rays should exhibit a broad spectrum peaking between 2 and 3 MeV for

dipole emission; in agreement with experimental results. Mollenauer⁽¹²¹⁾ finds that for charged-particle reactions induced by ^4He and ^{12}C ions (i.e. involving high angular momenta) gamma rays consist predominantly of quadrupole radiation. Vandenbosch et al.⁽⁶²⁾ interpret Mollenauer's results in terms of decay of states of high angular momenta which were 'forced' to emit quadrupole radiation in order to get rid of their high angular momenta. In our work, the average angular momentum of the compound nucleus when formed with protons of energy 33 MeV is about 6 \hbar compared to 20 - 38 \hbar (for carbon ion reactions) according to Mollenauer. Some quadrupole radiation which could be expected from the high spin end of the distribution would not be important for isomer ratio calculations, as those states would have populated the high spin isomer.⁽⁶²⁾

The calculations reported here are therefore based on the assumption that gamma rays consist of dipole transitions. The empirical formula suggested by Vonach et al.⁽⁶⁹⁾

$$E_{\gamma} = 4 \left[\left(\frac{E}{a} - \frac{5}{2} \right) \right]^{1/2} \quad (50)$$

was used for the computation of the number of gamma rays. (This formula is only slightly different from that of Strutinski's⁽¹²⁰⁾ formula, $E_{\gamma} = 2(\ell + 1) \sqrt{\frac{E}{a}}$, which was derived using a level density of $\rho \propto \exp[2(aU)^{1/2}]$, while equation (50) is a close approximation to the one derived by assuming the level density as $\rho \propto U^{-2} \exp[2(aU)^{1/2}]$). The calculated average energy of the gamma ray, \bar{E}_{γ} , was subtracted from the initial excitation

energy E , to compute the average energy of the next gamma ray. The process was continued till the excitation energy was less than 2 MeV. The choice of excitation energy at which the isomer-deciding transition (of any multipolarity) is emitted is somewhat arbitrary. The prescription of Vonach et al.⁽⁶⁹⁾ was followed in this way. For excitation energies greater than 2 MeV, it was assumed that the next gamma ray did not contain any of the 'deciding' gamma-ray transition. For excitation energies between 1 and 2 MeV, it was assumed that the probability for the emission of the isomer-deciding transition is $(2 - E)$ while the probability for a gamma ray preceding the final gamma-ray transition is $(E - 1)$. For excitation energies below 1 MeV, the final gamma ray was assumed to be emitted.

The effect of arbitrariness in the last assumption was checked⁽⁶⁹⁾ in one case (Fig. 46) by assuming the energy boundaries as 1.5 - 0.75 and 2.5 - 1.5 MeV besides the condition of 2 - 1 MeV as described in the preceding paragraph. These choices give up to 0.5 gamma rays more or less than the 2 - 1 MeV condition used. An addition or subtraction of 0.5 gamma rays (upper limit) was made to the number of gamma rays obtained as a result of the 2 - 1 MeV boundary condition, and shown in Fig. 46.

V-3.4. Transmission Coefficients

A set of transmission coefficients corresponds to a particular velocity of projectile and projectile-target system.

The compound nucleus was assumed to be formed by protons of discrete energy for a calculation of the isomer ratio

at a particular energy of bombardment (although the reported energy spread in the beam is ± 2 MeV). The associated transmission coefficients were calculated by the optical model potential and parameters due to Perey⁽¹²²⁾ and Hodgson et al.⁽¹²³⁾ (Table XXV, Appendix). Transmission coefficients were also calculated using a square-well potential in a calculation similar to that of Feshbach, Shapiro and Weisskopf.⁽¹²⁴⁾

The transmission coefficients corresponding to the 'calculated average energies' (Section V-3.2) of neutrons were obtained by optical model calculations using parameters due to Campbell et al.⁽¹²⁵⁾ (Table XXVI, Appendix). Transmission coefficients were also calculated using a square-well potential in a manner similar to Feld et al.⁽¹²⁶⁾

In the calculations described below, unless stated to the contrary, it should be assumed that optical model transmission coefficients have been used wherever required.

V-3.5. Level Density Parameter

For free nucleons confined in a nucleus of radius R, this parameter is given⁽¹²⁷⁾ by

$$a = \frac{\pi^2}{4} \frac{2^{7/3}}{(9\pi)^{2/3}} \cdot \frac{mR^2}{\hbar^2} (N^{1/3} + Z^{1/3}) \quad (51)$$

By making a simplifying assumption that $N = Z = \frac{A}{2}$ and defining $R = r_0 A^{1/3}$, (51) reduces to

$$a = 2\left(\frac{\pi}{3}\right)^{4/3} \cdot \frac{mr_0^2}{\hbar^2} A \quad (52)$$

as given by Bodansky. (18) Again substituting for m (the nucleon mass) and \hbar , one gets

$$a = 0.0512 r_0^2 A \text{ MeV}^{-1} \quad (53)$$

where r_0 is now a radius parameter in fermis. For $r_0 = 1.2$, $a = \frac{A}{13.5}$ and for $r_0 = 1.5$, $a = \frac{A}{8.7}$. Thus reasonable values of 'a' should range between these limits. The calculations reported below, however, mostly needed much larger values of the level density parameters to agree with the experimental results. The calculations were therefore performed for various values of level density parameters.

V-4. SPIN DISTRIBUTIONS AT DIFFERENT STAGES
OF DE-EXCITATION AND DETERMINATION
OF ISOMER RATIO

Figure 34 demonstrated how the spin distribution of the compound nuclei changes with the energy of the projectiles. Figure 41 shows the spin distribution at different stages of the de-excitation process. The spin cutoff parameters, required at each de-excitation stage, were obtained from the superconductor model and a level density parameter of 16 MeV^{-1} . The gamma transitions were assumed to be dipole in nature.

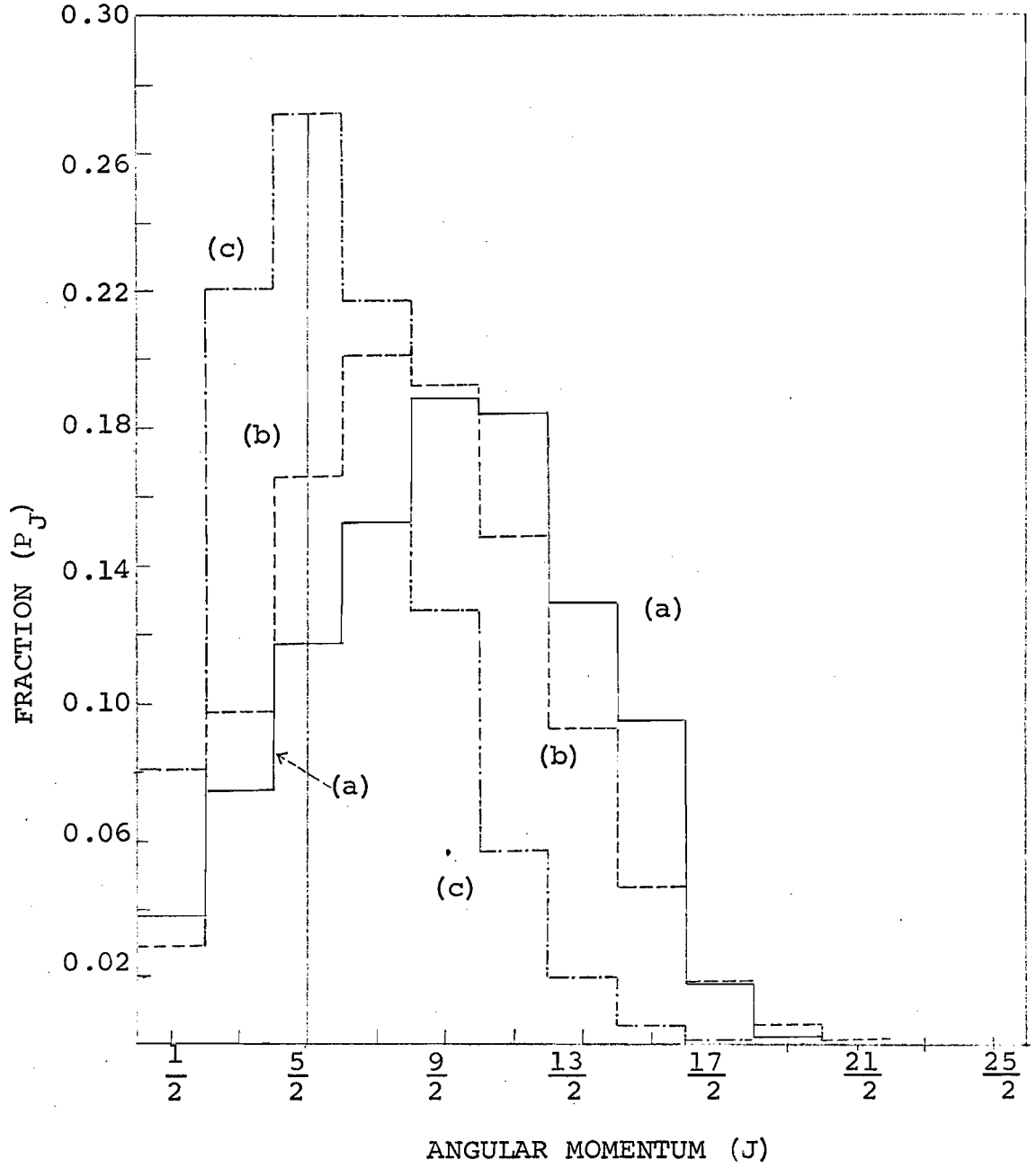
Curve (a) represents the spin distribution for the initial compound nucleus formed by protons of energy 24 MeV with target nuclei of ^{88}Sr . The spin distribution following the

Figure 41

SPIN DISTRIBUTION AT VARIOUS STAGES OF THE CALCULATION
FOR THE $^{88}\text{Sr}(p, 2n)^{87\text{m}, \text{g}}\text{Y}$ REACTION, AT 24 MeV, USING
SUPERCONDUCTOR MODEL AND $a = \frac{A}{5.5}$ (16 MeV^{-1})

- (a) Solid curve corresponds to the distribution in angular momentum of the compound nucleus ($^{88}\text{Sr} + p \rightarrow ^{88}\text{Y}$).
- (b) Dashed curve corresponds to the spin distribution following emission of the second neutron.
- (c) Dash-and-dot curve corresponds to the changed spin distribution following the emission of the third gamma ray.

[Spin distributions following the emission of first neutron and first and second gamma rays are not shown. The vertical bar at $J = \frac{5}{2}$ indicates the dividing point. States to the left of the bar populate the ground state ($I = \frac{1}{2}$) and states to the right populate the metastable state ($I = \frac{9}{2}$)]



emission of the first neutron is not shown in the diagram while curve (b) shows the spin distribution following the emission of the second neutron. The distributions following the emission of first and second gamma ray are again not indicated in the diagram, whereas curve (c) shows the distribution following the emission of a third gamma ray. In this case, this gamma ray is next to the last gamma ray and the isomer ratio is obtained by dividing the distribution at $J = \frac{5}{2}$. (Recall that the metastable state has a spin of $\frac{9}{2}$ while for the ground state $I = 1/2$.) States with J greater or less than $\frac{5}{2}$ are assumed to populate metastable and ground state respectively, whereas half the states from $J = \frac{5}{2}$ are assumed to decay to each of the metastable and ground states. This is indicated by the straight line at $J = \frac{5}{2}$ in the diagram.

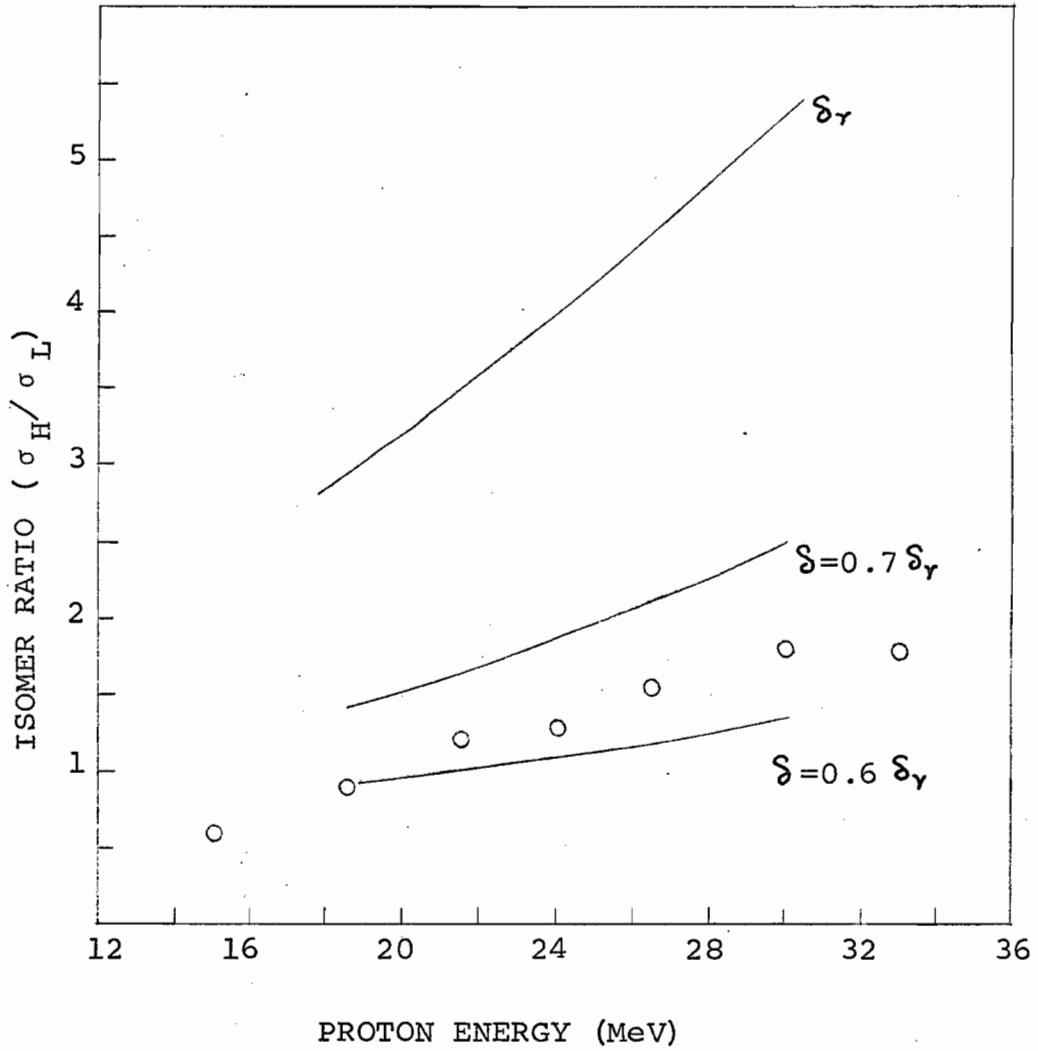
V-5. COMPARISON OF EXPERIMENTAL RESULTS WITH CALCULATIONS

The calculated results reported below are based on various choices of parameters as discussed in Section V-3. Invariably, the experimental points have been represented by 'open circles' while a smooth curve (full line) is drawn through the calculated points.

Figure 42 shows results calculated on the basis of the simple Fermi model. The calculated results, using spin cutoff parameter values obtained from rigid body moment of inertia and level density parameter of $a = \frac{A}{8}$, are very high compared to experimental results; in agreement with the observations of

Figure 42

A COMPARISON OF EXPERIMENTAL ISOMER RATIOS (OPEN CIRCLES)
AND CALCULATIONS (FULL LINES) BASED ON FRACTIONAL SPIN
CUTOFF PARAMETER VALUES (FRACTIONS INDICATED) OBTAINED
FROM THE SIMPLE FERMI MODEL AND $a = \frac{A}{8}$ (11 MeV⁻¹)



many workers. However, agreement with experimental results is obtained by using $S = 0.64 S_r$ (S_r denotes the spin cutoff parameters obtained from the simple Fermi model) which corresponds to $I = 0.4 I_r$, approximately.

The calculated results in Fig. 43 are in accordance with spin cutoff parameter values obtained from a shifted Fermi gas model and various choices of level density parameter ($a = \frac{A}{8} = 11$; $\frac{A}{5.5} = 16$; $\frac{A}{4} = 22 \text{ MeV}^{-1}$). The calculated results for the more reasonable values of $a = \frac{A}{8}$ are very high compared to the experimental results; which are in agreement with results computed by using $a = \frac{A}{4}$.

In another attempt, the level density parameter value of $a = \frac{A}{8}$ was retained while the spin cutoff parameter values were reduced by multiplying S_{SF} with a constant fraction, which in turn corresponded to a reduced moment of inertia. The calculations were performed using $S = 0.8 S_{SF}$ and $S = 0.75 S_{SF}$ and the results are shown in Fig. 44. (S_{SF} = spin cutoff parameter due to shifted Fermi model.) The experimental results are in very good agreement with the calculated values for $S = 0.75 S_{SF}$ which corresponded to an effective moment of inertia $I = 0.57 I_r$. The latter result is in good agreement with the value of $I = 0.65 I_r$, reported by Vandenbosch et al. (62) for similar calculations of $^{85}\text{Rb}(\alpha, 2n)$ and $^{87}\text{Sr}(d, 2n)$ reactions.

Figure 45 shows comparison of experimental and calculated results using spin cutoff parameter values obtained from the independent pairing model. The results are indicated

Figure 43

A COMPARISON OF EXPERIMENTAL ISOMER
RATIOS (OPEN CIRCLES) WITH CALCULATIONS (FULL LINES)
BASED ON THE SHIFTED FERMI GAS MODEL AND
INDICATED VALUES OF THE LEVEL DENSITY PARAMETER

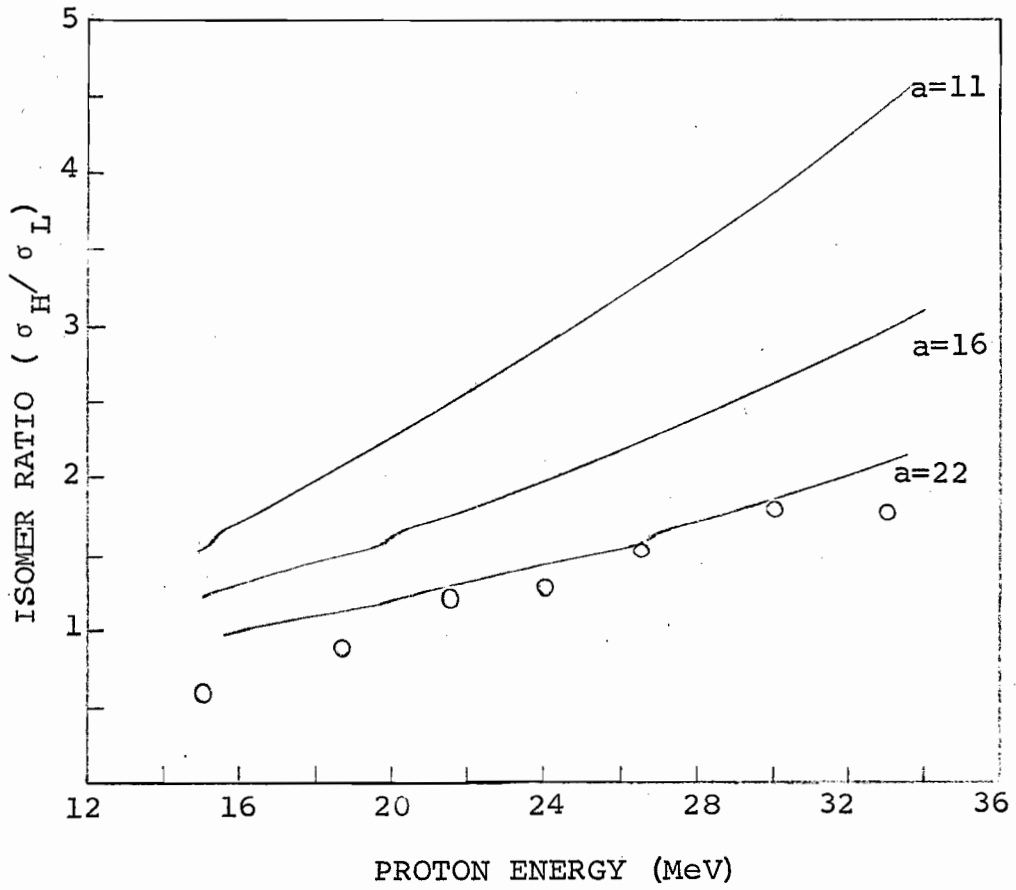


Figure 44

A COMPARISON OF EXPERIMENTAL ISOMER RATIOS (OPEN CIRCLES)
AND CALCULATIONS (FULL LINES) BASED ON FRACTIONAL SPIN
CUTOFF PARAMETER VALUES (FRACTIONS INDICATED) OBTAINED
FROM THE SHIFTED FERMI GAS MODEL AND $a = \frac{A}{8}$ (11 MeV⁻¹)

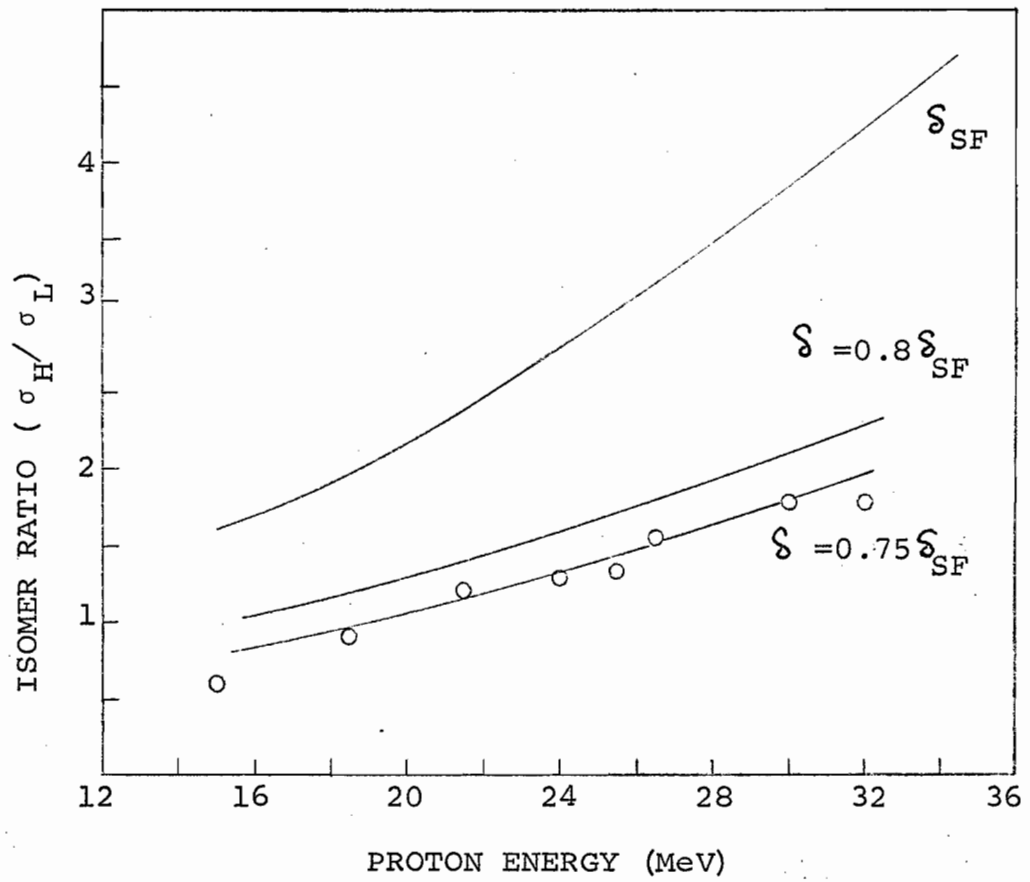
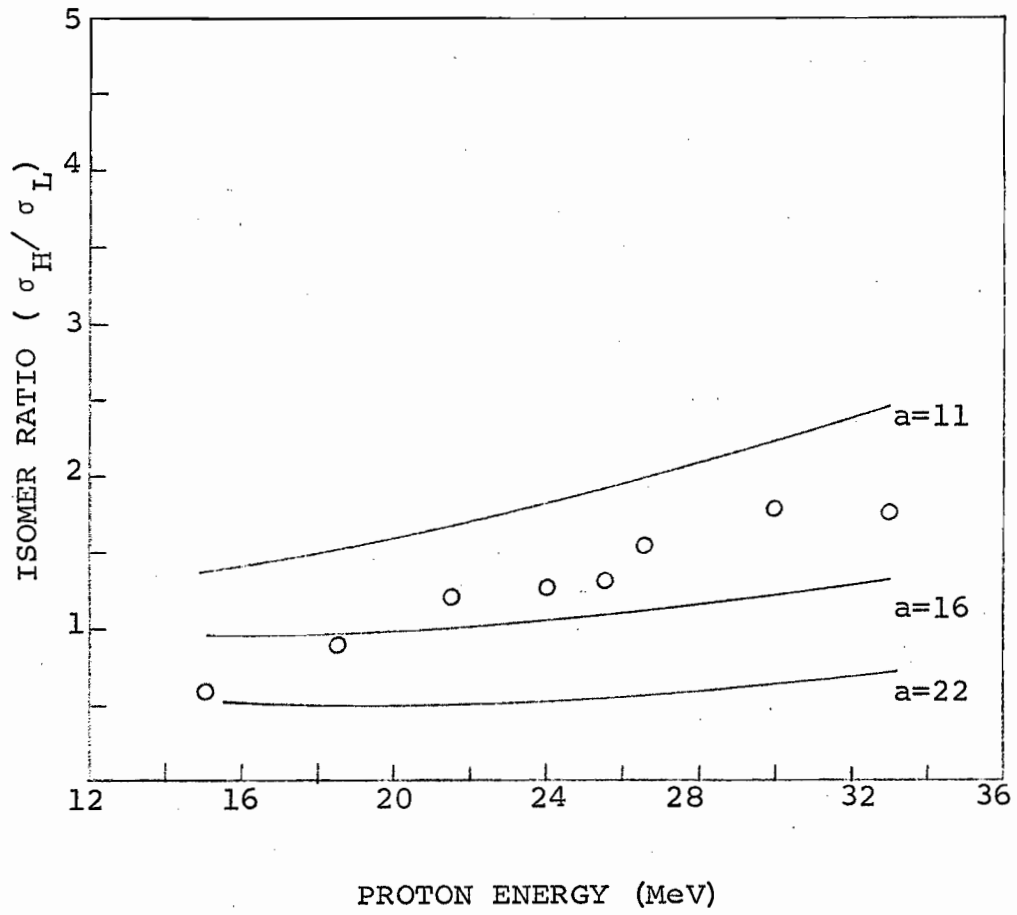


Figure 45

A COMPARISON OF EXPERIMENTAL ISOMER
RATIOS (OPEN CIRCLES) WITH CALCULATIONS (FULL LINES)
BASED ON THE INDEPENDENT PAIRING MODEL AND
INDICATED VALUES OF THE LEVEL DENSITY PARAMETER



to be in agreement with level density parameter value $a = 13 \text{ MeV}^{-1}$ ($\sim \frac{A}{7}$). Figure 46 shows the results obtained from the superconductor model and various choices of level density parameter; and the experimental results are seen to be in good agreement with the values computed with $a = 16 \text{ MeV}^{-1}$.

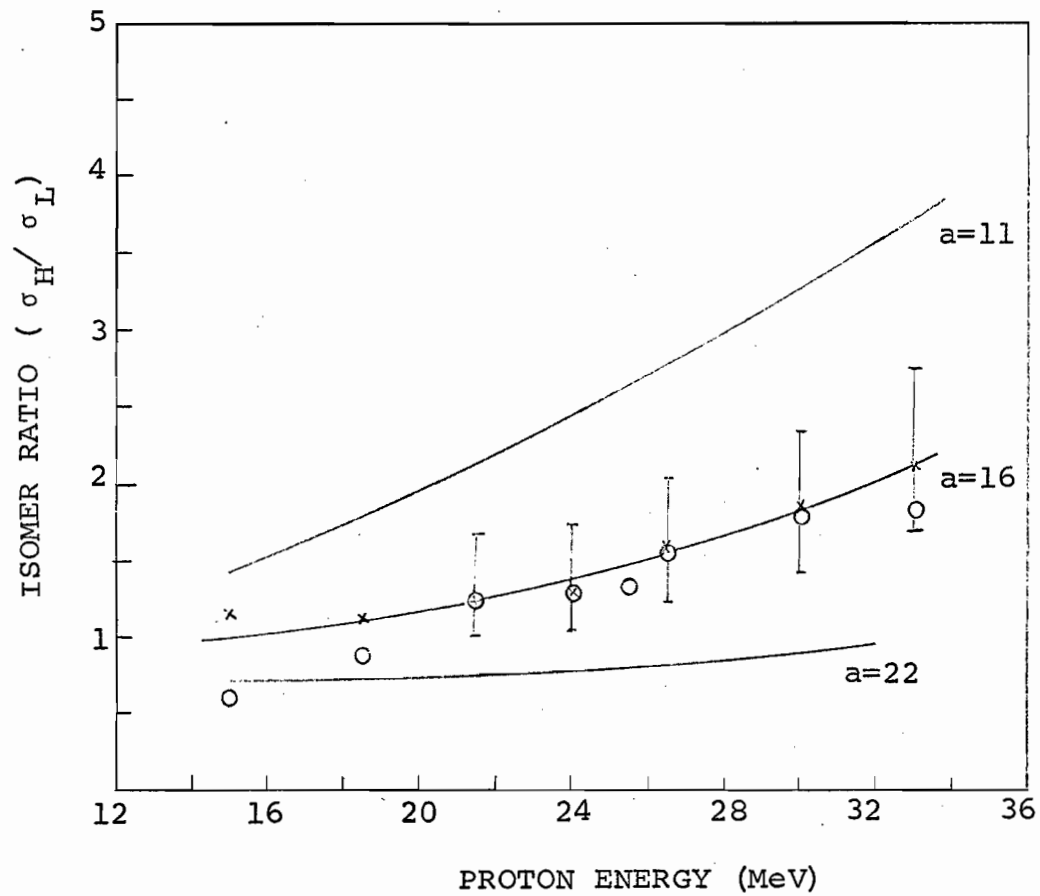
The results described above can be understood by looking at the graphs (Figs. 35-40) of spin cutoff parameter values versus excitation energies. The independent pairing model yields spin cutoff parameter values which are considerably lower, at almost all excitation energies, than those obtained from any other model. The calculations therefore reflect this in requiring a relatively small value of the level density parameter ($\sim \frac{A}{7}$) in order to produce agreement between experimental and calculated results. The superconductor model, on the other hand, gives spin cutoff parameter values which are low at low excitation energies but approach Fermi gas values at higher excitation energies (Figs. 35-40). An intermediate value of the level density parameter ($\sim \frac{A}{5.5}$), between the Fermi gas model and the independent pairing model, is therefore required for the task. A shifted Fermi gas model will obviously require an even higher value of the level density parameter ($\sim \frac{A}{4}$).

It is not gratifying to have obtained such a high value of the level density parameter. Yet it should be pointed out that the isomer ratios of $^{87\text{m,g}}\text{Y}$ obtained from reactions $^{85}\text{Rb}(\alpha, 2n)$, $^{87}\text{Sr}(d, 2n)$ and $^{88}\text{Sr}(p, 2n)$, which proceed via the same compound nucleus, are consistent among themselves. Nearly

Figure 46

A COMPARISON OF EXPERIMENTAL ISOMER
RATIOS (OPEN CIRCLES) WITH CALCULATIONS (FULL LINES)
BASED ON THE SUPERCONDUCTOR MODEL AND INDICATED
VALUES OF THE LEVEL DENSITY PARAMETER

[The crosses (x) denote the calculated isomer ratios for $a = 16 \text{ MeV}^{-1}$ and corresponding energy of protons. The vertical bars represent the changes in isomer ratios when the number of gamma rays is changed by ± 0.5 as discussed in Section V-3.3.]



the same value of the level density parameter is required to obtain a fit of calculated and experimental results using any of the models.

V-6. EFFECT OF TRANSMISSION COEFFICIENTS ON ISOMER RATIOS

Transmission coefficients were calculated using a square-well potential and the optical model with parameters due to Perey⁽¹²²⁾ and Hodgson et al.⁽¹²³⁾ for protons and Campbell et al.⁽¹²⁵⁾ for neutrons (Section V-3.4). Isomer ratios were calculated using these two sets of transmission coefficients while the remaining parameters, for a particular energy of protons, were identical. The results are presented in Table XXII. (Spin cutoff parameter values were obtained from the superconductor model and level density parameter $a = 16 \text{ MeV}^{-1}$.)

Table XXII

COMPARISON OF ISOMER RATIOS OBTAINED USING SQUARE-WELL AND OPTICAL MODEL TRANSMISSION COEFFICIENTS

Proton Energy (MeV)	Isomer Ratios with Transmission Coefficients computed with		
	Optical Model Parameters	Square-well potential with $r_0 = 1.5 \text{ F}$	Square-well potential with $r_0 = 1.7 \text{ F}$
18.5	1.12	1.02	1.23
24.0	1.29	1.24	1.50
30.0	1.87	1.85	2.23

It is thus seen that isomer ratios computed by square-well transmission coefficients, using $r_0 = 1.5 \text{ F}$, are in very good agreement with those obtained by using the optical model transmission coefficients.

V-7. EXCITATION FUNCTIONS

It has been shown in the introduction that a nuclear reaction can be described with the aid of compound nucleus and direct interaction mechanisms. At low excitation energies, (< 50 MeV), many workers^(13,29,128-37) have performed evaporation calculations using equation (6). To include the consequences of direct interaction mechanism, some workers^(13,136) have coupled the output from calculations of the cascade process to that of evaporation calculations using Monte Carlo techniques (Section I-5). The agreement with the experimental results has been fair. Esterlund and Pate⁽⁷⁾ analysed excitation function data for some alpha-induced reactions involving single particle emission via equation (9) (i.e. statistical model) with the explicit inclusion of angular momentum effects. Although they obtained reasonable values of the level density parameter ($\sim \frac{A}{8}$), the values for the ratio of the nuclear moment of inertia to that of the rigid body moment of inertia ($\frac{I}{I_r}$) were less than satisfying.

We have not attempted to perform any quantitative calculations for comparison with our experimental excitation function results. Reported below are, therefore, some of the qualitative features envisaged by the reaction mechanisms mentioned above, which could be visualized from the excitation function curves presented in Figs. 20,21,23,25,27,28,30,31 and 32. Excitation function measurements reported for other studies for reactions induced by protons, deuterons, ^3He and alpha

particles, etc., also substantiate many of these observations.

V-7.1. (p,xn) Reactions

The compound nucleus mechanism in conjunction with the statistical model predicts the formation of peaks in the excitation function curves, and the excitation function curves are expected to drop sharply as the proton energy increases beyond the peak energy values. The latter arises as the increasing proton energy successively facilitates the energy requirements for the emission of other particles. Much of this is borne out by the excitation function curves and especially the (p,xn) curves (Fig. 47). The curves also exhibit 'tails' in contradiction to compound statistical assumptions [as is very clearly manifested in the (p,n) excitation function curve] and are evidence in favour of a direct interaction mechanism.

Figure 47 shows the excitation functions of all the (p,xn) reactions studied in this work. The peak cross sections and the corresponding peak energies have also been tabulated in Table XXIII. For reactions involving the emission of more than two neutrons, the peak cross sections decrease as the number of emitted neutrons increase. This is because, at high energies, other reactions such as (p,pxn), (p,2pxn), etc., also become energetically feasible; and, as the total reaction cross section approaches a constant value, individual cross sections ought to decrease in magnitude.

Previous comparative studies with ^{63}Cu and ^{65}Cu (131,134), ^{69}Ga and ^{71}Ga (13), and amongst the nickel isotopes (130,137) have

Figure 47

EXPERIMENTAL EXCITATION FUNCTIONS FOR

$^{88}\text{Sr}(p, xn)$ REACTIONS

- - $^{88}\text{Sr}(p, n)^{88}\text{Y}$
- - $^{88}\text{Sr}(p, 2n)^{87}\text{Y}$
- △ - $^{88}\text{Sr}(p, 3n)^{86}\text{Y}$
- ◻ - $^{88}\text{Sr}(p, 4n)^{85}\text{Y}$
- ⊙ - $^{88}\text{Sr}(p, 5n)^{84}\text{Y}$

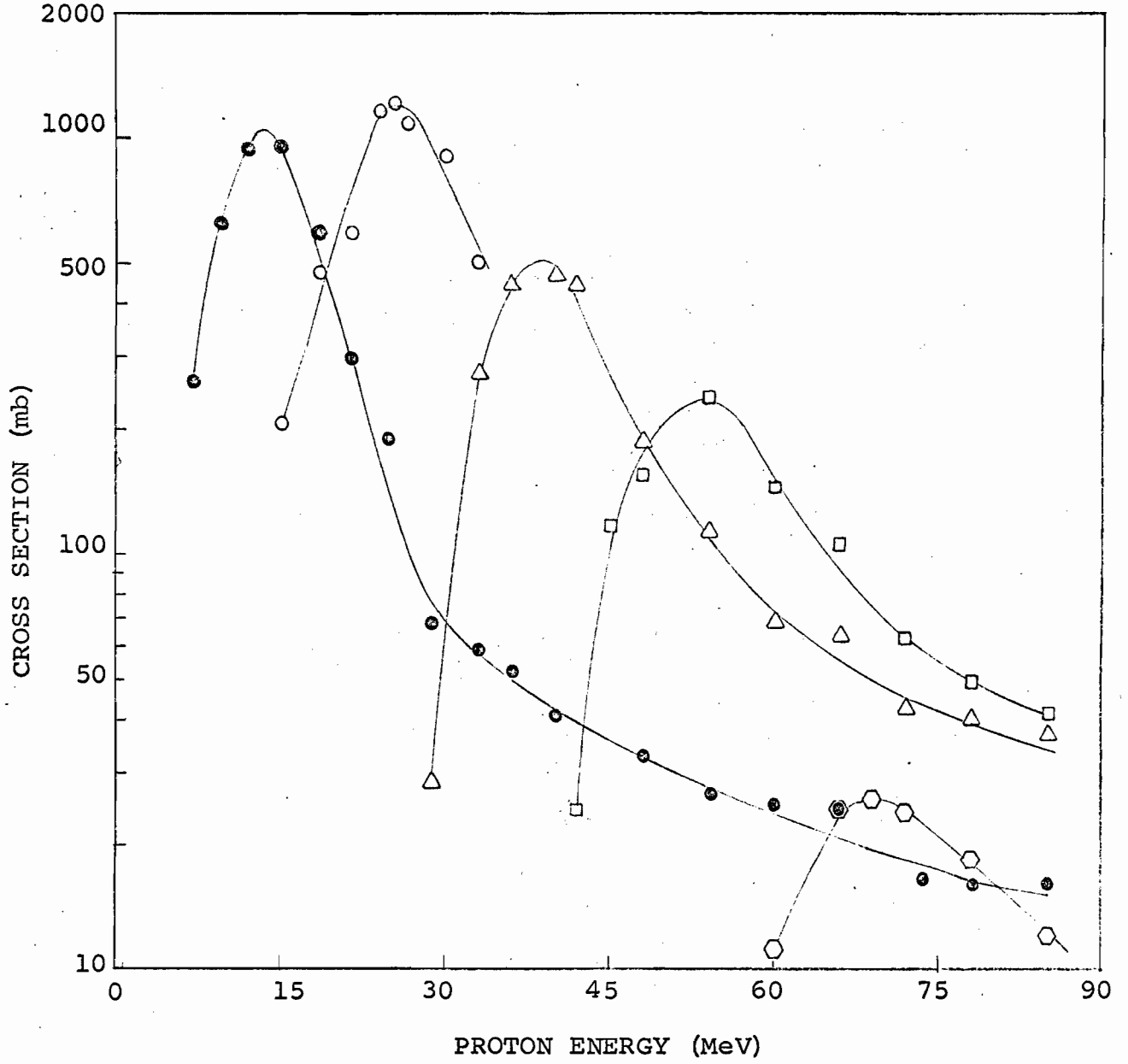


Table XXIII

PEAK CROSS SECTIONS AND ENERGIES FOR SOME
 PROTON-INDUCED REACTIONS IN ^{88}Sr AND $^{89}\text{Y}(136)$

Reaction	^{88}Sr (Target)		^{89}Y (Target)	
	Peak Energies (MeV)	Peak Cross Sections (mb)	Peak Energies (MeV)	Peak Cross Sections (mb)
(p,n)	13.5	1000	13	720
(p,2n)	25.5	1200	26	1380
(p,3n)	39	500	40	380
(p,4n)	54	230	55	80
(p,5n)	69	26	-	-
(p,p3n)	54	250	59	218
(p,2pn)	60	30	-	-
(p, α n)	36	32	-	-
(p,2p3n)	72	50	-	-
(p, α 2n)	48	73	-	-

shown that (α, xn) or (p, xn) cross sections are very much higher for the isotopes with larger numbers of neutrons. Of the four stable isotopes of strontium, ^{88}Sr is the most enriched in neutrons. Cross sections for the (p, xn) reactions for this isotope should therefore also be expected to be relatively high. Excitation function measurements for the (p, xn) and (p, pxn) products for proton-induced reactions in ^{89}Y have recently been reported⁽¹³⁶⁾ from this laboratory and the peak cross sections and corresponding energies have also been tabulated in Table XXIII for comparison. While the peak cross sections for $(p, 2n)$ reactions are about the same in the two cases (and are maxima in both studies), the cross sections for other (p, xn) products are lower for reactions induced in ^{89}Y than in ^{88}Sr . One of the possible factors explaining the higher yields of (p, xn) reactions in this work is probably the higher enrichment in neutrons of ^{88}Sr . The N/Z ratio for ^{88}Sr is 1.316, for ^{87}Sr - 1.290, and for ^{89}Y - 1.282.

Albouy et al.⁽¹¹¹⁾ have recently reported the excitation function measurements for some (p, n) reactions. Included amongst them is the $^{88}\text{Sr}(p, n)$ reaction for a proton energy range of 65-150 MeV. The cross section values obtained by these workers have also been shown in Fig. 20. Their cross sections are somewhat higher than reported in this work.

V-7.2. $(p, p3n)$ Reaction

This is the only reaction studied amongst the (p, pxn) family, as the products of (p, pxn) reactions are either stable or

yield only partial cross sections. In common with other similar studies, the peak of the $^{88}\text{Sr}(p,p3n)$ reaction (Fig. 28) is shallow. The relatively slow decrease of the excitation function curve after crossing the peak, as compared to (p,xn) reactions, is indicative of strong preference for proton re-emission at these energies.

The isobaric ratio for $(p,4n)/(p,p3n)$ reactions is plotted in Fig. 48. Except near the thresholds of the reactions, the isobaric ratio steadily decreases with increasing energy, indicating the increasing relative probability for proton emission with the increase of proton bombardment energy. It may be remarked that, near the high energy end, approximately the same value of isobaric ratio (0.2 - 0.3) was obtained for $(p,xn)/[p,p(x-1)n]$ reactions in the studies of proton-induced reactions in yttrium. (136)

V-7.3. $(p,2pxn)$ Reactions

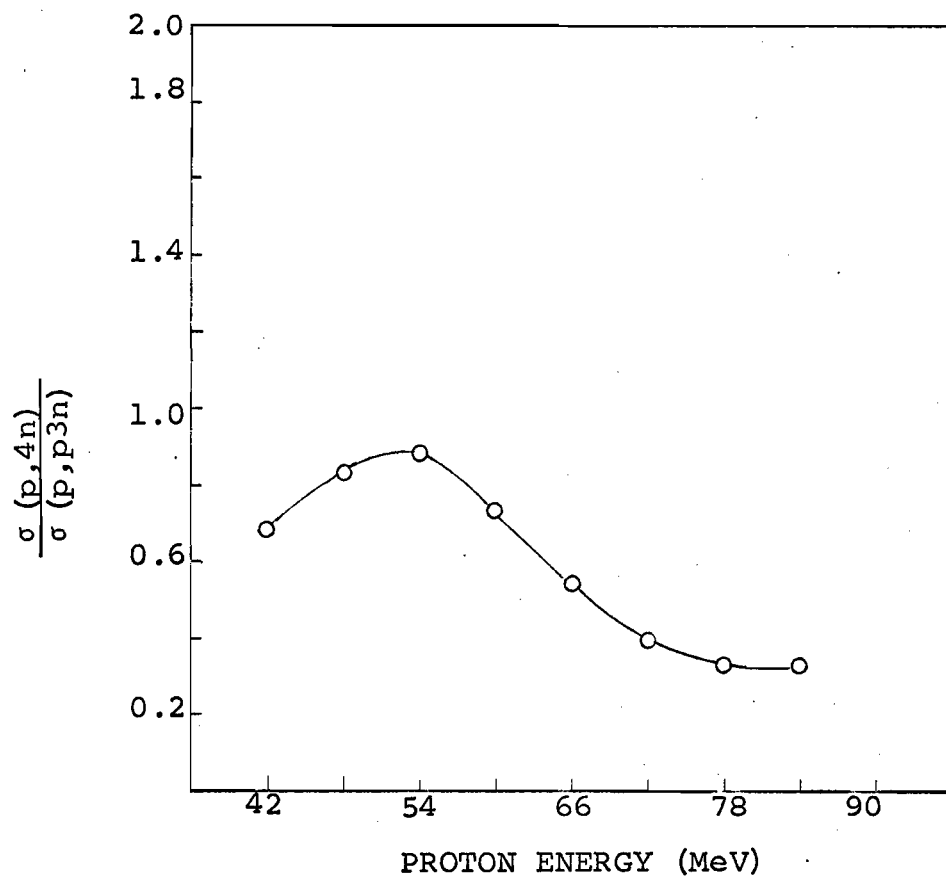
The measured excitation functions of this family are shown in Figs. 30-32.

The shape of the $(p,2pn)$ excitation function curve is similar to that observed by Porile et al. (13) for the $^{71}\text{Ga}(p,2pn)^{69}\text{Zn}$ reaction. The excitation function reaches its peak value and then decreases slowly. The relatively low cross sections for this reaction indicate 'difficulty' on the part of the excited nucleus to emit protons in preference to neutrons.

The excitation function curves for $(p,2p3n)$ and $(p,2p4n)$ reactions are typical in the sense that they exhibit

Figure 48

ISOBARIC YIELD RATIO FOR $(p,4n) / (p,p3n)$
REACTIONS VERSUS PROTON ENERGY



two peaks instead of one normally observed in medium energy nuclear reactions. The peaks are ascribed to two different reaction paths leading to the same product nuclide, i.e. a reaction which is assumed to proceed by the emission of two protons and three neutrons could also proceed by the emission of an alpha particle and a neutron. The thresholds for the reactions concerned are listed in Table XXIV.

Table XXIV

COMPARISON OF THRESHOLDS FOR (p,2pxn) AND
[p,α(x-2)n] REACTIONS

<u>Reaction</u>	<u>Threshold*</u> (MeV)
$^{88}\text{Sr}(p,2p3n)^{84}\text{Rb}$	40.1
$^{88}\text{Sr}(p,\alpha n)^{84}\text{Rb}$	11.5
$^{88}\text{Sr}(p,2p4n)^{83}\text{Rb}^+$	48.3
$^{88}\text{Sr}(p,\alpha 2n)^{83}\text{Rb}$	19.6

*Q values obtained from the 'mass excess' tables of Wapstra et al. (112)

+Mass excess table of Wapstra et al. does not give the mass excess for ^{83}Rb . Seeger's (138) table indicates that the mass excess for ^{84}Rb and ^{83}Rb are very nearly the same. The mass excess of ^{84}Rb from the table by Wapstra et al. was therefore used for ^{83}Rb .

Fulmer and Goodman⁽¹³⁹⁾ have conducted a survey of (p,α) reactions induced by protons of energy ranging between 9.5 and 23 MeV and in numerous elements throughout the periodic table. From their energy and angular distribution studies, they concluded that for $Z \leq 50$ a large fraction of (p,α) reactions proceeds by compound nucleus reactions and that 'alpha particles experience a lower coulomb barrier in leaving an excited compound nucleus than in entering a ground state nucleus'. The competitive behaviour of $(p,\alpha n)$ and $(p,\alpha 2n)$ excitation function curves in this work also supports the compound nucleus mechanism for these reactions.

Many workers^(130-32,137) have reported the excitation function measurements for the reactions involving alpha emission in the case of medium energy alpha-induced reactions for target nuclei in the medium mass region. They have also been able to correlate their results with statistical model calculations; but the possibility for the re-emission of alpha particles could not be completely ruled out. The relative magnitude of the two peaks in both excitation function curves indicates a substantial probability for alpha emission even when the projectile is not an alpha particle.

VI. SUMMARY

Excitation functions for the (p, xn) ($x = 1 - 5$), $(p, p3n)$ and $(p, 2pxn)$ ($x = 1, 3, 4$) reactions induced in ^{88}Sr by protons of energies from 7 to 85 MeV have been measured by radiochemical techniques. Shapes of the excitation function curves and their intercomparison show various features which are in accordance with compound nucleus and direct interaction mechanisms. Excitation functions for the $(p, 2p3n)$ and $(p, 2p4n)$ reactions exhibit two peaks. Threshold considerations rule out the possibility for the occurrence of these reactions at energies where their products are observed. Observation of these products at such energies is more consistent with the assumption of $(p, \alpha n)$ and $(p, \alpha 2n)$ reactions, and the first peaks of each of the excitation function curves are assigned to these two reactions. The competitive behaviour of $(p, \alpha n)$ and $(p, \alpha 2n)$ excitation function curves suggests that these reactions proceed predominantly by compound nucleus mechanism.

The ratios of the formation cross sections of the high spin isomer to that of low spin as a function of proton energy have been obtained for the products of $(p, 2n)$, $(p, 3n)$, $(p, 4n)$ and $(p, p3n)$ reactions. Qualitative considerations are presented to explain certain features of these curves. Comparison of the experimental isomer ratios for the $^{88}\text{Sr}(p, 2n)^{87}\text{Y}$, $^{85}\text{Rb}(\alpha, 2n)^{87}\text{Y}$ and $^{87}\text{Sr}(d, 2n)^{87}\text{Y}$ reactions, when all the reactions proceed via the same compound nucleus, showed distinctly the effect of

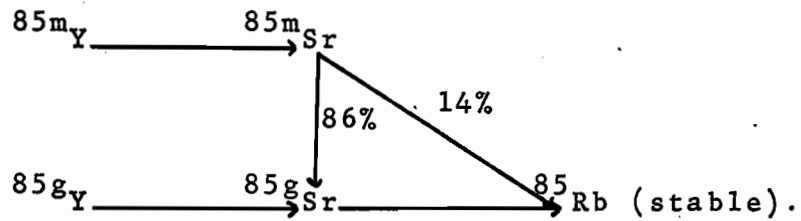
angular momentum on the formation cross sections of isomers, at a particular excitation energy of the compound nucleus. Quantitative calculations based on the Vandenbosch-Huizenga formalism for the isomer ratios of $^{85}\text{Rb}(\alpha, 2n)$ and $^{87}\text{Sr}(d, 2n)$ reactions have been performed by Vandenbosch et al. using spin cutoff parameters obtained from various models. Similar calculations using spin cutoff parameters obtained from a simple Fermi gas model, a shifted Fermi gas model, an independent pairing model and a superconductor model have been performed in this work. In all these cases, higher values of the level density parameter (but very nearly the same) than those considered reasonable ($\frac{A}{8} - \frac{A}{12}$) were required to obtain agreement between experimental and calculated results.

Computer programs were written to calculate the transmission coefficients using the optical model and square-well potentials as required in the calculation of isomer ratios.

APPENDIX

App.-1. CALCULATIONS FOR THE DISINTEGRATION RATES OF THE GROUND AND METASTABLE STATES OF ^{85}Sr

The relevant part of the mass chain of ^{85}Sr is



Since it is desirable to discuss the corrections for both isomers separately, this is done as follows.

^{85m}Sr : This isomeric species forms both independently during bombardment and as a result of decay from ^{85m}Y during and after the bombardment till strontium activities are separated from the yttrium fraction. Let us denote D_1^0 and D_{2c}^0 as the disintegration rates for the times at the end of bombardment and $t_s - t_0 = t_1$ as the time interval between the end of bombardment and separation of the strontium sample from the yttrium fraction. The disintegration rate D_2^s for ^{85m}Sr at the time of separation is given by

$$D_2^s = \frac{\lambda_2}{\lambda_2 - \lambda_1} D_1^0 (e^{-\lambda_1 t_1} - e^{-\lambda_2 t_1}) + D_{2c}^0 e^{-\lambda_2 t_1} \quad (\text{A-1})$$

Thus, knowing D_2^s , D_1^0 , t_1 and the decay constants, D_{2c}^0 could be found.

The correction for the growth of ^{85m}Sr from ^{85m}Y during the bombardment is very similar to the growth of the ground state of an isomeric nuclide when the metastable state decays completely to the ground state. The correction is therefore given by (22) (Section III-3.1)

$$D_2^o = D_{2c}^o - \frac{D_1^o}{1 - e^{-\lambda_1 t_b}} \left[1 + \frac{\lambda_1 e^{-\lambda_2 t_b} - \lambda_2 e^{-\lambda_1 t_b}}{\lambda_2 - \lambda_1} \right] \quad (\text{A-2})$$

where t_b is the duration of bombardment.

^{85g}Sr : The corrections for this isomer can be divided into three parts:

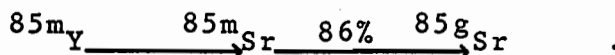
(i) After the separation time: Let D_{4c}^o , D_4^{s1} and D_4 denote the disintegration rates for ^{85g}Sr for times at the end of bombardment, separation from yttrium fraction and at any time. As the metastable state is short-lived compared to the ground state, the case becomes very similar to that described in deriving equation (7) (Section III-3.1) and we have

$$D_4 = \left[\frac{0.86 \lambda_4}{\lambda_2 - \lambda_4} D_2^s + D_4^{s1} \right] e^{-\lambda_4 t}$$

A plot of $\log D_4$ versus time will be a straight line and if D_4^G represents the disintegration rate extrapolated at separation time, we will obtain

$$D_4^{s1} = D_4^G - \frac{0.86 \lambda_4}{\lambda_2 - \lambda_4} D_2^s \quad (\text{A-3})$$

(ii) Between the End of Bombardment and Separation Time:
 In this interval ^{85g}Sr grows from ^{85g}Y and via the chain



The correction for the latter could be obtained from the knowledge of disintegration rates of ^{85m}Y and ^{85m}Sr for the times at the end of bombardment, i.e. D_1^0 and D_{2c}^0 respectively. The rate equation for ^{85g}Sr (only due to this decay chain and assuming D_4 to be zero at the end of bombardment) is given by

$$\frac{dN_4}{dt} = 0.86 \lambda_2 N_2 - \lambda_4 N_4 \quad (\text{A-4})$$

where N_2 is obtained from the familiar equation

$$N_2 = \frac{\lambda_1}{\lambda_2 - \lambda_1} N_1^0 (e^{-\lambda_1 t} - e^{-\lambda_2 t}) + N_{2c}^0 e^{-\lambda_2 t} \quad (\text{A-5})$$

Substituting (A-5) in (A-4), integrating and applying the boundary condition $N_4 = 0$ at $t = 0$, we get

$$D_4 = 0.86 \frac{\lambda_2 \lambda_4}{\lambda_2 - \lambda_1} D_1^0 \left[\frac{e^{-\lambda_4 t_1} - e^{-\lambda_1 t_1}}{\lambda_1 - \lambda_4} - \frac{e^{-\lambda_4 t_1} - e^{-\lambda_2 t_1}}{\lambda_2 - \lambda_4} \right] + 0.86 D_{2c}^0 \frac{\lambda_4 (e^{-\lambda_4 t_1} - e^{-\lambda_2 t_1})}{\lambda_2 - \lambda_4} \quad (\text{A-6})$$

Subtracting D_4 from D_4^{s1} , one obtains

$$D_4^s = D_4^{s1} - D_4 \quad (\text{A-7})$$

The disintegration D_4^s is now to be corrected for growth from ^{85g}Y , which is very similar to the conditions represented by equation (A-1). Therefore

$$D_4^s = \frac{\lambda_4}{\lambda_4 - \lambda_3} D_3^o (e^{-\lambda_3 t_1} - e^{-\lambda_4 t_1}) + D_{4c}^o e^{-\lambda_4 t_1}$$

or

$$D_{4c}^o = D_4^s e^{\lambda_4 t_1} - \frac{\lambda_4}{\lambda_3 - \lambda_4} D_3^o (1 - e^{(\lambda_4 - \lambda_3) t_1}) \quad (\text{A-8})$$

where D_3^o is the disintegration rate for the independent formation of ^{85g}Y and λ_3 represents its decay constant.

(iii) During the Bombardment: The rate equation for the formation of ^{85g}Sr during the bombardment is given by

$$\frac{dN_4}{dt} = 0.86 \lambda_2 N_2 + \lambda_3 N_3 + R_4 - \lambda_4 N_4 \quad (\text{A-9})$$

where R_4 is the rate for the formation of ^{85g}Sr for a particular flux of protons and is given by

$$\lambda_4 N_4 = R_4 (1 - e^{-\lambda_4 t}) \quad (\text{A-10})$$

The rate of formation of ^{85m}Sr is given by

$$\frac{dN_2}{dt} = \lambda_1 N_1 + R_2 - \lambda_2 N_2 \quad (\text{A-11})$$

which yields on integration (as shown in Section III-3.1)

$$N_2 = \frac{R_1 + R_2}{\lambda_2} (1 - e^{-\lambda_2 t}) + \frac{R_1}{\lambda_1 - \lambda_2} (e^{-\lambda_1 t} - e^{-\lambda_2 t}) \quad (A-12)$$

Substituting for N_3 from an equation similar to (A-10) and substituting for N_2 from (A-12) in equation (A-9), one obtains

$$\begin{aligned} \frac{dN_4}{dt} + \lambda_4 N_4 = & R_4 + 0.86 (R_1 + R_2) (1 - e^{-\lambda_2 t}) \\ & + 0.86 \frac{R_1 \lambda_2}{\lambda_1 - \lambda_2} (e^{-\lambda_1 t} - e^{-\lambda_2 t}) + R_3 (1 - e^{-\lambda_3 t}) \end{aligned} \quad (A-13)$$

Integrating (A-13) and applying the boundary condition of $N_4 = 0$ at $t = 0$, one gets for $t = t_b$

$$\begin{aligned} D_4^0 = D_{4c}^0 - 0.86 (R_1 + R_2) & \left[(1 - e^{-\lambda_4 t_b}) - \frac{\lambda_4}{\lambda_2 - \lambda_4} (e^{-\lambda_4 t_b} - e^{-\lambda_2 t_b}) \right] \\ - 0.86 R_1 \frac{\lambda_2}{\lambda_2 - \lambda_1} & \left[\frac{\lambda_4 (e^{-\lambda_4 t_b} - e^{-\lambda_2 t_b})}{\lambda_2 - \lambda_4} - \frac{\lambda_4}{\lambda_1 - \lambda_4} (e^{-\lambda_4 t_b} - e^{-\lambda_1 t_b}) \right] \\ - R_3 & \left[(1 - e^{-\lambda_4 t_b}) - \frac{\lambda_4}{\lambda_3 - \lambda_4} (e^{-\lambda_4 t_b} - e^{-\lambda_3 t_b}) \right] \end{aligned} \quad (A-14)$$

where R_1 , R_2 and R_3 are now obtained from equations like

$$R_1 = \frac{D_1^0}{(1 - e^{-\lambda_1 t_b})} \quad (A-15)$$

All the calculations leading to equations (A-2) and (A-14) which

give the disintegration rates for the independent formation of ^{85m}Sr and ^{85g}Sr respectively, for times at the end of bombardment, were carried out with the aid of the computer.

App.-2. OPTICAL MODEL AND TRANSMISSION
COEFFICIENTS

When a nucleon or a group of nucleons is incident on a nucleus, interactions amongst different nucleons set in. The resulting many-body problem is extremely difficult to handle. The optical model replaces the many-body problem by a two-body interaction between the incident particle and the target nucleus as a whole. The latter interaction is described by a complex nuclear potential of the form

$$V(r) = V_c(r) + V_o f(r) + iW_o g(r) + (V_{s_o} + iW_{s_o}) h(r) \vec{l} \cdot \vec{\sigma} \quad (\text{A-16})$$

Various terms appearing in (A-16) are defined as follows.

(i) $V_c(r)$ denotes the Coulomb potential which combines with the nuclear potential when a charged particle is incident on a target nucleus. It has been found⁽¹⁴⁰⁾ that it is not necessary to take the diffuse edge of the nucleus into account, for all practical purposes, in deriving the potential. The Coulomb potential is therefore taken as that produced by a uniform charge distribution of radius R_c and is given by

$$V_c(r) = \frac{Z_I Z_T e^2}{2R_c} \left(3 - \frac{r^2}{R_c^2} \right) \quad \text{--- for } r \leq R_c$$

and

$$V_c(r) = \frac{Z_I Z_T e^2}{r} \quad \text{----- for } r > R_c \quad (\text{A-17})$$

where Z_I and Z_T are the charges for the incident particle and target nucleus respectively.

(ii) The form factor, $f(r)$, describes the radial variation of the real potential $V_0 f(r)$. The former is usually taken as that of the Saxon-Wood type and is given by

$$f(r, r_{os}, a_s) = \frac{1}{1 + \exp[(r - r_{os} A^{1/3})/a_s]} \quad (A-18)$$

where r_{os} and a_s are the radius and the diffuseness of the nuclear surface parameters. The potential V_0 is sometimes denoted as V_s .

(iii) The imaginary potential, $W_0 g(r)$, is usually divided into two parts [$W_s f(r)$ and $W_d g(r)$]. The first part, denoted by $W_s f(r)$ corresponds to the volume component and has the same form factor [$f(r, r_{oi}, a_i)$] as that given by (A-18). The second part $W_d g(r)$ refers to the surface component (peaking on the surface) and has a form factor which is commonly taken either as that for a Gaussian, given by

$$g(r) = \exp[-(r - R_G)/b^2] \quad (A-19)$$

where R_G and b are the Gaussian radius and width respectively; or as a normalized derivative of $f(r, r_{oi}, a_i)$ as given by

$$g(r) = 4a_i \frac{d}{dr} f(r, r_{oi}, a_i) \quad (A-20)$$

the factor $4a_i$ being the normalization constant so that the surface form factor can have unity as its maximum value.

(iv) The last term in (A-16) represents the correction to the central potential due to spin-orbit interaction and is taken to be proportional to $\vec{\ell} \cdot \vec{\sigma}$, where $\vec{\ell}$ and $\vec{\sigma}$ are the angular momentum and Pauli spin operators respectively.

As in atomic physics, the most familiar form for this potential is that of the Thomas form. The form factor $h(r)$ is therefore given by

$$h(r) = - \frac{b}{r} \cdot \frac{d}{dr} (f, r_{os}, a_s) \quad (A-21)$$

where the constant 'b' is usually related to the squares of the Compton wave-length for the pion or the proton, with the resulting potentials (real and imaginary components, V_{so} and W_{so} respectively) affected accordingly. The negative sign is introduced so that the function describing the radial variation is kept positive.

For incident particles of zero spin, e.g. alpha particles, the spin-orbit potential term is obviously absent from (A-16). When the incident particles of spin 's' are incident on targets of zero spin, the intrinsic spin 's' could couple with orbital angular momentum ' ℓ ' in $(2s + 1)$ ways, leading to $(2s + 1)$ values for the nuclear potential. The argument leads to two values for the nuclear potential for neutrons or protons ($s = \frac{1}{2}$), three values for deuterons ($s = 1$) and so on. When the spins of both incident particle and target nucleus are non-zero, the problem becomes very much more complicated.

The time-independent Schrödinger wave equation could now be written as

$$-\frac{\hbar^2}{2\mu} \nabla^2 \Psi + V(r) = E \Psi \quad (\text{A-22})$$

where $V(r)$ is given by (A-16) and μ and E are the reduced mass and centre-of-mass energy for the projectile-target system. The wave function, Ψ , is next expanded as a sum over radial, angular and spin functions. As we are interested in the interaction of projectiles of spin one-half with the targets of zero spin, the eigen values of $\vec{l} \cdot \vec{\sigma}$ corresponding to the two-spin orientations with $j = l + \frac{1}{2}$ and $j = l - \frac{1}{2}$ are found to be $\frac{l}{2}$ and $-\frac{1}{2}(l + 1)$ respectively (as discussed above). The substitution of expansion of Ψ in the Schrodinger equation, therefore, leads to its separation into two differential equations for each l as

$$\frac{d^2 u_l^+(x)}{dx^2} + \left[1 - \frac{V_c}{E} - \frac{V_s f(x) + i[W_s f(x) + W_d g(x)]}{E} - \frac{l}{2E} (V_{so} + iW_{so}) h(x) - \frac{l(l+1)}{x^2} \right] u_l^+(x) = 0 \quad (\text{A-23})$$

$$\frac{d^2 u_l^-(x)}{dx^2} + \left[1 - \frac{V_c}{E} - \frac{V_s f(x) + i[W_s f(x) + W_d g(x)]}{E} + \frac{l+1}{2E} (V_{so} + iW_{so}) h(x) - \frac{l(l+1)}{x^2} \right] u_l^-(x) = 0$$

where the substitution $x = kr$ and $k = \frac{2\mu E}{\hbar^2}^{1/2}$ is also made.

The symbols u_{ℓ}^{+} and u_{ℓ}^{-} are the radial wave functions for the ℓ^{th} partial wave and angular momentum values of $j = \ell + \frac{1}{2}$ and $j = \ell - \frac{1}{2}$ respectively.

Outside the nuclear boundary, the nuclear and spin orbit potentials are zero and the equations (A-23) reduce to

$$\frac{d^2 u_{\ell}(x)}{dx^2} + \left[1 - \frac{2\gamma}{x} - \frac{\ell(\ell+1)}{x^2} \right] u_{\ell}(x) = 0 \quad (\text{A-24})$$

where $\gamma = \frac{\mu Z_I Z_T}{k \hbar^2}$.

Estimation of the reaction cross section is made as follows. A plane wave could be split into incoming and outgoing spherical waves. As a result of nuclear reaction, the amplitude of the outgoing wave is changed. If η_{ℓ}^{+} (+ corresponds to $j = \ell + \frac{1}{2}$ and - to $j = \ell - \frac{1}{2}$) represents the relative amplitude of the outgoing wave, at a large distance from the nuclear boundary, the reaction cross section is given⁽¹⁴⁰⁾ by

$$\sigma_r = \pi \kappa^2 \sum_{\ell=0}^{\infty} (\ell+1) (1 - |\eta_{\ell}^{+}|^2) + \ell(1 - |\eta_{\ell}^{-}|^2) \quad (\text{A-25})$$

where $\kappa = \frac{1}{k}$. The quantities $(1 - |\eta_{\ell}^{+}|^2)$ and $(1 - |\eta_{\ell}^{-}|^2)$ which give the fraction of particles (of ℓ^{th} partial wave and angular momentum values of $j = \ell + \frac{1}{2}$ and $j = \ell - \frac{1}{2}$ respectively) removed from the entrance channel are termed Transmission Coefficients. A computed transmission coefficient therefore refers to a particular ' ℓ ' and ' j ' value.

The relations between η_l^+ and logarithmic derivative (f_l^+) of the wave function (u_l^+) at the nuclear boundary are given by many authors. (140,141,145) They are reproduced below.

$$\frac{+}{l} = \frac{f_l^+ - \Delta_l + is_l}{f_l^+ - \Delta_l - is_l} \cdot \frac{G_l - iF_l}{G_l + iF_l} \cdot \exp(2i\sigma_l) \Big|_{x=X} \quad (\text{A-26})$$

$$\Delta_l = X \left[\frac{G_l G_l' + F_l F_l'}{G_l^2 + F_l^2} \right]_{x=X} \quad (\text{A-27})$$

$$s_l = X \left[\frac{G_l F_l' - F_l G_l'}{G_l^2 + F_l^2} \right]_{x=X} \quad (\text{A-28})$$

$$= \frac{X}{G_l^2(X) + F_l^2(X)}$$

because $G_l F_l' - F_l G_l' = 1$ (A-29)

Equation (A-29) is a Wronskian relationship and was used as a 'check' in the calculations of regular and irregular solutions F_l and G_l respectively of equation (A-24). X corresponds to the radius at which the nuclear field is assumed to be negligible and σ_l is the Coulomb phase shift, which is obviously zero for neutrons and has a negligible effect for the type of energies of protons employed in this work. The asymptotic behaviour of regular and irregular solutions is given by

$$F_\ell \cong \sin \left[x - \frac{\ell\pi}{2} - \gamma \ln(2x) + \sigma_\ell \right] \quad (\text{A-30})$$

$$G_\ell \cong \cos \left[x - \frac{\ell\pi}{2} - \gamma \ln(2x) + \sigma_\ell \right]$$

for charged particles; and

$$F_\ell \cong \sin \left(x - \frac{\ell\pi}{2} \right) \quad (\text{A-31})$$

and
$$G_\ell \cong \cos \left(x - \frac{\ell\pi}{2} \right)$$

for neutrons. The solution F_ℓ and G_ℓ , for neutrons, can be written in terms of spherical Bessel and Neuman functions:

$$F_\ell(x) = x j_\ell(x) \quad (\text{A-32})$$

and
$$G_\ell(x) = -x n_\ell(x)$$

The solutions F_ℓ and G_ℓ , for charged particles, also called Coulomb wave functions cannot be written in terms of elementary functions because they depend both on x and γ parameters. Different methods^(142,144) are available depending on the values of these parameters, and they are used in the program.

To calculate the logarithmic derivative (f_ℓ^+) , the Schrodinger wave equation (A-23) is integrated twice for each value of ℓ . The procedure is exactly the same as that used in ⁽¹⁴⁾ABACUS-1.

Further details are available in the attached program.

App.-3. SQUARE-WELL MODEL TRANSMISSION
COEFFICIENTS

The calculations of transmission coefficients by this model were made using the assumptions outlined by Blatt and Weisskopf. They are as follows:

(i) The nucleus is a sphere of well-defined surface and has a radius equal to $r_0 A^{1/3}$. The effective radius, R , is given by

$$R = r_0 A^{1/3} + \rho \quad (A-33)$$

where ρ is the radius of the incident particle. For neutrons and protons, ρ is assumed to be zero and for deuterons and alpha particles it is taken to be equal to 1.2 F. For $r < R$, there is a strong interaction and the projectile shares its energy rapidly with the nucleons of the target nucleus.

(ii) The effective potential $U_\ell(r)$ is given by

$$U_\ell(r) = V_c(r) + \frac{\hbar^2}{2\mu} \frac{\ell(\ell+1)}{r^2} \quad \text{--- for } r > R \quad (A-34)$$

and $U_\ell(r) \cong -U_0 = -\frac{\hbar^2}{2\mu} K_0^2 \quad \text{----- for } r < R$

where K_0 is obtained from the energy corresponding to the top of the Fermi distribution. For nucleons it is given⁽¹⁴⁵⁾ by

$$K_0^2 = \frac{2\mu}{\hbar^2} \mathcal{E}' = \left(\frac{9\pi}{8}\right)^{2/3} \cdot \frac{1}{r_0^2} \quad (A-35)$$

where \mathcal{E}' is the kinetic energy of the incident nucleon, which it

would acquire inside the nucleus, if it entered without appreciable kinetic energy. [Other terms in (A-34) and (A-35) have the same meanings as in the previous section.] For $r_0 = 1.5 F$, one obtains

$$K_0 \cong 1 \times 10^{-13} \text{ cm}^{-1}. \quad (\text{A-36})$$

(iii) It is assumed that, once inside the nucleus, the incident particle has very small probability for re-emission in the entrance channel. Under this assumption, the wave function will have roughly the form of the outgoing wave only, i.e.

$$u_\ell \sim \exp(-iKr) \text{ --- for } r < R \quad (\text{A-37})$$

where K is the wave number of the particle inside the nucleus and is given by

$$K = (K_0^2 + k^2)^{1/2} \quad (\text{A-38})$$

The term k in equation (A-38) is the wave number corresponding to the channel energy of the incident particle. The logarithmic derivative is obtained from (A-37) and is found to be

$$f_\ell = -iKR \quad (\text{A-39})$$

The substitution of equation (A-39) in (A-26) and simplification results in the equation of the reaction cross section as

$$\sigma_r = \pi \lambda^2 \sum_{\ell=0}^{\infty} (2\ell + 1) \frac{4s_\ell KR}{\Delta_\ell^2 + (KR + s_\ell)^2} \quad (\text{A-40})$$

where the transmission coefficient is represented by

$$T_{\ell} = \frac{4s_{\ell}KR}{\Delta_{\ell}^2 + (KR + s_{\ell})^2} \quad (A-41)$$

All the terms, except K, in equation (A-40) or (A-41) are defined in the previous section and are obtained in the same way.

The Fortran IV listings of the computer programs using both these models (optical and square-well potential) are attached at the end of this thesis.

App.-4 PARAMETERS USED FOR THE CALCULATION OF TRANSMISSION COEFFICIENTS (OPTICAL MODEL)

As mentioned in Section V-3.4, the parameters for the calculation of transmission coefficients for protons were obtained from Perey⁽¹²²⁾ and Hodgson et al.⁽¹²³⁾ The real potential V_s was calculated⁽¹²²⁾ from the equation

$$V_s = 53.3 - 0.55 E + \frac{0.4 Z}{A^{1/3}} + 27 \frac{(N - Z)}{A} \quad (A-42)$$

which for proton - ⁸⁸Sr system reduces to

$$V_s = 60.4 - 0.55 E \quad (A-43)$$

Equation (A-43) was slightly changed to take into account the results of Hodgson et al.⁽¹²³⁾ for the calculation of proton transmission coefficients at 30 and 33 MeV (Table XXV). The imaginary potential had a surface component only and the form factor was that given by (A-20). The radius and

Table XXV

PARAMETERS ^(122,123) FOR THE PROTON
TRANSMISSION COEFFICIENTS

Proton Energy (MeV)	V _s (MeV)	VREI	W _d (MeV)	V _{os} (MeV)
15	60.4	-0.55	13.5	7.0
18.5	60.4	-0.55	13.5	8.5
21.5	60.4	-0.55	13.5	8.5
24	60.4	-0.55	13.5	8.5
26.5	60.4	-0.55	13.5	8.5
30	62.0	-0.55	13.5	6.0
33	62.0	-0.55	13.5	6.0

diffuseness of the nuclear surface parameters were

$$r_{os} = r_{oi} = r_o = 1.25 F \quad (R_c = r_o A^{1/3})$$

$$a_{os} = 0.65 F \quad \text{and} \quad a_{oi} = 0.47 F.$$

Parameters which are not mentioned in the table are zero and the term VREI refers to the variation of the real potential with energy. The strengths of the potentials are negative in magnitude.

For neutrons, the parameters were taken from Campbell et al. ⁽¹²⁵⁾ They used the potential

$$V = - \frac{V_0(1 + i\mathcal{S})}{1 + \exp[2(\frac{r - R}{d})]} \quad (\text{A-44})$$

The factor $\mathcal{S} = 0.06$, when multiplied with V_0 , gives the strength of the imaginary potential. No spin orbit term was used, and the absent terms in Table XXVI are also zero.

Table XXVI

PARAMETERS FOR THE NEUTRON TRANSMISSION COEFFICIENT

V	W_s	R	d/2
(MeV)	(MeV)	(F)	(F)
52	3.12	$(1.15 A^{1/3} + 0.4)$	0.52

REFERENCES

1. N. Bohr, Nature, 137, 344 (1936).
2. H.A. Bethe, Phys. Rev., 47, 747 (1935).
3. V.F. Weisskopf, Phys. Rev., 52, 295 (1937).
4. T. Ericson, Advan. Phys., 9, 425 (1960).
5. T.D. Thomas, Nucl. Phys., 53, 558 (1964).
6. C. Hurwitz, S.J. Spencer, R.A. Esterlund, B.D. Pate, and J.B. Reynolds, Nucl. Phys., 54, 65 (1964).
7. R.A. Esterlund and B.D. Pate, Nucl. Phys., 69, 401 (1965).
8. T. Ericson, Phys. Rev. Letters, 5, 430 (1960);
Proc. International Conference on Nuclear Structure,
Kingston, Canada (1960). Ed. by D.A. Bromley
and E.W. Vogt.
9. L. Cranberg, as quoted by Ericson in Ref. 8.
10. S.N. Ghoshal, Phys. Rev., 80, 939 (1950).
11. W. John, Phys. Rev., 103, 704 (1956).
12. G.V.S. Rayudu and L. Yaffe, Can. J. Chem., 41, 2544 (1963).
13. N.T. Porile, S. Tanaka, H. Amano, M. Furukawa, S. Iwata, and M. Yagi, Nucl. Phys., 43, 500 (1963).
14. J.R. Grover and R.J. Nagle, Phys. Rev., 134, B1248 (1964).
15. R. Sherr and F. Brady, Phys. Rev., 124, 1928 (1961).
16. N.O. Lassen and N.O. Roy Poulsen, International Conference on
Low Energy Physics, Paris, July (1958).
17. L. Wolfenstein, Phys. Rev., 82, 690 (1951).
18. D. Bodansky, Ann. Rev. Nucl. Sci., 12, 79 (1962).
19. D. Bodansky, R.K. Cole, W.G. Cross, C.R. Gruhn, and I. Halpern,
Phys. Rev., 126, 1082 (1962).
20. R. Serber, Phys. Rev., 72, 1114 (1947).
21. L.J. Cook, E.M. McMillan, J.M. Peterson, and D.C. Sewell,
Phys. Rev., 75, 7 (1949).

22. P.C. Gugelot, Phys. Rev., 93, 425 (1954).
23. R.M. Eisberg and G. Igo, Phys. Rev., 93, 1039 (1954).
24. B.L. Cohen, Phys. Rev., 105, 1549 (1957).
25. N. Austern, S.T. Butler, and E. McManus, Phys. Rev.,
92, 350 (1953).
26. R.J. Griffiths and R.M. Eisberg, Nucl. Phys., 12, 225 (1959).
27. T.M. Kavanagh and R.E. Bell, Can. J. Phys., 39, 1172 (1961).
28. R.M. Eisberg, Proc. International Conference on Nuclear
Structure, Kingston, Canada (1960). Ed. by
D.A. Bromley and E.W. Vogt. (University of
Toronto Press, Toronto)
29. I. Dostrovsky, Z. Fraenkel, and G. Friedlander, Phys. Rev.,
116, 683 (1959).
30. N. Metropolis, R. Bivins, M. Storm, A. Turkevich, J.M. Miller,
and G. Friedlander, Phys. Rev., 110, 185 (1958).
N. Metropolis, R. Bivins, M. Storm, G.M. Miller, and
G. Friedlander, Phys. Rev., 110, 204 (1958).
31. H.W. Bertini, Phys. Rev., 131, 1801 (1963).
32. M.L. Goldberger, Phys. Rev., 74, 1268 (1948).
33. G. Rudstam, Ph.D Thesis (1956) 'Spallation of Medium Weight
Elements', University of Uppsala, Uppsala, Sweden.
34. G. Bernardini, E.T. Booth, and S.J. Lindenbaum, Phys. Rev.,
88, 1017 (1952).
35. G.C. Morrison, H. Muirhead, and W.G.V. Rosser, Phil. Mag.,
44, 1326 (1953).
36. H. McManus, W.T. Sharp, and H. Gellman, Phys. Rev.,
93, 924 (1954).
37. J.W. Meadows, Phys. Rev., 98, 744 (1955).
38. K.J. LeCouteur, Proc. Phys. Soc. (London), A63, 259 (1950).
39. Y. Fujimoto and Y. Yamaguchi, Progr. Theoret. Phys., 4, 468 (1949).
Ibid. 5, 787 (1950).
40. Y. Yamaguchi, Progr. Theoret. Phys., 5, 142 (1950).

41. J.D. Jackson, Can. J. Phys., 34, 767 (1956).
Ibid. 35, 21 (1957).
42. J.M. Blatt and V.F. Weisskopf, 'Theoretical Nuclear Physics',
Chapter VIII, P. 345 (John Wiley and Sons,
New York, 1952).
43. M.M. Shapiro, Phys. Rev., 90, 171 (1953).
44. H.H. Barschall, Phys. Rev., 86, 431 (1952).
45. M. Walt and H.H. Barschall, Phys. Rev., 93, 1062 (1954).
46. H. Feshbach, C.E. Porter, and V.F. Weisskopf, Phys. Rev.,
96, 448 (1954).
47. P.C. Gugelot, Phys. Rev., 87, 525 (1952).
48. V.F. Weisskopf, Physica, 22, 952 (1956).
49. V.F. Weisskopf, Physics Today, 14, No. 7, 18 (1961).
50. V.F. Weisskopf, Rev. Mod. Phys., 29, 174 (1957).
51. G. Friedlander, J.W. Kennedy, and J.M. Miller, 'Nuclear and
Radiochemistry', Chapter 8, P. 254 (John Wiley
and Sons, New York, Second Edition).
52. C.F. von Weizsäcker, Naturwiss, 24, 813 (1936).
53. J.M. Blatt and V.F. Weisskopf, 'Theoretical Nuclear Physics',
Chapter XII, P. 623 (John Wiley and Sons,
New York, 1952).
54. H. Bethe, Rev. Mod. Phys., 9, 69 (1937).
55. C. Bloch, Phys. Rev., 93, 1094 (1954).
56. J.M.B. Lang and K.J. LeCouteur, Proc. Phys. Soc. (London),
A67, 586 (1954).
57. R. Vandenbosch and J.R. Huizenga, Phys. Rev., 120, 1313 (1960).
58. D.W. Seegmiller, Lawrence Radiation Laboratory Report,
UCRL-10850 (unpublished) (1963).
59. R.L. Kiefer, Lawrence Radiation Laboratory Report,
UCRL-11049 (unpublished) (1963).
60. C. Bishop, J.R. Huizenga, and J.P. Hummel, Phys. Rev.,
135, B401 (1964).

61. C. Riley, K. Uneo, and B. Linder, Phys. Rev., 135, B1340 (1964).
62. R. Vandenbosch, L. Haskin, and J.C. Norman, Phys. Rev.,
137, B1134 (1965).
63. T. Matsuo, J.M. Matuszek, N.D. Dudey, and T.T. Sugihara,
Phys. Rev., 139, B886 (1965).
64. R.S. Tilbury and L. Yaffe, Can. J. Chem., 41, 2634 (1963).
65. H. Hurwitz and H.A. Bethe, Phys. Rev., 81, 898 (1951).
66. D.W. Lang and K.J. LeCouter, Nucl. Phys., 14, 21 (1959).
67. D.W. Lang, Nucl. Phys., 42, 353 (1963).
68. J. Bardeen, L.N. Cooper, and J.R. Schrieffer, Phys. Rev.,
108, 1175 (1957).
69. H.K. Vonach, R. Vandenbosch, and J.R. Huizenga, Nucl. Phys.,
60, 70 (1964).
70. J. Wing, Argonne National Laboratory Report, ANL-6598,
September (1962).
71. R.M. Sternheimer, Phys. Rev., 115, 137 (1959).
72. K.A. Kraus and F. Nelson, Proc. International Conference on the
Peaceful Uses of Atomic Energy, Vol. 17
(United Nations, Geneva, 1955).
73. D. Dyrssen and S. Ekberg, Acta Chemica Scandinavica,
13, 1909 (1959).
74. T.H. Handley and C.L. Burros, Anal. Chem., 31, 332 (1959).
75. C.F. Goeking, C.L. Ghann, and E.I. Wyatt, Anal. Chem.,
35, 1434 (1963).
76. E.B. Sandell, 'Colorimetric Determination of Traces of Metals',
Chapter XXXV, P. 748 (Interscience Publishers,
New York, 1959, Third Edition).
77. F.J. Welcher, 'The Analytical Uses of Ethylenediamine
Tetra-acetic Acid', Chapter VII, P. 143
(D. Van Nostrand Company, Inc., Princeton,
New Jersey, 1957).
78. A.I. Vogel, 'A Textbook of Quantitative Inorganic Analysis',
Chapter V, P. 560 (Longmans, 1961).
79. F.J. Welcher, as ref. 77, Chapter XII, P. 241.

80. F.J. Welcher, as ref. 77, Chapter VIII, P. 149.
81. B.D. Pate and L. Yaffe, Can. J. Chem., 33, 15 (1955).
82. B.D. Pate and L. Yaffe, Ibid. 33, 610 (1955).
83. B.D. Pate and L. Yaffe, Ibid. 33, 929 (1955).
84. B.D. Pate and L. Yaffe, Ibid. 33, 1656 (1955).
85. B.D. Pate and L. Yaffe, Ibid. 34, 265 (1956).
86. N.H. Lazar, R.C. Davis, and P.R. Bell, I.R.E. Transactions on Nuclear Science, NS-3, No. 4, 136 (1956).
87. R.L. Heath and F. Schroeder, Idaho Report, IDO-16149 (1955).
88. M.I. Kalkstein and J.M. Hollander, University of California Radiation Laboratory Report, UCRL-2764 (1954), (Unpublished).
89. G. Grant, M. May, and G.V.S. Rayudu, as reported in G. Grant's Ph.D Thesis, McGill University (1961).
90. R.L. Chase, 'Nuclear Pulse Spectrometry', Chapter 7, P. 165, (McGraw-Hill Book Company, Inc., New York, 1961).
91. R.M. Humes, G.F. Dell, Jr., W.D. Ploughe, and H.J. Hausman, Phys. Rev., 130, 1522 (1963).
92. Nuclear Data Sheets, National Research Council, National Academy of Sciences, U.S.A.
93. L. Yaffe and J.B. Fishman, 'Metrology of Radionuclides', International Atomic Energy Agency, Vienna, 1960, P. 185.
94. N.H. Lazar, IRE Transactions on Nuclear Science, NS-5, 138 (1958).
95. R.L. Heath, 'Scintillation Spectrometry Gamma-Ray Spectrum Catalogue', IDO-16408 (1957).
96. S. Meghir and L. Yaffe, to be published.
97. S.M. Shafroth, Nucl. Phys., 28, 649 (1961).
98. J.I. Rhode, O.E. Johnson, and W.G. Smith, Phys. Rev., 129, 815 (1963).
99. L.G. Mann and P. Axel, Phys. Rev., 84, 221 (1951).

100. T. Yamazaki, H. Ikegami, and M. Sakai, Nucl. Phys.,
30, 68 (1962).
101. L. Haskin and R. Vandenbosch, Phys. Rev., 123, 184 (1961).
102. Y.E. Kim, D.J. Horen, and J.M. Hollander, Nucl. Phys.,
31, 447 (1962).
103. B. Van Nooijen, W. Lourens, H. Van Krugten, and H. Wapstra,
Nucl. Phys., 63, 241 (1965).
104. D.J. Horen and W.H. Kelly, Bull. Am. Phys. Soc., 7, 341 (1962).
105. I. Dostrovsky, S. Katcoff, and R.W. Stoenner, Phys. Rev.,
132, 2600 (1963).
106. W.J. Nieckarz and A.A. Caretto, J. Inorg. Nucl. Chem.,
27, 919 (1965).
107. V. Maxia, W.H. Kelly, and D.J. Horen, J. Inorg. Nucl. Chem.,
24, 1175 (1962).
108. P.C. Simms, A. Namenson, T.H. Wei, and C.S. Wu, Phys. Rev.,
138, B777 (1965).
109. I. Dostrovsky, S. Katcoff, and R.W. Stoenner, Phys. Rev.,
136, B44 (1964).
110. J.B. Cumming and N.T. Porile, Phys. Rev., 122, 1267 (1961).
111. P.J. Albouy, M. Gusakow, N. Poffé, H. Sergolle, and L. Valentin,
J. de Phys. et le Radium, 23, 1000 (1962).
112. L.A. König, J.H.E. Mattauch, and A.H. Wapstra, Nucl. Phys.,
31, 18 (1962).
113. J.R. Huizenga and R. Vandenbosch, Phys. Rev., 120, 1305 (1960).
114. W.L. Hafner, J.R. Huizenga, and R. Vandenbosch, Argonne
National Laboratory Report, ANL-6662,
December (1962) (unpublished).
115. N.D. Dudey and T.T. Sugihara, Phys. Rev., 139, B896 (1965).
116. J.L. Need, Phys. Rev., 129, 1302 (1963).
117. P.E. Nemirovsky and Yu. V. Adamchuk, Nucl. Phys.,
39, 551 (1962).
118. J.M. Blatt and V.F. Weisskopf, 'Theoretical Nuclear Physics',
Chapter VIII, P. 365 (John Wiley and
Sons, New York, 1952).

119. C.T. Bishop, Argonne National Laboratory Report, ANL-6405 (1961).
120. V.M. Strutinski, L.V. Groshev, and M.K. Akimova, Nucl. Phys., 16, 657 (1960).
121. J.F. Mollenauer, Phys. Rev., 127, 867 (1962).
122. F.G. Perey, Phys. Rev., 131, 745 (1963).
123. R.C. Barrett, A.D. Hill, and P.E. Hodgson, Nucl. Phys., 62, 133 (1965).
124. H. Feshbach, M.M. Shapiro, and V.F. Weisskopf, Atomic Energy Commission Report, NYO-3077 (1953) (unpublished).
125. E.J. Campbell, H. Feshbach, C.E. Porter, and V.F. Weisskopf, MIT Technical Report No. 73, February (1960) (unpublished).
126. B.T. Feld, H. Feshbach, M.L. Goldberger, H. Goldstein and V.F. Weisskopf, Atomic Energy Commission Report NYO-636 (1951) (unpublished).
127. D.B. Beard and A. McLellan, Phys. Rev., 131, 2664 (1963).
128. K.L. Chen and J.M. Miller, Phys. Rev., 134, B1269 (1964).
129. R.L. Hahn and J.M. Miller, Phys. Rev., 124, 1879 (1961).
130. F.S. Houck and J.M. Miller, Phys. Rev., 123, 231 (1961).
131. N.T. Porile and D.L. Morrison, Phys. Rev., 116, 1193 (1959).
132. N.T. Porile, Phys. Rev., 115, 939 (1959).
133. S. Fukushima, S. Hayashi, S. Kume, H. Okamura, K. Otozai, K. Sakamoto, and Y. Yoshizawa, Nucl. Phys., 41, 275 (1963).
134. E.A. Bryant, D.F.R. Cochran, and J.D. Knight, Phys. Rev., 130, 1512 (1963).
135. Marshall Blann and George Merkel, Phys. Rev., 131, 764 (1963).
136. G.B. Saha, N.T. Porile, and L. Yaffe, Phys. Rev., 144, 962 (1966).
137. S. Tanaka, J. Phys. Soc. Japan, 15, 2159 (1960).
138. P.A. Seeger, Nucl. Phys., 25, 1 (1961).
139. C.B. Fulmer and C.D. Goodman, Phys. Rev., 117, 1339 (1960).

140. B. Buch, R.N. Maddison, and P.E. Hodgson, *Phil. Mag.*,
5, 1181 (1960).
141. E.H. Auerbach, N.C. Francis, D.T. Goldman, and C.R. Lubitz,
ABACUS-1; A Program for the Calculation of
Nuclear Cross Sections using the Cloudy
Crystal Ball Model, KAPL-3020, June (1964)
(unpublished).
142. C.E. Fröeberg, *Rev. Mod. Phys.*, 27, 399 (1955).
143. I. Stegun and M. Abramowitz, *Phys. Rev.*, 98, 1851 (1955).
144. 'Handbook of Mathematical Functions', edited by I. Stegun
and M. Abramowitz, Chapter 14 (Dover
Publications Inc., New York, 1965).
145. J.M. Blatt and V.F. Weisskopf, 'Theoretical Nuclear Physics'
Chapter VIII (John Wiley and
Sons, New York, 1952).

SOURCE STATEMENT

```
SIBFTC MAIN
C OPTICAL MODEL TRANSMISSION COEFFICIENTS
  DIMENSION VR(501),VS(501),VC(501),VI(501),VISS(501),USM(501),USP(
101),FJ(100),FN(100)
  COMPLEX ZSP,ZSM,USM,USP,DENM1,DENM2,FLSM,FLSP,ETALSM,ETALSP,CDLSL
1,CDLSL2,CGFXL1,CGFXL2
  COMMON/W/F(100),G(100),FD,GD
401 READ(5,1)
1  FORMAT(72H
  1
  READ(5,5)NMP,LMAX,1MPF,S,ES,ZZP,ENERGY,PM,TM
5  FORMAT(2I3,12,F4.0,F3.0,F5.0,3F10.0)
  READ(5,3)R1,A1,R2,A2,RC,RCU,MN
3  FORMAT(6F10.0,13)
  READ(5,4)VRE,VIS,VIV,VSR
4  FORMAT(4F10.0)
  READ(5,7)VRE1,VRE2,VIS1,VIS2,VIV1,VIV2
7  FORMAT(6F10.0)
  WRITE(6,25)
25  FORMAT(1H1,20X,65HOPTICAL MODEL TRANSMISSION COEFFICIENTS, D.
1. SACHDEV PPROGRAM//)
  WRITE(6,1)
  IF(PM)9001,101,104
101 IF(ZZP)9002,102,103
102 PM=1.0086654
  GO TO 104
103 PM=1.007276608
104 TRED=TM/(TM+PM)
  IF(ES)106,105,106
105 ELAB=ENERGY
  ECM=ELAB*TRED
  GO TO 107
106 ECM=ENERGY
  ELAB=ECM/TRED
107 REDM=1.66034*PM*TRED
  WNK=SQRT(3.2042*REDM*ECM)
  WNK=WNK/10.545
  PLSQ=31.415926536/(WNK*WNK)
  IF(ZZP)108,109,108
108 ETA=SQRT((PM*1.660434)/(3.2042*ELAB))
  ETA=(0.480298*C.480298*ZZP*ETA)/1.0545.
  GO TO 114
109 ETA=0.0
114 IF(MN)110,111,110
110 A13=TM**0.33333333
  R1=R1*A13
  R2=R2*A13
  IF(ZZP)116,117,116
116 RC=RC*A13
  GO TO 111
117 RC=0.0
111 IF(RCU)113,112,115
112 RCU=AMAX1(R1+5.*A1,R2+5.*A2)
  GO TO 115
113 RCU=R1-RCU*A1
```

SOURCE STATEMENT

```

115  X=WNK*RCO
      WRITE(6,12)PM,7M,FLAB,ECM
12   FORMAT(1H0,2X,10HPROJ MASS=E15.8,2X,3HAMU,3X,12HTARGET MASS=E15.8,
12X,3HAMU,3X,5HELAB=E15.8,2X,3HMEV,3X,4HECM=E15.8,2X,3HMEV/)
      WRITE(6,11)VRE,VRE1,VRE2,VIS,VIS1,VIS2
11   FORMAT(1H0,5X,4HVRE=F7.3,4X,5HVRE1=F7.3,4X,5HVRE2=F7.3,4X,4HVIS=F7
1.3,4X,5HVIS1=F7.3,4X,5HVIS2=F7.3/)
      WRITE(6,13)VIV,VIV1,VIV2,VSR
13   FORMAT(1H0,5X,4HVIV=F7.3,4X,5HVIV1=F7.3,4X,5HVIV2=F7.3,4X,4HVSR=F7
1.3/)
      WRITE(6,14)R1,A1,RC
14   FORMAT(1H0,17HREAL WELL RADIUS=E15.8,2X,6HFERMIS,3X,22HDIFFUSINESS
1 REAL-WELL=E15.8,2X,6HFERMIS,3X,14HCHARGE RADIUS=E15.8,2X,6HFERMIS
2/)
      WRITE(6,15)R2,A2,RCO
15   FORMAT(1H0,18HIMAG. WELL RADIUS=E15.8,2X,6HFERMIS,3X,23HDIFFUSENES
1S IMAG. WELL=E15.8,2X,6HFERMIS,3X,12HWELL CUTOFF=E15.8,2X,6HFERMIS
2/)
      WRITE(6,26)NMP,S,ZZP,PLSQ
26   FORMAT(1H0,22HNUMBER OF MESH POINTS=I3,5X,14HSPIN OF PROJ.=F5.1,5X
1,15HCHARGE PRODUCT=F6.1,4X,5HPLSQ=E15.8/)
      WRITE(6,16)X,ETA,WNK
16   FORMAT(1H0,10X,4HRHO=E15.8,15X,4HETA=E15.8,15X,14HWAVE NUMBER K=E1
15.8,2X,9HIN-FERMIS/)
      TCS=0.0
      VRE=VRE+VRE1*ECM+VRE2*ECM
      VIS=VIS+VIS1*ECM+VIS2*ECM
      VIV=VIV+VIV1*ECM+VIV2*ECM
      WRITE(6,17)VRE,VSR
17   FORMAT(1H0,21HREAL POTENTIAL DEPTH=E15.8,2X,3HMEV,3X,32HREAL SPIN-
1ORBIT POTENTIAL DEPTH=E15.8,2X,3HMEV/)
      WRITE(6,18)VIS,VIV
18   FORMAT(1H0,30HSURFACE IMAG. POTENTIAL DEPTH=E15.8,2X,3HMEV,10X,29H
1VOLUME IMAG. POTENTIAL DEPTH=E15.8,2X,3HMEV/)
      WRITE(6,21)
21   FORMAT(1H0,2X,1HL,5X,1HJ,8X,3HTLM,6X,16HPARTIAL CS MBARN,4X,1HJ,8X
1,3HTLP,4X,16HPARTIAL CS MBARN,4X,9HCSL MBARN,5X,14HTOTAL CS MBARN,
23X,9HWRUNSKIAN)
      IF(NMP-50)141,141,142
141  FNMP=NMP
      NMP=IFIX(FNMP*X)
      FNMP=NMP
      GO TO 144
142  FNMP=NMP
144  NMP1=NMP+1
      FNMP1=FNMP1
      NMPM1=NMP-1
      FNMPM1=FNMPM1
      DELTAR=RCO/FNMPM1
      DELTAX=WNK*DELTAR
C    REAL SAXON POTENTIAL
      R=0.0
      DO 150 I=1,NMP
      EX1=(R-R1)/A1
      IF(EX1-50.0)147,146,146

```

SOURCE STATEMENT

```
146 VR(I)=0.0
    GO TO 150
147 IF(EX1+50.0)148,148,149
148 VR(I)=-VRE
    GO TO 150
149 VR(I)=-VRE/(1.0+EXP(EX1))
150 R=R+DELTAR
C   SPIN ORBIT POTENTIAL
    IF(S)128,128,128
126 DO 127 I=2,NMP
127 VS(I)=0.0
    GO TO 129
128 R=0.0
    B=-2./A1
    DO 151 I=2,NMP
    R=R+DELTAR
    BS=-VR(I)/VRE
151 VS(I)=(B*(BS-BS**2))/R
C   IMAGINARY POTENTIAL
129 IF(VIV)133,135,133
133 R=0.0
    DO 136 I=1,NMP
    EX2=(R-R2)/A2
    IF(EX2-50.0)172,171,171
171 VI(I)=0.0
    GO TO 136
172 IF(EX2+50.0)174,174,175
174 VI(I)=-VIV
    GO TO 136
175 VI(I)=-VIV/(1.0+EXP(EX2))
136 R=R+DELTAR
135 IF(IMP)137,159,138
137 R=0.0
    B=-VIS
    DO 134 I=1,NMP
    EX3=EXP(-(((R-R2)/A2)**2))
    VISS(I)=B*EX3
134 R=R+DELTAR
    GO TO 156
138 R=0.0
    B=-VIS*4.0
152 DO 153 I=1,NMP
    EX4=EXP((R-R2)/A2)
    VISS(I)=(B*EX4)/(1.0+EX4)**2
153 R=R+DELTAR
158 IF (VIV)157,156,157
157 VI(I)=VI(I)+VISS(I)
    GO TO 159
156 DO 176 I=1,NMP
176 VI(I)=VISS(I)
C   COULOMB POTENTIAL
159 IF(ZZP)160,180,160
160 IF(KC-KCD)161,161,9009
161 R=0.0
    B=1.439898687*ZZP
```

SOURCE STATEMENT

```
B1=(1.5*B)/RC
B2=(0.5*B)/RC**3
KQ=IFIX((RC*FNMPM1)/RCO+1.5)
DO 162 I=1,KQ
VC(I)=B1-B2*R**2
162 R=R+DELTAR
IF(RC-RCO)163,180,9009
163 KQ=KQ+1
DO 165 I=KQ,NMP
VC(I)=B/R
165 R=R+DELTAR
DO 170 I=1,NMP
170 VR(I)=VR(I)+VC(I)
180 CLMAX=1.5*X+5.0
LL=IFIX(CLMAX)
LL=MAX0(LL,LMAX)
IF(ZZP)299,300,299
300 FN(1)=-COS(X)/X
FN(2)=(FN(1)-SIN(X))/X
IF(LL-2)720,720,702
702 FJ0=SIN(X)/X
LX=MAX0(LL+30,65)
FJ(LX+2)=1.0E-10
FJ(LX+1)=1.0E-10*(2.0*FLOAT(LX+1)+1.0)/X
L1=LX+1
DO 705 I=1,LX
I1=L1-I
FI1=I1
FJ(I1)=FJ(I1+1)*(2.0*FI1+1.0)/X-FJ(I1+2)
IF(FJ(I1)-1.0E+25)705,705,707
705 CONTINUE
GO TO 710
707 DO 709 I2=I1,LX
709 FJ(I2)=1.0E-10*FJ(I2)
GO TO 705
710 RENORM=FJ0/FJ(1)
DO 712 I=1,2
712 FJ(I)=FJ(I)*RENORM
L1=LL+1
DO 715 I=3,L1
FJ(I)=FJ(I)*RENORM
RI=I
715 FN(I)=(2.0*RI-3.0)*FN(I-1)/X-FN(I-2)
GO TO 301
720 FJ(1)=SIN(X)/X
FJ(2)=(FJ(1)-COS(X))/X
GO TO 301
299 ETASQ=ETA*ETA
ETA2=ETA*2.0
IF(ETA-4.0)1101,1140,1140
1101 CALL ASYMP(ETA,X)
GO TO 1500
1140 IF(ETA-10.)1145,1150,1150
1145 IF(X-10.)1190,1150,1150
1150 IF(ETA*ETA+4.0*ETA+3.0-(12.0*X)/5.0)1101,1160,1160
```

SOURCE STATEMENT

```
1160 IF(ETA-(15.0*X)/30.0+3.5)1170,1170,1180
1170 CALL RICAT2(ETA,X)
      GO TO 1500
1180 IF(ETA-(13.0*X)/5.0-3.0)1190,1200,1200
1190 CALL TRANS(ETA,X)
      GO TO 1500
1200 CALL RICAT1(ETA,X)
1500 G(2)=((1.0/X+ETA)*G(1)-GD)/SQRT(1.0+ETASQ)
      LL=LL+1
      IF(LL-2)575,575,571
571 DO 572 I=3,LL
      FL=I-2
572 G(1)=((2.0*FL+1.0)*(ETA+FL*(FL+1.0)/X)*G(I-1)-(FL+1.0)*SQRT(FL**2
1ETASQ)*G(I-2))/FL/SQRT((FL+1.0)**2+ETASQ)
575 LX=MAXD(LL+30,65)
      F(LX+2)=0.
      F(LX+1)=1.0E-10
      DO 578 I=1,LX
      I1=LX-1
      FL=I1+1
      F(I1+1)=((2.0*FL+1.0)*(ETA+FL*(FL+1.0)/X)*F(I1+2)-FL*SQRT((FL+1.0
1**2+ETASQ)*F(I1+3))/(FL+1.0)/SQRT(FL**2+ETASQ)
      IF(F(I1+1)-1.E14) 578,576,576
576 DO 577 I2=11,LX
577 F(I2+1)=1.0E-22*F(I2+1)
578 CONTINUE
      RENORM=SQRT(1.0+ETASQ)*(F(1)*G(2)-F(2)*G(1))
      DO 580 I1=1,LX
580 F(I1)=F(I1)/RENORM
      FD=(1.0+F(1)*GD)/G(1)
      ETAX=ETASQ+16.0
      SIGO=-ETA+ETA/2.*ALOG(ETAX)+3.5*ATAN(ETA/4.)-(ATAN(ETA)+ATAN(ETA/
1.0)+ATAN(ETA/3.0))-ETA/12.0/ETAX*(1.0+(ETASQ-48.0)/30.0/ETAX**2+(
2TA**4-160.*ETASQ+1280.)/105.0/ETAX**4)
      ALPHA1=ATAN(ETA)
      SIGL=SIGO-ALPHA1
301 DO 400 L=0,LL
      FL=L
      IF(ZZP)302,305,302
302 FXL=F(L+1)
      GXL=G(L+1)
      SLS=FL+1.0
      ALPHA=ATAN(ETA/SLS)
      SIGL=SIGL+ALPHA
      SIG2L=2.0*SIGL
      CSIG2L=COS(SIG2L)
      SSIG2L=SIN(SIG2L)
      IF(L)304,303,304
303 FDL=FD
      GDL=GD
      GO TO 310
304 DC1=(SQRT(ETA*ETA+FL*FL))/FL
      DC2=ETA/FL+FL/X
      FDL=DC1*F(L)-DC2*F(L+1)
      GDL=DC1*G(L)-DC2*G(L+1)
```

SOURCE STATEMENT

```
GO TO 310
305 FXL=X*FJ(L+1)
    GXL=-X*FN(L+1)
    IF(L)307,306,307
306 FDL=GXL
    GDL=-FXL
    GO TO 310
307 FDL=X*FJ(L)-FL*FJ(L+1)
    GDL=-X*FN(L)+FL*FN(L+1)
310 RON=FDL*GXL-FXL*GDL
    SL=X/(FXL*FXL+GXL*GXL)
    DELTAL=SL*(GXL*GDL+FXL*FDL)
    CGFXL1=CMPLX(GXL,-FXL)
    CGFXL2=CMPLX(GXL,FXL)
    CDLSL1=CMPLX(DELTAL,-SL)
    CDLSL2=CMPLX(DELTAL,SL)
C  INTEGERATION OF SCHRODINGER WAVE EQUATION
    USM(1)=CMPLX(0.0,0.0)
    USP(1)=CMPLX(0.0,0.0)
    USM(2)=CMPLX(1.0E-8,1.0E-8)
    USP(2)=CMPLX(1.0E-8,1.0E-8)
    D0=DELTAX**2
    D1=D0/ECM
    D2=2.0-D0
    FL1=FL+1.0
    D3=FL*FL1*D0
    IF(S)182,181,182
181 SO=0.0
    GO TO 185
182 SO=FL*VSR*D1
    SOM=-FL1*VSR*D1
185 DO 187 I=1,NMPM1
    X=FLOAT(I)*DELTAX
    DR=D2+D3/X**2+D1*VR(I+1)
    DI=D1*VI(I+1)
    DR1=DR+SO*VS(I+1)
    ZSP=CMPLX(DR1,DI)
    IF(S)186,187,186
186 DR2=DR+SOM*VS(I+1)
    ZSM=CMPLX(DR2,DI)
    USM(I+2)=USM(I+1)*ZSM-USM(I)
187 USP(I+2)=USP(I+1)*ZSP-USP(I)
    IF(S)188,189,188
188 IF (L)191,189,191
191 DENM1=(2.0*USM(NMP))/FNMPM1
    FLSM=(USM(NMP1)-USM(NMPM1))/DENM1
    ETALSM=((FLSM-CDLSL1)*CGFXL1)/((FLSM-CDLSL2)*CGFXL2)
    ETAREM=REAL(ETALSM)
    ETAIMM=AIMAG(ETALSM)
    IF(ZZP)5015,5017,5015
5015 ETARE1=ETAREM*CSIG2L-ETAIMM*SSIG2L
    ETAIM1=ETAREM*SSIG2L+ETAIMM*CSIG2L
    ETAREM=ETARE1
    ETAIMM=ETAIM1
5017 TLM=1.0-(ETAREM**2+ETAIMM**2)
```

SOURCE STATEMENT

```
CS1=PLSQ*FL*TLM
SJ1=FL-0.5
GO TO 192
189 TLM=0.0
    CS1=0.0
    SJ1=0.0
192 DENM2=(2.0*USP(NMP))/FNMPM1
    FLSP=(USP(NMP1)-USP(NMPM1))/DENM2
    ETALSP=((FLSP-CDLSL1)*CGFXL1)/((FLSP-CDLSL2)*CGFXL2)
    ETARE=REAL(ETALSP)
    ETAIM=AIMAG(ETALSP)
    IF(ZZP)5019,5021,5019
5019 ETARE2=ETARE*CSIG2L-ETAIM*SSIG2L
    ETAIM2=ETARE*SSIG2L+ETAIM*CSIG2L
    ETARE=ETARE2
    ETAIM=ETAIM2
5021 TLP=1.0-(ETARE**2+ETAIM**2)
    SJ2=FL+0.5
    IF(S)193,194,193
193 CS2=PLSQ*FL1*TLP
    CS=CS1+CS2
    GO TO 195
194 CS2=0.0
    CS=PLSQ*(2.0*FL+1.0)*TLP
195 TCS=TCS+CS
400 WRITE(6,8113)L,SJ1,TLM,CS1,SJ2,TLP,CS2,CS,TCS,RON
8113 FORMAT(1H0,1X,I2,2X,F5.1,2X,F11.8,2X,E15.8,2X,F5.1,2X,F11.8,2X,E1
1.8,2X,E15.8,2X,E15.8,2X,F11.8)
GO TO 401
9001 WRITE(6,31)
31  FORMAT(12X,25HERROR MESSAGE PM NEGATIVE)
GO TO 9999
9002 WRITE(6,32)
32  FORMAT(12X,37HERROR MESSAGE CHARGE PRODUCT NEGATIVE)
GO TO 9999
9009 WRITE(6,33)
33  FORMAT(12X,23HERROR MESSAGE RC GT RCO)
9999 CALL EXIT
END
```

SSAGES FOR ABOVE ASSEMBLY

SOURCE STATEMENT

```

$IBFTC SP1
SUBROUTINE ASYMP(ETA,X)
DIMENSION AA(31),BA(31),SA(31),TA(31),PA(31),QA(31),SUMS(31),SUMT(
131),SUMP(31),SUMQ(31)
COMMON/W/F(100),G(100),FD,GD
IF(X-ETA-8.0)1102,1120,1120
1102 IF(X-ETA)1115,1110,1110
1110 N=IFIX(X-ETA)
NTM=10*(9-N)+1
RD=FLOAT(9-N)
X1=X+RD
H=-0.1
GO TO 1121
1115 N=IFIX(ETA-X)
NTM=10*(N+9)+1
RD=FLOAT(9+N)
X1=X+RD
H=-0.1
GO TO 1121
1120 X1=X
1121 ETASQ=ETA*ETA
DO 1125 N=1,25
RA=N-1
SA(1)=1.0
TA(1)=0.0
PA(1)=0.0
QA(1)=1.0-ETA/X1
SUMS(1)=1.0
SUMT(1)=0.0
SUMP(1)=0.0
SUMQ(1)=1.0-ETA/X1
AA(N)=((2.0*RA+1.0)*ETA)/(2.0*X1*(RA+1.0))
BA(N)=(ETASQ-RA*(RA+1.0))/(2.0*X1*(RA+1.0))
SA(N+1)=AA(N)*SA(N)-BA(N)*TA(N)
TA(N+1)=AA(N)*TA(N)+BA(N)*SA(N)
PA(N+1)=AA(N)*PA(N)-BA(N)*QA(N)-SA(N+1)/X1
QA(N+1)=AA(N)*QA(N)+BA(N)*PA(N)-TA(N+1)/X1
SUMS(N+1)=SUMS(N)+SA(N+1)
SUMT(N+1)=SUMT(N)+TA(N+1)
SUMP(N+1)=SUMP(N)+PA(N+1)
1125 SUMQ(N+1)=SUMQ(N)+QA(N+1)
585 ETAX=ETASQ+16.0
SIGO=-ETA+ETA/2.*ALOG(ETAX)+3.5*ATAN(ETA/4.)-(ATAN(ETA)+ATAN(ETA/2
1.0)+ATAN(ETA/3.0))-ETA/12.0/ETAX*(1.0+(ETASQ-48.0)/30.0/ETAX**2+(E
2TA**4-160.*ETASQ+1280.)/105.0/ETAX**4)
Z=ALOG(2.0*X1)
THETAO=X1-(ETA*Z)+SIGO
XA=COS(THETAO)
YA=SIN(THETAO)
F(1)=SUMT(26)*XA+SUMS(26)*YA
G(1)=SUMS(26)*XA-SUMT(26)*YA
FD=SUMQ(26)*XA+SUMP(26)*YA
GD=SUMP(26)*XA-SUMQ(26)*YA
RCN=FD*G(1)-F(1)*GD
IF(X-X1)1126,1135,1126
1126 CALL INTEG(H,NTM,ETA,X,X1)
1135 RETURN
END

```

SOURCE STATEMENT

```

$IBFTC SP2
SUBROUTINE RICAT1(ETA,X)
C COULOMB WAVE FUNCTION CALCULATIONS BY RICATTI METHOD FOR RHO LT 2E
COMMON/W/F(100),G(100),FD,GD
X1=X
T=X1/(2.0*ETA)
T2=T*T
T3=T2*T
T4=T2*T2
T5=T4*T
T6=T3*T3
T7=T6*T
T8=T4*T4
T9=T8*T
T10=T5*T5
TM=(1.-T)
TM2=TM*TM
TM3=TM2*TM
TM4=TM2*TM2
TM5=TM4*TM
TM6=TM3*TM3
TM7=TM6*TM
TM8=TM4*TM4
TM9=TM8*TM
TM10=TM5*TM5
P=SQRT(T*TM)
Q=SQRT(T)
S=ARCSIN(Q)
V=ALOG(T/TM)
G0=P+S-3.1415926536/2.
G1=V/4.
G2=-(8.*T2-12.*T+9.)/(48.*P*TM)
G3=(8.*T-3.)/(64.*T*TM3)
G4=(2048.*T6-9216.*T5+16128.*T4-13440.*T3-12240.*T2+7560.*T-1890.)
1/(92160.*P*I*TM4)
G5=(3.*(1024.*T3-448.*T2+208.*T-39.))/(8192.*T2*TM6)
G6=-((262144.*T10-1966080.*T9+6389760.*T8-11714560.*T7+13178880.*T6
1-9225216.*T5+13520640.*T4-3588480.*T3+2487240.*T2-873180.*T+130977
2.))/(10321920.*P*T2*TM7)
G7=((1105920.*T5-55296.*T4+314624.*T3-159552.*T2+45576.*T-5697.)/(3
193216.*T3*TM9)
GD0=P/T
GD1=1./(4.*T*TM)
GD2=-(8.*T-3.)/(32.*P*T*TM2)
GD3=(3.*(8.*T2-4.*T+1.))/(64.*T2*TM4)
GD4=-((1536.*T3-704.*T2+336.*T-63.)/(2048.*P*T2*TM5)
GD5=(3.*(2560.*T4-832.*T3+728.*T2-260.*T+39.))/(4096.*T3*TM7)
GD6=(-368640.*T5-30720.*T4+114944.*T3-57792.*T2+16632.*T-2079.)/(6
15536.*P*T3*TM8)
GD7=(3.*(860160.*T6+196608.*T5+308480.*T4-177280.*T3+73432.*T2-177
124.*T+1899.))/(131072.*T4*TM10)
R=2.*ETA
FIX0=G1+G2/R+G3/(R**2)+G4/(R**3)+G5/(R**4)+G6/(R**5)+G7/(R**6)
SIX0=G1-G2/R+G3/(R**2)-G4/(R**3)+G5/(R**4)-G6/(R**5)+G7/(R**6)
FI0=R*G0+FIX0

```

SOURCE STATEMENT

```
SIO=-R*GO+SIXO
DFIO=R*GD0+GD1+GD2/R+GD3/(R**2)+GD4/(R**3)+GD5/(R**5)+GD6/(R**5)+G
1D7/(R**6)
DSIO=-R*GD0+GD1-GD2/R+GD3/(R**2)-GD4/(R**3)+GD5/(R**4)-GD6/(R**5)+
1GD7/(R**6)
XC=EXP(FIO)
F(1)=XC/2.0
G(1)=EXP(SIO)
FD=(F(1)*DFIO)/R
GD=(G(1)*DSIO)/R
RETURN
END
```

SOURCE STATEMENT

```
$IBFTC SP3
SUBROUTINE RICAT2(ETA,X)
C COULOMB FUNCTION CALCULATIONS FOR L=0, RICATTI METHOD RHO GT ZETA
COMMON/W/F(100),G(100),FD,GD
X1=X
T=(2.0*ETA)/X1
T2=T*T
T3=T2*T
T4=T2*T2
T5=14*T
T6=T3*T3
T7=T6*T
T8=T4*T4
T9=T8*T
T10=T5*T5
TM=(1.-T)
TM2=TM*TM
TM3=TM2*TM
TM4=TM2*TM2
TM5=TM4*TM
TM6=TM3*TM3
TM7=TM6*TM
TM8=TM4*TM4
TM9=TM8*TM
TM10=TM5*TM5
R=2.*ETA
R2=R*R
R3=R2*R
R4=R2*R2
R5=R4*R
R6=R3*R3
R7=R6*R
R8=R4*R4
R9=R8*R
R10=R5*R5
Q=SQRT(1.-T)
V=ALOG((1.-Q)/(1.+Q))
S10=(-(8.*T3-3.*T4)/(64.*R2*TM3)+(3.*T5*(1024.-448.*T+208.*T2-39.*T
13)))/(8192.*R4*TM6)-(T7*(1105920.-55296.*T+314624.*T2-159552.*T3+45
2576.*T4-5697.*T5))/(393216.*R6*TM9)
F10=(R*(Q/T+V/2.))+3.1415926536/4.-(9.*T2-12.*T+8.)/(48.*R*Q*TM)-(
12048.-9216.*T+16128.*T2-13440.*T3-12240.*T4+7560.*T5-1890.*T6)/(92
2160.*R3*Q*TM4)-(130977.*T10-873180.*T9+2487240.*T8-3588480.*T7+135
320640.*T6-9225216.*T5+15178880.*T4-11714560.*T3+6389760.*T2-196608
40.*T+262144.0)/(10321920.*R5*Q*TM7)
A=Q/T2+(8.*T-3.*T2)/(32.*R2*Q*TM2)-(T3*(1536.-704.*T+336.*T2-63.*T
13))/(2048.*R4*Q*TM5)+(T5*(368640.-30720.*T+114944.*T2-57792.*T3+16
2632.*T4-2079.*T5))/(65536.*R6*Q*TM8)
B=1./(4.*R*TM)-(3.*T2*(T2-4.*T+8.))/(64.*R3*TM4)+(3.*T4*(2560.-832
1.*T+728.*T2-260.*T3+39.*T4))/(4096.*R5*TM7)-(3.*T6*(1899.*T6-17724
2.*T5+73432.*T4-177280.*T3+308480.*T2+196608.*T+860160.))/(131072.*
3R7*TM10)
S=EXP(S10)
UM=((1./(1.-T))**0.25)*S
SF10=SIN(F10)
```

SOURCE STATEMENT

```
CF10=COS(F10)
F(1)=UM*SF10
G(1)=UM*CF10
GD=-(T2*(A*F(1)+B*G(1)))
FD=-(T2*(B*F(1)-A*G(1)))
KUN=A*UM*UM*T2
RETURN
END
```

SOURCE STATEMENT

```

$IBFTC SP4
SUBROUTINE INTEG(H,NTM,ETA,X,X1)
C   COULOMB WAVE FUNCTIONS BY INTEGRATION
DIMENSION XR(100),YR(100),Y1R(100),AR(4),BR(4),CR(4),RR(5,3),PR(5,
13),QR(5,3),STEPR(5,3)
COMMON/W/F(100),G(100),FD,GD
I=1
XR(I)=X1
YR(I)=G(1)
Y1R(I)=GD
SQRTHF=SQRT(0.5)
AR(1)=0.5
AR(2)=1.0-SQRTHF
AR(3)=1.0+SQRTHF
AR(4)=0.16666666
BR(1)=2.0
BR(2)=1.0
BR(3)=BR(2)
BR(4)=BR(1)
CR(1)=AR(1)
CR(2)=AR(2)
CR(3)=AR(3)
CR(4)=CR(1)
QR(1,1)=0.0
QR(1,2)=0.0
QR(1,3)=0.0
ETA2=2.0*ETA
2   J=1
    K=1
    RR(1,1)=XR(1)
    RR(1,2)=YR(1)
    RR(1,3)=Y1R(1)
    K=K+1
9   PR(K,1)=H
    PR(K,2)=H*RR(K-1,3)
    PR(K,3)=H*RR(K-1,2)*((ETA2/RR(K-1,1))-1.0)
7   STEPR(K,J)=AR(K-1)*(PR(K,J)-(BR(K-1)*QR(K-1,J)))
    RR(K,J)=RR(K-1,J)+STEPR(K,J)
    QR(K,J)=QR(K-1,J)+3.0*STEPR(K,J)-CR(K-1)*PR(K,J)
    IF(J.GE.3)GO TO 10
    J=J+1
    GO TO 7
10  J=1
    IF(K.GE.5) GO TO 11
    K=K+1
    GO TO 9
11  I=I+1
    XR(I)=RR(5,1)
    YR(I)=RR(5,2)
    Y1R(I)=RR(5,3)
    QR(1,1)=QR(5,1)
    QR(1,2)=QR(5,2)
    QR(1,3)=QR(5,3)
    IF(H)1312,1312,1313
1312 IF(XR(I).LT.X)GO TO 20

```

SOURCE STATEMENT

```
      GO TO 1314
1313 IF (XR(1).GT.X)GO TO 20
1314 GO TO 2
20    G(1)=YR(NTM)
      GD=Y1R(NTM)
      RETURN
      END
```

SOURCE STATEMENT

```
$1BETC SP5
SUBROUTINE TRANS(ETA,X)
C COULOMB WAVE FUNCTIONS SUBROUTINE
COMMON /W/F(100),G(100),FD,GD
ETASQ=ETA**2
ETA6=ETA**6.166666667
A1=(0.0495957017+0.00245519918/ETASQ+0.000253468412/ETASQ**2)/ETA
1**1.33333333
B1=1.0-(0.00888888889+0.00091089581/ETASQ)/ETASQ
F(1)=0.70633264*ETA6*(B1-A1)
G(1)=1.22340402*ETA6*(B1+A1)
A2=(0.172826037+0.00358121485/ETASQ+0.000907396643/ETASQ**2)/ETA*
10.666666667
B2=1.+(0.000317460317+0.000311782468/ETASQ)/ETASQ
FD=0.408695732/ETA6*(B2+A2)
GD=-0.707881773/ETA6*(B2-A2)
X1=2.0*ETA
D=X-X1
IF(D)551,580,560
551 D=ABS(D)
NTM=IFIX(10.*D+1.0)
TNM=FLUAT(NTM-1)
H=-D/TNM
GO TO 565
560 NTM=IFIX(10.*D+1.0)
TNM=FLUAT(NTM-1)
H=D/TNM
565 CALL INTEG(H,NTM,ETA,X,X1)
580 RETURN
END
```

SOURCE STATEMENT

```

$IBFTC MAIN
C TRANSMISSION COEFFICIENTS USING SQUARE-WELL POTENTIAL
  DIMENSION FJ(100),FN(100)
  COMMON/W/F(100),G(100),FD,GD
10 READ(5,1)
1  FORMAT(72H
    1
  READ(5,3)LMAX,ES,ZZP,ENSTEP,ENERGY,EMAX,TM,PM,RP
3  FORMAT(I3,F2.0,2F5.0,5F10.0)
  WRITE(6,4)
4  FORMAT(1H1,115HCONTINUUM THEORY CROSS SECTIONS AND TRANSMISSION CO
  EFFICIENTS USING BLATT AND WEISSKOPF ASSUMPTIONS-----D.R.SACHDEV/)
  WRITE(6,1)
  IF(ENSTEP)9001,150,150
150 IF(TM)9001,9001,151
151 IF(RP)9001,9001,152
152 IF(ENERGY)9001,9001,153
153 IF(EMAX)9001,155,155
155 IF(PM)9001,101,104
101 WNKOSQ=((19.0*3.1415926536)/8.0)**0.66666667)/(RP*RP)
  RS=RP*(TM**0.33333333)
  IF(ZZP)9001,102,103
102 PM=1.0086654
  GO TO 110
103 PM=1.007276608
  GO TO 110
104 WNKOSQ=1.0
  RS=RP*((TM**0.33333333)+(PM**0.33333333))
110 WRITE(6,5)PM,TM,RP,ENSTEP,ZZP
5  FORMAT(2X,10HPROJ MASS=E15.8,2X,3HAMU,3X,12HTARGET MASS=E15.8,2X,3
  1HAMU,3X,3HRO=F5.2,5X,12HENERGY STEP=F8.5,2X,3HMEV,3X,4HZZP=F6.0/)
  TRED=TM/(TM+PM)
114 IF(ES)106,105,106
105 ELAB=ENERGY
  ECM=ELAB*TRED
  GO TO 107
106 ECM=ENERGY
  ELAB=ECM/TRED
107 REDM=1.66034*PM*TRED
  WNK=SQRT(3.2042*REDM*ECM)
  WNK=WNK/10.545
  X=WNK*RS
  WNKSQ=WNK*WNK
  PLSQ=31.415926536/WNKSQ
  WNKI=SQRT(WNKOSQ+WNKSQ)
  RK=WNKI*RS
  IF(ZZP)108,109,108
108 ETA=SQRT((PM*1.660434)/(3.2042*ELAB))
  ETA=(0.480298*0.480298*ZZP*ETA)/1.0545
  GO TO 120
109 ETA=0.0
120 WRITE(6,121)X,ETA,WNK,ELAB,ECM
121 FORMAT(5X,4HRHO=E15.8,2X,4HETA=E15.8,2X,14HWAVE NUMBER K=E15.8,2X,
  15HELAB=F7.3,3HMEV,2X,4HECM=F7.3,3HMEV/)
  CLL=AMIN1(1.5*X+1.0,X-ETA+6.0,1.34*(X-2.0*ETA+20.0))

```

SOURCE STATEMENT

```
LL=IFIX(CLL)
LL=MAX0(LL,LMAX,0)
IF(ZZP)299,300,299
300 FN(1)=-COS(X)/X
    FN(2)=(FN(1)-SIN(X))/X
    IF(LL-2)720,720,702
702 FJ0=SIN(X)/X
    LX=MAX0(LL+30,65)
    FJ(LX+2)=1.0E-10
    FJ(LX+1)=1.0E-10*(2.0*FLOAT(LX+1)+1.0)/X
    L1=LX+1
    DO 705 I=1,LX
        I1=L1-I
        F11=I1
        FJ(I1)=FJ(I1+1)*(2.0*F11+1.0)/X-FJ(I1+2)
        IF(FJ(I1)-1.0E+25)705,705,707
705 CONTINUE
    GO TO 710
707 DO 709 I2=I1,LX
709 FJ(I2)=1.0E-10*FJ(I2)
    GO TO 705
710 RENORM=FJ0/FJ(1)
    DO 712 I=1,2
712 FJ(I)=FJ(I)*RENORM
    L1=LL+1
    DO 715 I=3,L1
    FJ(I)=FJ(I)*RENORM
    RI=I
715 FN(I)=(2.0*RI-3.0)*FN(I-1)/X-FN(I-2)
    GO TO 122
720 FJ(1)=SIN(X)/X
    FJ(2)=(FJ(1)-COS(X))/X
    GO TO 122
299 ETASQ=ETA*ETA
    ETA2=ETA*2.0
    IF(ETA-4.0)1101,1140,1140
1101 CALL ASYMP(ETA,X)
    GO TO 1500
1140 IF(ETA-10.)1145,1150,1150
1145 IF(X-10.)1190,1150,1150
1150 IF(ETA*ETA+4.0*ETA+3.0-(12.0*X)/5.0)1101,1160,1160
1160 IF(ETA-(13.0*X)/30.0+3.5)1170,1180,1180
1170 CALL RICAT2(ETA,X)
    GO TO 1500
1180 IF(ETA-(3.0*X)/5.0-3.0)1190,1200,1200
1190 CALL TRANS(ETA,X)
    GO TO 1500
1200 CALL RICAT1(ETA,X)
1500 G(2)=((1.0/X+ETA)*G(1)-GD)/SQRT(1.0+ETASQ)
    LL=LL+1
    IF(LL-2)575,575,571
571 DO 572 I=3,LL
    FL=I-2
572 G(I)=((2.0*FL+1.0)*(ETA+FL*(FL+1.0)/X)*G(I-1)-(FL+1.0)*SQRT(FL**2+
    ETASQ)*G(I-2))/FL/SQRT((FL+1.0)**2+ETASQ)
```

SOURCE STATEMENT

```
575 LX=MAX0(LL+30,65)
    F(LX+2)=0.
    F(LX+1)=1.0E-10
    DO 578 I=1,LX
      I1=LX-I
      FL=I1+1
      F(I1+1)=((2.0*FL+1.0)*(ETA+FL*(FL+1.0)/X)*F(I1+2)-FL*SQRT((FL+1.0)
1**2+ETASQ)*F(I1+3))/(FL+1.0)/SQRT(FL**2+ETASQ)
      IF(F(I1+1)-1.E14) 578,576,576
576 DO 577 I2=I1,LX
577 F(I2+1)=1.0E-22*F(I2+1)
578 CONTINUE
    RENORM=SQRT(1.0+ETASQ)*(F(1)*G(2)-F(2)*G(1))
    DO 580 I1=1,LX
580 F(I1)=F(I1)/RENORM
    FD=(1.0+F(1)*GD)/G(1)
122 WRITE(6,27)
27  FORMAT(1H0,5X,1HL,6X,9HWRONSKIAN,10X,2HTL,9X,16HPARTIAL CS MBARN,6
1X,14HTOTAL CS MBARN/)
    SUMCS=0.0
    DO 400 L=0,LL
      FL=L
      IF(ZZP)302,305,302
302 FXL=F(L+1)
      GXL=G(L+1)
      IF(L)304,303,304
303 FDL=FD
      GDL=GD
      GO TO 310
304 DC1=(SQRT(ETA*ETA+FL*FL))/FL
      DC2=ETA/FL+FL/X
      FDL=DC1*F(L)-DC2*F(L+1)
      GDL=DC1*G(L)-DC2*G(L+1)
      GO TO 310
305 FXL=X*FJ(L+1)
      GXL=-X*FN(L+1)
      IF(L)307,306,307
306 FDL=GXL
      GDL=-FXL
      GO TO 310
307 FDL=X*FJ(L)-FL*FJ(L+1)
      GDL=-X*FN(L)+FL*FN(L+1)
310 RUN=FDL*GXL-FXL*GDL
      SL=X/(FXL*FXL+GXL*GXL)
      DELTAL=SL*(GXL*GDL+FXL*FDL)
      TL=(4.0*RK*SL)/(DELTAL*DELTAL+(RK+SL)*(RK+SL))
      CS=PLSQ*TL*(2.0*FL+1.)
      SUMCS=SUMCS+CS
400 WRITE(6,25)L,RUN,TL,CS,SUMCS
25  FURMAT(1H0,4X,13,5X,F11.8,5X,F11.8,5X,E15.8,5X,E15.8)
    IF(ENSTEP)157,10,157
157 IF(EMAX)9001,9001,160
160 IF(EMAX-ENERGY-ENSTEP)128,129,129
128 IF(EMAX-ENERGY)131,131,130
129 ENERGY=ENERGY+ENSTEP
```

SOURCE STATEMENT

```
GO TO 114
130 ENERGY=EMAX
GO TO 114
9001 WRITE(6,31)
31  FORMAT(1H0,46HERROR MESSAGE---DATA CARD NOT PUNCHED PROPERLY)
131 GO TO 10
END
```